MSC-00126
SUPPLEMENT 2

NATIONAL AERONAUTICS AND SPACE ADMINISTRATION

APOLLO 10 MISSION REPORT
SUPPLEMENT 2

DRA

GUIDANCE, NAVIGATION, AND CONTROL SYSTEMS PERFORMANCE ANALYSIS

(NASA-TM-X-69549) APOLLO 10 MISSION REPORT. SUPPLEMENT 2: GUIDANCE, NAVIGATION, AND CONTROL SYSTEMS PERFORMANCE ANALYSIS (NASA) 212 p

N73-73554

Unclas
00/99 15039

MANNED SPACECRAFT CENTER
HOUSTON, TEXAS
NOVEMBER 1969

MSC-00126
Supplement 2

APOLLO 10 MISSION REPORT

SUPPLEMENT 2

GUIDANCE, NAVIGATION, AND CONTROL SYSTEMS PERFORMANCE ANALYSIS

PREPARED BY

TRW Systems Group

APPROVED BY

James A. McDivitt
Manager, Apollo Spacecraft Program

NATIONAL AERONAUTICS AND SPACE ADMINISTRATION
MANNED SPACECRAFT CENTER
HOUSTON, TEXAS
November 1969

11176-H386-R0-00

PROJECT TECHNICAL REPORT
TASK E-38C

APOLLO X GUIDANCE, NAVIGATION AND CONTROL SYSTEMS PERFORMANCE ANALYSIS REPORT

NAS 9-8166

31 OCTOBER 1969

Prepared for
NATIONAL AERONAUTICS AND SPACE ADMINISTRATION
MANNED SPACECRAFT CENTER
HOUSTON, TEXAS

Prepared By
Guidance and Control Systems Department

Approved by J. E. Alexander
J. E. Alexander, Manager
Guidance and Control
Systems Department

TRW
SYSTEMS GROUP

NOMENCLATURE

AGS	Abort Guidance System
APS	Ascent Propulsion System
ASA	Abort Sensor Assembly
BET	Best Estimate Trajectory
BMAG	Body Mounted Attitude Gyro
CDH	Concentric Delta Height
CDU	Coupling Data Unit
CES	Control Electronics Section
cg	Center of gravity
CM	Command Module
CMC	Command Module Computer
CSI	Concentric Sequence Initiation
CSM	Command & Service Module
DAP	Digital Autopilot
DOI	Descent Orbit Insertion
DPS	Descent Propulsion System
FCI	Flight Control Integration
FDAI	Flight Director Attitude Indicator
GDA	Gimbal Drive Actuator
GET	Ground Elapsed Time (from liftoff)
GN&C	Guidance, Navigation & Control
HOPE	Houston Operations Predictor Estimator
IMU	Inertial Measurement Unit
ISS	Inertial Subsystem
IU	Instrumentation Unit (Saturn S-IVB)
LGC	Lunar Module Guidance Computer
LM	Lunar Module
LOI 1	Lunar Orbit Insertion #1
LOI 2	Lunar Orbit Insertion #2 (circularization)
LOS	Line-of-sight
LR	Landing Radar
MCC	Midcourse Correction
PGNCS	Primary Guidance Navigation & Control System

PTC	Passive Thermal Control
RCS	Reaction Control System
REFSMMAT	Reference to Stable Member Matrix
RR	Rendezvous Radar
RTCC	Real Time Computer Complex
S/C	Spacecraft
SPS	Service Propulsion System
SXT	Sextant
T/E	Transearth
TEI	Transearth Injection
TEVENT	Computer Stored Time of Discrete Event
THC	Translation Hand Controller
T/L	Translunar
TLI	Translunar Insertion
TM	Telemetry
TPI	Terminal Phase Initiation
TVC	Thrust Vector Control
Vg	Velocity-To-Be-Gained
VHF	Very High Frequency

TABLE OF CONTENTS

	Page
1.0 INTRODUCTION	1-1
1.1 General	1-1
2.0 SUMMARY	2-1
3.0 CSM IMU PERFORMANCE	3-1
3.1 ISS Errors	3-3
4.0 CSM DIGITAL AUTOPILOT	4-1
4.1 RCS DAP Performance	4-1
4.1.1 Attitude Maneuvers	4-1
4.1.2 Attitude Hold	4-2
4.1.3 Attitude Hold During RCS Translation	4-3
4.2 TVC DAP	
4.2.1 Engine Transients and Gimbal Positioning Errors	4-4
4.2.2 Propellant Slosh and S/C Body Bending	4-4
4.2.3 LOI 1	4-5
4.2.4 LOI 2	4-6
4.2.5 TEI	4-6
4.3 Entry DAP	4-7
4.3.1 Roll Control	4-7
4.3.2 Pitch and Yaw Control	4-8
5.0 LM DIGITAL AUTOPILOT	5-1

Table of Contents (Continued)

	Page
5.1 Descent Configuration	5-1
5.1.1 Attitude Hold for Heavy Descent Configuration	5-1
5.1.2 Automatic Maneuver to DOI Attitude	5-2
5.1.3 DPS Phasing Burn	5-2
5.2 Ascent Configuration	5-3
5.2.1 APS Insertion Burn	5-3
5.2.2 Attitude Hold for Heavy Ascent Configuration	5-5
5.2.3 Automatic Maneuvers to CSI Burn Attitude	5-5
5.2.4 Automatic Maneuver to TPI Burn Attitude	5-5
5.2.5 Terminal Phase Initiation (TPI)	5-5
5.2.6 Attitude Hold for Lightest Ascent	5-6
6.0 AGS ANALYSIS	6-1
6.1 Overall System Performance Summary	6-1
6.1.1 Velocity-To-Be-Gained Residual Comparisons	6-2
6.1.2 PGNCS/AGS Alignment Accuracy	6-3
6.1.3 Environment	6-3
6.2 Sensor Performance	
6.2.1 Coasting Flight Analysis	6-4
6.2.2 APS Burn to Depletion Analysis	6-5
6.2.3 Comparison of Sensor Analysis Results to AGS Error Models	6-8

Table of Contents (Continued)

	Page
6.2.4 Analysis Accuracy	6-10
7.0 OPTICS NAVIGATION SIGHTINGS	7-1
7.1 Star-Horizon SXT Sightings	7-1
7.2 Landmark Tracking	7-2
8.0 RENDEZVOUS NAVIGATION	8-1
8.1 Onboard Navigation	8-1
8.2 Rendezvous Targeting	8-1
9.0 LANDING RADAR VELOCITY AND ALTITUDE MEASUREMENTS	9-1
9.1 Results	9-1
9.2 Data Processing	9-1
10.0 CES PERFORMANCE	10-1
10.1 APS Depletion Burn	10-1
10.2 Coasting Flight	10-2
REFERENCES	R-1
APPENDIX A - AGS ANALYSIS METHODS	

TABLES

		Page
3-1	CSM IMU System Errors	3-5
3-2	IMU Error Sources	3-7
4-1	Apollo 10 Post-Burn Vg Components	4-10
6-1	Velocity-To-Be-Gained Residual Magnitudes	6-13
6-2	PGNCS/AGS Alignment Accuracy	6-14
6-3	Gyro Static Drift Measurements (Deg/Hr)	6-15
6-4	Accelerometer Static Bias Measurements	6-16
6-5	Error Set #1 - APS Burn to Depletion	6-17
6-6	Error Set #2 - APS Burn to Depletion	6-18
6-7	Performance Summary	6-19
6-8	Equivalent Accelerometer Bias Errors (APS Burn-To-Depletion), μg	6-20
6-9	Equivalent Gyro Bias Errors (APS Burn-To-Depletion), Deg/Hr	6-21
6-10	Standard Deviation of Accelerometer Biases	6-22
6-11	Accelerometer Bias Time Stability (Average of 10-Free-Flight Measurements Differenced with PIC Values)	6-22
6-12	Gyro Bias Repeatability	6-23
6-13	Gyro Bias Time Stability	6-23
6-14	Uncertainty In Sensor Performance Measurements (3σ)	6-24
7-1	SXT Lines-of-Sight Relative to Sun Line	7-4
8-1	Rendezvous Targeting Summary	8-2
8-2	Rendezvous Targeting Solutions	8-3

ILLUSTRATIONS

		Page
3-1	Uncompensated Ascent Velocity Comparison (G&N - S-IVB)	3-8
3-2	Uncompensated Ascent Velocity Comparison (G&N - S-IVB)	3-9
3-3	Uncompensated Ascent Velocity Comparison (G&N - S-IVB)	3-10
3-4	Uncompensated TLI Velocity Comparison (G&N - S-IVB)	3-11
3-5	Uncompensated TLI Velocity Comparison (G&N - S-IVB)	3-12
3-6	Uncompensated TLI Velocity Comparison (G&N - S-IVB)	3-13
3-7	Compensated Ascent Velocity Comparison (G&N - S-IVB)	3-14
3-8	Compensated Ascent Velocity Comparison (G&N - S-IVB)	3-15
3-9	Compensated Ascent Velocity Comparison (G&N - S-IVB)	3-16
3-10	Compensated TLI Velocity Comparison (G&N - S-IVB)	3-17
3-11	Compensated TLI Velocity Comparison (G&N - S-IVB)	3-18
3-12	Compensated TLI Velocity Comparison (G&N - S-IVB)	3-19
4-1	CSM/LM Maneuver to Evasive Burn Attitude	4-11
4-2	CSM Maneuver to T/E MCC Attitude	4-12
4-3a	CSM/LM X-Axis Attitude Hold	4-13
4-3b	CSM/LM Y-axis Attitude Hold	4-14

Illustrations (Continued)

	Page
4-3c CSM/LM Z-Axis Attitude Hold	4-15
4-4a CSM X-Axis Attitude Hold	4-16
4-4b CSM Y-Axis Attitude Hold	4-17
4-4c CSM Z-Axis Attitude Hold	4-18
4-5 CSM/LM Attitude Hold During LOI 2 Ullage	4-19
4-6a CSM X-Axis Attitude Hold During T/E MCC	4-20
4-6b CSM Y-Axis Attitude Hold During T/E MCC	4-21
4-6c CSM Z-Axis Attitude Hold During T/E MCC	4-22
4-7 Spacecraft Dynamics During Evasive Maneuver	4-23
4-8 Spacecraft Dynamics During MCC_2 Maneuver	4-24
4-9 Spacecraft Dynamics During Lunar Orbit Insertion	4-25
4-10 Spacecraft During Lunar Orbit Circularization	4-27
4-11 Spacecraft Dynamics During Transearth Injection	4-29
4-12 Pitch Engine Angle During LOI 2	4-31
4-13 Yaw Engine Angle During LOI 2	4-32
4-14 FDAI Body Pitch Rate During LOI 2	4-33
4-15 FDAI Body Yaw Rate During LOI 2	4-34
4-16 LOI 1 Pitch and Yaw Attitude Errors	4-36
4-17 LOI 1 Engine Trim Estimates	4-37
4-18 LOI 1 Cross-Axis Velocity	4-38
4-19 LOI 1 Roll Attitude Error	4-39
4-20 LOI 2 Burn Parameters	4-40

Illustrations (Continued)

		Page
4-21	TEI Pitch and Yaw Attitude Errors	4-41
4-22	TEI Engine Trim Estimates	4-42
4-23	TEI Cross-Axis Velocity	4-43
4-24	TEI Roll Attitude Error	4-44
4-25	Entry Roll Command/Bank Angle Histories	4-45
4-26	Entry Pitch Jets Activity	4-46
4-27	Entry Yaw Jets Activity	4-50
4-28	Entry Fuel Consumption Per Axes	4-54
4-29	Entry Pitch Rate Damping	4-55
5-1	Attitude Hold Prior to Automatic Maneuver to DOI Attitude	5-7
5-2	Attitude Hold Prior to Automatic Maneuver to DOI Attitude	5-8
5-3	Automatic Maneuver to DOI Attitude	5-9
5-4	Automatic Maneuver to DOI Attitude	5-10
5-5	Automatic Maneuver to DOI Attitude	5-11
5-6	DPS Phasing Burn and Attitude Hold	5-12
5-7	DPS Phasing Burn and Attitude Hold	5-13
5-8	DPS Phasing Burn and Attitude Hold	5-14
5-9	APS Insertion Burn	5-15
5-10	APS Insertion Burn	5-16
5-11	APS Insertion Burn	5-17
5-12	APS Insertion Burn	5-18

Illustrations (Continued)

		Page
5-13	APS Insertion Burn	5-19
5-14	APS Insertion Burn	5-20
5-15	P-Axis Phase Plane Attitude Hold Prior to APS Insertion Burn	5-21
5-16	U-Axis Phase Plane Attitude Hold Prior to APS Insertion Burn	5-22
5-17	V-Axis Phase Plane Attitude Hold Prior to APS Insertion Burn	5-23
5-18	Automatic Maneuver to CSI Attitude Desired and Actual Rates Vs. Time P-Axis	5-24
5-19	Automatic Maneuver to CSI Attitude Desired and Actual Rates Vs. Time U-Axis	5-25
5-20	Automatic Maneuver to CSI Attitude Desired and Actual Rates Vs. Time V-Axis	5-26
5-21	Automatic Maneuver to CSI Attitude CDU Angles	5-27
5-22	Automatic Maneuver to TPI Attitude Desired and Actual Rates Vs. Time U-Axis	5-28
5-23	Automatic Maneuver to TPI Attitude Desired and Actual Rates Vs. Time V-Axis	5-29
5-24	Automatic Maneuver to TPI Attitude CDU Angles	5-30
5-25	TPI Burn P-Axis Phase Plane	5-31
5-26	TPI Burn U-Axis Phase Plane	5-32
5-27	TPI Burn V-Axis Phase Plane	5-33
5-28a	Attitude Hold After APS Burn to Depletion	5-34
5-28b	Attitude Hold After APS Burn to Depletion	5-35

Illustrations (Continued)

		Page
5-29a	Attitude Hold After APS Burn to Depletion	5-36
5-29b	Attitude Hold After APS Burn to Depletion	5-37
5-30a	Attitude Hold After APS Burn to Depletion	5-38
5-30b	Attitude Hold After APS Burn to Depletion	5-39
6-1	AGS Velocity-To-Be-Gained Magnitude; APS Burn to Depletion	6-25
6-2	Body Rate Data Derived From Changing AGS Direction Cosines	6-27
6-3	AGS/PGNCS X Axis Integrated Body Rate Differences; Coasting Flight and APS Burn to Depletion	6-29
6-4	AGS/PGNCS Y Axis Integrated Body Rate Differences; Coasting Flight and APS Burn to Depletion	6-31
6-5	AGS/PGNCS Z Axis Integrated Body Rate Differences; Coasting Flight and APS Burn to Depletion	6-33
6-6	X Body Rate - APS Burn to Depletion	6-35
6-7	Y Body Rate - APS Burn to Depletion	6-36
6-8	Z Body Rate - APS Burn to Depletion	6-37
6-9	X Axis Sensed Acceleration - APS Burn to Depletion	6-38
6-10	X Axis Sensed Velocity - APS Burn to Depletion	6-39
6-11	Y Axis Sensed Velocity - APS Burn to Depletion	6-40
6-12	Z Axis Sensed Velocity - APS Burn to Depletion	6-41
6-13	Uncompensated Sensed X-Axis Velocity Difference PGNCS Gimbal Angles Used for Transform - APS Burn to Depletion	6-42

Illustrations (Continued)

		Page
6-14	Uncompensated Sensed Y-Axis Velocity Difference; PGNCS Gimbal Angles Used for Transform - APS Burn to Depletion	6-43
6-15	Uncompensated Sensed Z-Axis Velocity Difference; PGNCS Gimbal Angles Used for Transform - APS Burn to Depletion	6-44
6-16	Compensated Sensed X-Axis Velocity Difference; PGNCS Gimbal Angles Used for Transform - APS Burn to Depletion	6-45
6-17	Compensated Sensed Y-Axis Velocity Difference; PGNCS Gimbal Angles Used for Transform - APS Burn to Depletion	6-46
6-18	Compensated Sensed Z-Axis Velocity Difference; PGNCS Gimbal Angles Used for Transform - APS Burn to Depletion	6-47
6-19	Uncompensated Sensed X-Axis Velocity Difference; AGS Direction Cosines Used for Transform - APS Burn to Depletion	6-48
6-20	Uncompensated Sensed Y-Axis Velocity Difference; AGS Direction Cosines Used for Transform - APS Burn to Depletion	6-49
6-21	Uncompensated Sensed Z-Axis Velocity Difference; AGS Direction Cosines Used for Transform - APS Burn to Depletion	6-50
6-22	Compensated Sensed X-Axis Velocity Difference; AGS Direction Cosines Used for Transform - APS Burn To Depletion	6-51
6-23	Compensated Sensed Y-Axis Velocity Difference; AGS Direction Cosines Used for Transform - APS Burn To Depletion	6-52
6-24	Compensated Sensed Z-Axis Velocity Difference; AGS Direction Cosines Used for Transform - APS Burn to Depletion	6-53

Illustrations (Continued)

		Page
8-1	Comparison of CSM VHF Range & LM RR Range with BET Range	8-4
8-2	Comparison of LM Range Rate With BET Range Rate	8-5
8-3	Comparison of LGC & CMC Range & Range Rate Data During Rendezvous	8-6
9-1	LR Velocity Minus G&N Velocity (X Component)	9-3
9-2	LR Velocity Minus G&N Velocity (Y Component)	9-4
9-3	LR Velocity Minus G&N Velocity (Z Component)	9-5
9-4	Comparison of LR Measured Altitude and BET Altitude	9-6
9-5	Lunar Surface Profile Measured by Landing Radar	9-7
10-1	Pulse Ratio Modulator Characteristics	10-3

1.0 INTRODUCTION

1.1 GENERAL

This report presents the conclusions of the analyses of the inflight performance of the Apollo 10 mission (AS-505/CSM-106/LM-4) guidance, navigation and control equipment and is intended to supplement the Apollo 10 mission report (Reference 1). The report was prepared and submitted under MSC/TRW Task E-38C, "G&C Test Analysis." Results reported herein reflect a working interface between Task E-38C, MSC/TRW Task A-50, "Trajectory Reconstruction" and MSC/TRW Task E-72B, "G&C System Analysis." These tasks are highly interdependent and the cooperation and support of the A-50 and E-72 task personnel are gratefully acknowledged.

2.0 SUMMARY

CSM IMU performance was near nominal based on error separation studies conducted for the boost and TLI phases. A set of error terms for each phase was derived, each set compatible with the other, which provided a satisfactory fit to the observed system errors. During the translunar and transearth coast the IMU remained powered up and considerable data were obtained on IMU freeflight drift characteristics and PIPA bias stability.

The performance of the CSM DAP was satisfactory. The peak attitude errors during the DAP controlled SPS burns were 0.5 deg or less. The RCS DAP performance during attitude hold, automatic maneuvers, ullage, and RCS translation burns were satisfactory. The entry DAP performed nominally with 33.0 lbs of RCS propellant used.

SXT midcourse navigation sightings performed during translunar and transearth flight were evaluated. The trunnion bias and noise values obtained were comparable with previous flights but unusually wide variations in earth horizon bias (0.82 to 20.6 nm) were observed on this flight in comparisons to previous missions. Cause for this wide variation could not be correlated with the latitude of the point of tangency or sun angles relative to the two lines-of-sight.

LM IMU performance was acceptable based on the near nominal execution of the LM orbital maneuvers. No error separation studies were conducted due to the short durations and low accelerations of the LM burns. Some question did arise on Apollo 10 as to the integrity of the X IMU gyro. One of the AOT alignments yielded a X sm torquing angle which corresponded to a gyro drift of 14 meru. One sigma drift uncertainty is 2 meru. Numerous procedural, hardware and systematic problems were considered which would cause the large drift or would yield a false torquing angle. Due to the good hardware performance both before and after the problem occurred,a probable hardware failure mode was not evident. Procedures were thoroughly reviewed and no

procedural anomaly was apparent. A systematic error was dismissed since one of the earlier alignments was checked against an independent CSM IMU alignment and the errors were acceptable. Another possible cause is an error in one of the sighting vectors. Confidence in the sighting data is normally based on a star angle difference check which is a comparison of the calculated subtended angle between the two AOT sighting vectors with the theoretical angle between the two stars. A good check can be obtained however, in the presence of a significant sighting error, if the two stars lie in a plane which contains two of the platform axes. This was the case for this alignment and it's most probable that a sighting error caused an erroneous torquing angle.

Performance of the LM DAP during coasting and powered flight appeared nominal. Automatic attitude hold and automatic maneuvers at 2 deg/sec in the descent configuration were performed in accordance with the software design. Automatic attitude hold of the ascent configuration for both the wide and narrow deadbands was quite satisfactory.

Landing Radar data obtained during the first pass through perigee (6.65 nm altitude) after the DOI maneuver indicated the radar was functioning properly and accurately measuring the LM relative velocity and altitude above the surface. Considerable confidence in the LR system for the lunar landing mission was gained from the data.

The LM active rendezvous was conducted without incident and the total ΔV required to perform the LM maneuvers was within one percent of the nominal ΔV. All of the burn solutions were solved for by the LGC based solely on rendezvous radar data to correct for any trajectory dispersions.

Overall performance of the Abort Guidance System (AGS) was excellent. State vector initializations and PGNCS/AGS alignments were smoothly accomplished within expected accuracies. An Abort Sensor Assembly (ASA) error separation study for the APS burn to depletion yielded instrument errors well within the 3σ AGS capability estimates. In general the ASA performed with high accuracy and the gyro bias stability was exceptionally good.

3.0 CSM IMU PERFORMANCE

Apollo 10 CSM IMU performance analysis was based upon velocity comparisons for the boost and TLI thrusting periods.

The uncompensated velocity (no error compensation) differences appear in Figures 3-1 through 3-6. The compensated (velocity residuals resulting from a comparison of the Apollo G&N data, corrected for a best fit set of errors, compared to the S-IVB IU data) velocity comparisons are shown in Figures 3-7 through 3-12. Derived error sets to fit boost and TLI are presented in Table 3-1. The error sources considered and their respective definitions are presented in Table 3-2. Any errors in the booster data are included in the Apollo G&N data. Sensed velocity errors at insertion (approximately 703 seconds GET) were -2.82, -29.11, and -5.08 ft/sec for the $\dot{X}$, $\dot{Y}$, and $\dot{Z}$ axes. The difference is derived by taking Apollo G&N minus external reference. At the completion of TLI (approximately 9550 seconds GET), the velocity errors accrued during TLI were 15.11, 4.79, and -3.19 ft/sec for the $\dot{X}$, $\dot{Y}$, and $\dot{Z}$ axes. These sensed boost and TLI errors may also be observed from their corresponding uncompensated plot.

The maximum deviation between any set of corresponding error sources was 0.85σ. In total, 34 error sources were derived for boost and 34 for TLI. Satisfactory ISS performance has been established using the generalized approach set forth in paragraph 3.1 of this analysis. Evaluating the 34 error sources individually (as opposed to the relative basis between boost and TLI) reveals the ADSRAY (Y accelerometer drift due to acceleration along the spin axis) and ADIAX (X acceleration drift due to acceleration along the input axis) and ADIAZ (Z acceleration drift due to acceleration along the input axis) slightly exceeded the 1σ instrument stability estimate during boost and TLI. These are discussed in the ISS Errors Paragraph 3.1.1.

It is worthy of noting that the $\dot{X}$, $\dot{Y}$, and $\dot{Z}$ velocity offsets for boost and TLI (VOX, VOY, and VOZ) were difficult to obtain for each fit because of the unrealistic data available at the start of boost and TLI burns. For example the X acceleration measured by the S-IVB indicated a step change from -0.5 ft/sec^2 for the first two seconds of data to +0.5 ft/sec for the next 2 seconds. The Apollo G&N measured -0.1 ft/sec^2 for the total 4 seconds. As a result the first 4 seconds of S-IVB data was edited out and an X offset was formed based on the subsequent data.

The Apollo 11 G&C system accuracy analysis was based on the determination of a common set of errors which resulted in small residuals for both the boost to orbit phase and the translunar insertion phase. At the same time, several constraints were imposed on the errors used. The bias values for accelerometers and gyros were forced to be in close agreement with inflight determined values and other error terms which were preflight calibrated were chosen to agree favorably with calibration histories. Due to various physical factors such as actual acceleration sensitive parameter shifts during the boost phase and degradation of the reference data between the two flight phases (2.6 hours of drift between ascent and TLI) it was again recognized that all of the above conditions could not be met at all times. Based on engineering judgement, the approach pursued was to determine two sets of error sources with minimum variations ($\leq 1\sigma$) between the two flight phases. The error terms derived from the analyses are presented in Table 3.1, and using these values, the G&N corrected trajectories fit the respective external measurement trajectories. The maximum deviation between the derived ascent and TLI error sources was 0.85σ.

For each of the two flight phases, two trajectories were generated by MSFC as a basis for comparison. One boost/TLI trajectory was the "Edited S-IVBIUTM" trajectory and the other was the "Final S-IVB Observed Mass Point Trajectory" (OMPT). The trajectory designated "Final S-IVB OMPT" is normally considered the best estimate trajectory for the boost and TLI phases but was again rejected due to inconsistencies

in the trajectory characteristics throughout the boost phase and TLI phases. Similar problems have been encountered with the OMPT on previous flights and in all cases no reasonable set of error sources could be found which effected a good boost and TLI comparison (Reference 2 and 3). The "Edited S-IVBIUTM" trajectory was again accepted as most realistic. It should be pointed out that the first 4 seconds of IU Boost data is suspect due to the high vibration levels during this time. For this reason, the velocity offset values are chosen to optimize the "fit." These velocity offsets will cause considerable vertical curve shifts since their corresponding partial derivatives are unity. Consequently, values are chosen that more realistically follow the data trends after the first 4 seconds for each of the $\dot{X}$, $\dot{Y}$, and $\dot{Z}$ axes.

The major difference between the OMPT and "Edited S-IVBIUTM" is that the OMPT has been corrected for booster guidance errors. No allowance has been made for these errors; any that exist are included in the Apollo G&N errors. Analysis has shown, however, that these errors have less effect on the indicated performance of the Apollo G&N than the "corrections" included in the OMPT (Reference 3).

3.1 ISS ERRORS

It is worthy of noting that, even though the derived boost and TLI errors were within 0.85σ of each other for the evaluation of these flight phases, the ADSRAY (Y accelerometer drift due to acceleration along the spin axis) error source derived for ascent was 1.98σ and 1.12σ for TLI. The derived ADSRAY value was -9.91 meru/g for ascent and -5.67 meru/g for TLI. These values were within 1.89σ and .8σ of the a priori ADSRAY error estimates for boost and TLI. There was nothing in the preflight test history which would explain the large errors required to make the fit. Although no explanation based on preflight data exists for the large ADSRAY term reasonable confidence in the value remains due to the consistent requirement for this value to obtain a good fit and due to the close agreement with the value obtained for the TLI phase.

The derived ADIAX (X acceleration drift due to acceleration along the input axis) values were 1.08σ for boost and 1.16σ for TLI. Based upon the initial error estimates at start of boost and TLI, the derived ADIAX error values were within the 1σ performance criteria. Using the initial estimates as a reference for comparison the derived values were .9σ for boost and .2σ for TLI.

The derived ADIAZ (Z acceleration drift due to acceleration along the input axis) values were -9.86 meru/g for boost and -13.8 meru/g for TLI. Preflight test history data trends indicated the value was moving toward negative. Preflight test history of ADIAZ for the time interval 24 February 69 to 3 April 69, shows a negative trend from 12.75 meru/g to 8.75 meru/g. For prelaunch load on 18 May a value of 11 meru/g was inserted into the CMC for ADIAZ compensation. An initial error estimate of -2.4 meru/g existed before liftoff. The determined values were within .9σ and .5σ of the initial ADIAZ error estimates. There is also reasonable confidence in the ADIAZ values due to the consistent requirement of these values to obtain a good "fit."

Reviewing the three relatively large ISS errors, ADSRAY, ADIAX and ADIAZ, it is worthy of noting that ADSRAY was the only error that exceeded the 1σ instrument stability estimate when the derived values are compared with an initial error estimate based on preflight data.

Error Source	Preflight Data Mean	Flight Load	Expected Error*	Standard Deviation	Preflight Expected 1σ Bounds Maximum	Preflight Expected 1σ Bounds Minimum	Ascent Output Error Value	TLI Output Error Value	|(Ascent Output Error Value) − (TLI Output Error Value)| / σ	Comments
VOX (ft/sec)	NA	NA	NA	NA	NA	NA	0.209	- 0.523	NA	Not comparable due to state vector update between ascent and TLI.
VOY (ft/sec)	NA	NA	NA	NA	NA	NA	- 0.999	- 0.013	NA	
VOZ (ft/sec)	NA	NA	NA	NA	NA	NA	- 0.706	0.621	NA	
DT (sec)	NA	NA	NA	NA	NA	NA	0.007	0.0004	NA	
ACBX (cm/sec²)	- 0.065	- 0.27	- 0.205	0.20	0.405	0.005	- 0.030	- 0.032	NA	Output error values established from inflight measurements
ACBY (cm/sec²)	- 0.055	- 0.07	0.015	0.20	0.215	- 0.185	- 0.088	- 0.089	NA	
ACBZ (cm/sec²)	- 0.045	- 0.05	0.005	0.20	0.205	- 0.195	0.110	0.114	NA	
SFEX (ppm)	-178.250	-100	- 78.25	116	37.75	-194.25	19.34	19.2	0.01σ	
SFEY (ppm)	-237	-230	- 7	116	109	-123	10.72	35.6	0.2σ	Insensitive in ascent
SFEZ (ppm)	-129	- 80	- 49	116	67	-165	80.14	-17.2	0.84σ	
MXAZ (arc sec)	NA	NA	NA	20	20	- 20	- 0.2	3.6	0.19σ	
MXAY (arc sec)	NA	NA	NA	20	20	- 20	- 19.7	- 13.2	0.33σ	
MYAZ (arc sec)	NA	NA	NA	20	20	- 20	0	- 5.1	0.26σ	
MYAX (arc sec)	NA	NA	NA	20	20	- 20	15.6	18.1	0.13σ	
MZAY (arc sec)	NA	NA	NA	20	20	- 20	- 13.5	- 20.9	0.37σ	
MZAX (arc sec)	NA	NA	NA	20	20	- 20	4.7	- 4.5	0.46σ	
NBDX (meru)	- 0.433	0.4	0.033	2	2.033	- 1.967	- 1.7	- 1.7	NA	Output error values established from inflight measurements
NBDY (meru)	- 1.300	1.3	0	2	2.0	- 2.0	1.35	1.35	NA	
NBDZ (meru)	0.866	1.2	- 0.334	2	1.666	- 2.334	0.015	0.015	NA	
ADIAX (meru/g)	2.300	1.0	1.3	8	9.3	- 6.7	8.5	9.33	0.10σ	
ADIAY (meru/g)	8.700	13.0	- 4.3	8	3.7	- 12.3	- 1.66	0.8	0.31σ	Insensitive in ascent
ADIAZ (meru/g)	8.600	11.0	- 2.4	8	5.6	- 10.4	- 9.86	- 13.8	0.49σ	
ADSRAX (meru/g)	9.800	10.0	- 0.2	5.0	4.8	- 5.2	- 0.113	1.11	0.24σ	Insensitive in TLI
ADSRAY (meru/g)	3.400	3.0	0.4	5.0	5.4	- 4.6	- 9.91	- 5.66	0.85σ	
ADSRAZ (meru/g)	0.9	7.0	- 6.1	5.0	- 1.1	- 11.1	- 6.37	- 5.93	0.09σ	Insensitive in ascent
ADOAX (meru/g)	3.27	NA	3.27	2-5**	8.27	- 1.73	- 3.85	- 3.57	0.06σ	
ADOAY (meru/g)	- 0.275	NA	- 0.275	2-5**	4.725	- 5.276	4.43	4.13	0.06σ	
ADOAZ (meru/g)	0.825	NA	0.825	2-5**	5.825	- 4.175	- 3.13	- 3.0	0.03σ	
MLMX (arc sec)	NA	NA	NA	50***	50***	- 50***	16	-143	NA	Not comparable. TLI values based on platform misalignments and 2.5 hours drift before TLI.
MLMY (arc sec)	NA	NA	NA	50***	50***	- 50***	- 33	334	NA	
MLMZ (arc sec)	NA	NA	NA	50***	50***	- 50***	0	- 86	NA	

* Data mean minus flight load.

** Recent unofficial measurements by MIT.

*** Boost Phase only.

NA = Not applicable

Table 3-1 CSM IMU SYSTEM ERRORS

Table 3.2 IMU ERROR SOURCES

Apollo Mnemonic	Accelerometer Errors	Apollo Mnemonic	Gyro Errors
ACBX ACBY ACBZ	Bias	ADIAX ADIAY ADIAZ	Drift rate sensitivity to acceleration along input axis.
SFEX SFEY SFEZ	Scale Factor	ADSRAX ADSRAY ADSRAZ	Drift rate sensitivity to acceleration along spin axis.
NCXX NCYY NCZZ	SF sensitivity to input acceleration supared.	ADOAX ADOAY ADOAZ	Drift rate sensitivity to acceleration along output axis.
	IKMSL is the misalignment of accelerometer "I" toward the "K" the platform axis.	ADSXX ADSYY ADSZZ	Drift rate sensitivity to acceleration squared along the spin reference axis.
(not modeled)	SF sensitivity to coupling of acceleration along input and output axes (ppm/g)	NBDX NBDY NBDZ	Constant drift rate
	Platform Errors		
	Platform misalignment		
	Timing Error		
	Velocity Offset		

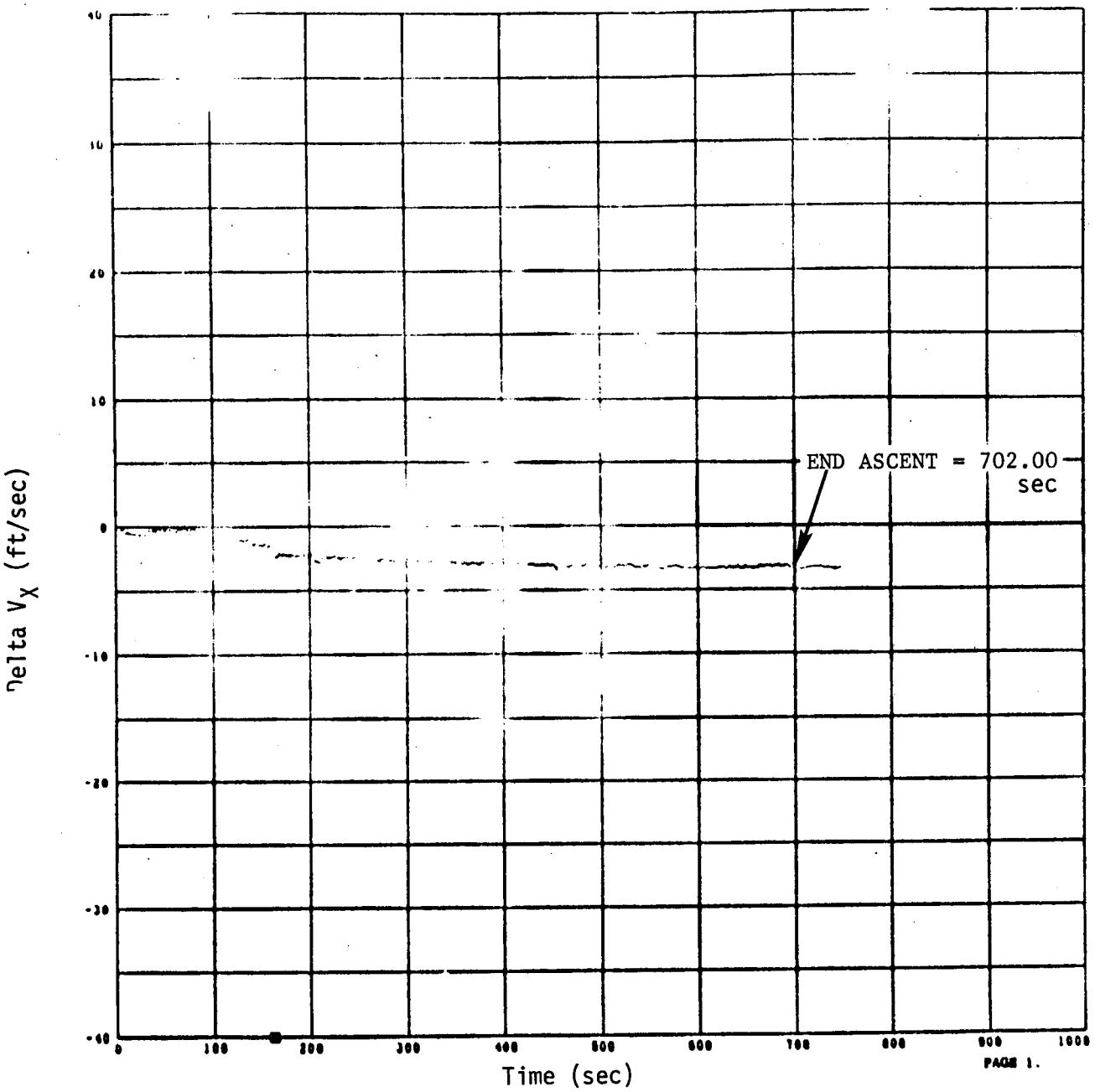

Figure 3-1 Uncompensated Ascent Velocity Comparison (G&N - S-IVB)

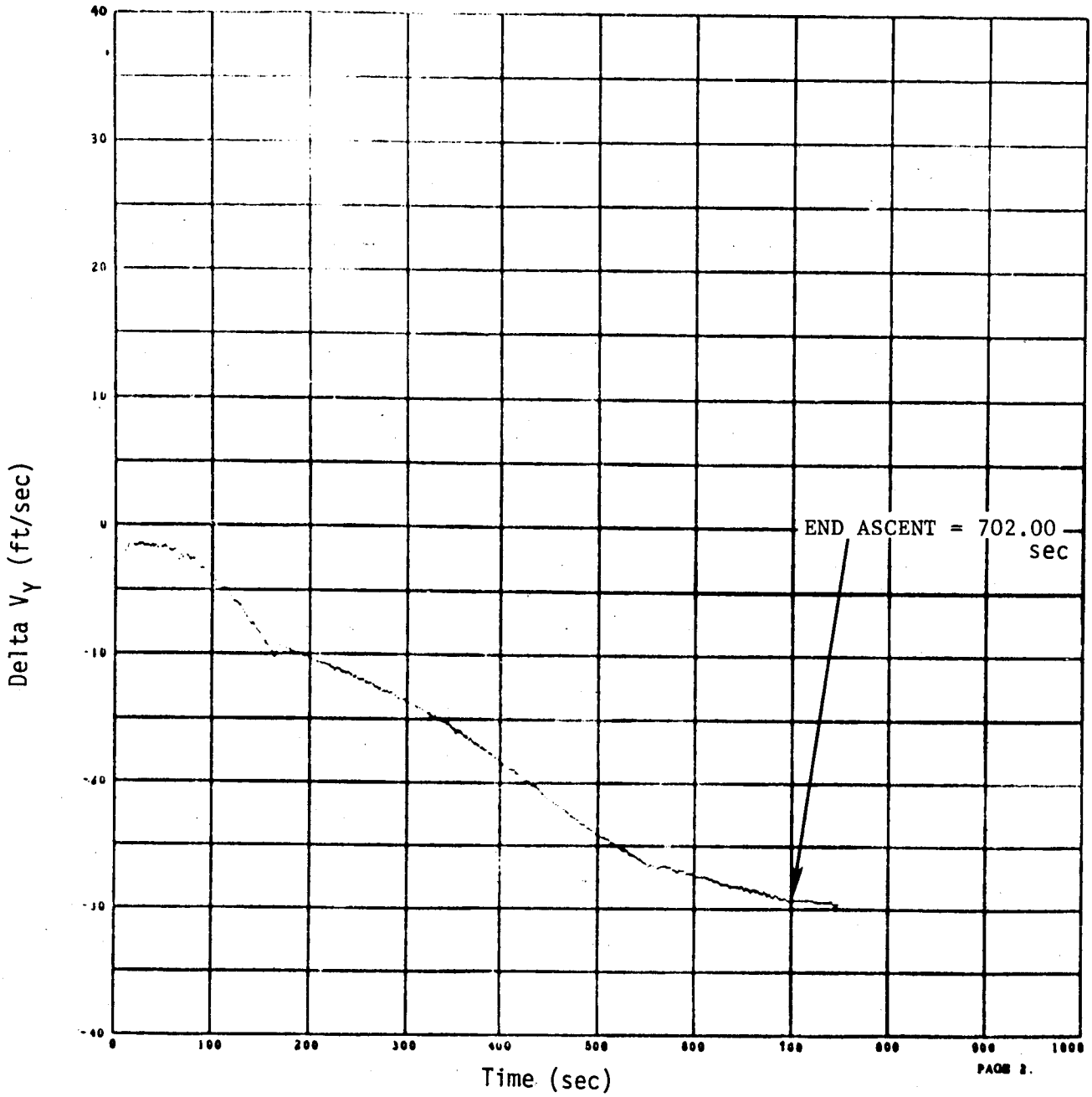

Figure 3-2 Uncompensated Ascent Velocity Comparison (G&N - S-IVB)

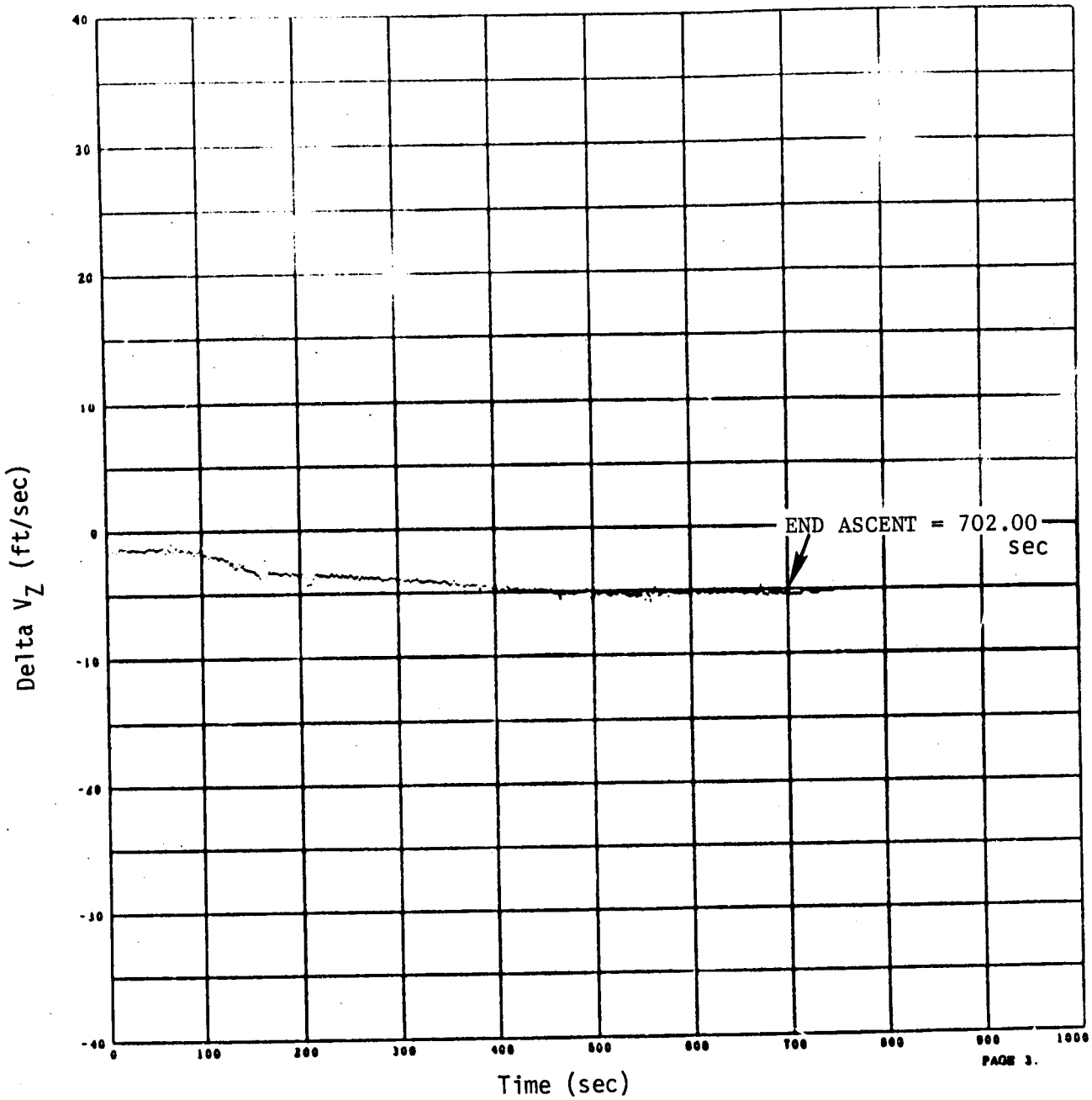

Figure 3-3 Uncompensated Ascent Velocity Comparison (G&N - S-IVB)

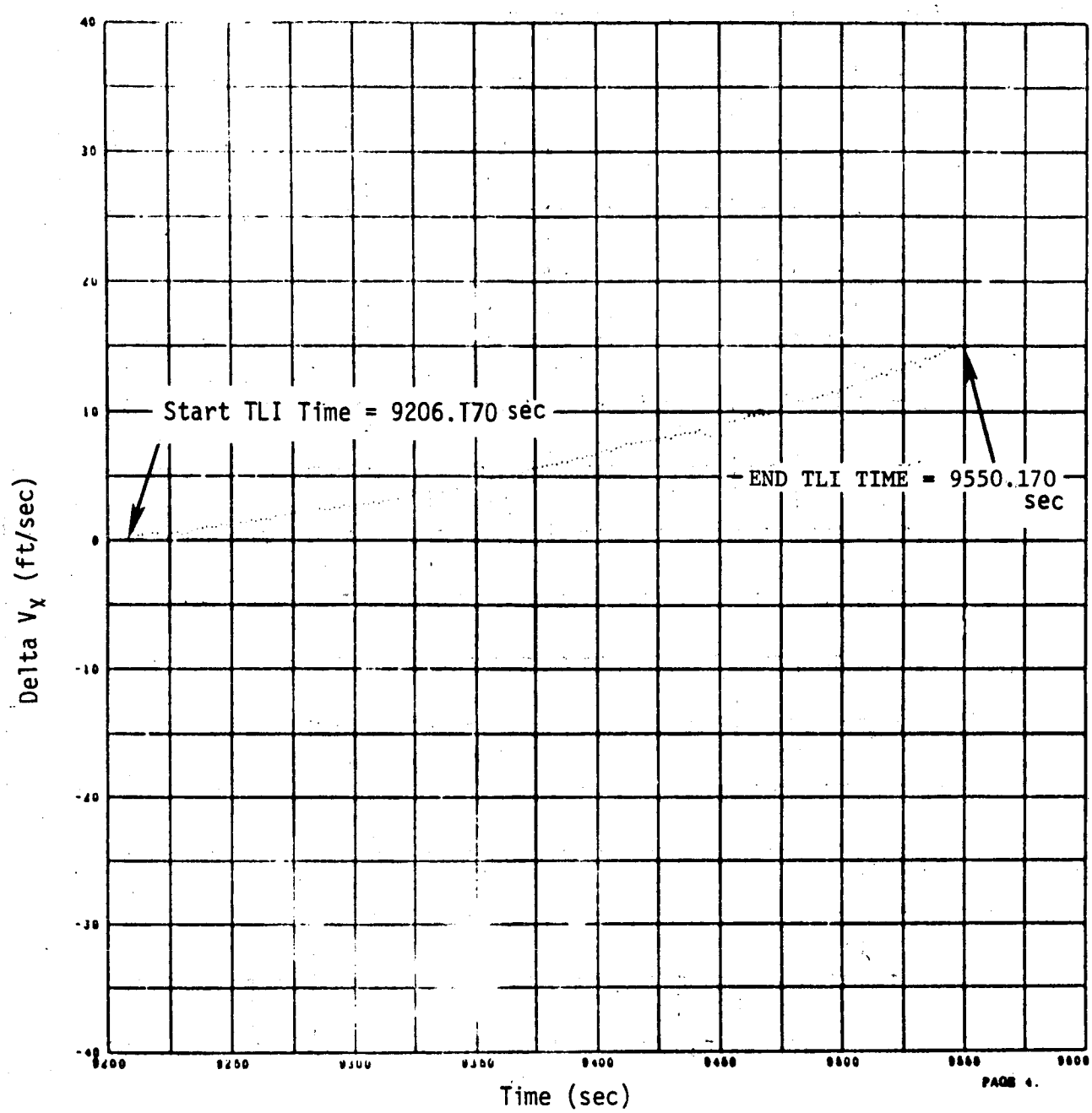

Figure 3-4 Uncompensated TLI Velocity Comparison (G&N - S-IVB)

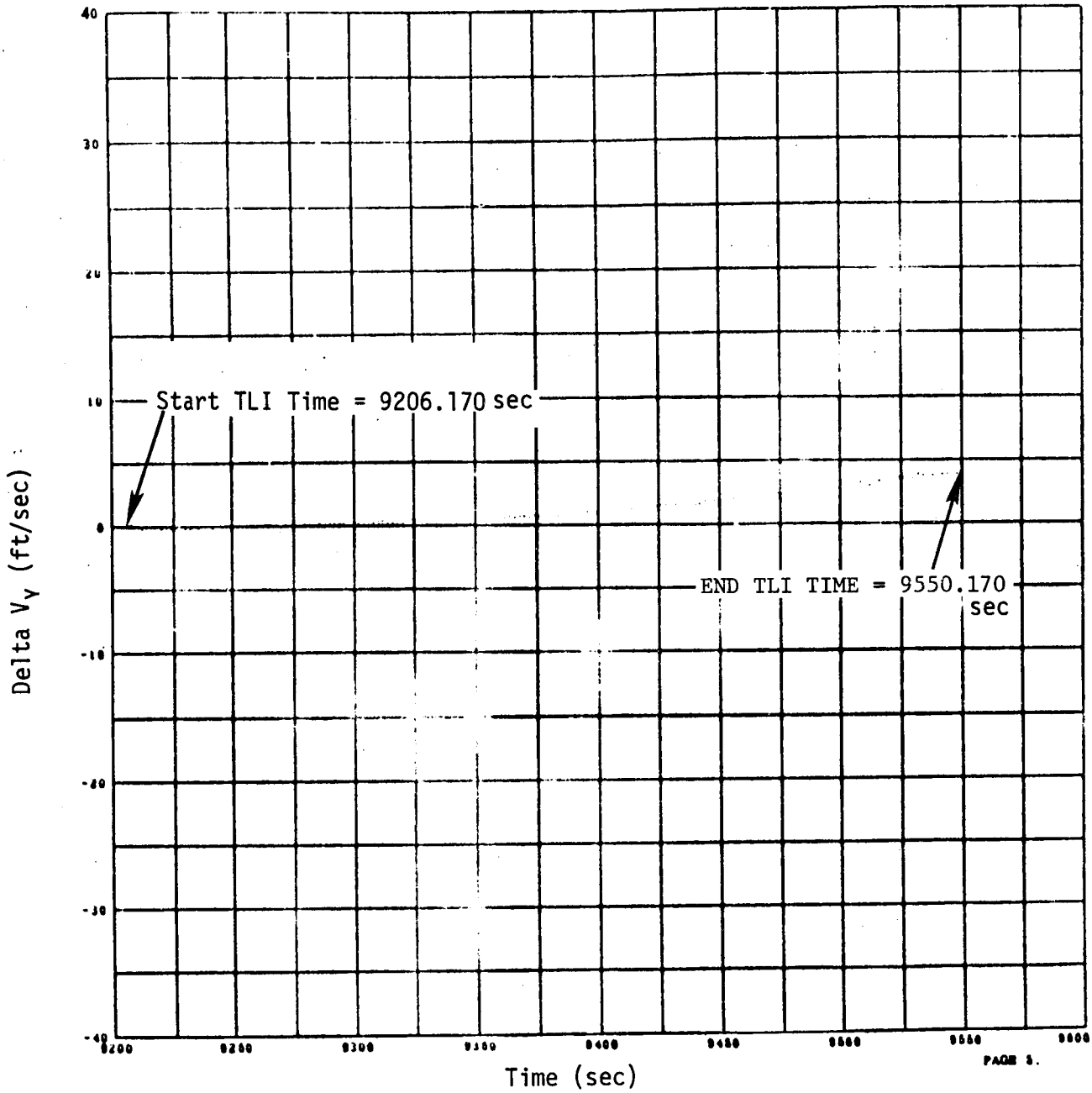

Figure 3-5 Uncompensated TLI Velocity Comparison (G&N - S-IVB)

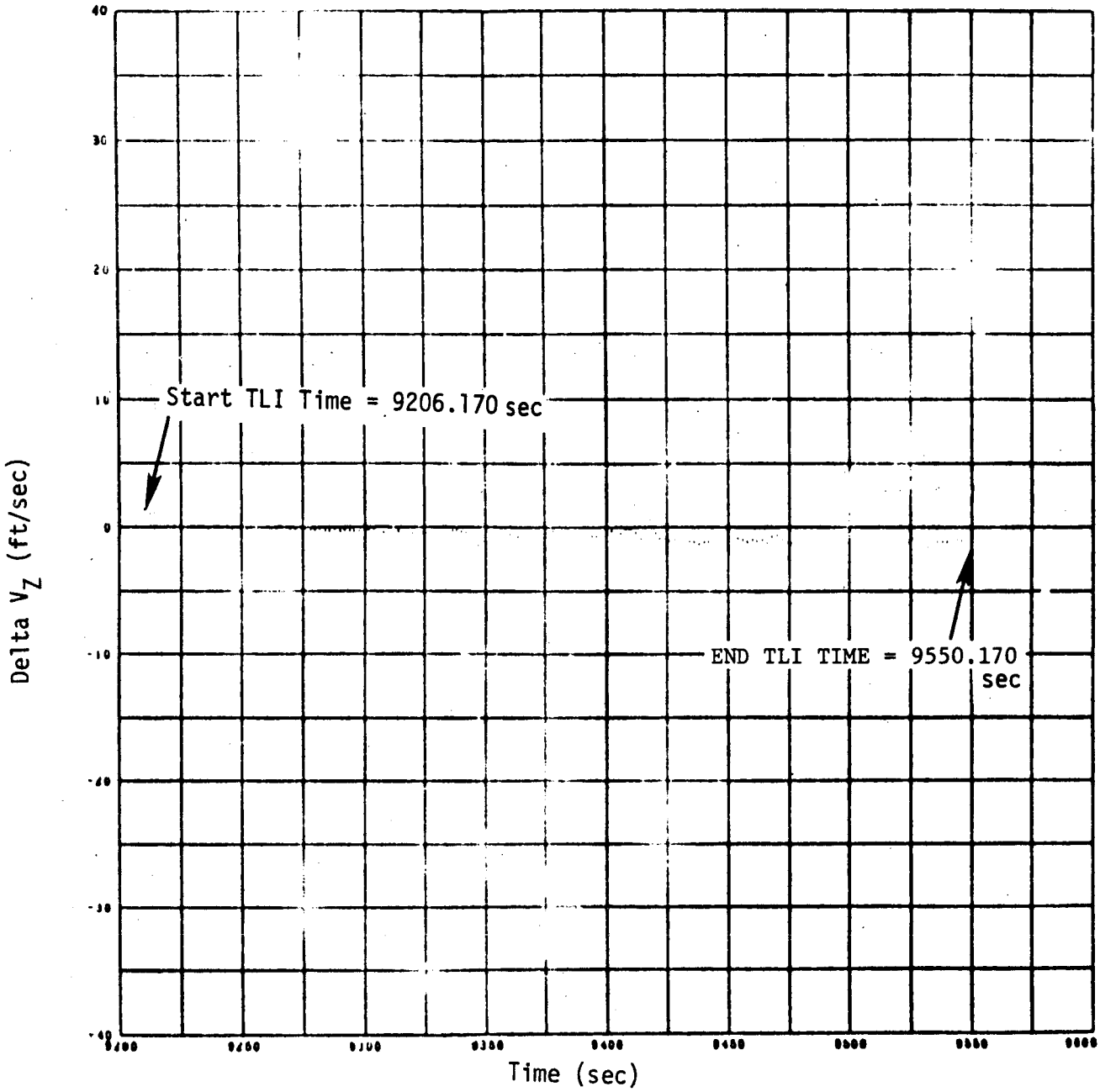

Figure 3-6 Uncompensated TLI Velocity Comparison (G&N - S-IVB)

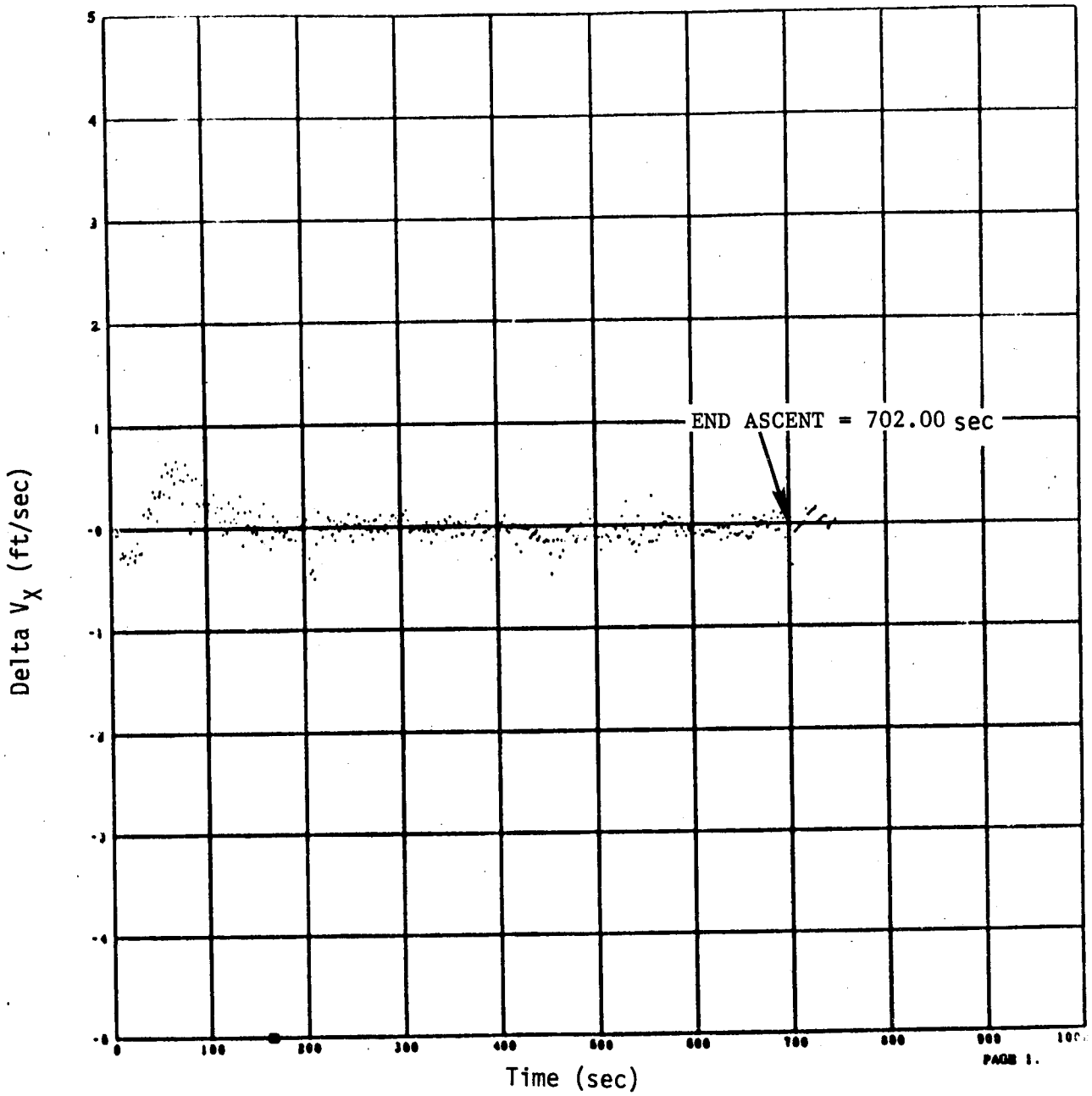

Figure 3-7 Compensated Ascent Velocity Comparison (G&N - S-IVB)

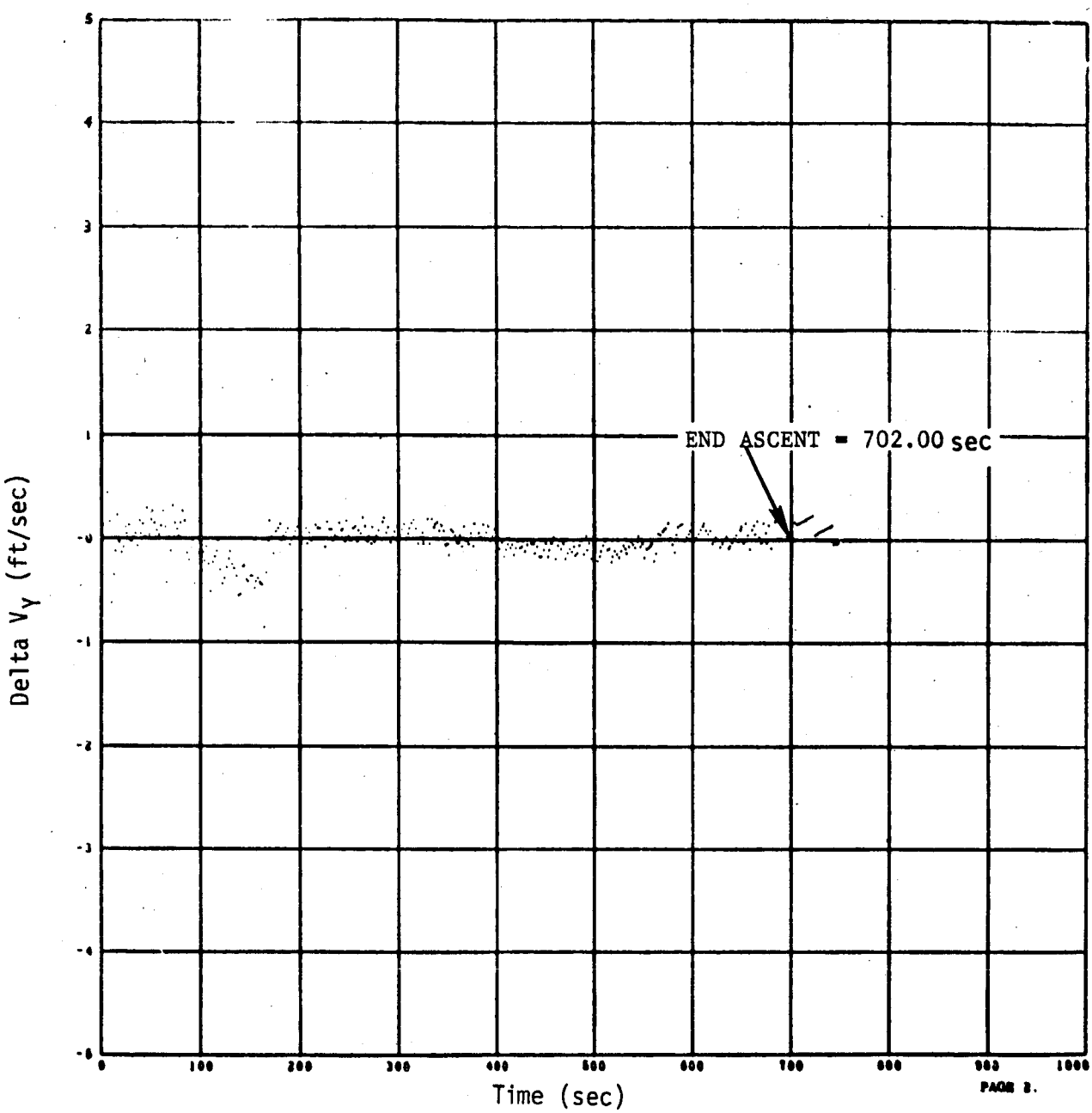

Figure 3-8 Compensated Ascent Velocity Comparison (G&N - S-IVB)

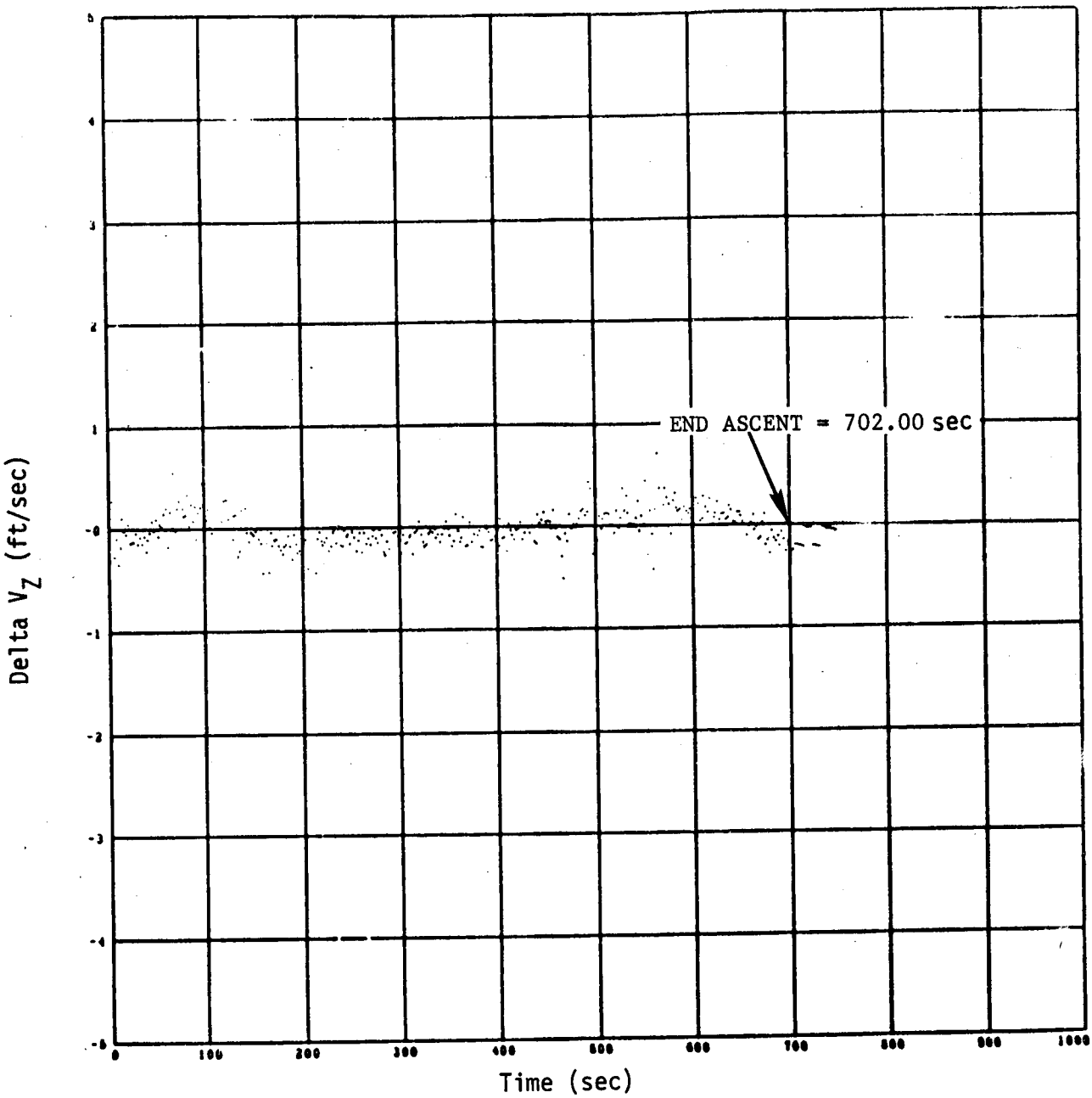

Figure 3-9 Compensated Ascent Velocity Comparison (G&N - S-IVB)

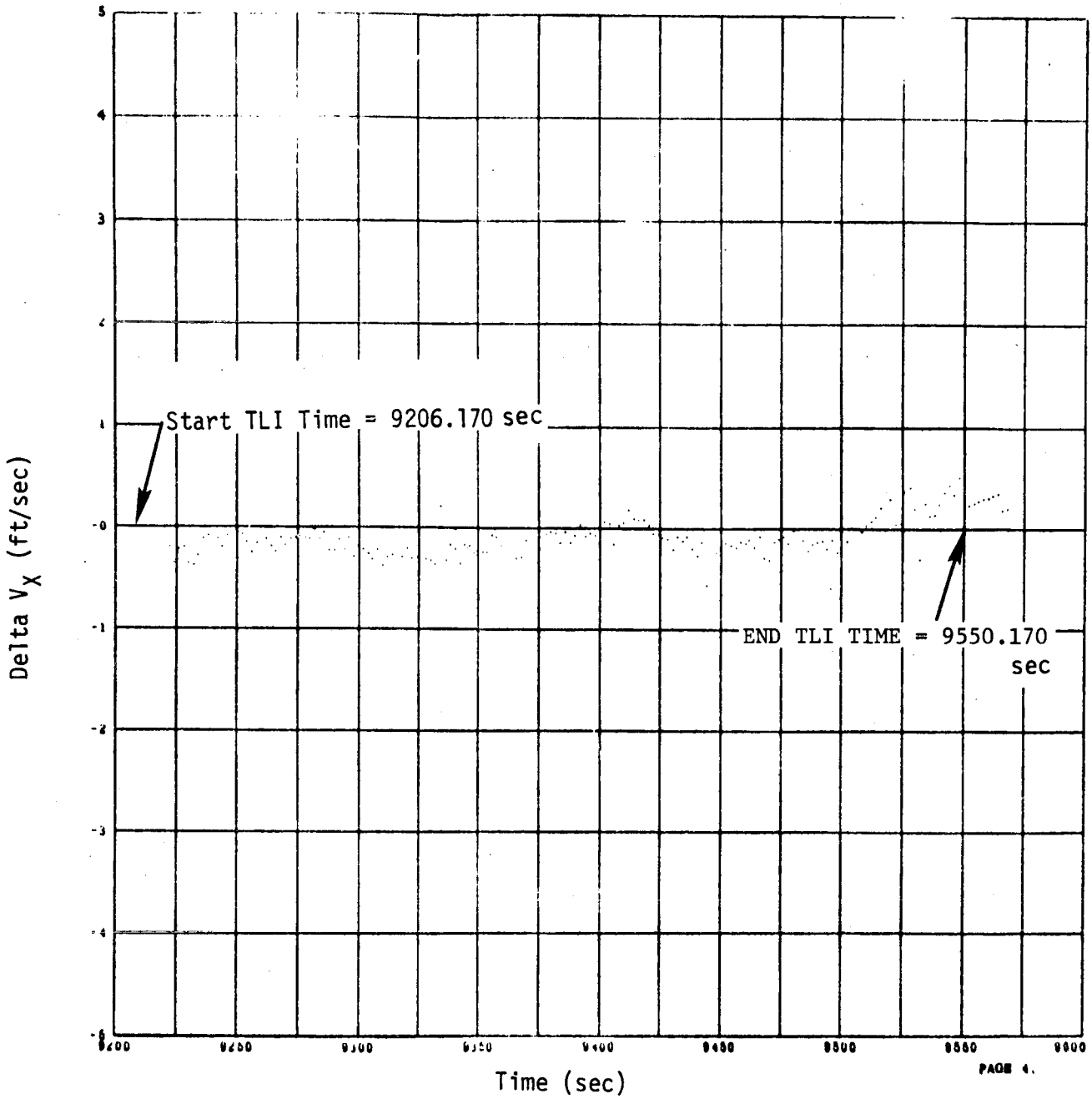

Figure 3-10 Compensated TLI Velocity Comparison (G&N - S-IVB)

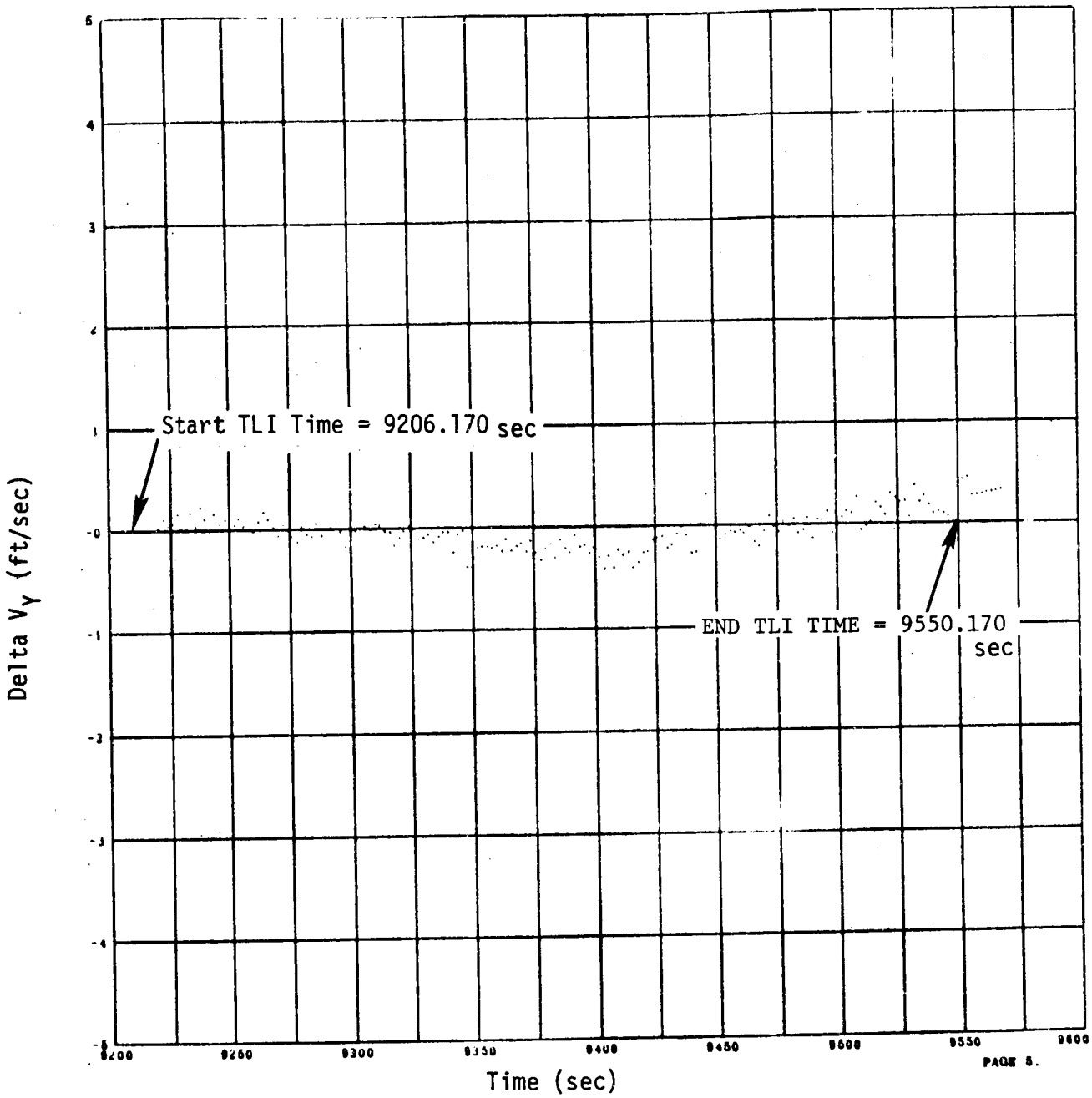

Figure 3-11 Compensated TLI Velocity Comparison (G&N - S-IVB)

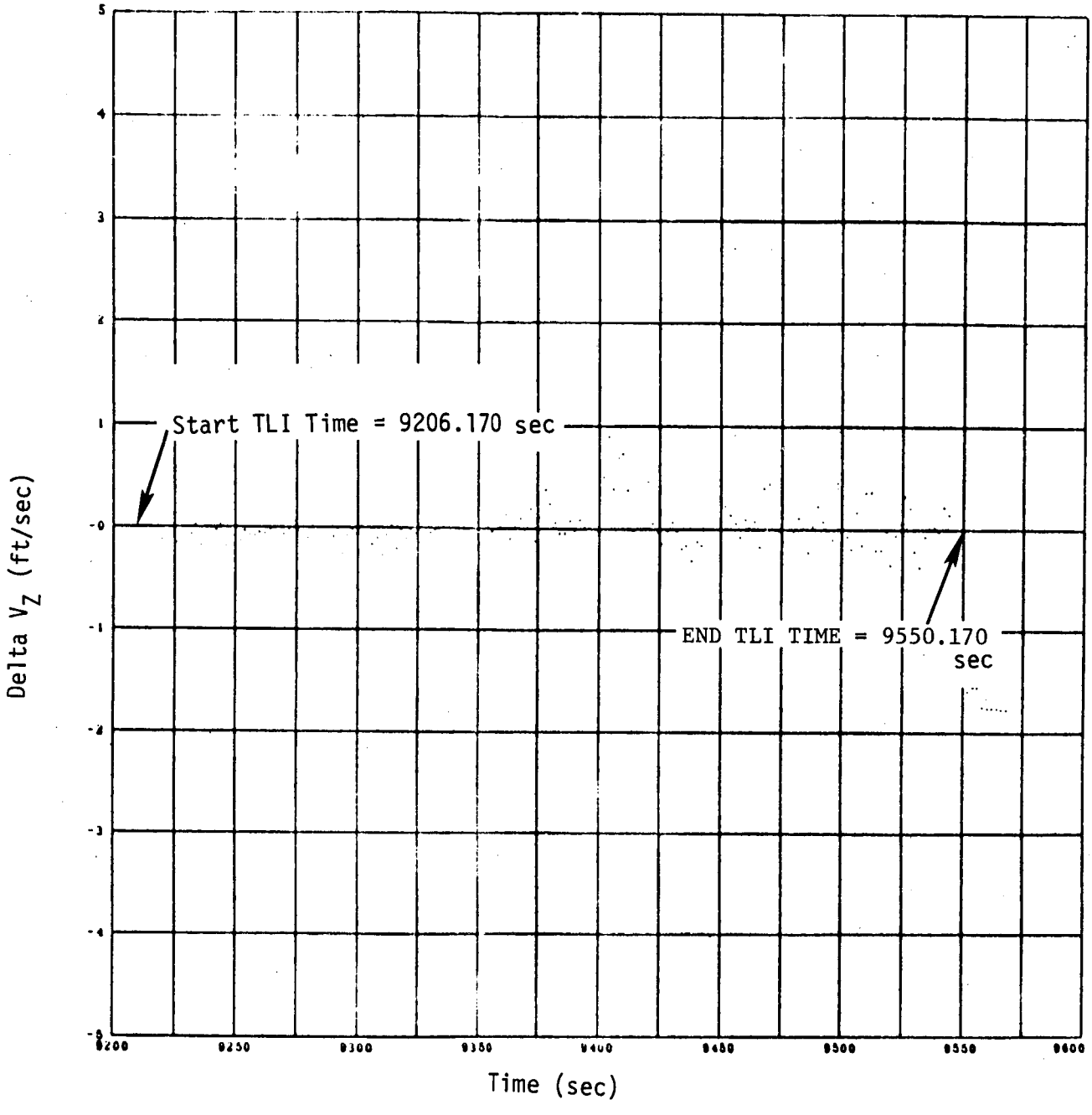

Figure 3-12 Compensated TLI Velocity Comparison (G&N - S-IVB)

4.0 CSM DIGITAL AUTOPILOT

CMC control of the S/C was employed extensively during this mission and all three autopilots performed nominally. Because only minor changes are to be made to the CSM flight program for subsequent missions, the excellent performance of the DAP's during the mission adds to an already high confidence level in the CSM program for upcoming lunar landing missions.

4.1 RCS DAP PERFORMANCE

Extensive use was made of the RCS DAP for maneuvering to desired attitudes for SPS burns, PTC initialization, or navigation sightings. All PTC periods were implemented under CMC control. Periods of RCS DAP performance during attitude maneuvers, attitude hold, attitude hold during RCS translation, and passive thermal control were analyzed and are discussed in subsequent paragraphs.

4.1.1 Attitude Maneuvers

Following LM withdrawal from the S-IVB, the docked CSM/LM performed an evasive maneuver to avoid recontact. The docked S/C during this maneuver was heavy, approximately 94,150 lbs. S/C roll, pitch, and yaw gimbal angles at attitude maneuver initiation were -54, -37 and -48 deg, respectively. The final desired gimbal angles were 61, -105 and -2 deg. A maneuver rate of .2 deg/sec was employed, with the desired rotation rates being .158, -.107 and .060 deg/sec about the vehicle X, Y, and Z axes. Figure 4-1 presents time history plots of DAP-measured S/C body rates during the first 4 minutes of this automatic maneuver. The actual rates converged to the desired values with overshoots of .02 deg/sec or less in all axes.

Figure 4-2 presents time histories of DAP-computed body rates during an RCS-controlled automatic maneuver to the T/E MCC attitude. The S/C

weight was a light 25,500 lbs. Initial roll, pitch, and yaw gimbal angles were -93, -152, and -12 deg and the desired final values were 0, 129, and 0 deg. Figure 4-2 shows that the actual body rates during this maneuver did not converge to the desired rates as well as during the maneuver to evasive burn attitude. This occurred because of the lower vehicle weight and inertia values, which resulted in larger rotation accelerations from RCS firings and increased cross-axis coupling effects.

4.1.2 Attitude Hold

Three minutes of attitude hold immediately following the maneuver to the CSM/LM evasive burn attitude are illustrated in the phase plane plots of Figures 4-3a to 4-3c. The phase planes of Figures 4-4a to 4-4c contain 6 minutes of CSM-alone attitude hold immediately following the maneuver to T/E MCC attitude. Narrow (.5 deg) attitude error deadbands were employed during both periods. These figures do not precisely represent the RCS attitude plotted at 2 second intervals, which is the downlink frequency of the phase plane attitude errors. Also, the downlinked rates are 20 words apart (.4 sec) from the attitude errors; therefore, the rate/error data are only approximately time homogeneous. However, they are close enough to give a general picture of RCS DAP performance during these attitude hold periods. One must allow some leeway when viewing these plots, e.g., not all jet firings will appear to be initiated just after crossing the phase plane deadbands (dashed lines in the figures).

In general, the motions of the rate/error points in Figures 4-3a to 4-3c appear nominal and in accord with the phase plane attitude hold logic. The only anomalous-looking motion occurs near the +.5 deg attitude error deadband in Figure 4-3a where the measured rate changes sign several times with no roll jets being fired. However, the rates involved are quite low (less than .01 deg/sec in magnitude) and the sign

changes can be attributed to cross-axis coupling, since, during this time period, there is necessarily frequent pitch jet activity as the pitch phase plane point "walks" up the left-hand deadband boundary of Figure 4-3b.

Much more cross-axis coupling is evident in Figures 4-4a to 4-4c for the period of CSM-alone attitude hold. In particular, the anomalous-looking roll rate reversal (Figure 4-4a) coming just before 188:19:09 GET and the confusing phase plane histories near the left-hand pitch and yaw deadband boundaries (Figures 4-4b and 4-4c) are good examples of the effects of cross-axis coupling on a light S/C, especially when both pitch and yaw errors are near the deadbands at the same time.

The limit cycle set up in Figure 4-4a is of minimum impulse type with a 2-jet pair of minimum impulse roll firings causing a rate change of approximately .07 deg/sec. The rate change produced by the minimum impulse firing for the CSM/LM configuration seen in Figure 4-3a is down by a factor of four from this value. This is consistent with the reciprocal roll moments of inertia, which are also down by the same factor.

4.1.3 Attitude Hold During RCS Translation

The lunar orbit circularization burn (LOI 2) was preceded by a 2-jet ullage of 16 seconds duration using quads A/C. During this period the RCS DAP maintained S/C attitude errors within the narrow attitude hold deadbands. Figure 4-5 illustrates RCS DAP performance during this ullage period. All attitude errors at ignition (80:25:08 GET) were of magnitude .6 deg or less. Comparable attitude hold performance was also observed during ullage preceding TEI.

Only one T/E MCC was required during Apollo 10. Figures 4-6a to 4-6c plot the attitude hold phase planes during this RCS translation. Initial rate excursions which result from +X translation, are negative in all axes. The positive rate excursions that follow result from a small +Z translation input. Figures 4-6a to 4-6c verify that the RCS

DAP correctly implemented THC inputs during this MCC. Post burn velocity-to-be-gained (vg) components were only 0, -.1, and -.1 ft/sec in the S/C X, Y, and Z direction, respectively.

4.2 TVC DAP

Five SPS burns were made during Apollo 10. They consisted of a docked evasive maneuver from the vicinity of the S-IVB, T/L MCC, lunar orbit insertion (LOI 1), lunar orbit circularization (LOI 2), and transearth injection (TEI). Figures 4-7, 4-8, 4-9, 4-10 and 4-11 show the spacecraft dynamics during the five burns. Table 4-1 shows the post-burn Vg components displayed on the DSKY via Noun 85 before and after RCS residuals nulling. In Table 4-1, the only post-burn ΔV component that seems out of line is the Y-axis Vg value after TEI. As discussed below, this is attributable to the TVC DAP cg tracker loop not being able to adequately follow the rapidly moving S/C cg at this light vehicle weight. Table 4-1 also shows that TVC performance generally improved with increased burn time.

4.2.1 Engine Transients and Gimbal Positioning Errors

Figures 4-12 and 4-13 are plots of time histories of pitch and yaw engine gimbal positions for the entire LOI 2 burn. Also included, at the downlink frequency of once per second, are values of pitch and yaw engine commands. For this burn, the peak-to-peak engine gimbal transients at ignition were quite small, .5 deg in pitch and +.2 deg in yaw. These errors decreased practically to zero after SPS cutoff. Largely similar ignition transients and steady state gimbal positioning errors were observed during LOI 1 and TEI.

4.2.2 Propellant Slosh and S/C Body Bending

Propellant slosh and body bending effects were detected during the various burns by examining FDAI body rates. These rates are the output values of caged BMAG's, sampled once every 10 msec. Figures 4-14 and 4-15 present FDAI pitch and yaw body rates during LOI 2. This particular burn was chosen for plotting purposes because it was short enough to make a detailed plot feasible and because it exhibits both slosh and bending effects.

Eight or nine cycles of body bending can be detected in pitch at the beginning of Figure 4-14. The bending frequency is approximately 2.785 Hz. Propellant slosh at a frequency of approximately 0.469 Hz can be seen in the yaw rate plot of Figure 4-15. Although roll rate is not plotted, it also exhibited sloshing effects of approximately this same frequency.

During LOI 1, propellant slosh effects were not seen in pitch or yaw. They were observed in roll at approximately 0.350 Hz, persisting for about the first minute and 15 seconds of the burn. Body bending of approximately 2.466 Hz was noted in pitch and yaw, lasting for seven cycles or less.

No bending effects were observed during the undocked TEI burn. Propellant slosh at a frequency of 0.652 Hz was noted in all three axes. The pitch oscillations were damped out after 70 seconds while the roll and yaw oscillations persisted for almost the entire burn time. However, these slosh oscillations never appeared to diverge and represented no stability problems.

Comparing data from the various burns, it is seen that propellant slosh and body bending frequencies both increased with decreasing vehicle weight. This trend is consistent with preflight simulations.

4.2.3 LOI 1

Figures 4-16 through 4-19 present burn parameters for LOI 1. The pitch and yaw attitude error histories of Figure 4-16 are impressively small, approximately .1 to .2 deg. In Figure 4-17 the estimated pitch engine trim angle became asymptotic one minute before SPS cutoff. The yaw trim estimate never became asymptotic but the total cg change was only .6 deg over a 6 minute period, so the TVC cg tracker loop had no difficulty in following its motion. Cross-axis velocities plotted in Figure 4-18 are oscillatory because the granularity of the V_g data from which these values were calculated is .25 ft/sec in all axes, which is of the same order of magnitude as the cross-axis velocity values being

computed. However, a trend from approximately .35 ft/sec shortly after ignition to .12 ft/sec at engine cutoff is observable. Figure 4-19 presents a time history of TVC roll DAP attitude error during LOI 1. The behavior observed is similar to that noted during previous flights, where an external torque causes the roll error to bounce off the negative deadband limit, rather than traverse from minus to plus, etc. However, only four roll firings were required during the entire 6 minute burn.

4.2.4 LOI 2

Figure 4-20 presents time histories of DAP pitch and yaw attitude errors, roll gimbal angle error, pitch and yaw engine trim estimates (PACTOFF and YACTOFF), and cross-axis velocity component during LOI 2. The peak attitude error magnitudes were .4 deg in pitch and .2 deg in yaw. The cross-axis velocity values were computed from downlinked Vg's which are available every two seconds, or once per average G cycle. The value plotted in the figure is the component of Vg normal to the preburn Vg vector. The peak cross-axis velocity mangitude during LOI 2 was 1.2 ft/sec, decreasing to .45 ft/sec at SPS engine cutoff.

4.2.5 TEI

TEI burn parameters are presented in Figures 4-21 through 4-24. The peak pitch attitude error magnitude was .6 deg while the yaw error grew slowly during the burn to a final value of .35 deg. This steady buildup occurred because the yaw cg tracker could not adequately follow the rapidly moving cg of this lightweight vehicle. As seen in Figure 4-22, the yaw cg trim estimate changed by 1.8 deg during the 2 minute and 45 second burn. Contrasting this with yaw cg motion during LOI 1, it is seen that the travel rate during TEI was approximately 6.5 times as fast as during LOI 1. This inability to follow the cg trim position caused the 1.6 ft/sec Y-axis ΔV error seen in Table 4-1. Figure 4-23 implies that practically all of this 1.6 ft/sec V_g consisted of cross-axis velocity error. The peak cross axis velocity

was 3.6 ft/sec, occurring 20 seconds after ignition. In contrast to LOI 1, the outer gimbal angle error during TEI (Figure 4-24) traveled back and forth between the positive and negative deadband limits.

4.3 ENTRY DAP

A few seconds before entry communications blackout, control of the command module was handed over to the CMC. For the next 20 seconds, the exoatmospheric entry DAP maintained the desired entry orientation (roll, pitch, and yaw gimbal angles equal to 0, 153 and 1 deg) using the .1 second attitude hold phase plane for pitch and yaw control and the 2-second predictive DAP in roll. After the vehicle drag level reached .05 G, the atmospheric entry DAP assumed control of the S/C and remained in command for the duration of the entry phase. The atmospheric DAP consists of the 2-second predictor logic in roll and rate damping in pitch and yaw. The RCS system A thruster ring was employed during the entire period of CMC entry DAP control.

4.3.1 Roll Control

Control of the CM bank angle was maintained by the 2-second predictive DAP, which performs the function of driving the S/C bank angle in response to roll commands issued every 2 seconds by entry guidance. Figure 4-25 presents time histories of commanded and actual S/C roll angles. The entry roll DAP closely followed the commands issued by entry guidance. Performance of the roll DAP was consistent with preflight simulations and results of previous missions.

Entry guidance commanded a typical roll-down maneuver after the CMC assumed control and DAP succeeded in driving the S/C bank angle to lift down (180 deg roll angle) within a time lapse of 14 seconds. The DAP required only 11 seconds for the roll-up maneuver initiated 30 seconds later. The time difference arose primarily because the roll-down command sequence included 6 seconds worth of 80-90 deg bank angle commands, thus limiting the peal roll rate attained. The roll-up commands sequenced directly from full lift down to full lift-up.

4.3.2 Pitch and Yaw Control

For 20 seconds after initiation of CMC entry DAP control (before .05 G), the pitch and yaw DAP functions consisted of attitude hold about the desired entry attitude. After .05 G, the pitch and yaw functions were changed to rate damping with the pitch rate nominally being controlled to 0 ± 2 deg/sec and the yaw rate to within $\pm$ 2 deg/sec of p tan α. p is the S/C roll rate and tan α is the tangent of the angle of attack. These rate damping functions are required in order to maintain a state of coordinated S/C roll. In CMC program Comanche 45, the value used for tan α was a constant, equal to -.34202, which is approximately the tangent of -20 deg, the expected hypersonic trim angle of attack for a vehicle L/D ratio of 0.3.

For the majority of the entry phase, the S/C was so stable that very few pitch or yaw jet firings were required and these were usually needed only during periods of large roll maneuvers. Figures 4-26 and 4-27 present complete summaries of post-.05 G pitch and yaw jet activity. Dramatic increases in jet activity are seen during the last 2 minutes before drogue chutes deployment. Similar behavior has been noted during previous missions. It is largely attributable to rapidly changing vehicle aerodynamics as the S/C velocity approaches the transonic region. This increase is also seen in Figure 4-28, which presents time histories of entry fuel usage per axes. Thirty-three lbs of RCS propellant were required for the entry of Apollo 10 (after .05 G). The table below breaks down this propellant usage on a per axes basis and contrasts

the total amounts used with the consumption during the final 2 minutes of entry.

Jet	Total Fuel (lbs)	Total During Final 2 Minutes (lbs)
+P	1.00	0.72
-P	3.90	3.66
+Y	2.26	1.81
-Y	1.98	1.85
+R	8.88	2.67
-R	14.98	3.92
TOTAL	33.00	

All pitch and yaw rate damping firings occurred nominally, i.e., only when the respective measured rates fell outside the 2 deg/sec rate deadband. Figure 4-24 illustrates a short (9-second) period of pitch jet activity, along with values of DAP-computed pitch rate every 200 msec. DAP rates are actually computed every 100 msec, but only half of them are downlinked; therefore, not every pitch firing can be directly verified. However, as seen in Figure 4-29, every downlinked pitch rate value falling outside the $\pm$ 2 deg/sec deadbands correctly resulted in a pitch jet firing in the proper direction. All other pitch and yaw jet activity, for which corresponding rate data were available, was similarly verified.

Table 4-1 APOLLO 10 POST-BURN Vg COMPONENTS

	Noun 85 ΔV Residuals (ft/sec)					
	Before RCS Nulling			After RCS Nulling		
Maneuver	X	Y	Z	X	Y	Z
Evasive	1.0	0.3	0.7	-	-	-
T/L MCC	-.9	-0.1	0.3	-0.2	0.0	0.3
LOI 1	0.0	-0.2	0.0	-	-	-
LOI 2	0.5	-0.4	-0.4	-	-	-
TEI	0.3	1.6	-0.1	0.2	1.6	-0.2

- Means no RCS nulling was attempted

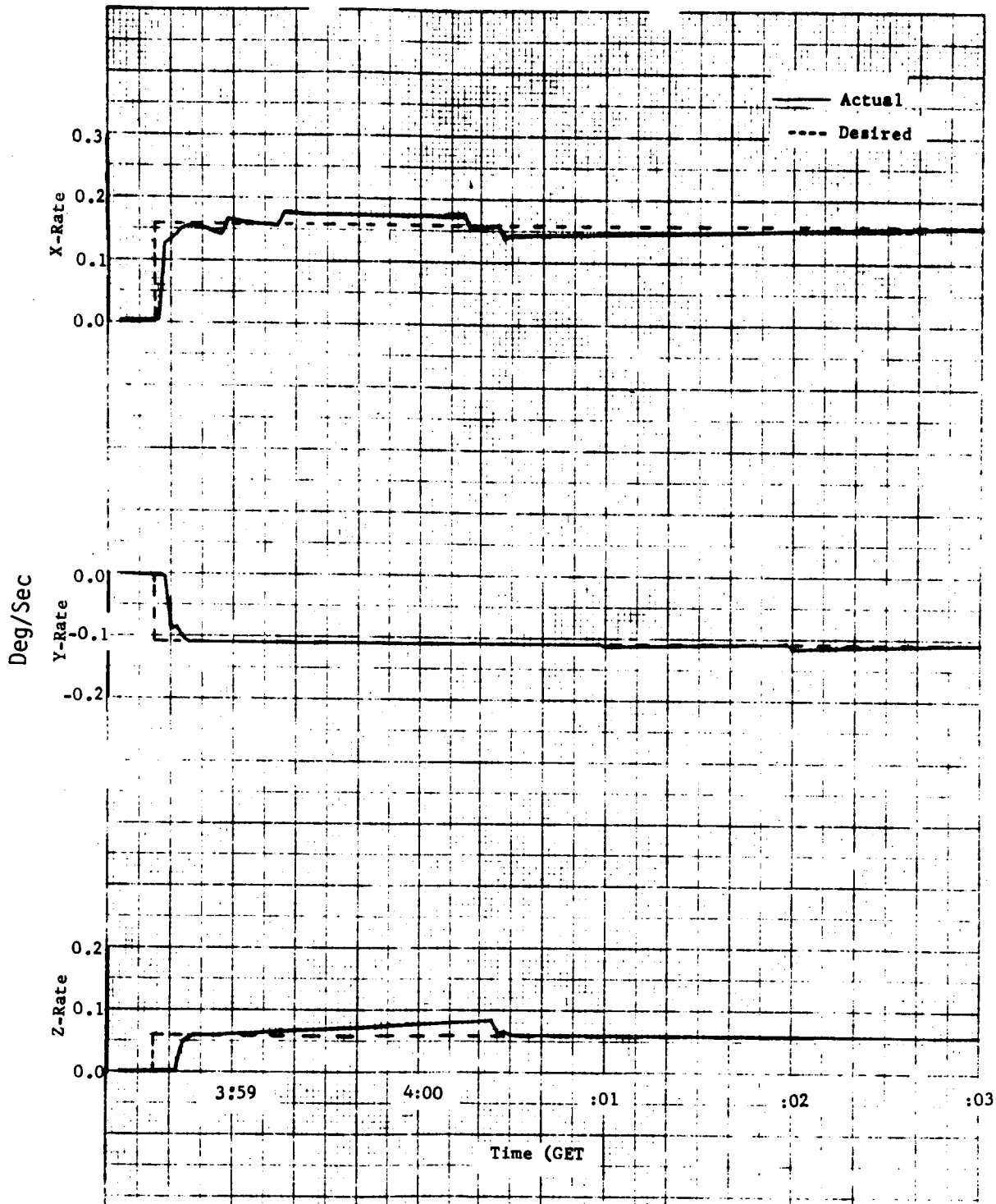

Figure 4-1 CSM/LM MANEUVER TO EVASIVE BURN ATTITUDE

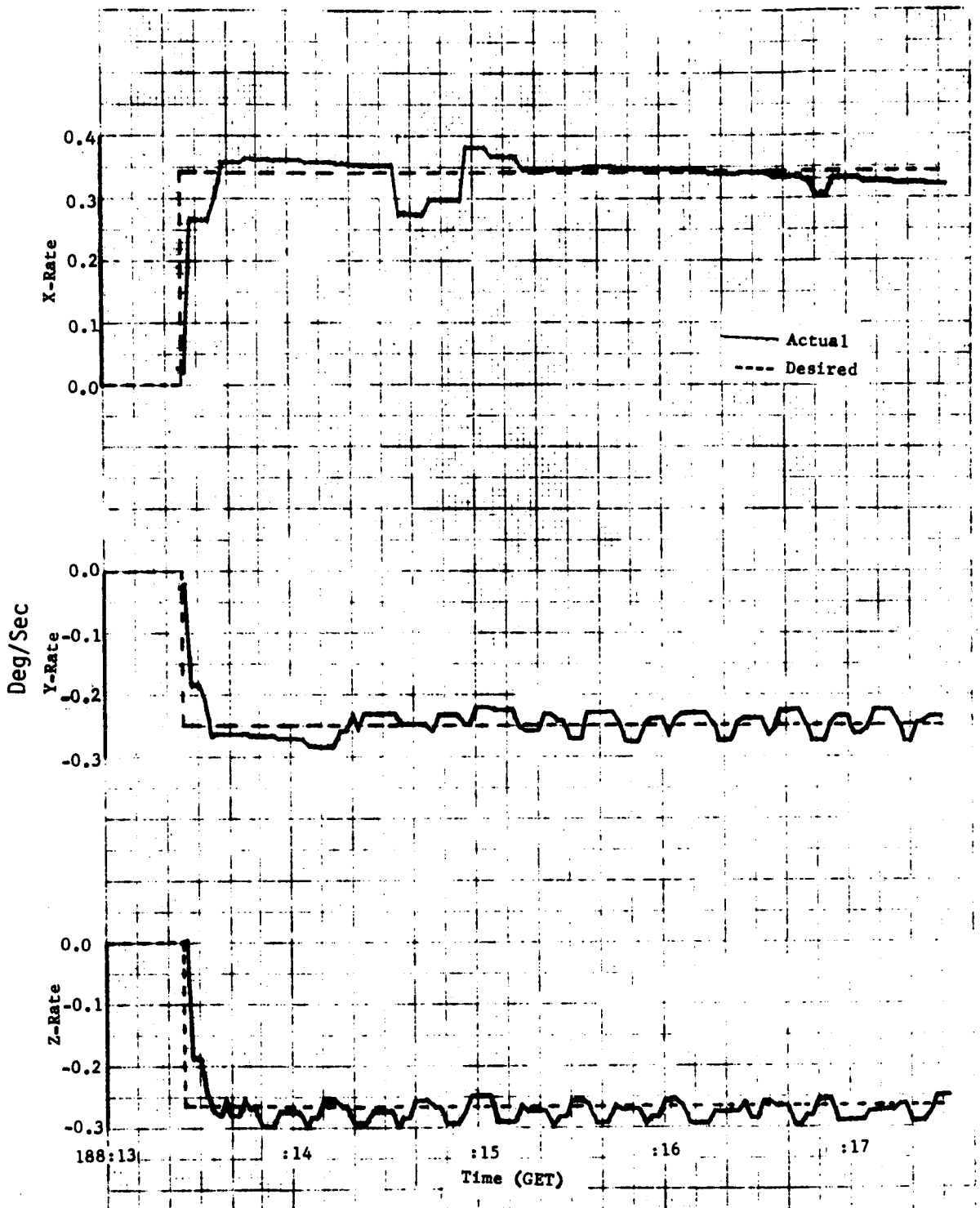

Figure 4-2 CSM MANEUVER TO T/E MCC ATTITUDE

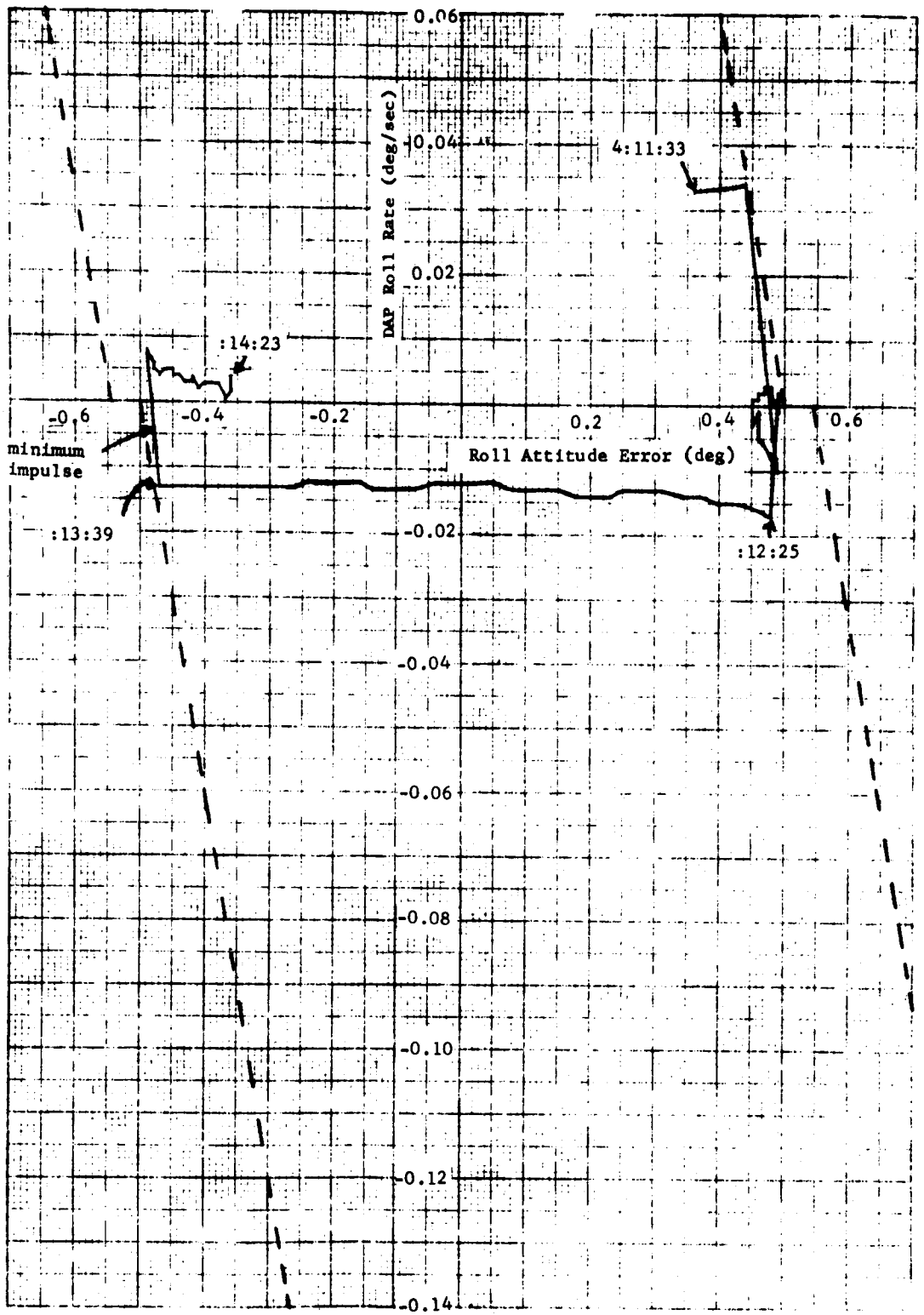

Figure 4-3a CSM/LM X-AXIS ATTITUDE HOLD

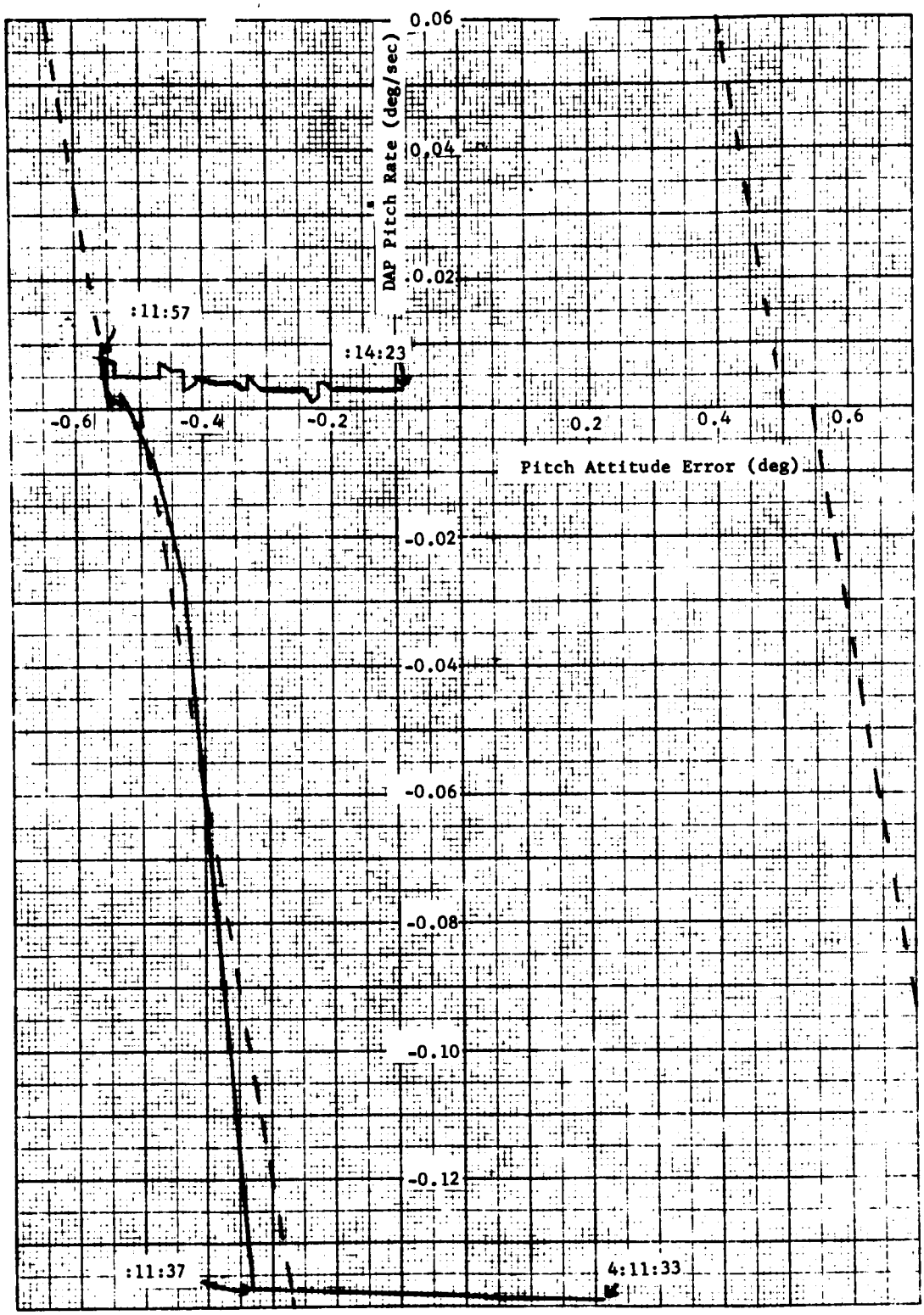

Figure 4-3b CSM/LM Y-AXIS ATTITUDE HOLD

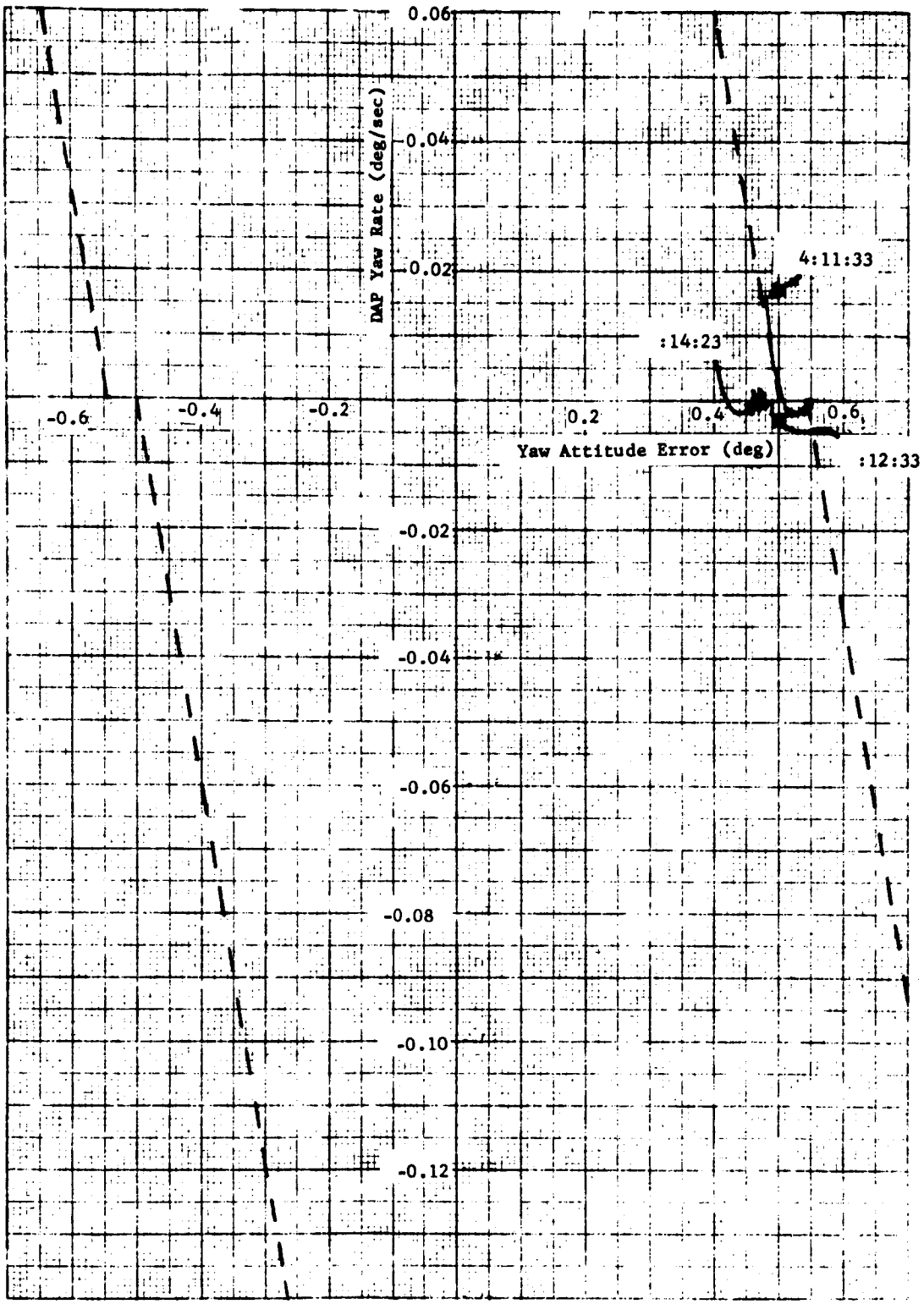

Figure 4-3c CSM/LM Z-AXIS ATTITUDE HOLD

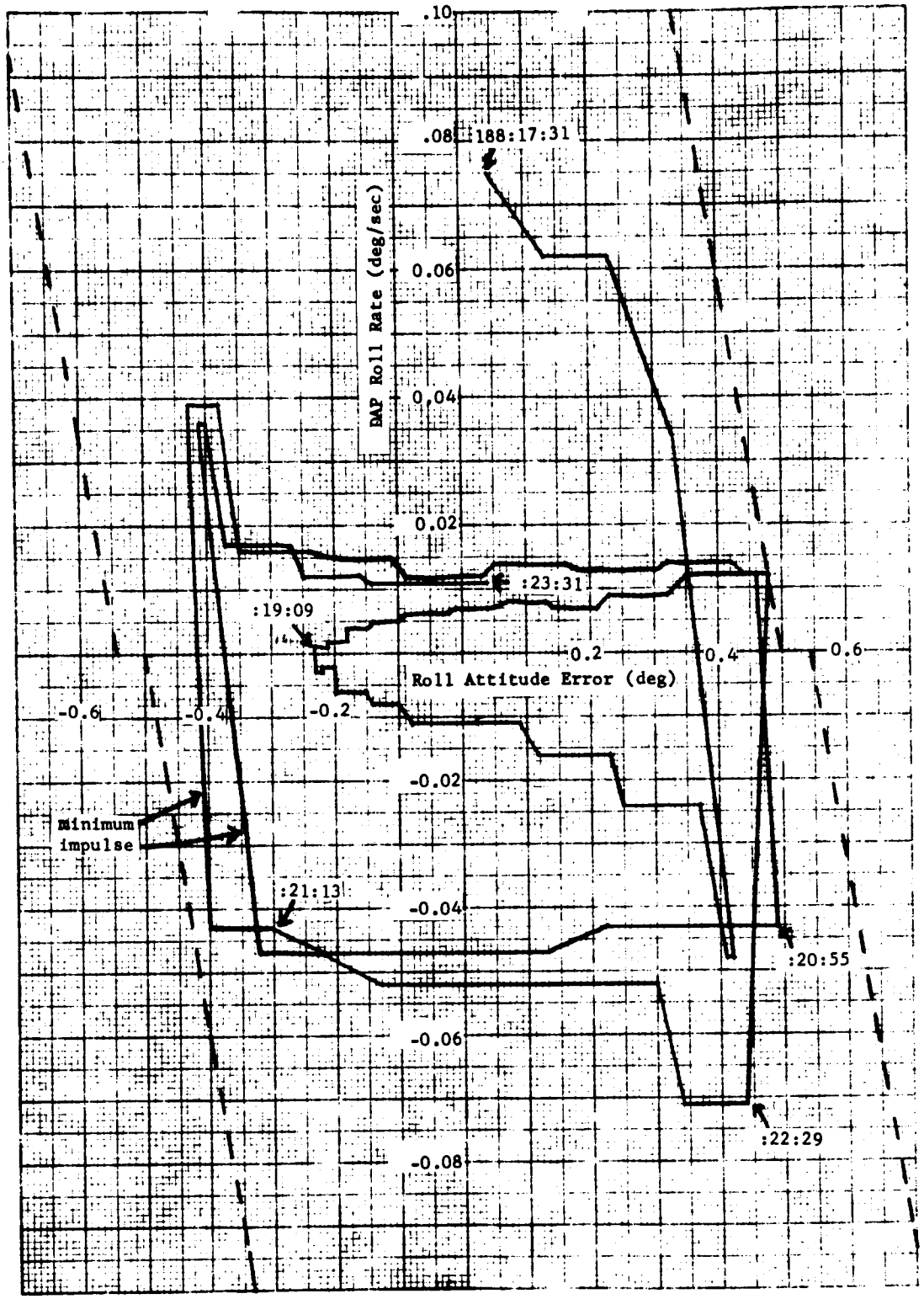

Figure 4-4a CSM X-AXIS ATTITUDE HOLD

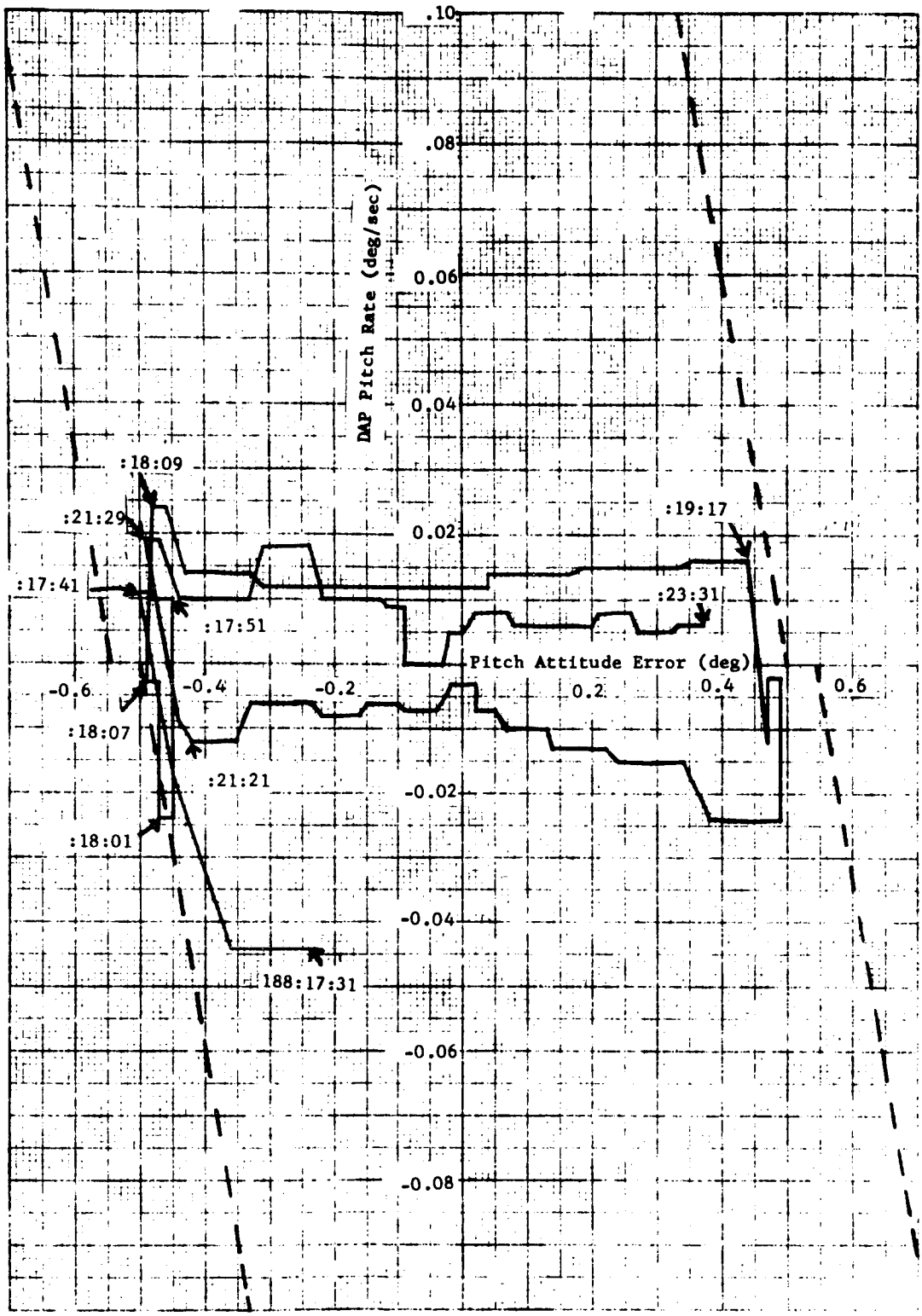

Figure 4-4b CSM Y-AXIS ATTITUDE HOLD

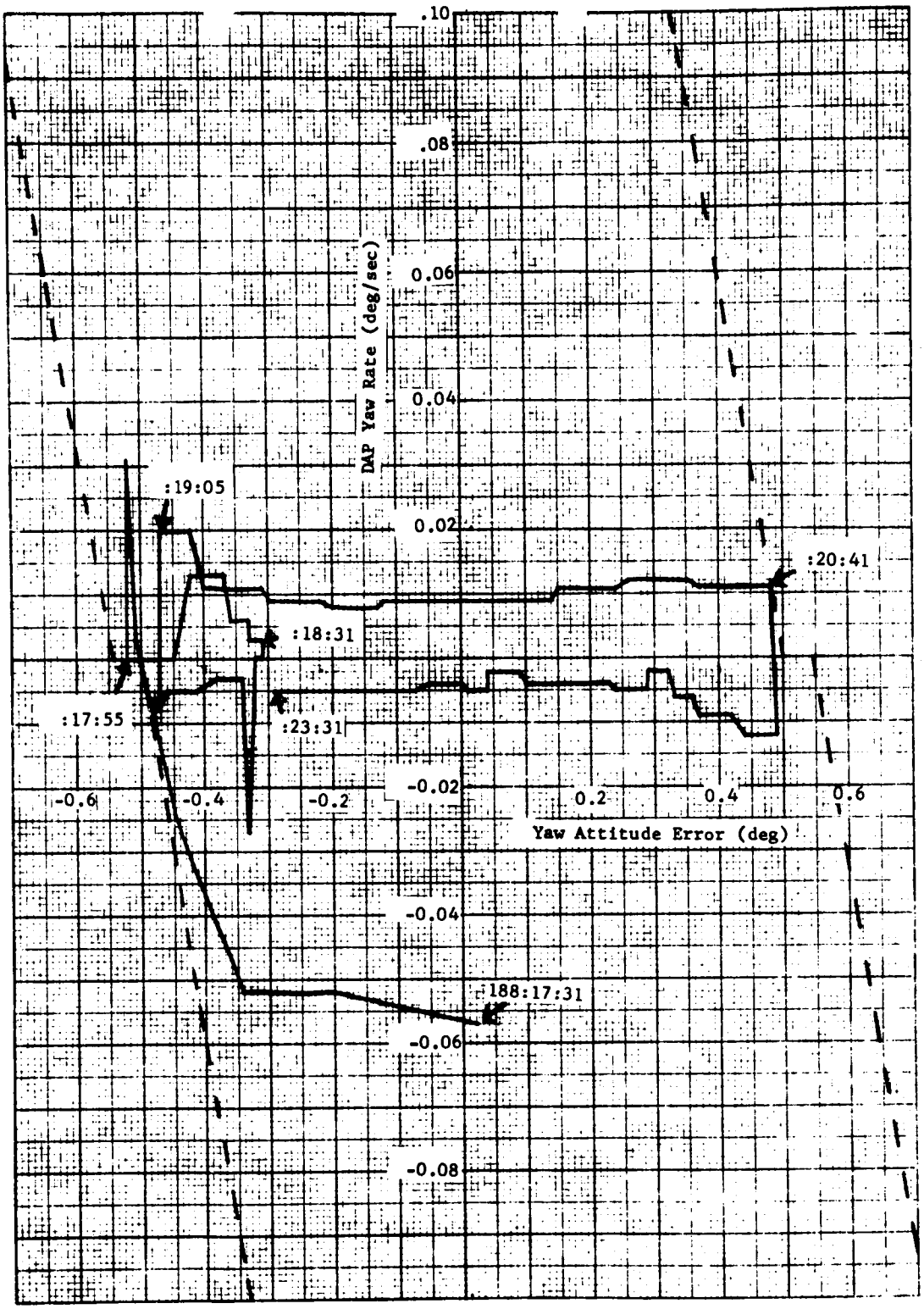

Figure 4-4c CSM Z-AXIS ATTITUDE HOLD

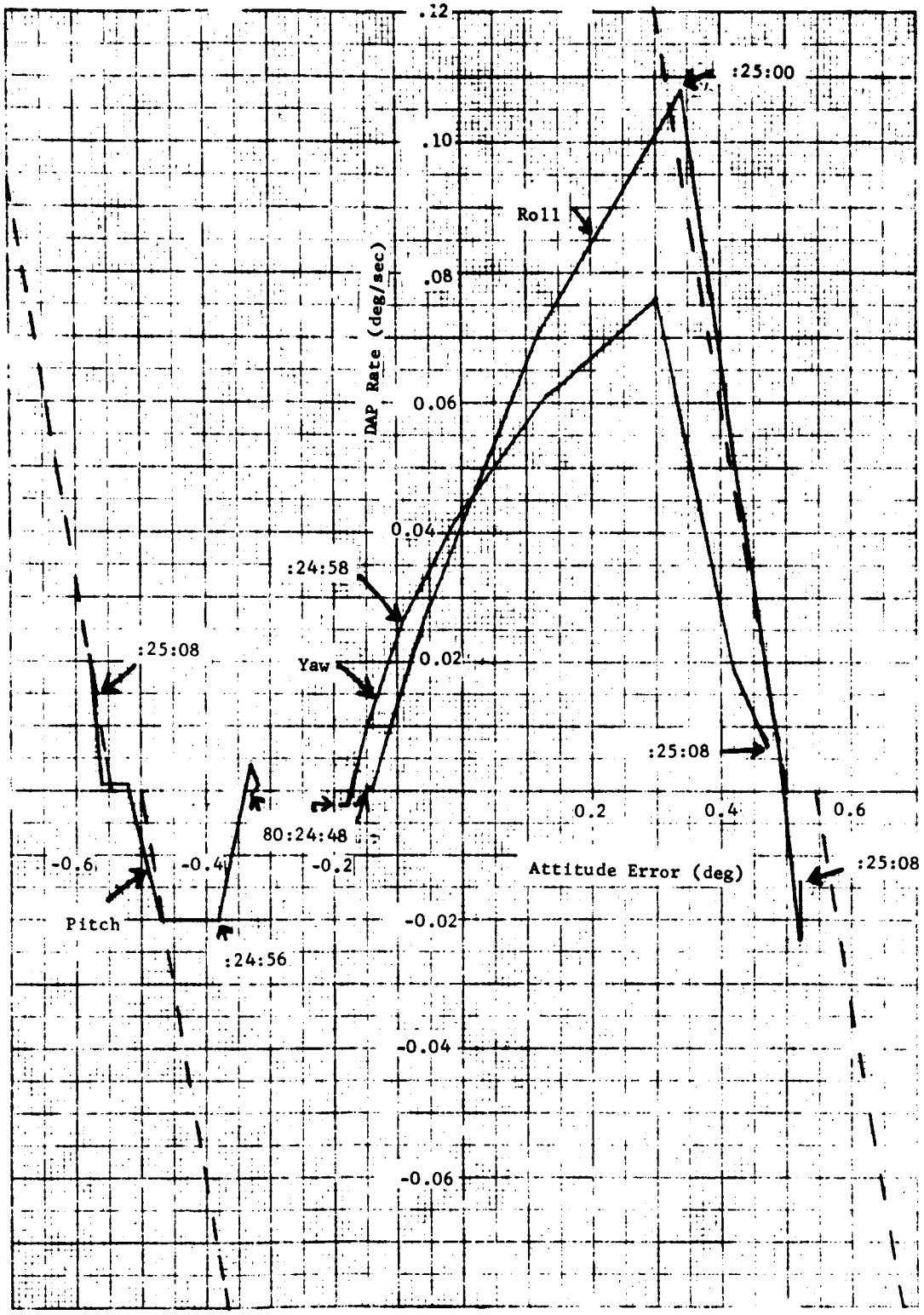

Figure 4-5 CSM/LM ATTITUDE HOLD DURING LOI 2 ULLAGE

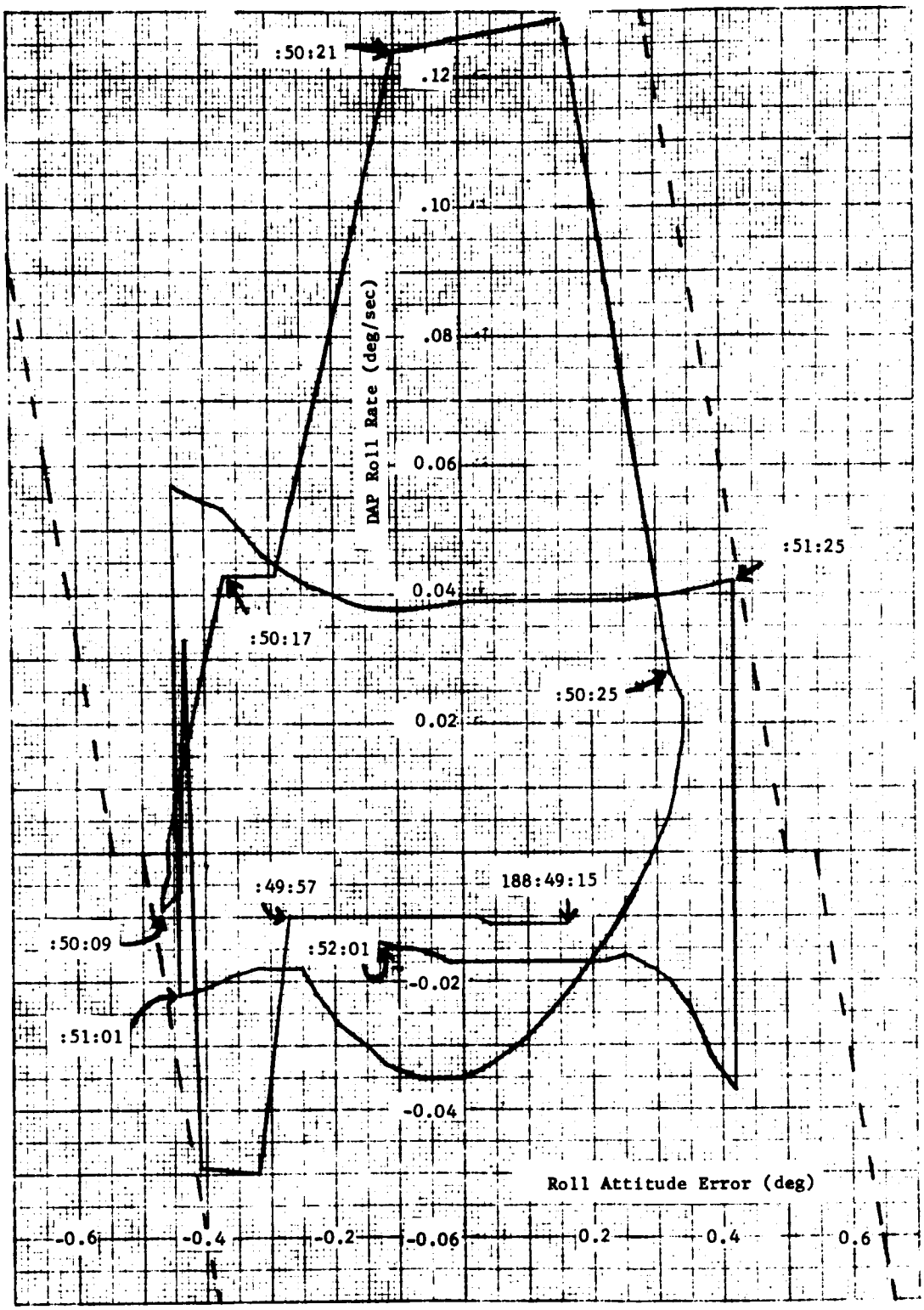

Figure 4-6a CSM X-AXIS ATTITUDE HOLD DURING T/E MCC

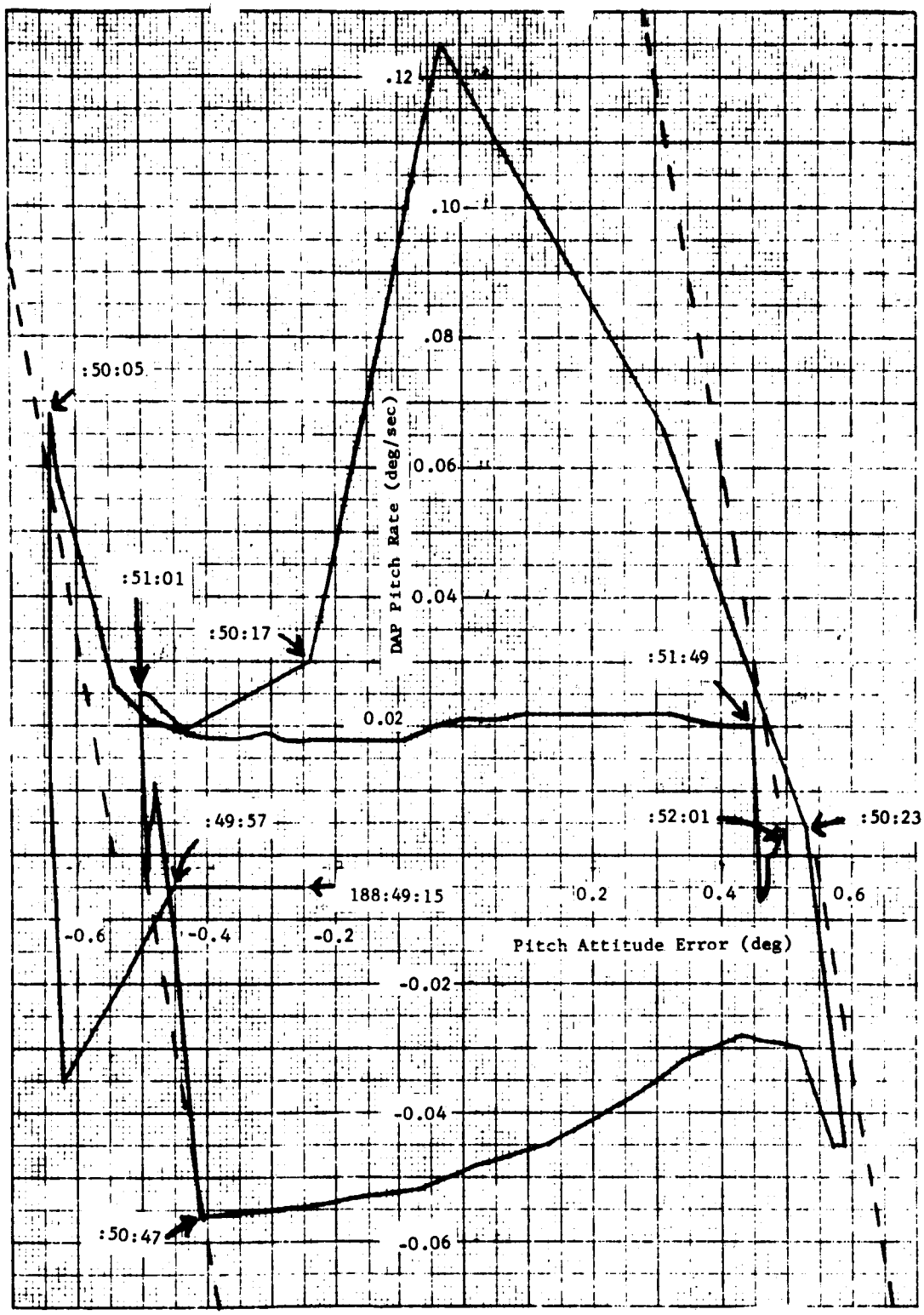

Figure 4-6b CSM Y-AXIS ATTITUDE HOLD DURING T/E MCC

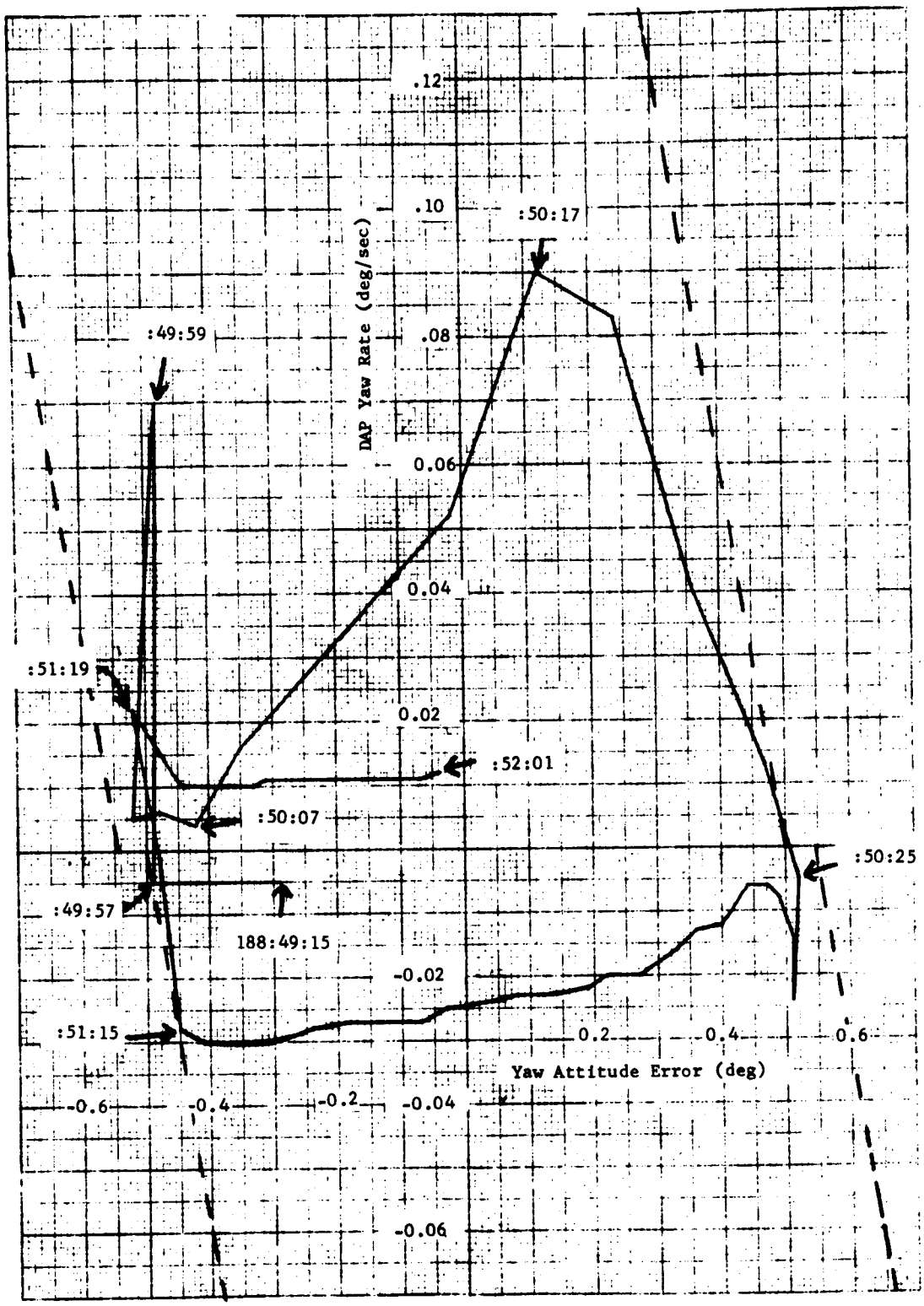

Figure 4-6c CSM Z-AXIS ATTITUDE HOLD DURING T/E MCC

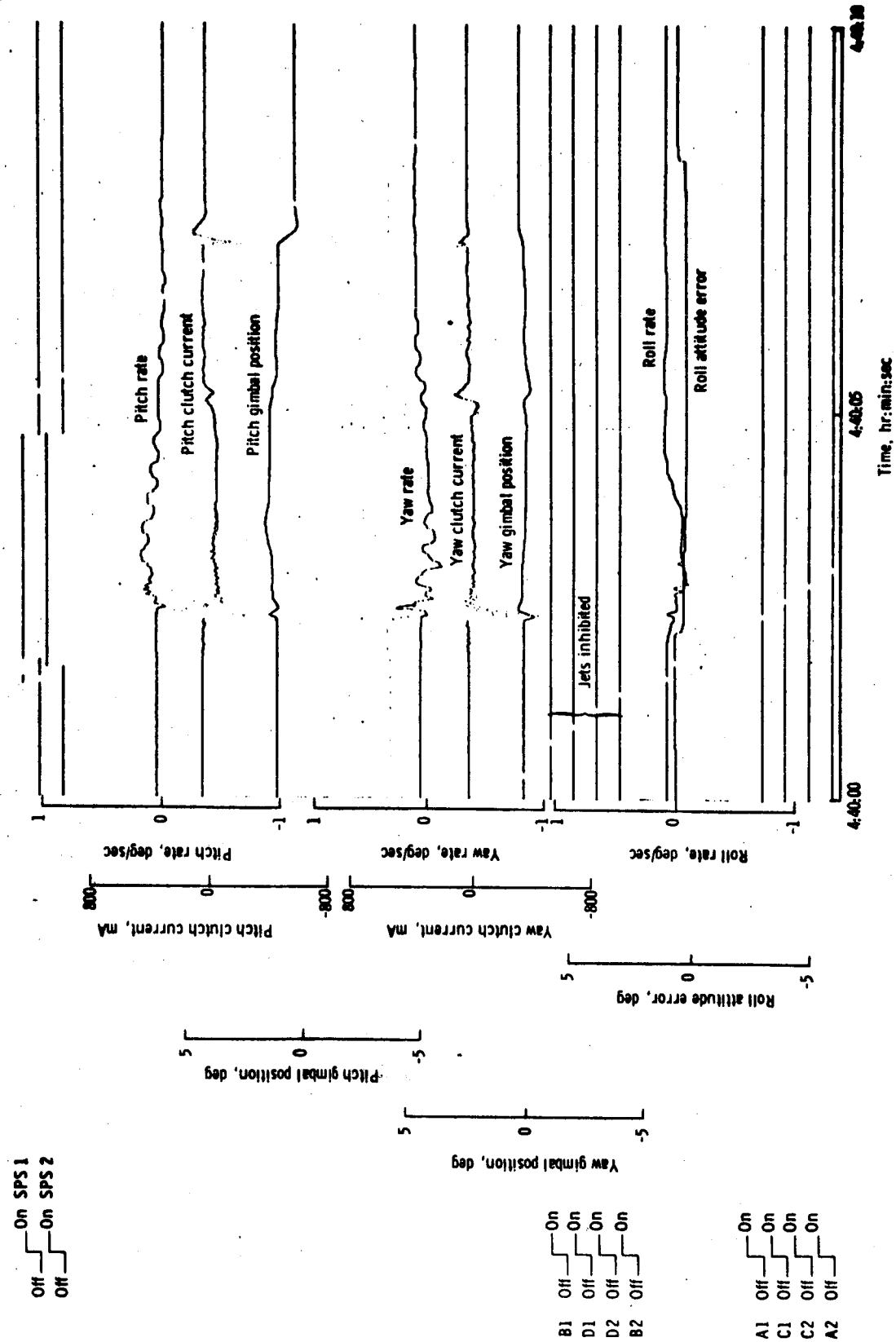

Figure 4-7 SPACECRAFT DYNAMICS DURING EVASIVE MANEUVER

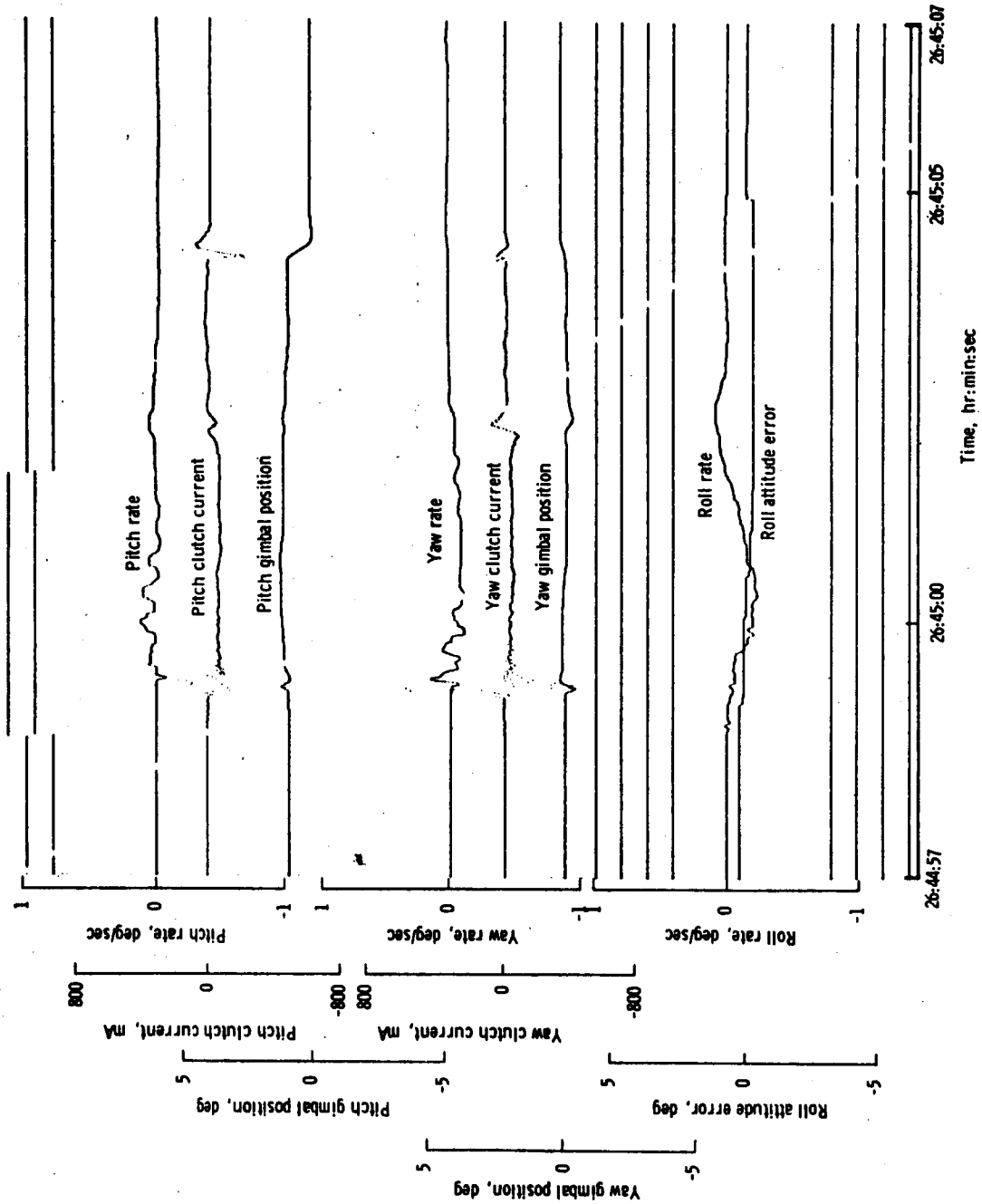

Figure 4-8 SPACECRAFT DYNAMICS DURING MCC_2 MANEUVER

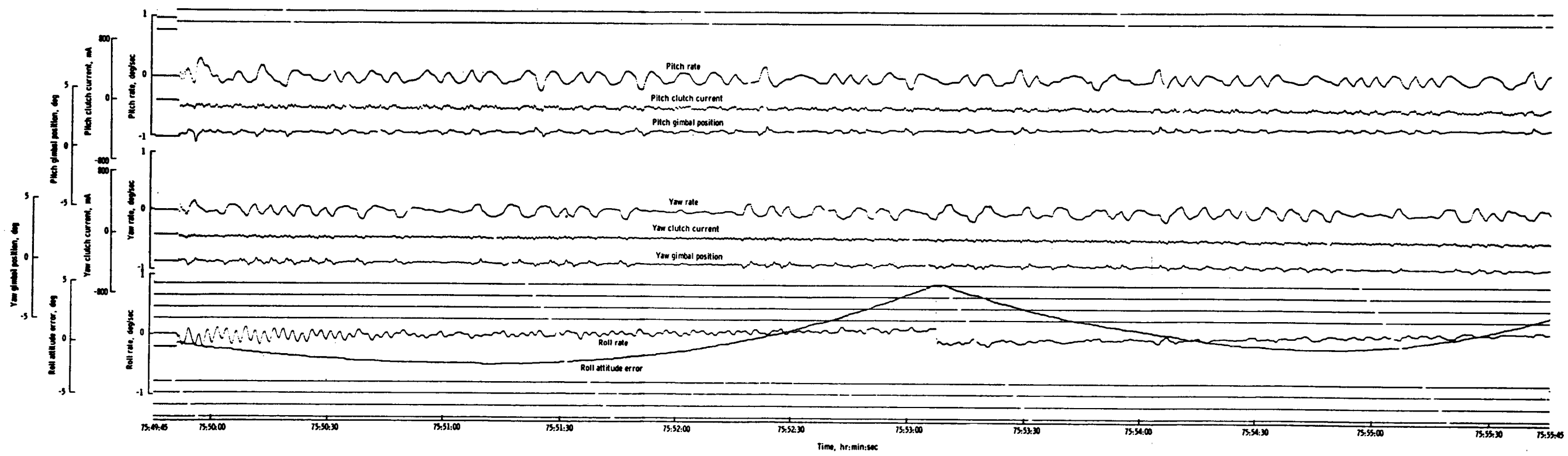

Figure 4-9 SPACECRAFT DYNAMICS DURING LUNAR ORBIT INSERTION

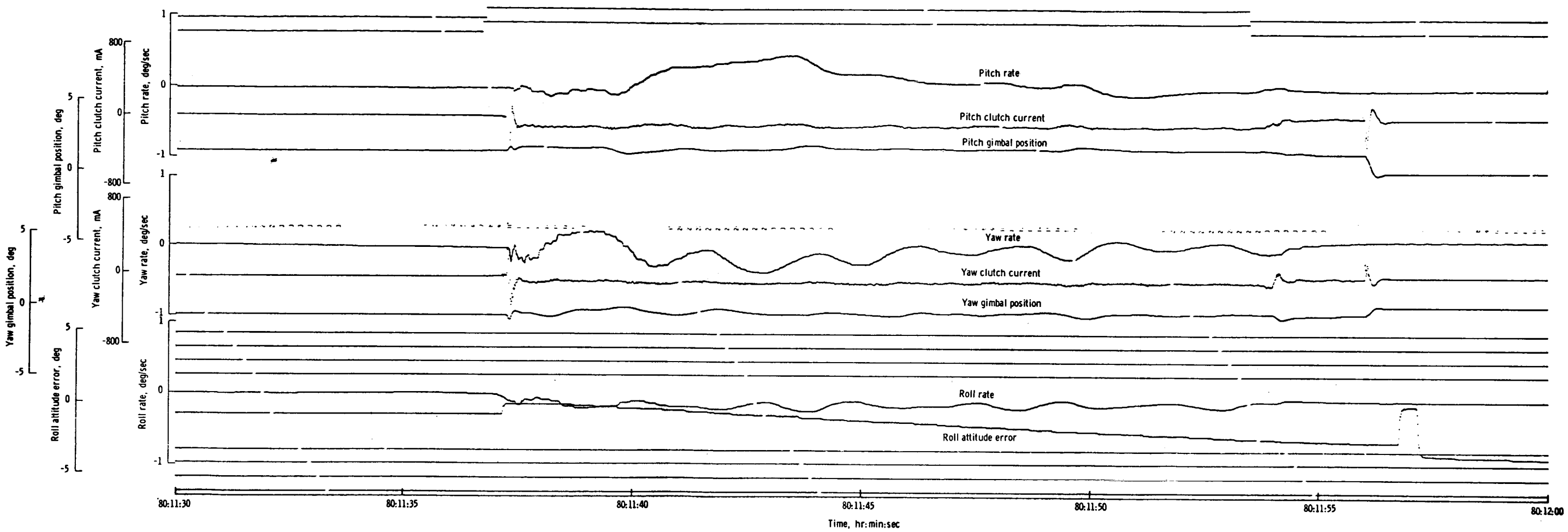

Figure 4-10 SPACECRAFT DURING LUNAR ORBIT CIRCULARIZATION

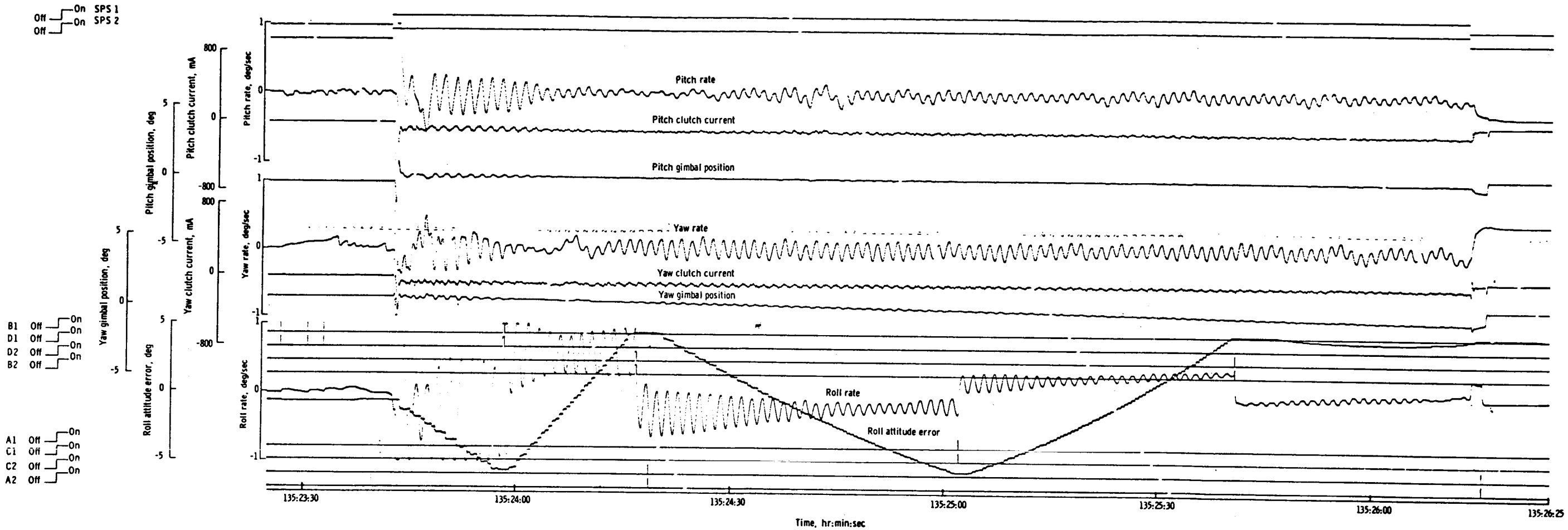

Figure 4-11 SPACECRAFT DYNAMICS DURING TRANSEARTH INJECTION

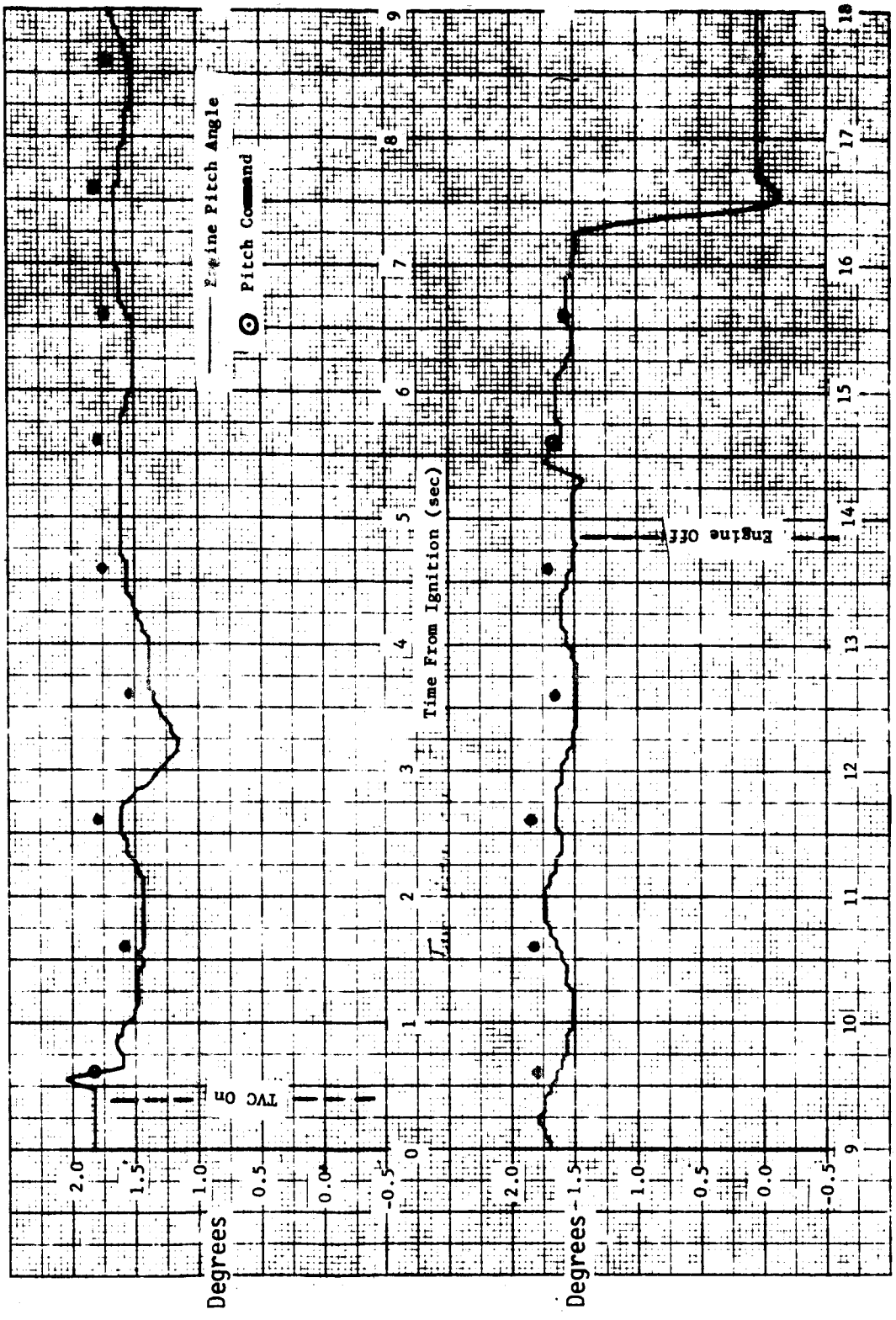

Figure 4-12 PITCH ENGINE ANGLE DURING LOI 2

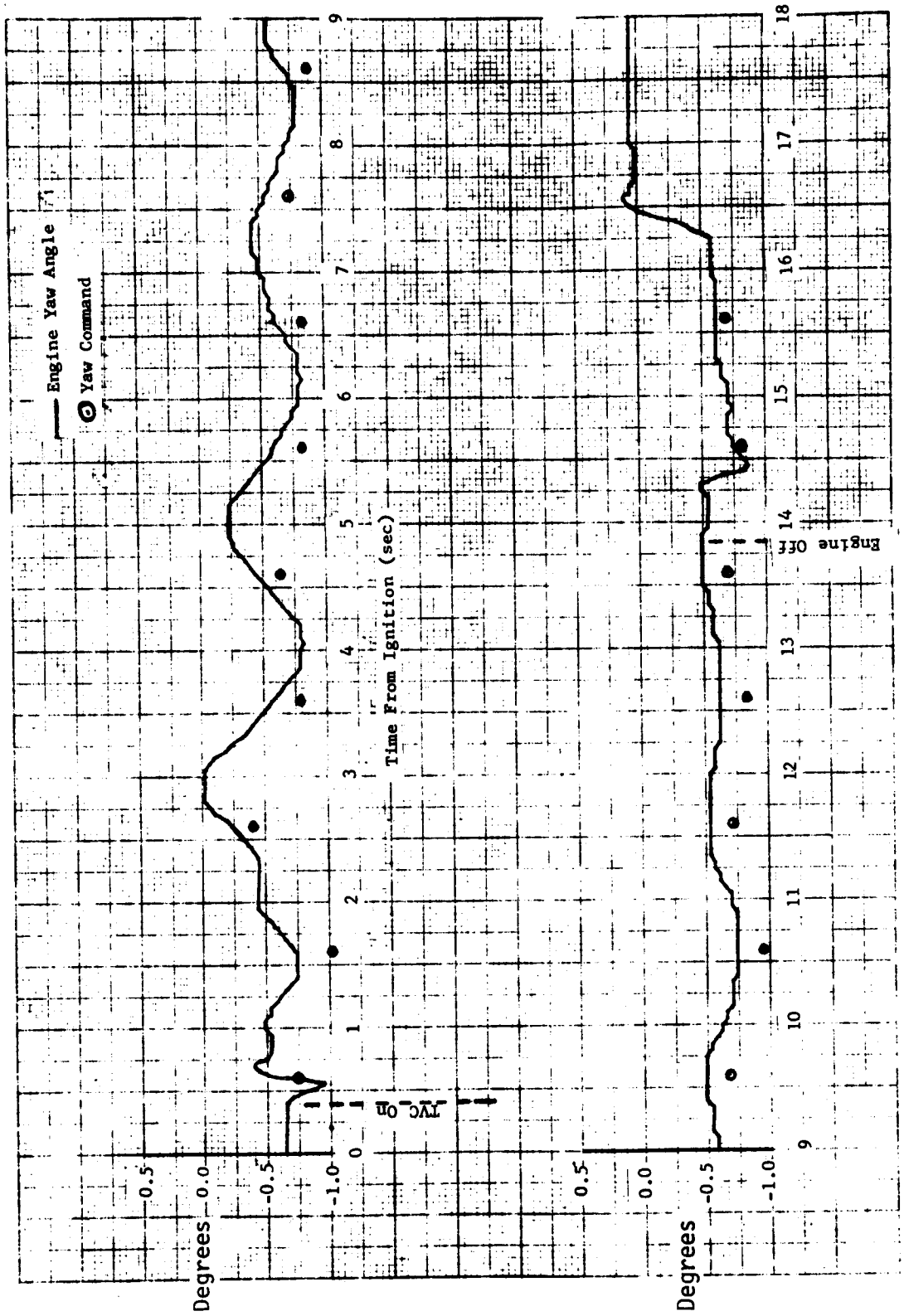

Figure 4-13 YAW ENGINE ANGLE DURING LOI 2

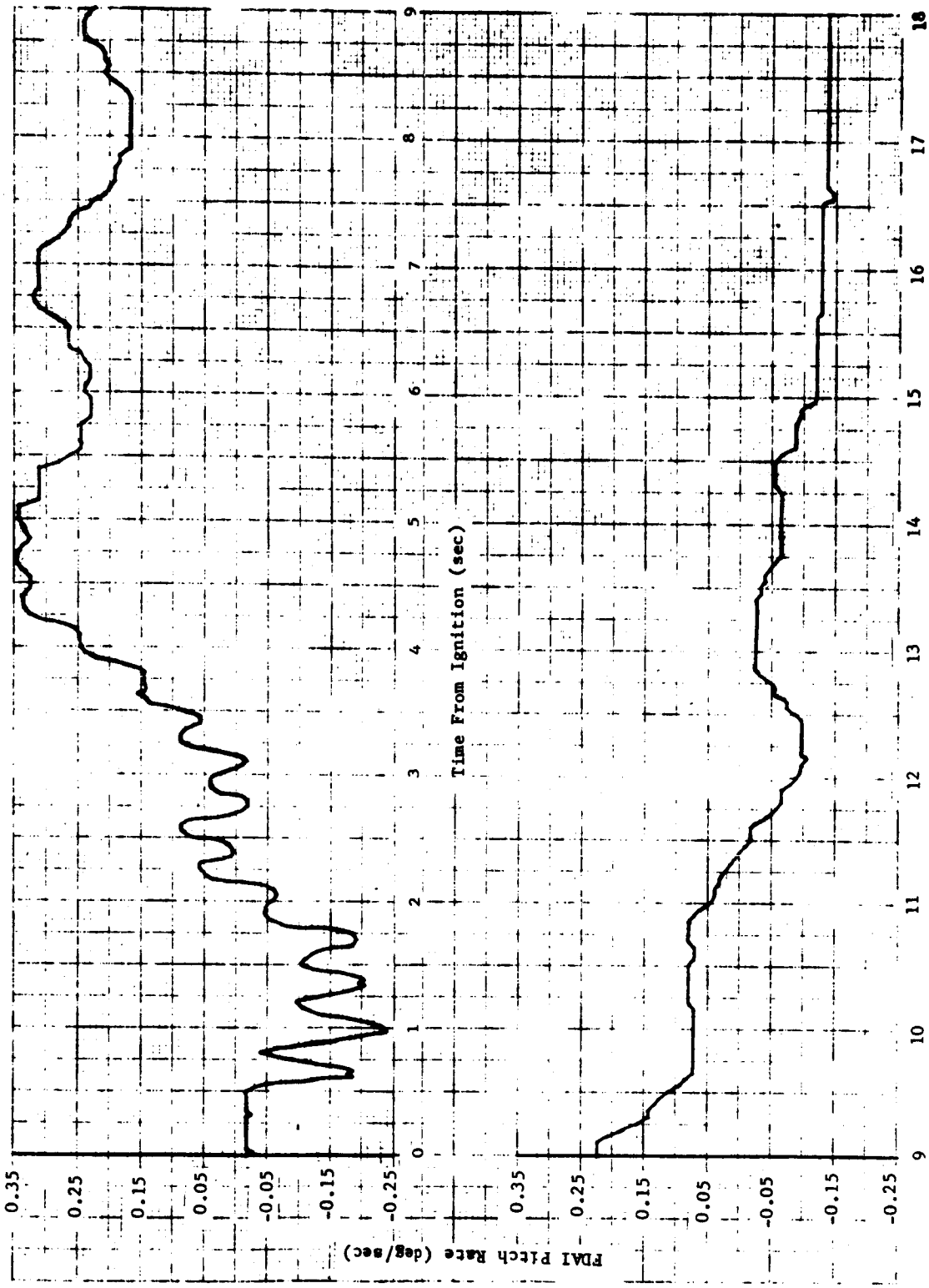

Figure 4-14 FDAI BODY PITCH RATE DURING LOI 2

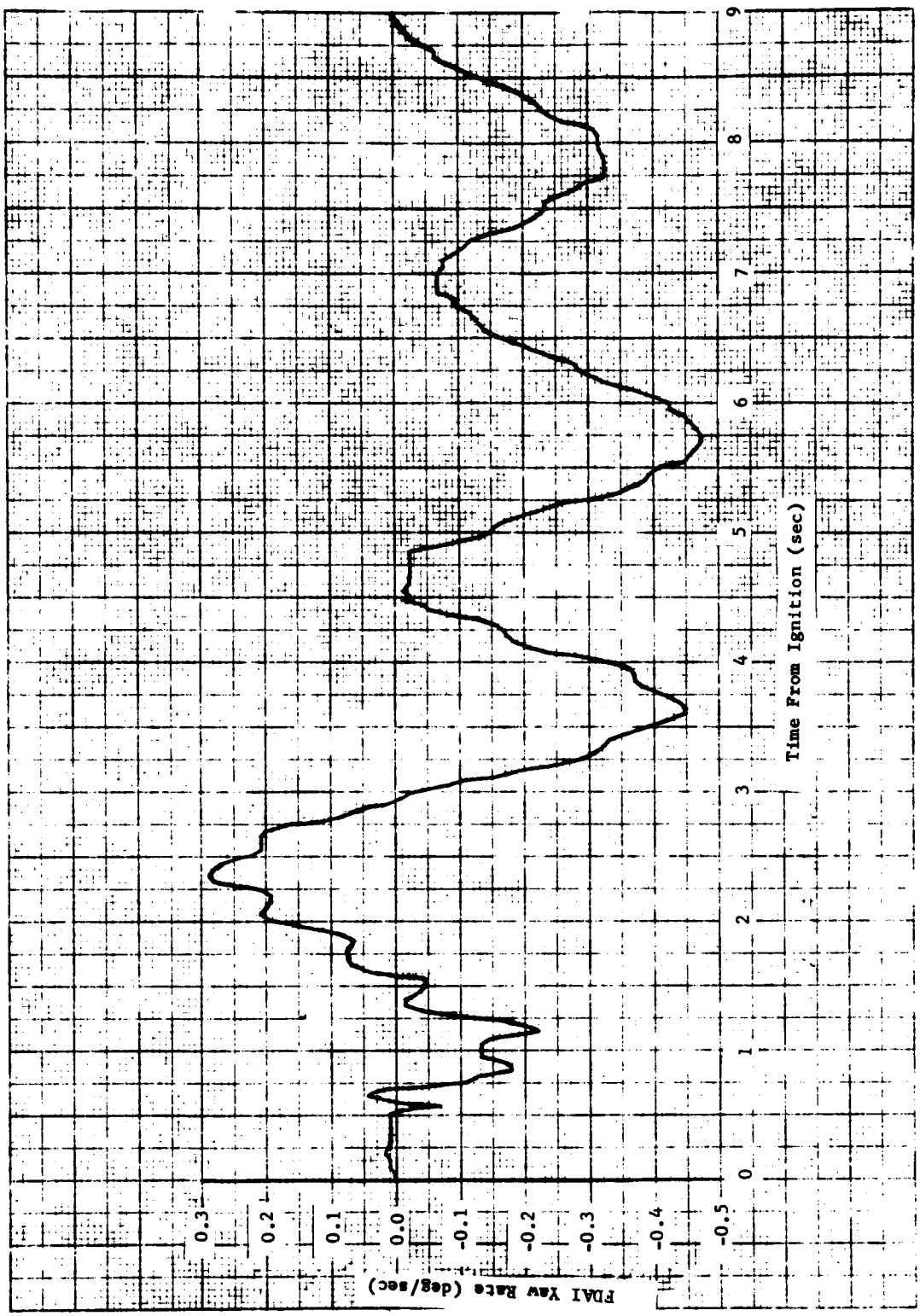

Figure 4-15 FDAI BODY YAW RATE DURING LOI 2

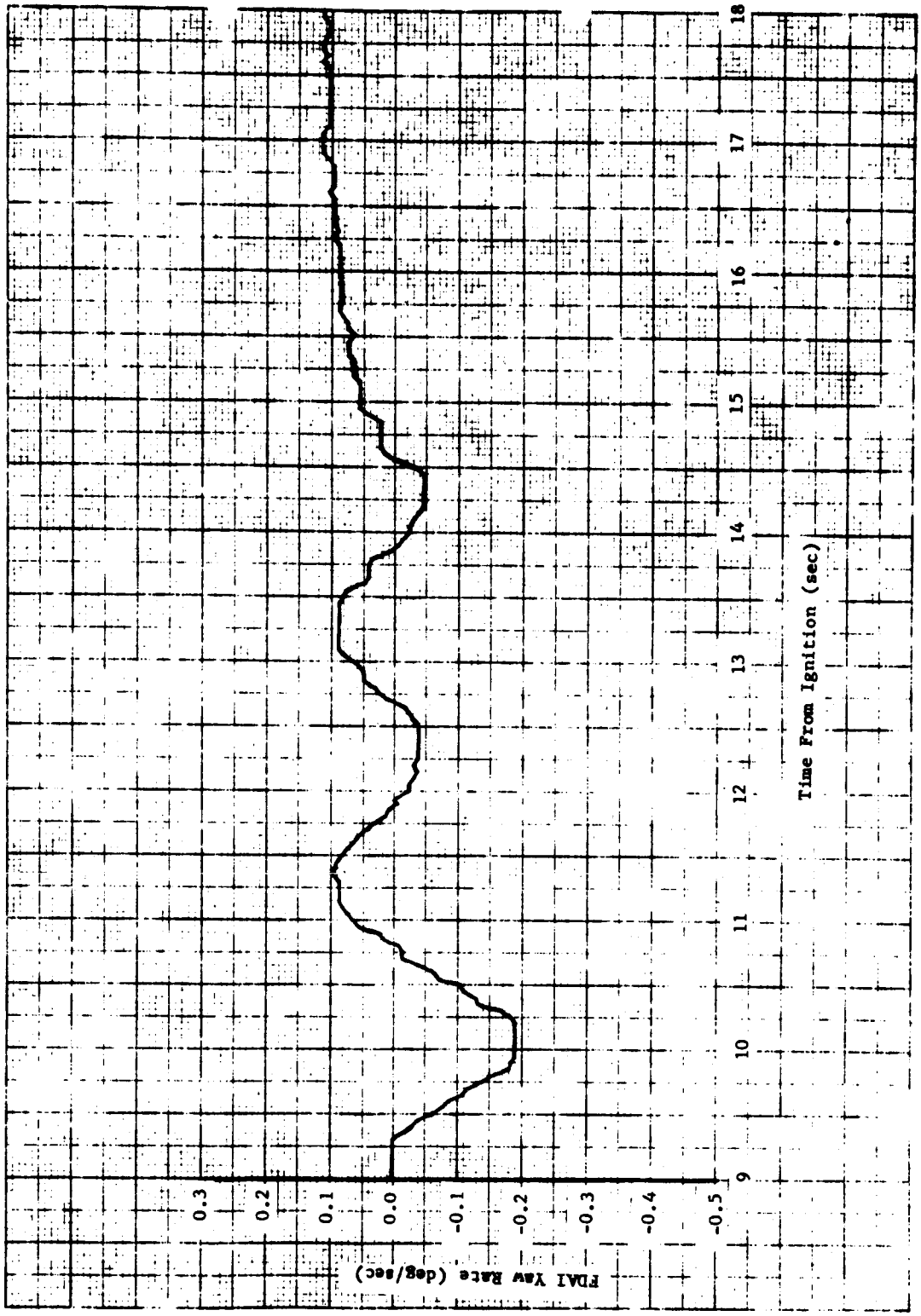

Figure 4-15 FDAI BODY YAW RATE DURING LOI 2 (CONT.)

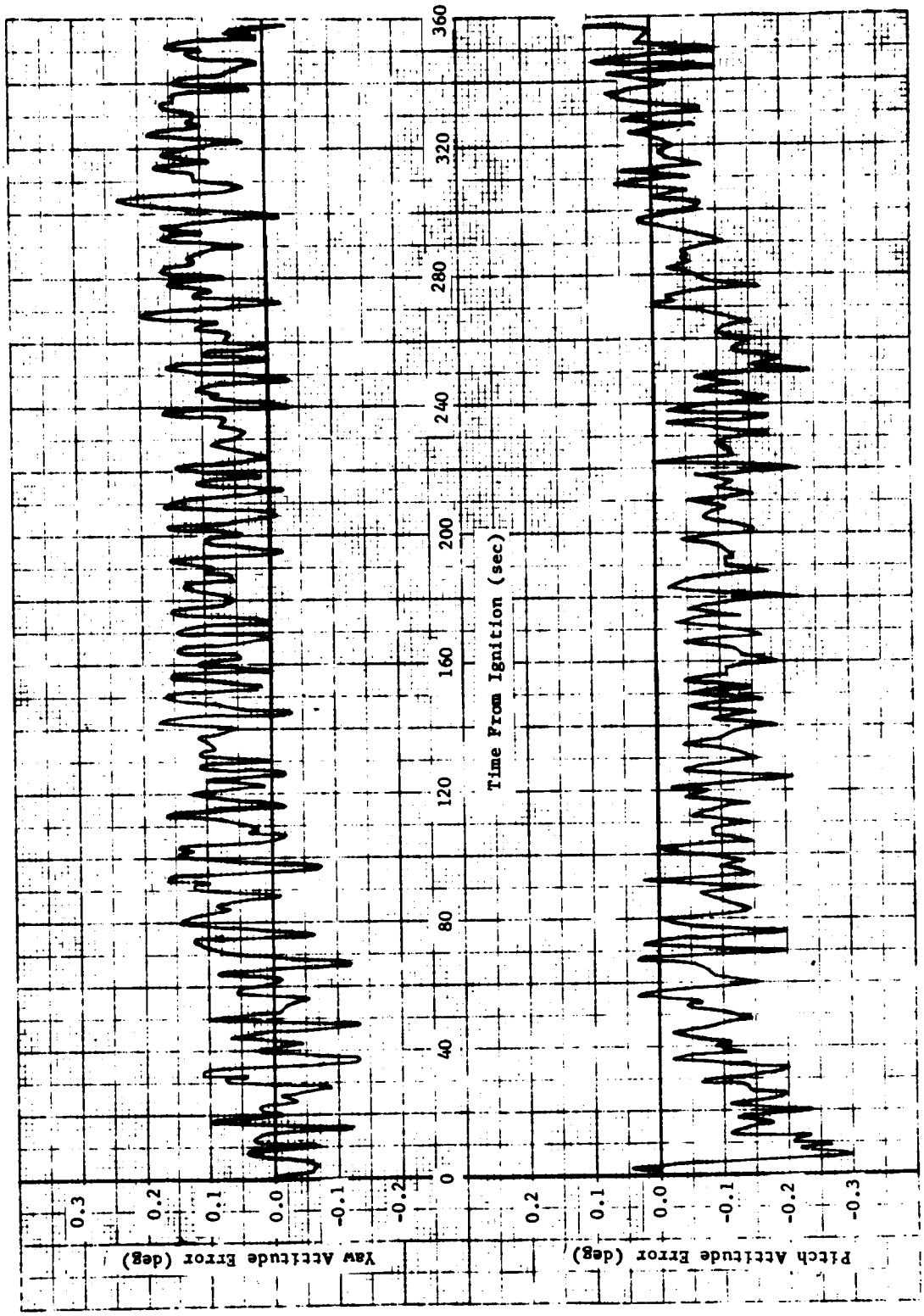

Figure 4-16 LOI 1 PITCH AND YAW ATTITUDE ERRORS

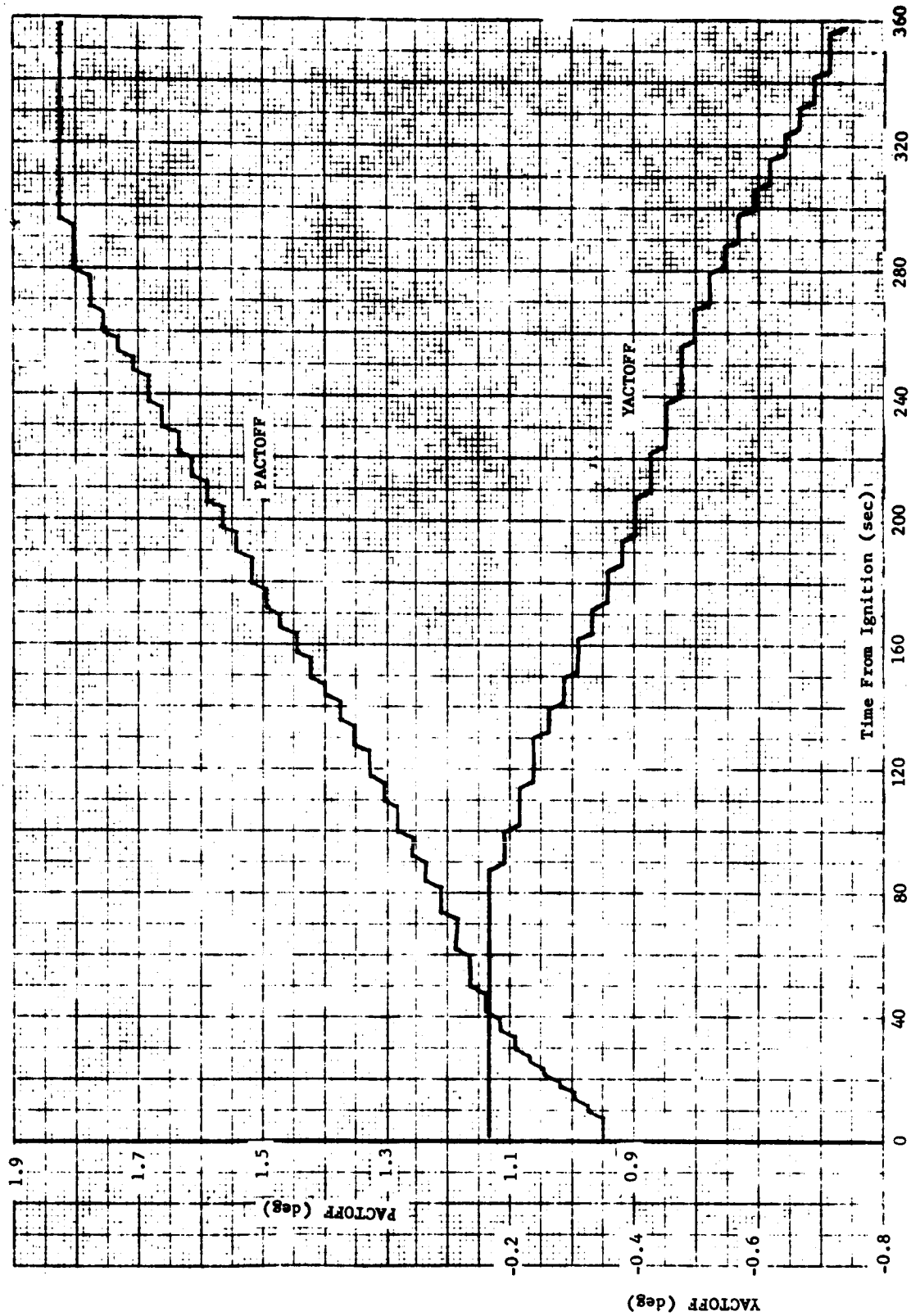

Figure 4-17 LOI 1 ENGINE TRIM ESTIMATES

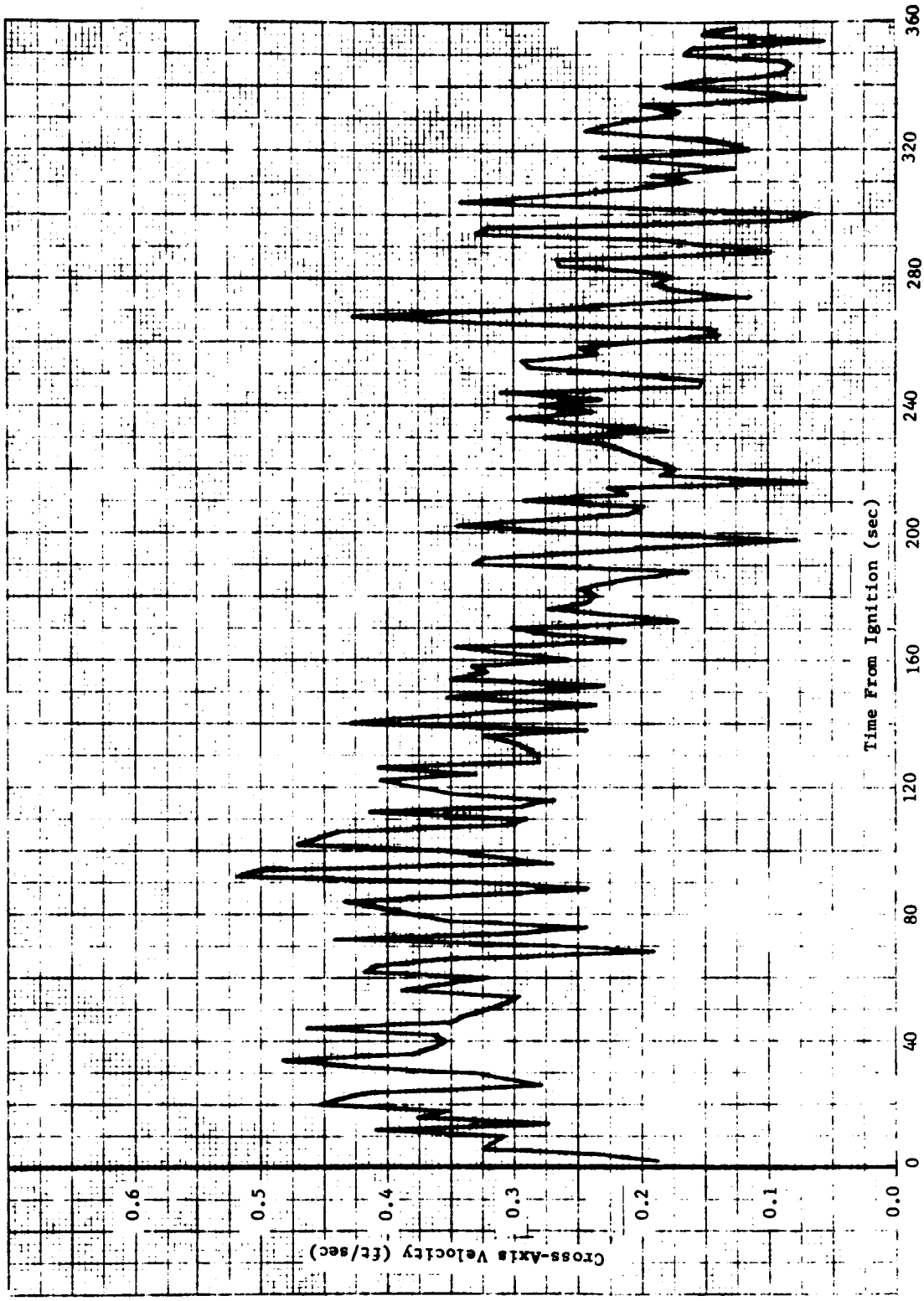

Figure 4-18 LOI 1 CROSS-AXIS VELOCITY

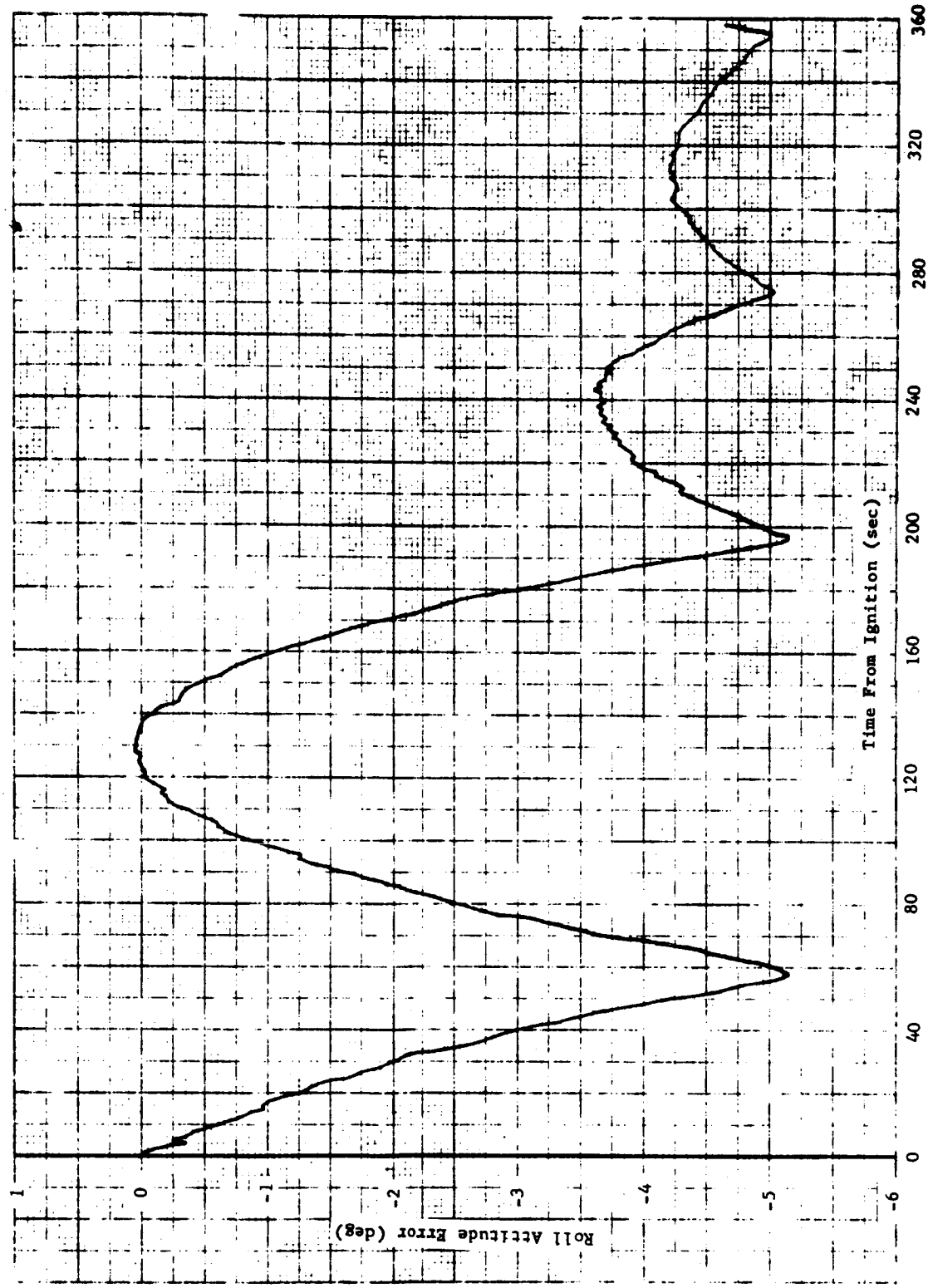

Figure 4-19 LOI 1 ROLL ATTITUDE ERROR

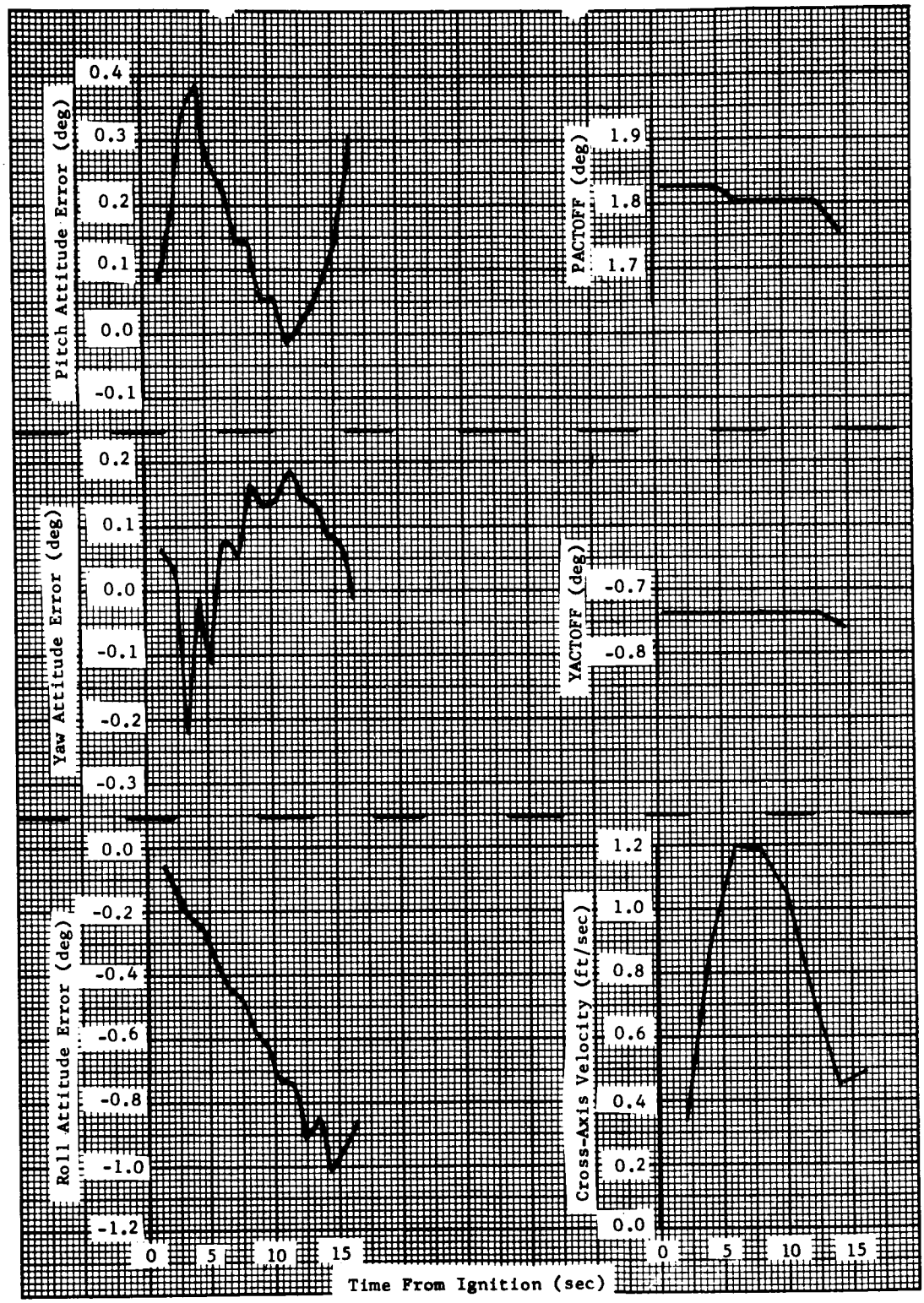

Figure 4-20 LOI 2 BURN PARAMETERS

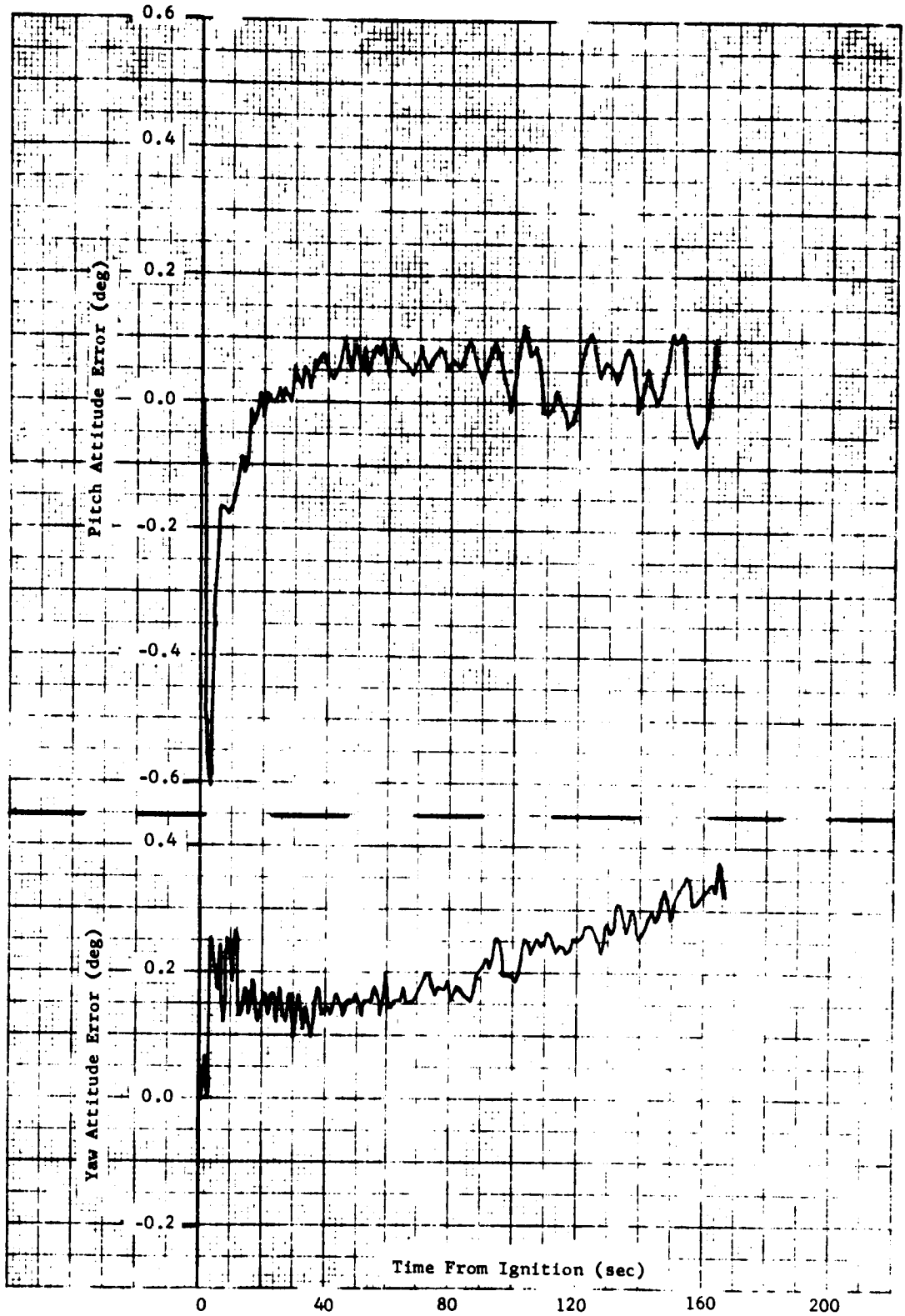

Figure 4-21 TEI PITCH AND YAW ATTITUDE ERRORS

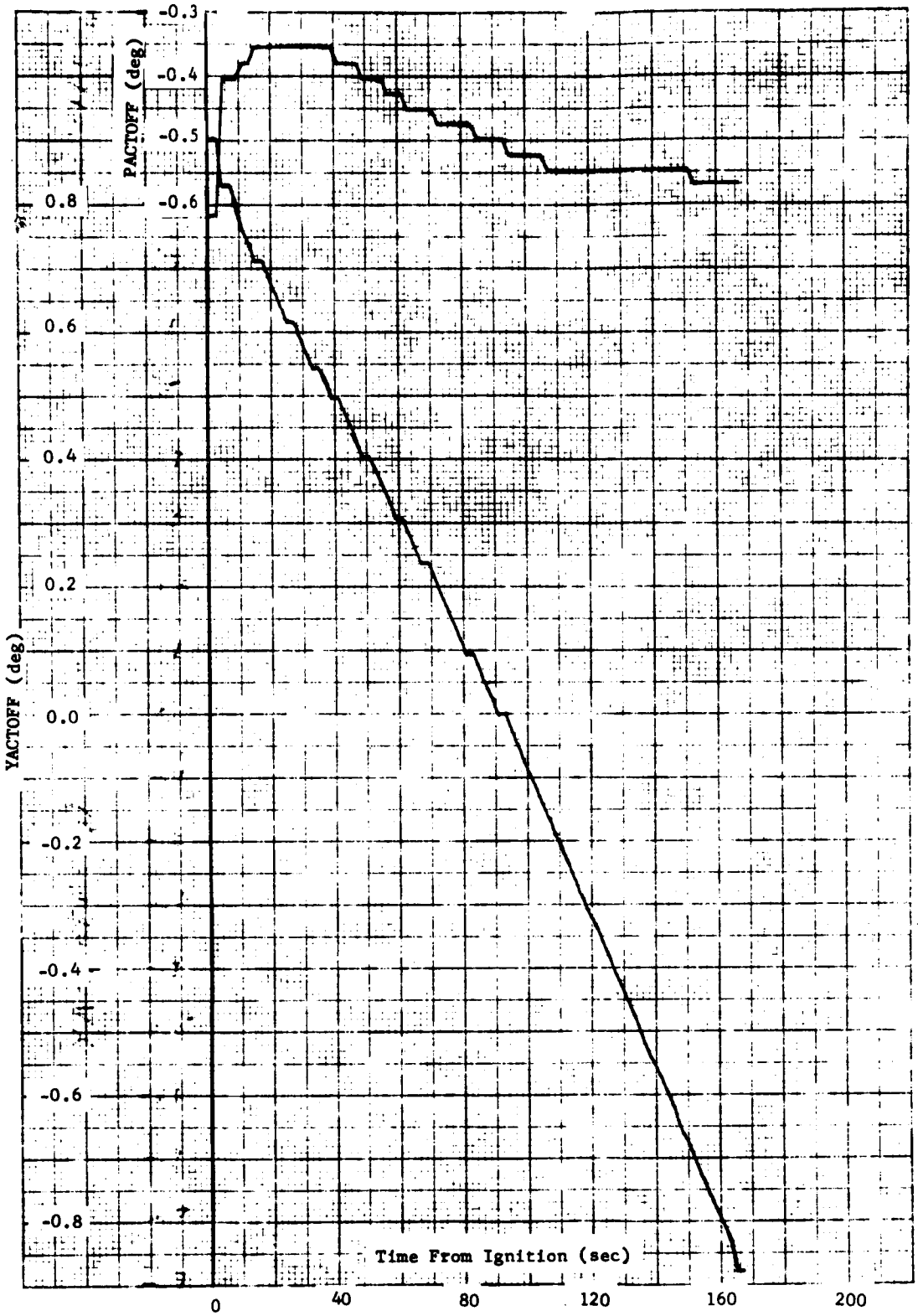

Figure 4-22 TEI ENGINE TRIM ESTIMATES

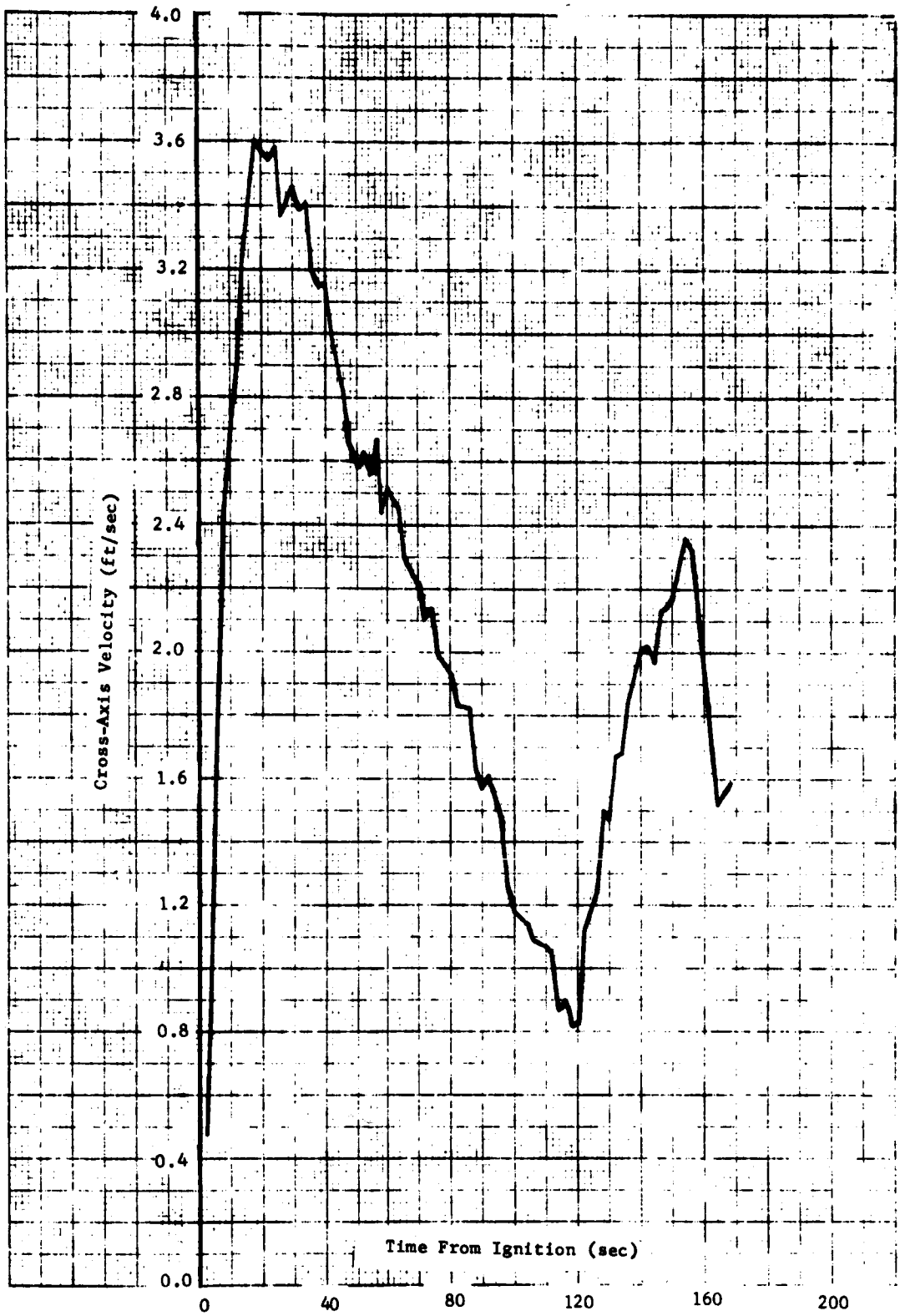

Figure 4-23 TEI CROSS-AXIS VELOCITY

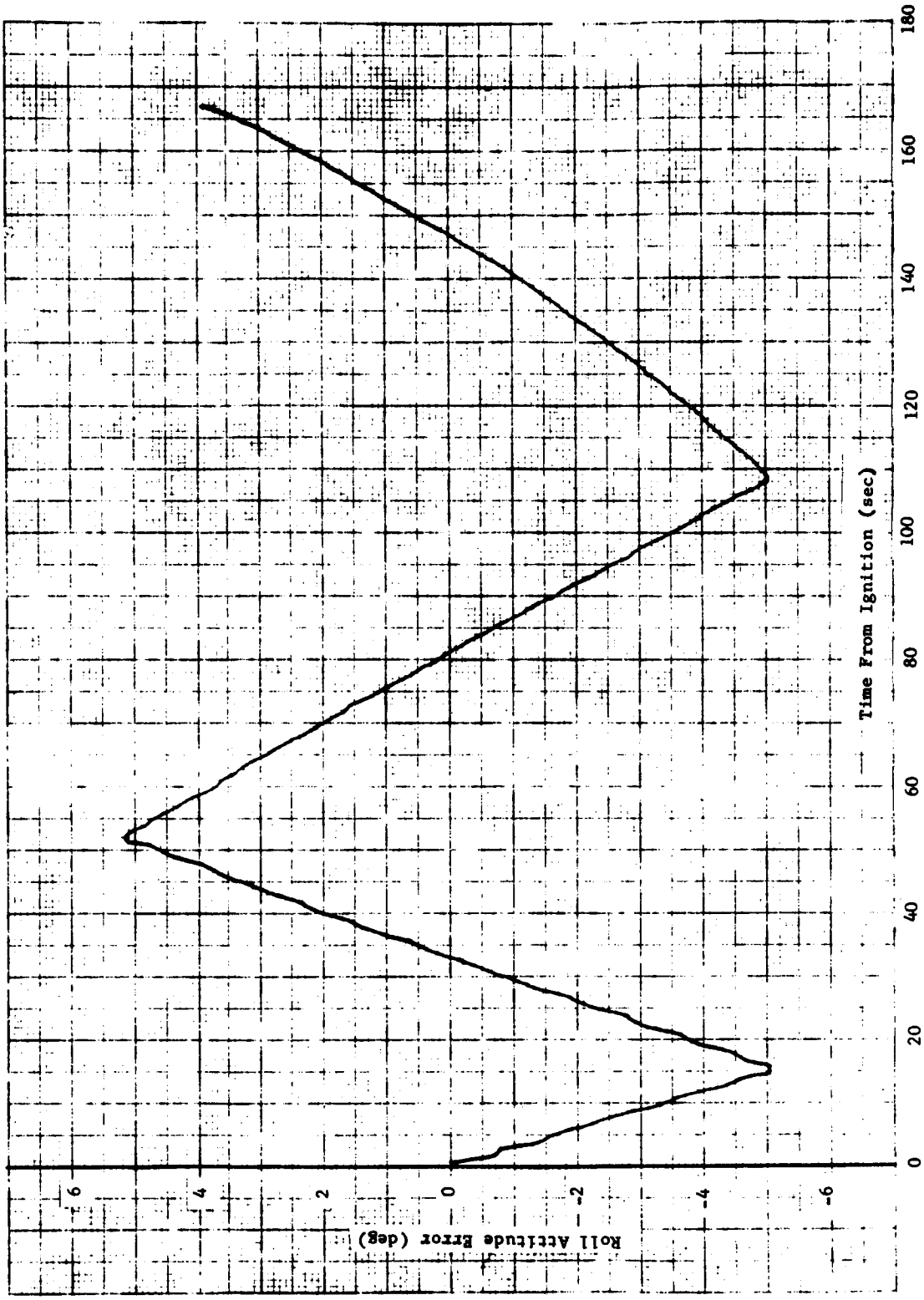

Figure 4-24 TEI ROLL ATTITUDE ERROR

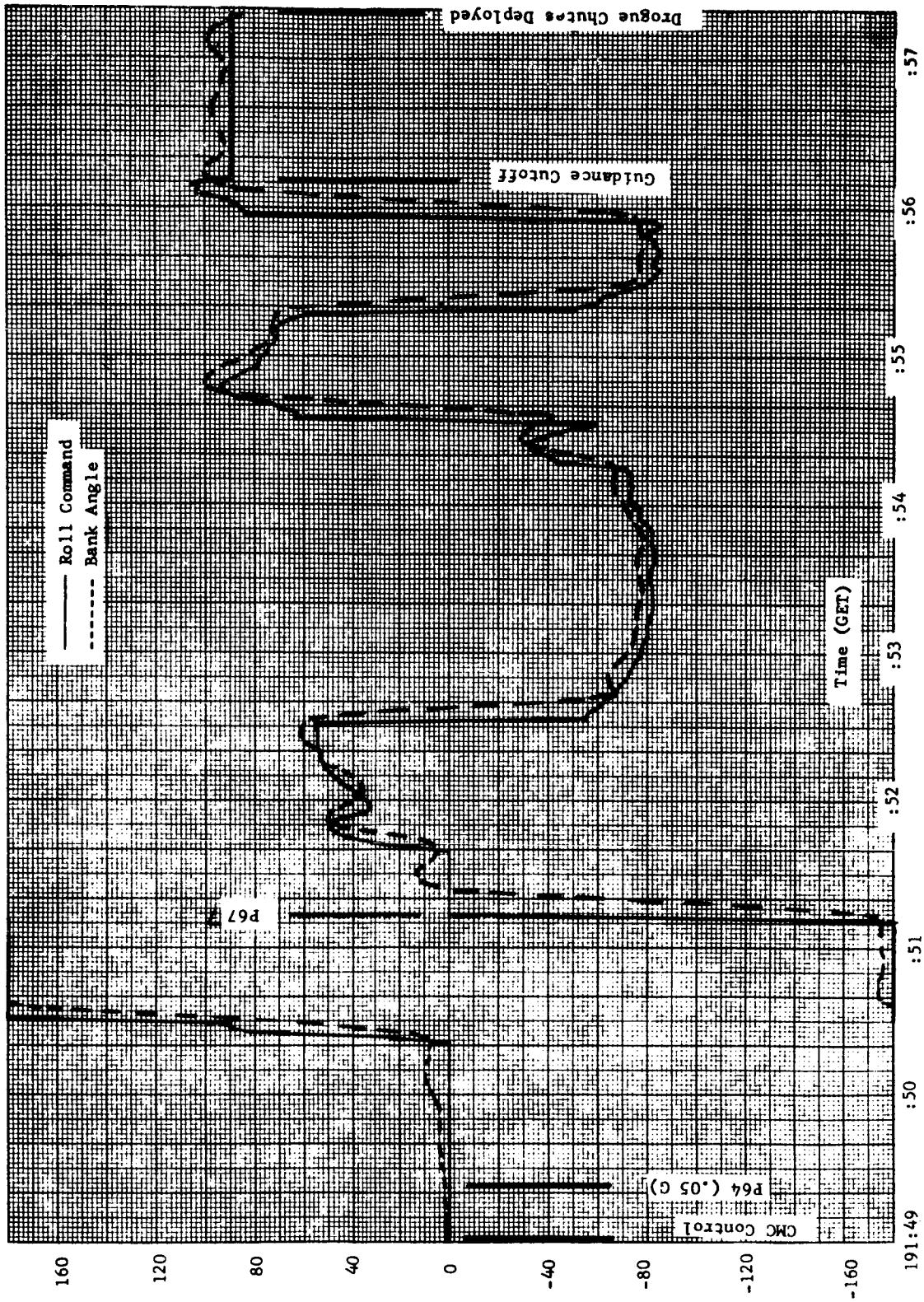

Figure 4-25 ENTRY ROLL COMMAND/BANK ANGLE HISTORIES

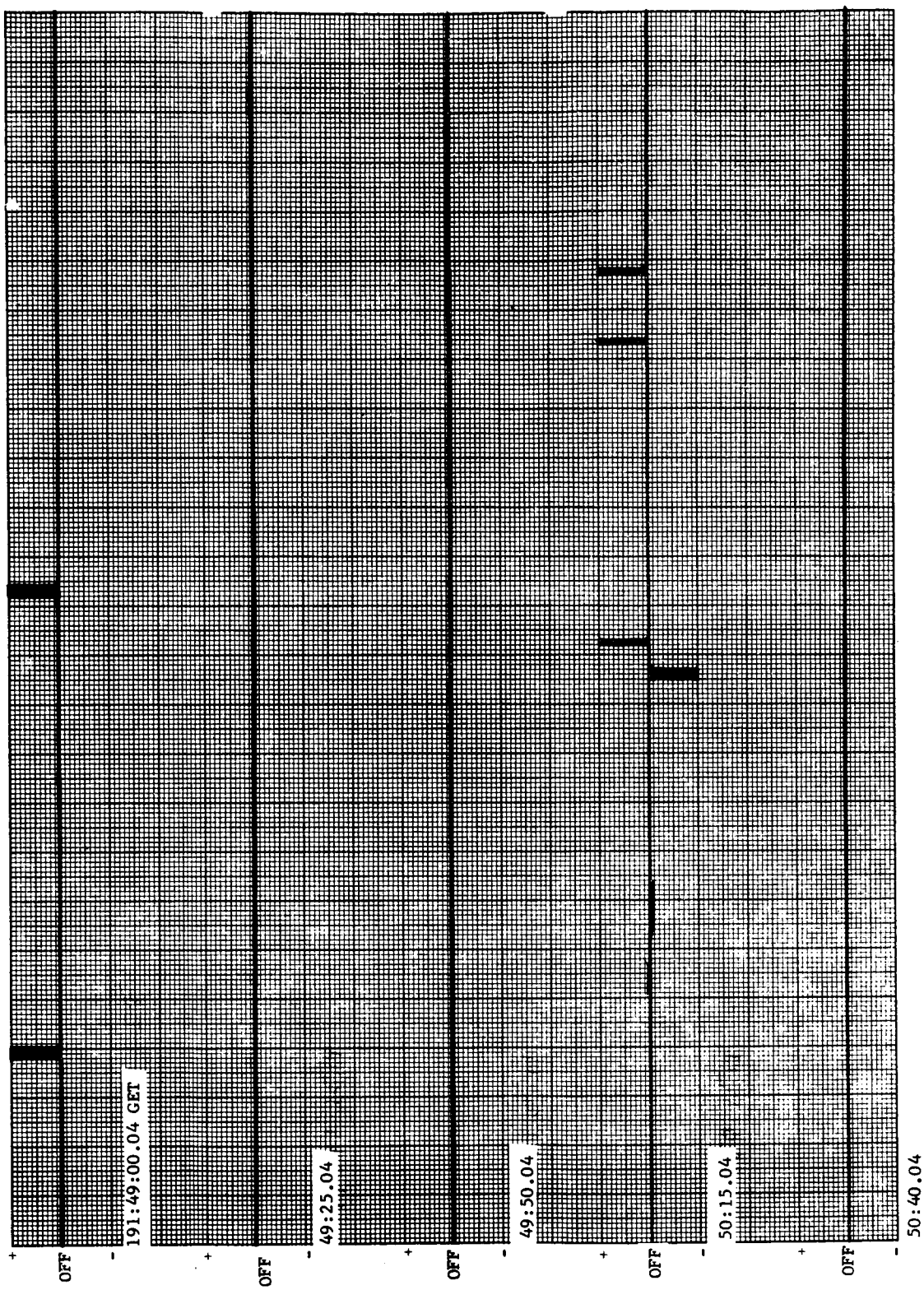

Figure 4-26 ENTRY PITCH JETS ACTIVITY

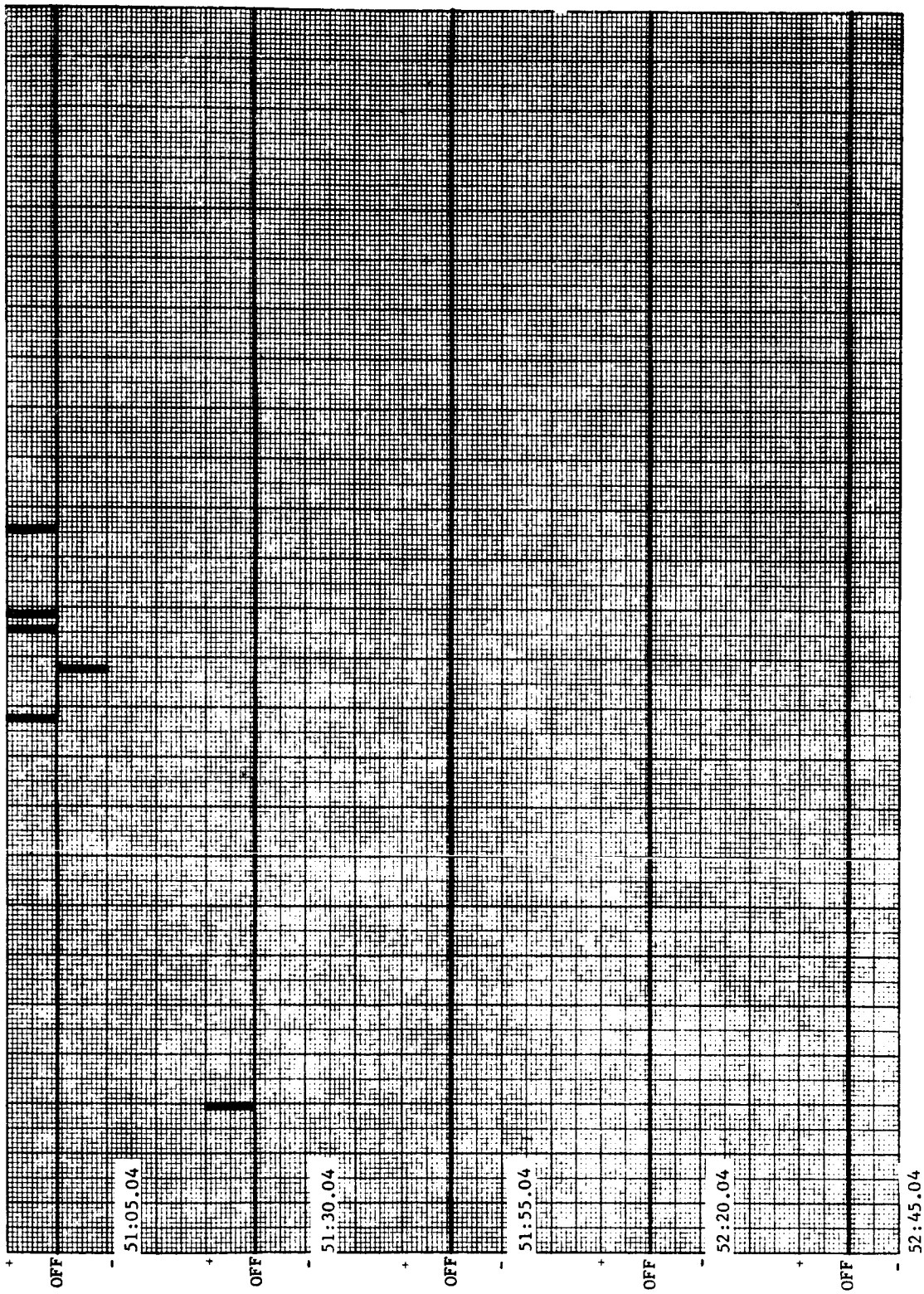

Figure 4-26 ENTRY PITCH JETS ACTIVITY (CONT.)

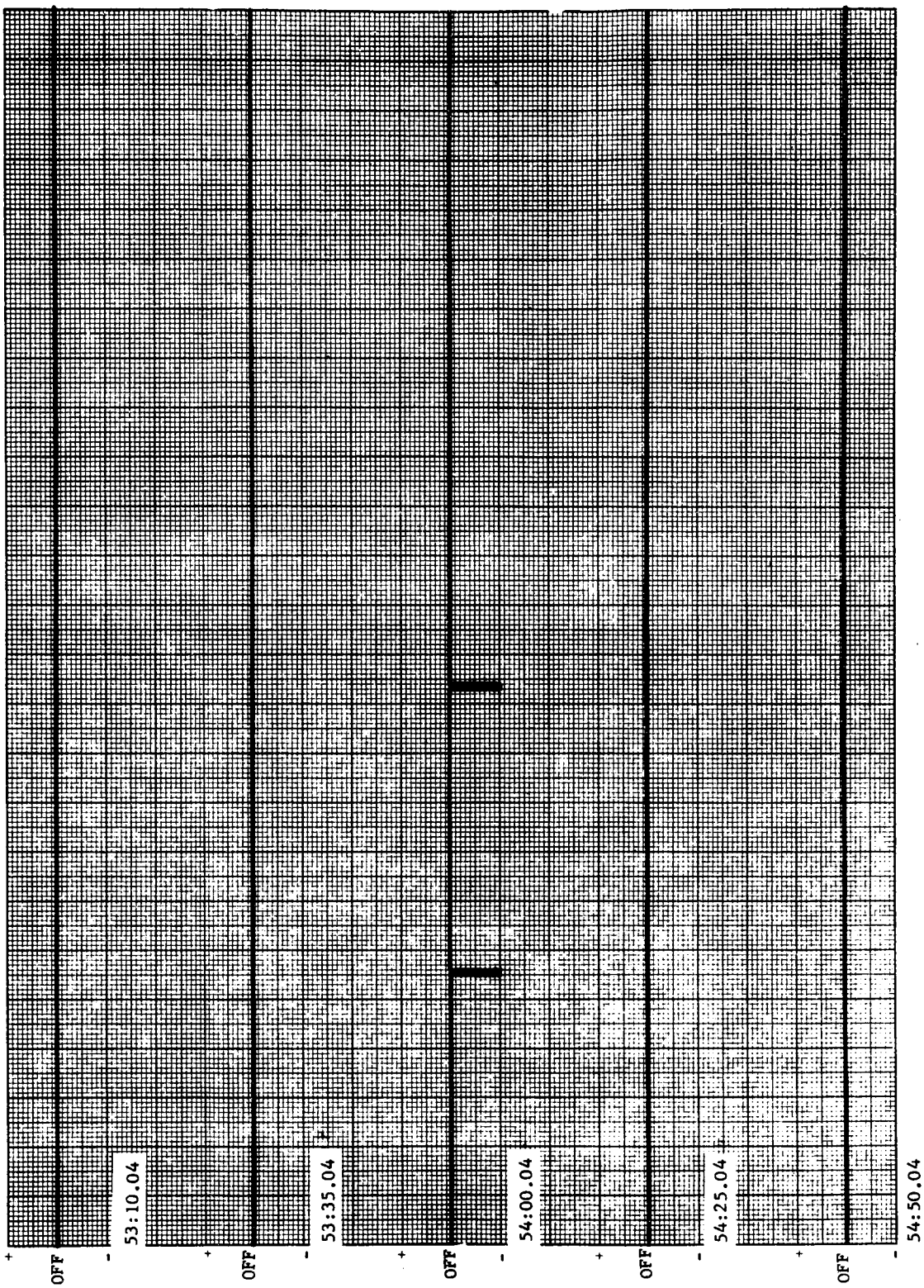

Figure 4-26 ENTRY PITCH JETS ACTIVITY (CONT.)

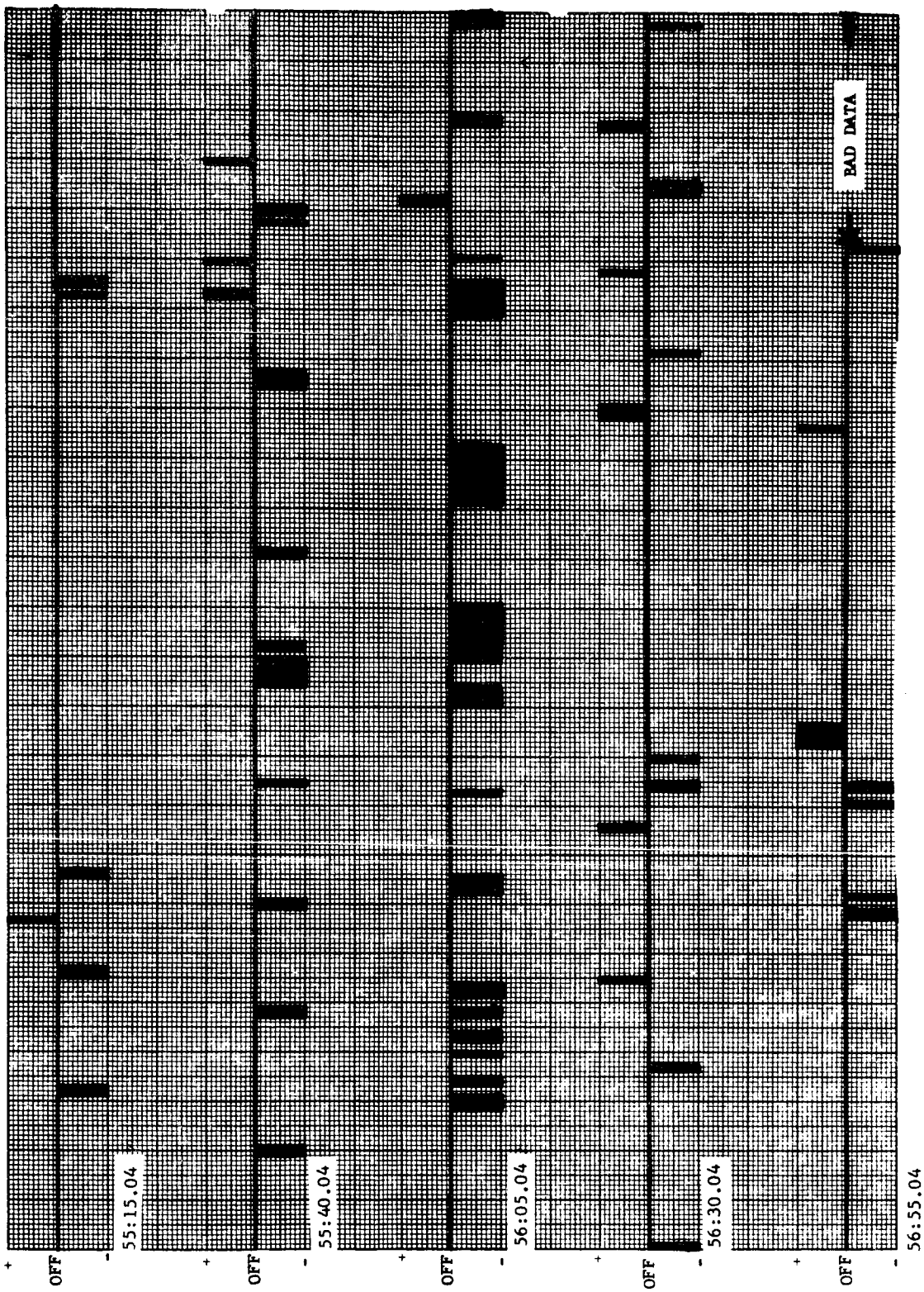

Figure 4-26 ENTRY PITCH JETS ACTIVITY (CONCLUDED)

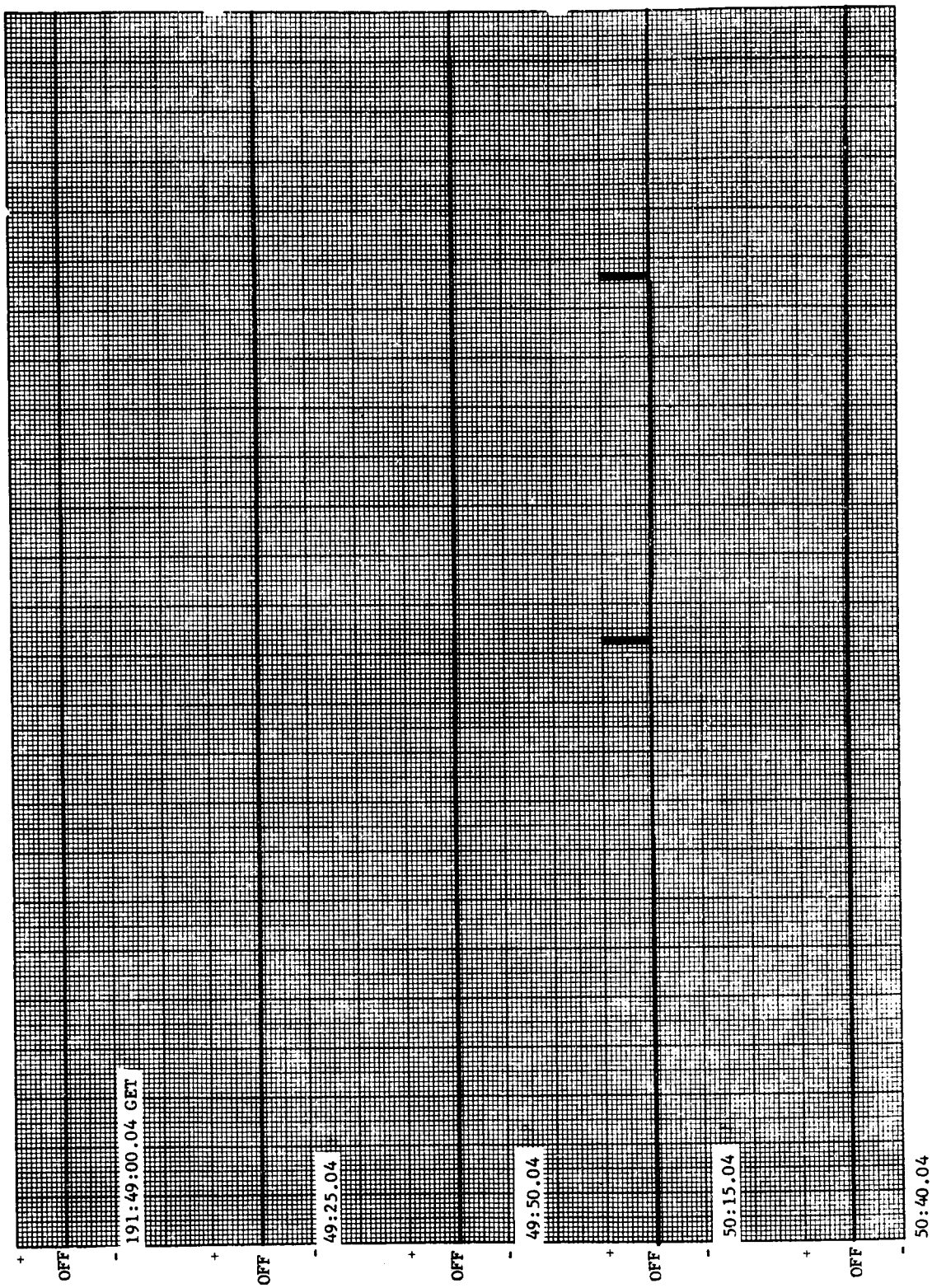

Figure 4-27 ENTRY YAW JETS ACTIVITY

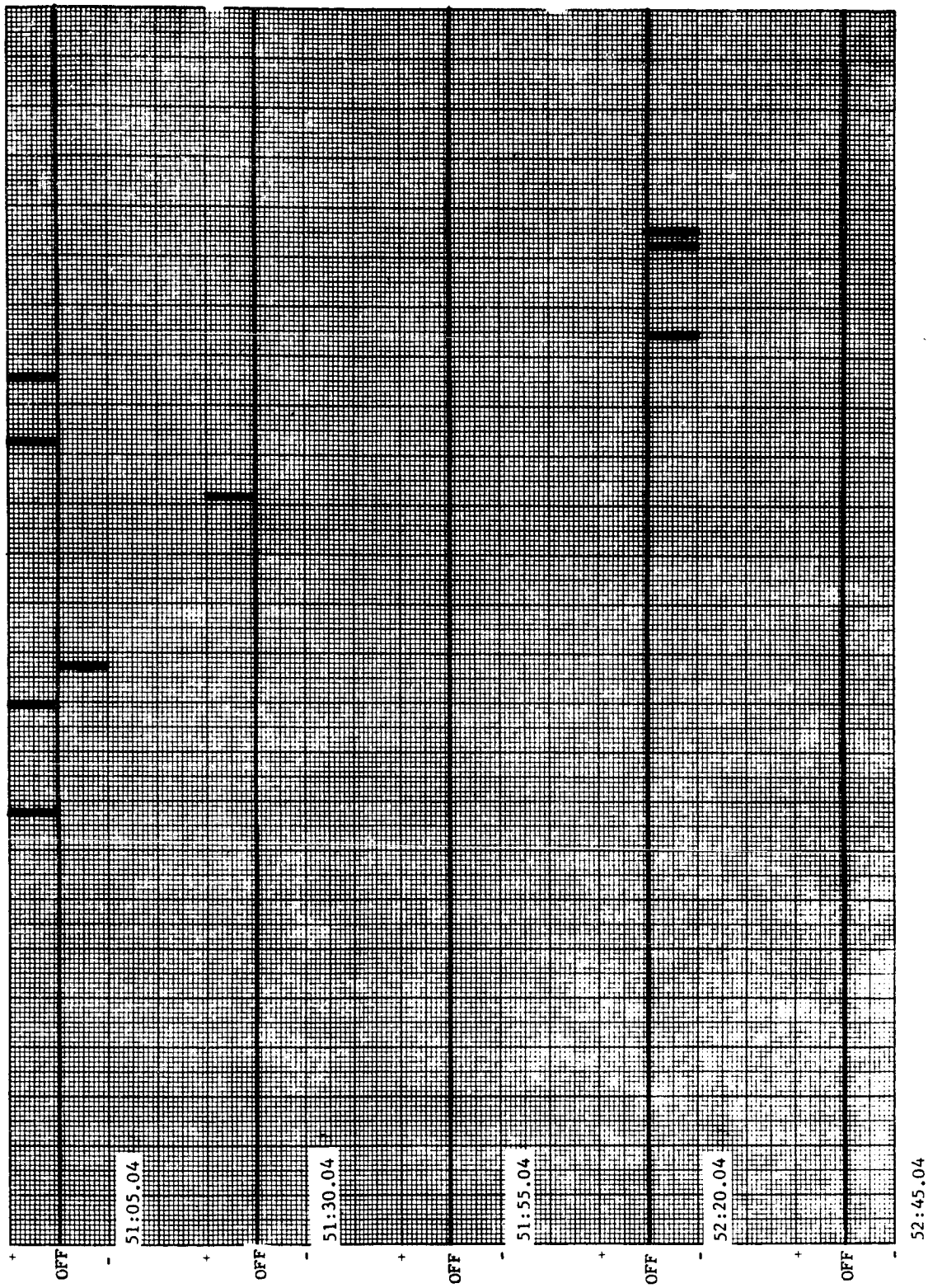

Figure 4-27 ENTRY YAW JETS ACTIVITY (CONT.)

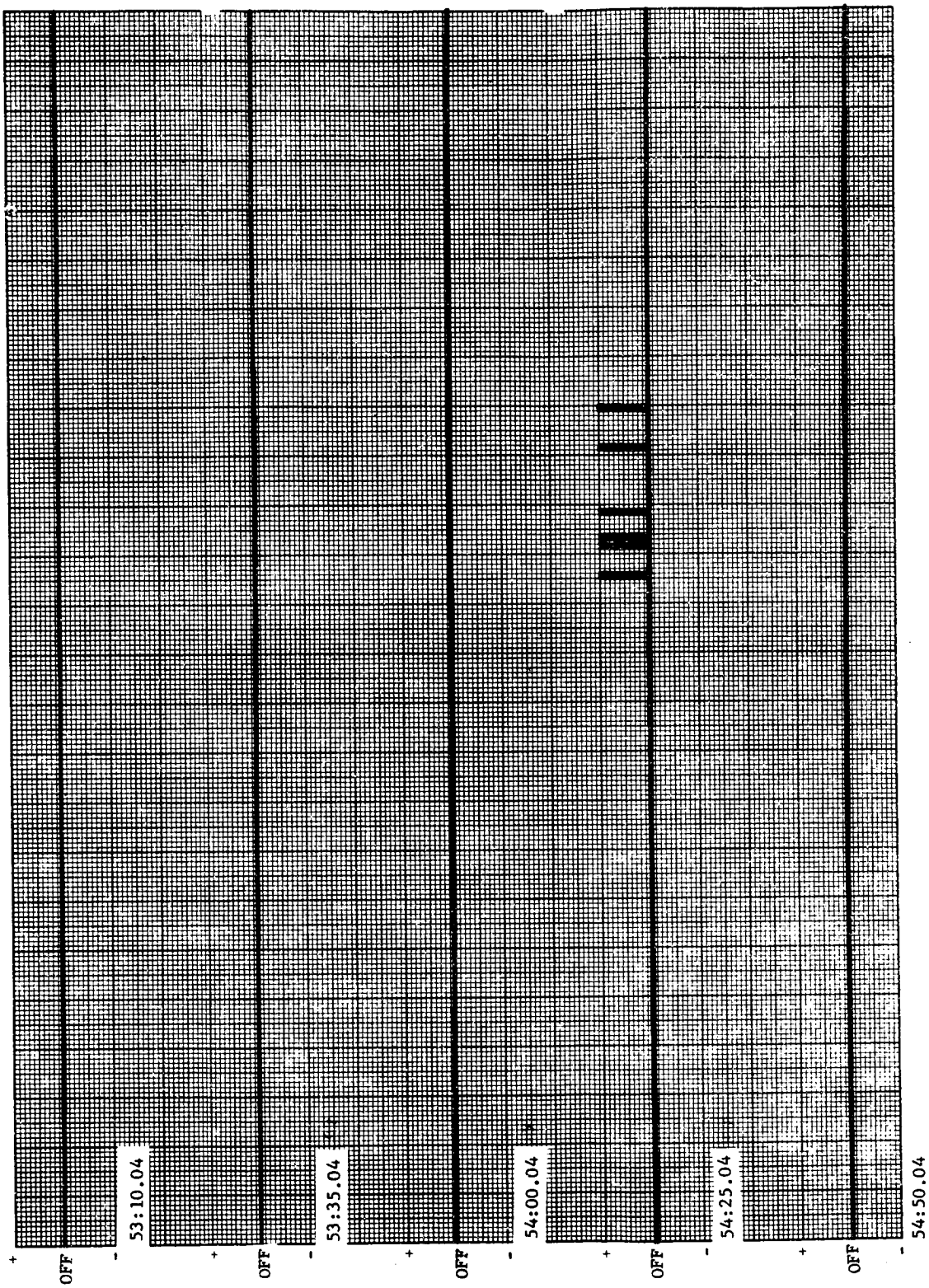

Figure 4-27 ENTRY YAW JETS ACTIVITY (CONT.)

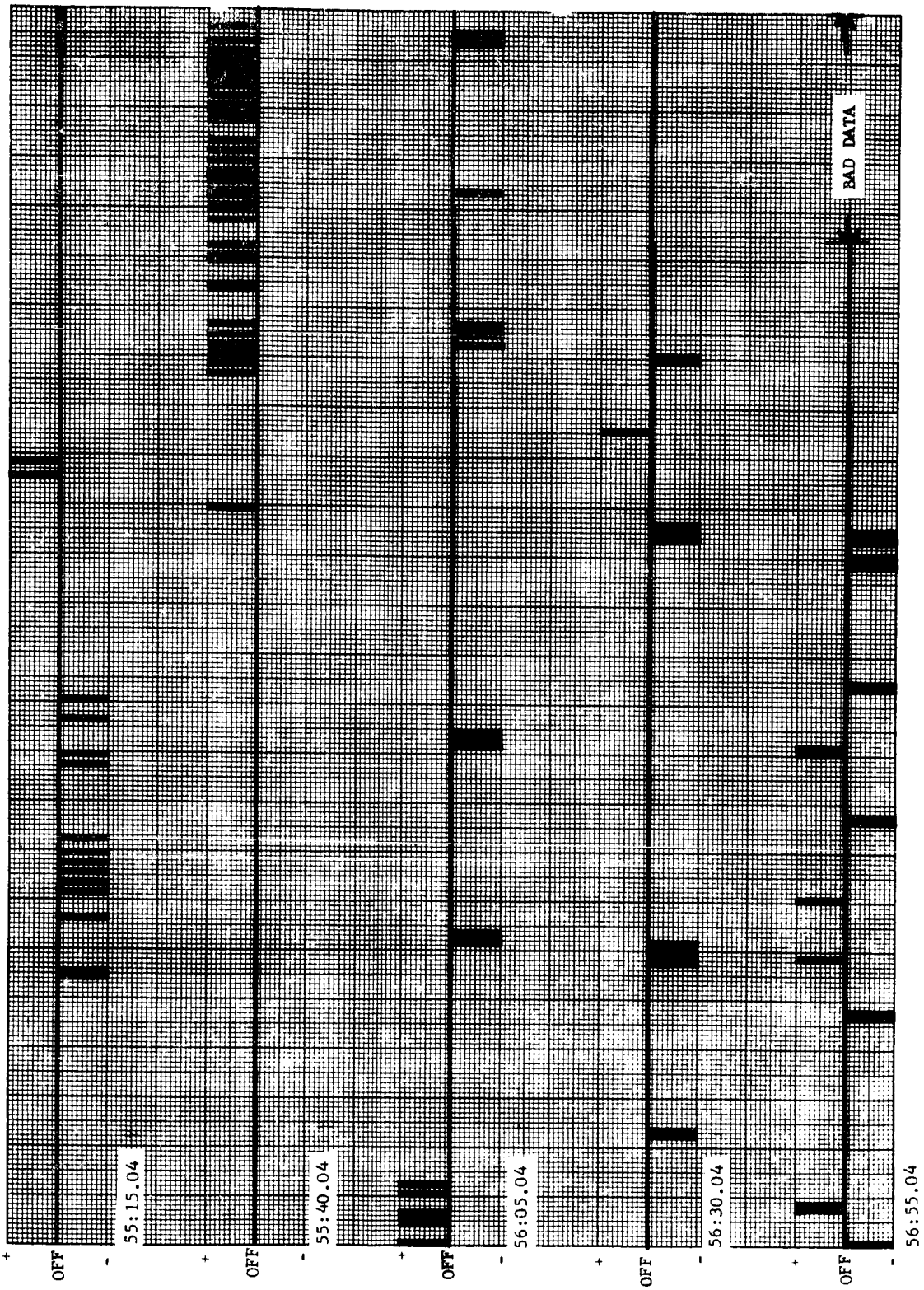

Figure 4-27 ENTRY YAW JETS ACTIVITY (CONCLUDED)

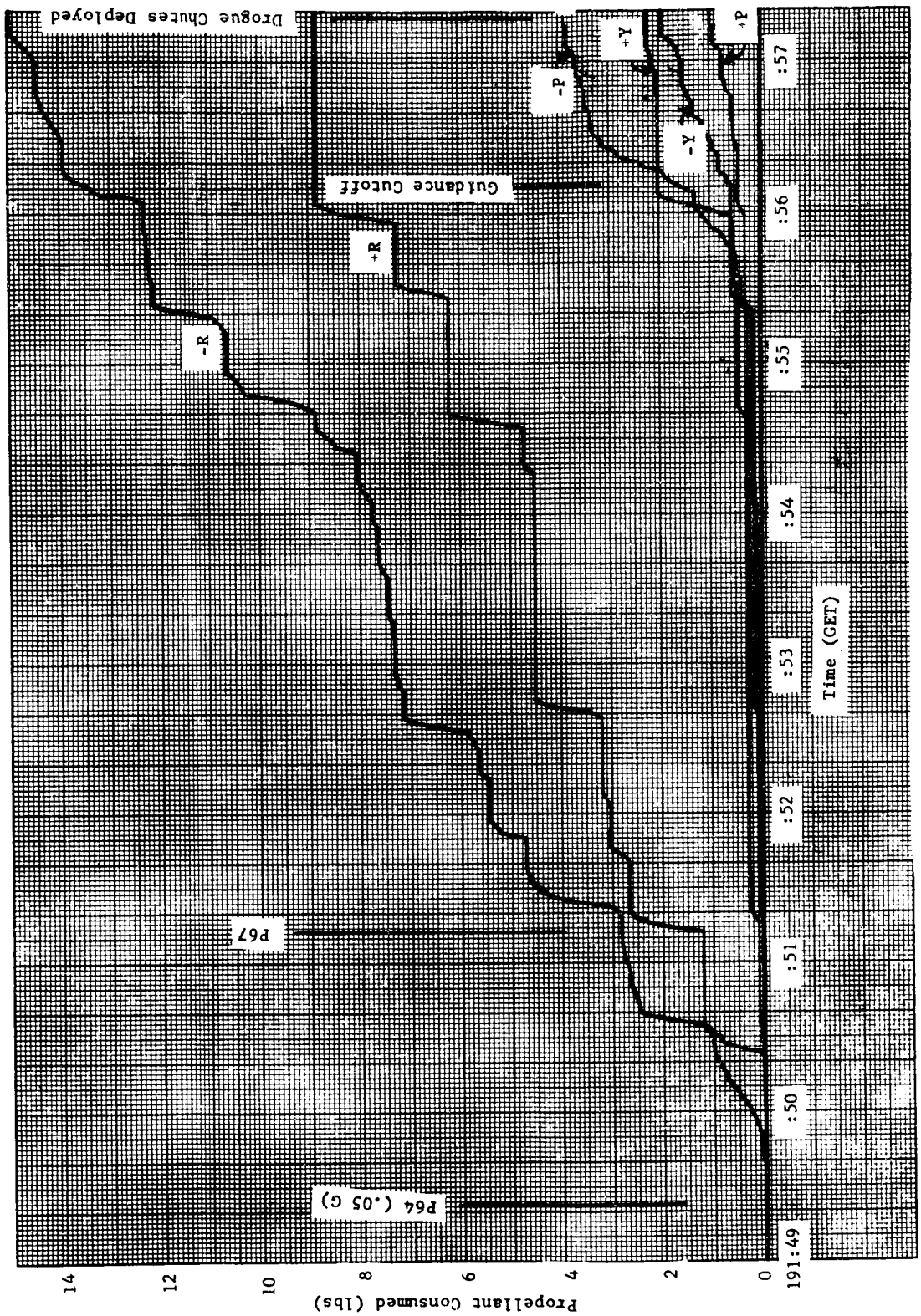

Figure 4-28 ENTRY FUEL CONSUMPTION PER AXES

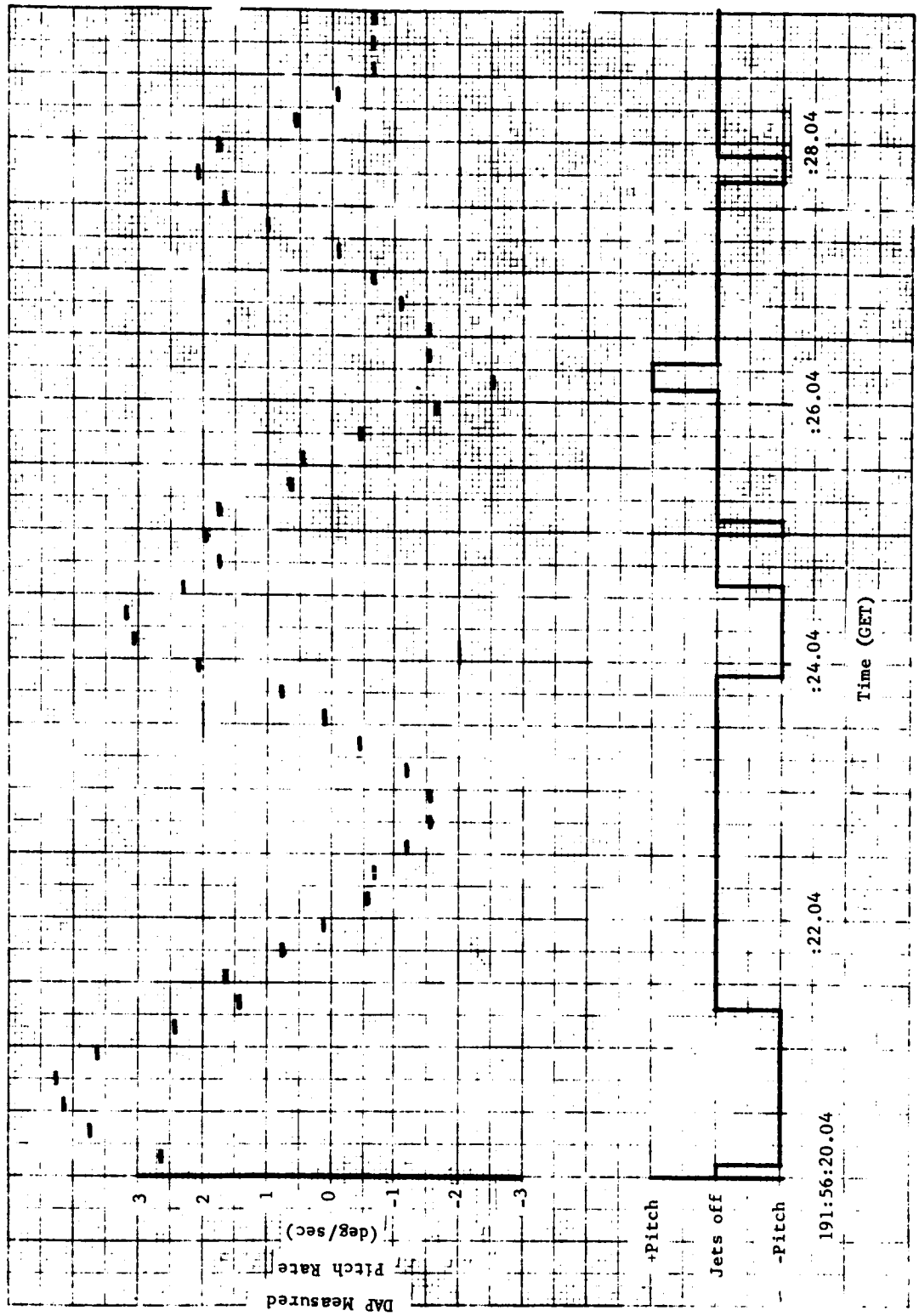

Figure 4-29 ENTRY PITCH RATE DAMPING

5.0 LM DIGITAL AUTOPILOT

The LM DAP controlled two distinct configurations during the mission: Descent and Ascent.

The LM DAP was not used for control purposes during periods when the configuration consisted of LM/CSM docked. Periods of attitude hold, automatic maneuvers, and PGNCS controlled burns were analyzed. Based on the data reviewed DAP performance was excellent.

5.1 DESCENT CONFIGURATION

There were two burns performed in the descent configuration under PGNCS control; Descent Orbit Insertion and Phasing. DOI was behind the moon and no TM data were available.

5.1.1 Attitude Hold for Heavy Descent Configuration

Figures 5-1 and 5-2 show phase plane plots for a period of attitude hold prior to the automatic maneuver to DOI attitude. The time range for the U and V-axes phase planes is 99:06:32 to 99:07:24 GET. This period of attitude hold is for the heaviest descent configuration. A phase plane plot was not included for the P axis since the attitude errors were less than 0.05 deg and the magnitude of the P-axis rate error was less than 0.006 deg/sec. A single +U jet firing occurred during the time period used for the U-axis phase plane shown in Figure 5-1. Minimum deadband (0.3 deg) was set. The V-axis phase plane shown in Figure 5-2 required two -V jet firings. The V-axis attitude error was approximately equal to 0.4 deg when the second -V firing occurred which is in accordance with the phase plane logic (Reference 4). The firing can not occur when the rate error is zero, allowing larger attitude errors to be attained. However, a jet firing will occur when the rate error becomes non-zero.

5.1.2 Automatic Maneuver to DOI Attitude

An automatic maneuver to DOI attitude started at 99:07:34.425 GET. The P, U, and V-axis rate responses are shown in Figures 5-3, 5-4, and 5-5. The maneuver rate was 2.0 deg/sec with commanded rates about all 3 axes. The estimated rates followed the desired rates well. The complete automatic maneuver is not shown because a data dropout occurred before the maneuver was completed. At the time of this data dropout the CDU's were approximately 6.5 deg, 16 deg, and 4.8 deg from the final desired CDU's for the X, Y, and Z axes. Actual and desired rates about the U and V-axes were approximately equal when the data dropout occurred.

5.1.3 DPS Phasing Burn

Jets 6 and 14 were used for a 2-jet ullage prior to the burn starting at 100:58:18.495. Jet 14 was toggled during the ullage to maintain attitude control. The maximum attitude errors during ullage were -0.55, +1.87 and +1.00 deg for the P, U, and V axes, respectively. Ullage ended at 100:58:26.675. Data showed the DPS on at 100:58:26.573 with a burn duration of 40 seconds. Throttle up from 11.9% to 92.5% occurred at 100:58:51.938. No difficulty with the ΔV monitor was encountered since the ΔV threshold limit of 36 cm/sec was exceeded at the time of the second sampling of the PIPA counts (approximately 4 seconds after ignition). The thrust remained well above the threshold limit throughout the burn.

A gimbal fail indication occurred at 100:58:38.425 approximately 12 seconds after ignition. This indication of a gimbal fail was removed at 100:59:06.425. The GDA's appear to have worked nominally in steering and tracking the cg. The alarm occurred during a period of time when the GDA's were reversing directions and is believed to have been caused by coasting. It was known prior to the flight that this alarm would probably occur.

During Apollo 10, the GDA drive rates exceeded the maximum specification value of 0.0662 in/sec $\pm$10% (Reference 3) as was observed on Apollo 9. This factor does not influence the controllability of

the DAP during the burn, but would lead to errors in positioning the engine bell prior to a burn.

Figures 5-6, 5-7, and 5-8 show phase plane plots for the DPS phasing burn with brief periods of attitude hold before and after the burn. Numerous jet firings occurred throughout the burn and the ullage period as required by the phase plane logic for attitude control. The peak angular rates about the U and V axes were -1.22 deg/sec and -0.78 deg/sec, respectively. The peak attitude errors for both axes were less than 1.75 deg. The burn deadband was one deg. The deadband for the attitude hold before and after the burn was 0.3 degree. The phase plane plots cover the period of both deadbands during the time range from 100:57:08.425 to 100:59:09.425 GET. In general, the maximum attitude errors and attitude errors at maximum thrust for this burn were comparable to the preflight simulation results. The estimated rates for the simulation results were also comparable to the actual rates during the burn. The actual burn used approximately 6.67 lbs of RCS fuel, whereas 7.73 lbs of RCS fuel were required in the preflight simulation test. This was nominal behavior since the actual burn started from an assumed trimmed-up position and the simulation run had an initial 3σ mistrim.

5.2 ASCENT CONFIGURATION

After staging the APS Insertion Burn was performed under PGNCS control followed by CSI, an AGS controlled CDH, PGNCS controlled TPI, CSM active docking, LM jettison, and CSM active separation. The final burn was the APS Burn-to-Depletion

5.2.1 APS Insertion Burn

Ullage for the APS Insertion burn was initiated at 102:54:58.685 and terminated at 102:55:02.795. Jets 2, 6, 10 and 14 were used for the 4-jet ullage with jets 6 and 10 toggling to maintain attitude control. The maximum attitude errors during ullage were -0.48, -1.16 and +1.08 deg for P, U, and V axes, respectively. The DAP DATA LOAD ROUTINE (R03)

was executed after entering P42. This resulted in the deadband for the burn being changed to 0.3 deg rather than the usual one degree deadband. The R03 execution also commanded a 4-jet ullage rather than a 2-jet ullage due to the data previously loaded into R03. Ignition was at 102:55:01.40 (TEVENT Data) with cutoff at 102:55:16.95 GET. Burn performance was nominal for the minimum deadband. The LGC estimate of LM mass decreased 176.4 lbs during the burn. No difficulty with the ΔV monitor was encountered since the ΔV threshold of 308 cm/sec was exceeded at the time of the second sampling of the PIPA counts (approximately 4 seconds after ignition). The thrust remained well above the threshold limit throughout the burn.

Figures 5-9, 5-10 and 5-11 show the P, U, and V axes attitude errors versus time for the APS Insertion burn. The maximum attitude errors near the start of the burn. were -0.48, 1.18, and -2.30 deg for the P, U, and V axes, respectively. The jet firing logic was effective in rapidly reducing the errors to maintain the 0.3 deg deadband. A plot of P, U, and V axes rate errors versus time is shown in Figures 5-12, 5-13 and 5-14. The maximum rate errors during the APS Insertion burn were -1.17, +2.51, and -2.16 deg/sec for the P, U, and V axes, respectively. Some P-axis jet firings were required to maintain attitude control. The majority of the jet firings were -U and +V. The cg offset apparently caused predominantly positive U-axis errors and negative V-axis errors. Some +U and -V jet firings were also required. In general, the maximum attitude errors were less than the errors observed in preflight simulation. More RCS activity was required than predicted by preflight tests. The preflight simulation results required 6.19 lbs of RCS fuel and the actual flight required 10.47 lbs of RCS fuel. These results were expected since the preflight tests used one deg deadband for the burn, whereas the APS Insertion burn during Apollo 10 used a 0.3 deg deadband and a 4-jet rather than a 2-jet ullage.

5.2.2 Attitude Hold for Heavy Ascent Configuration

P, U, and V axes phase plane plots are shown in Figures 5-15, 5-16, and 5-17 for a period of attitude hold prior to the APS Insertion burn. The time range used was 102:53:18.425 to 102:54:29.425 GET. The phase plane logic maintained a good limit cycle for this heavy ascent configuration with a 0.3 deg deadband desired.

5.2.3 Automatic Maneuvers to CSI Burn Attitude

An automatic maneuver to CSI attitude was initiated at 103:01:13.425 GET. The maneuver rate was 2 deg/sec with commanded rates about all 3 axes. Figures 5-18, 5-19, and 5-20 show the rate response for the P, U, and V axes during the automatic maneuver. Figure 5-21 shows the change in the actual CDU angles during the automatic maneuver. Only eight readable data points were available and no attempt was made to evaluate the maneuver.

5.2.4 Automatic Manevuer to TPI Burn Attitude

An automatic maneuver to TPI attitude was initiated at 105:18:02.425 GET. The maneuver rate was 2.0 deg/sec with rates commanded about the U and V axes. Figures 5-22 and 5-23 show the U and V axes rate responses during the automatic maneuver. Figure 5-24 shows the change in the CDU angles during the automatic maneuver.

5.2.5 Terminal Phase Initiation (TPI)

TPI was a 4-jet RCS burn beginning at 105:22:55.575. Jets 2, 6, 10, and 14 were used during the burn with jets 6 and 10 toggling to maintain attitude control. The maximum attitude errors during the burn were +0.68, -1.27, and +1.33 deg for the P, U, and V axes. The maximum rate errors during the burn were -0.38, +0.59, and -1.10 deg/sec for the P, U, and V axes, respectively. Figures 5-25, 5-26 and 5-27 present phase plane plots for the P, U, and V axes during the burn. Numerous +U and -V jet firings were required during the burn to maintain attitude control. These firings were achieved when jets 10 and 6 were turned off with jets 2 and 14 remaining on. Some P jet couples were also

required by the phase plane logic. Due to the position of the cg, the U and V attitude error remained near the deadband limit for the duration of the burn. The cg position of the cg, the U and V attitude error remained near the deadband limit for the duration of the burn. The cg position had a tendency to produce -U and +V attitude errors during this RCS burn.

5.2.6 Attitude Hold for Lightest Ascent

Figure 5-28a shows a P axis phase plane plot for a period of attitude hold after the APS burn to depletion. The time period covered is 116:15:53.445 to 116:16:54.445 GET. The deadband was initially 0.3 deg and then it was changed to 5 deg. The change in deadband was very smooth. Figure 5-28b shows the P axis phase plane with 5 deg deadband from 116:16:54.445 to 116:21:41.445 GET. Figure 5-29a shows the U axis phase plane (116:15:53.445 to 116:16:49.445) with narrow deadband and the U-axis phase plane with wide deadband is shown in Figure 5-29b (116:16:49.445 to 116:21:39.445). Figure 5-30a shows the V-axis phase plane (116:15:53.445 to 116:16:54.445) with narrow deadband. The V-axis phase plane (116:16:54.445 to 116:21:35.445) with wide deadband is shown in Figure 5-30b. The phase plane logic maintained a good deadband for this light ascent configuration.

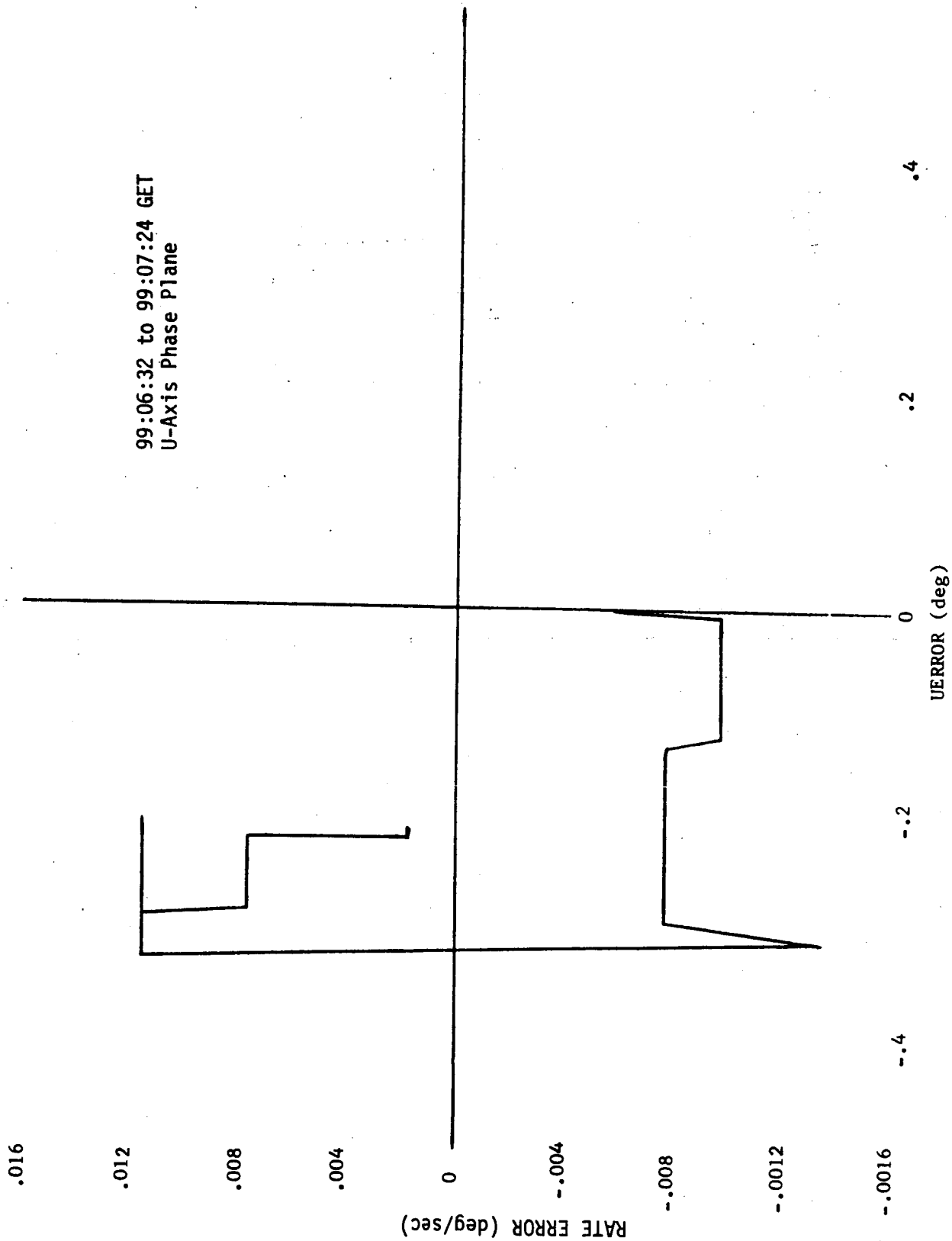

Figure 5-1 ATTITUDE HOLD PRIOR TO AUTOMATIC MANEUVER TO DOI ATTITUDE

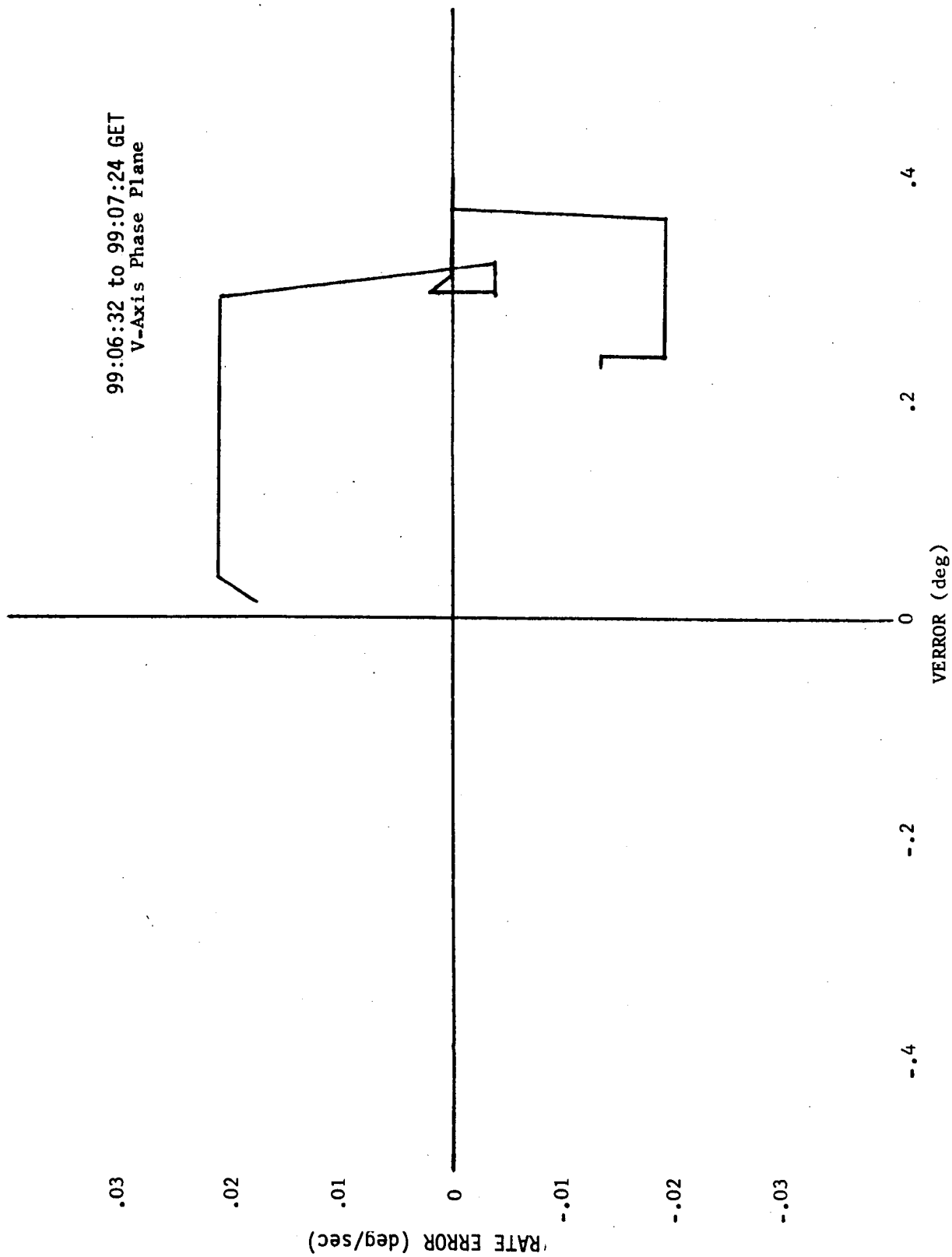

Figure 5-2 ATTITUDE HOLD PRIOR TO AUTOMATIC MANEUVER TO DOI ATTITUDE

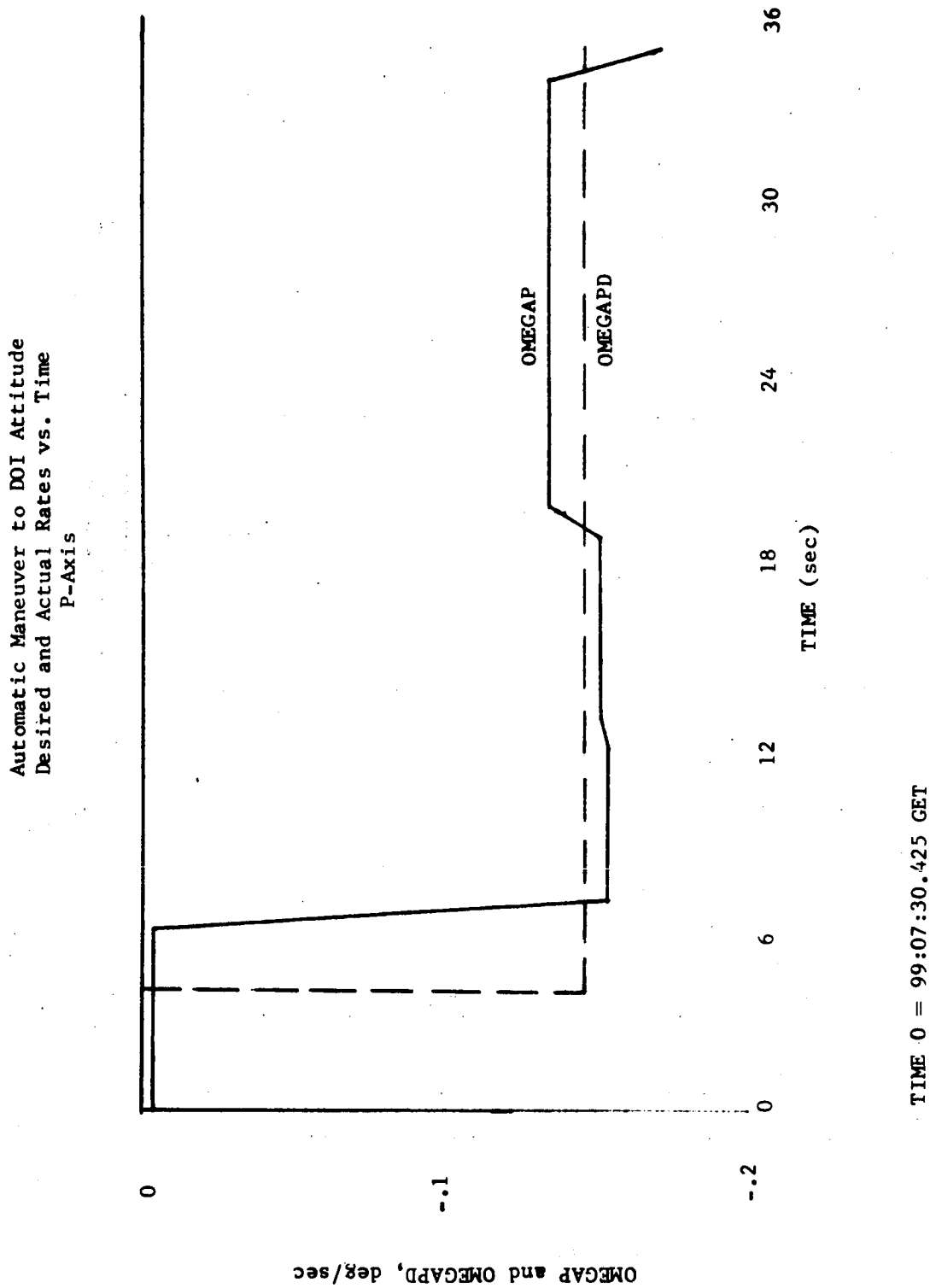

Figure 5-3 AUTOMATIC MANEUVER TO DOI ATTITUDE

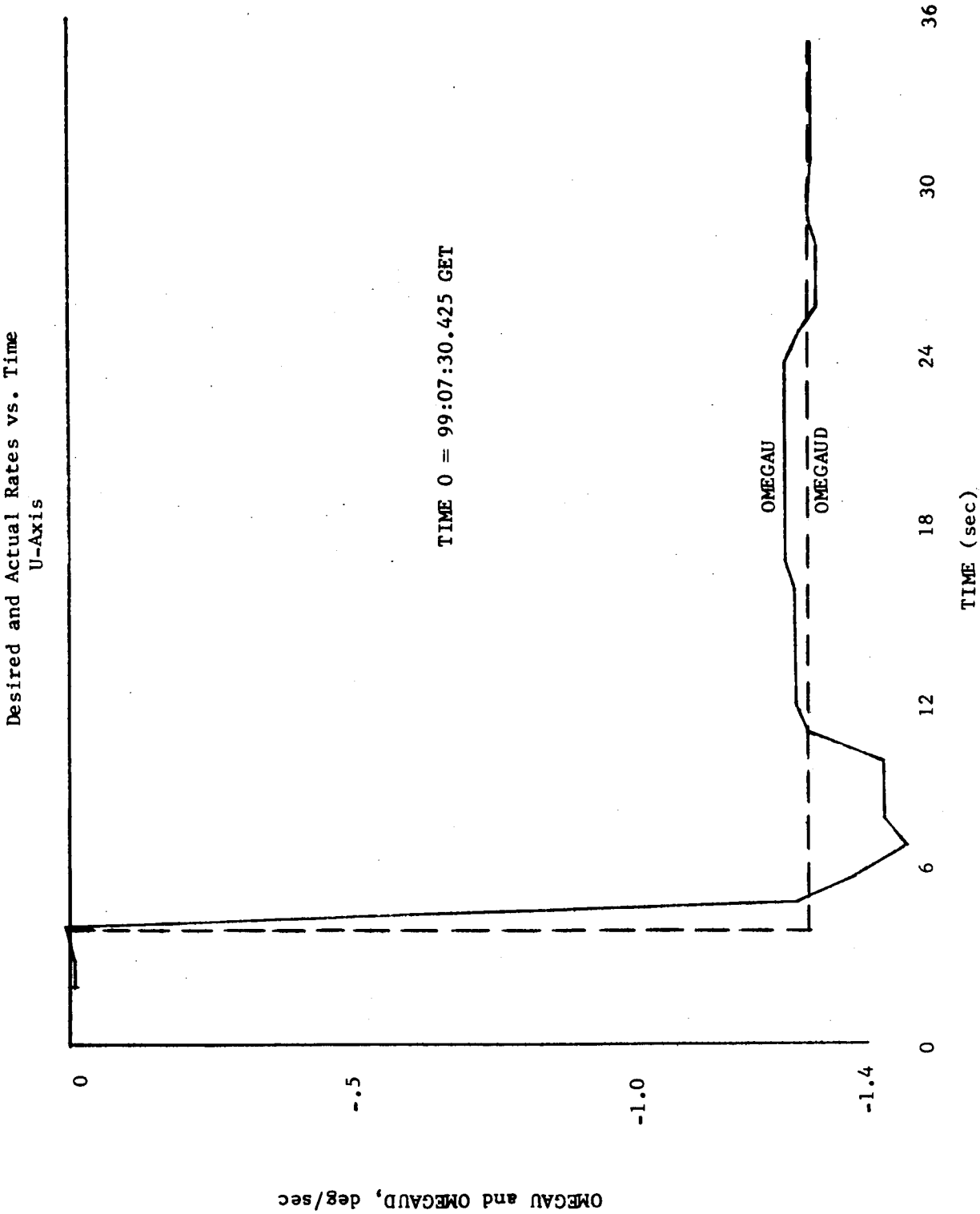

Figure 5-4 AUTOMATIC MANEUVER TO DOI ATTITUDE

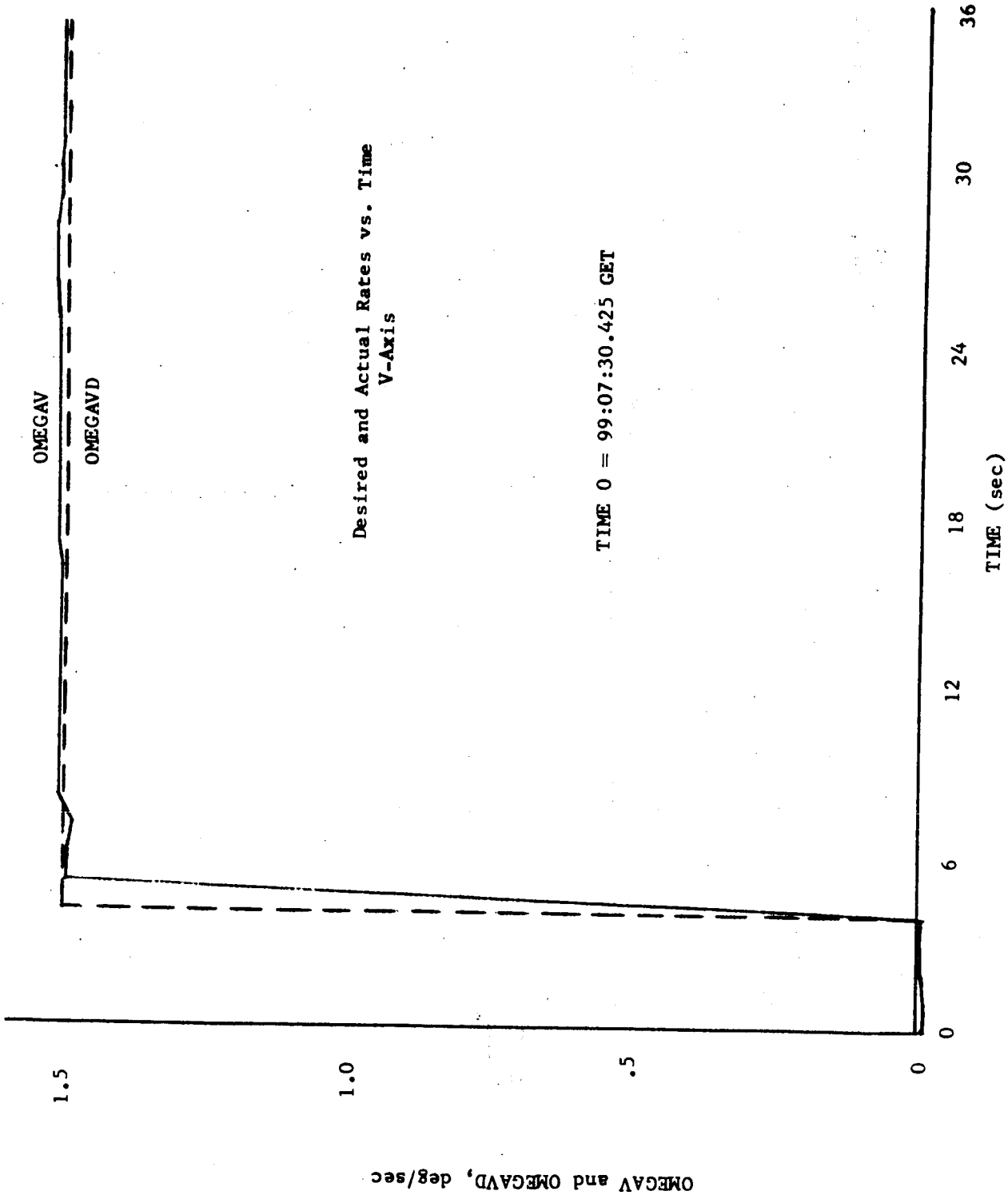

Figure 5-5 AUTOMATIC MANEUVER TO DOI ATTITUDE

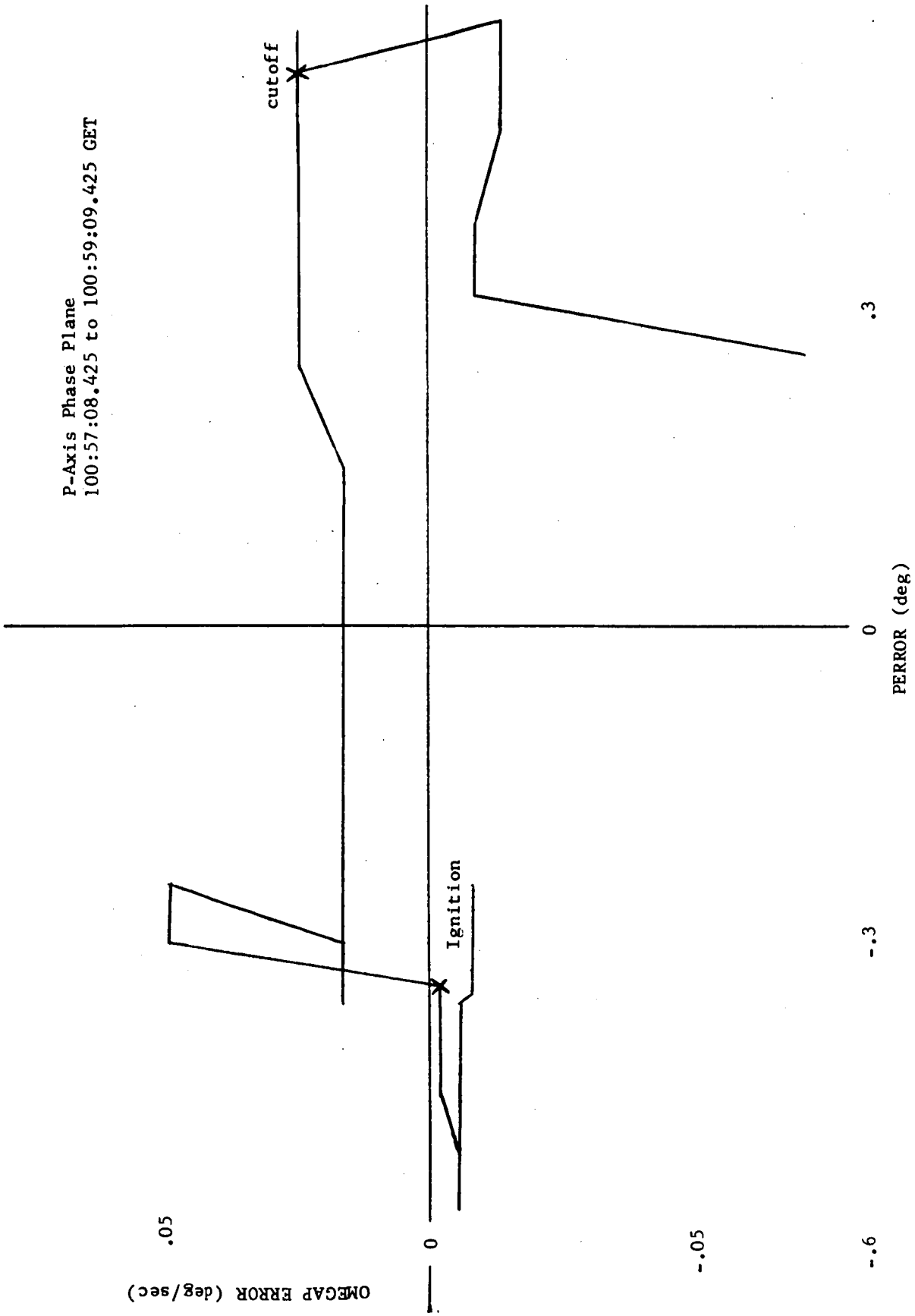

Figure 5-6 DPS PHASING BURN AND ATTITUDE HOLD

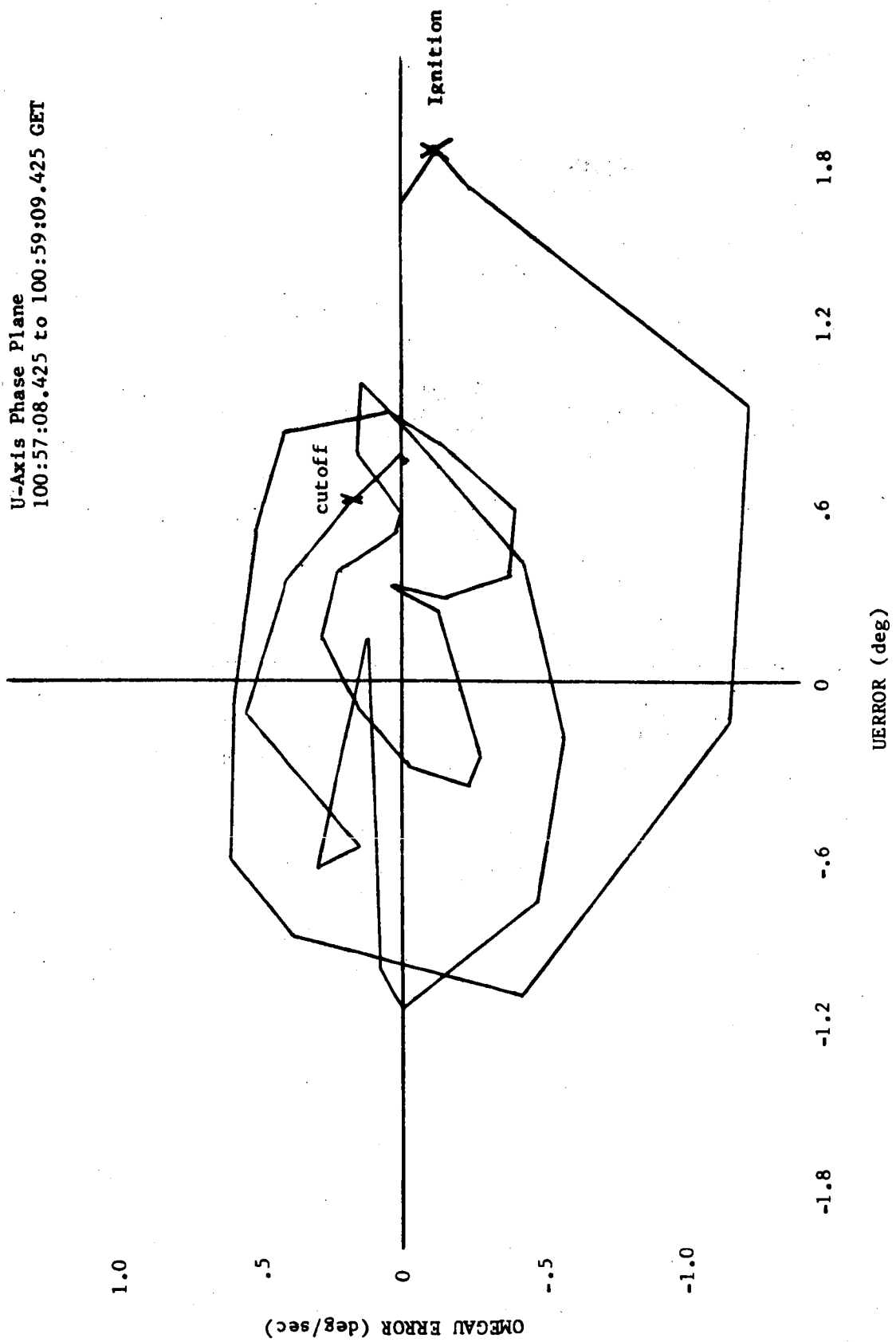

Figure 5-7 DPS PHASING BURN AND ATTITUDE HOLD

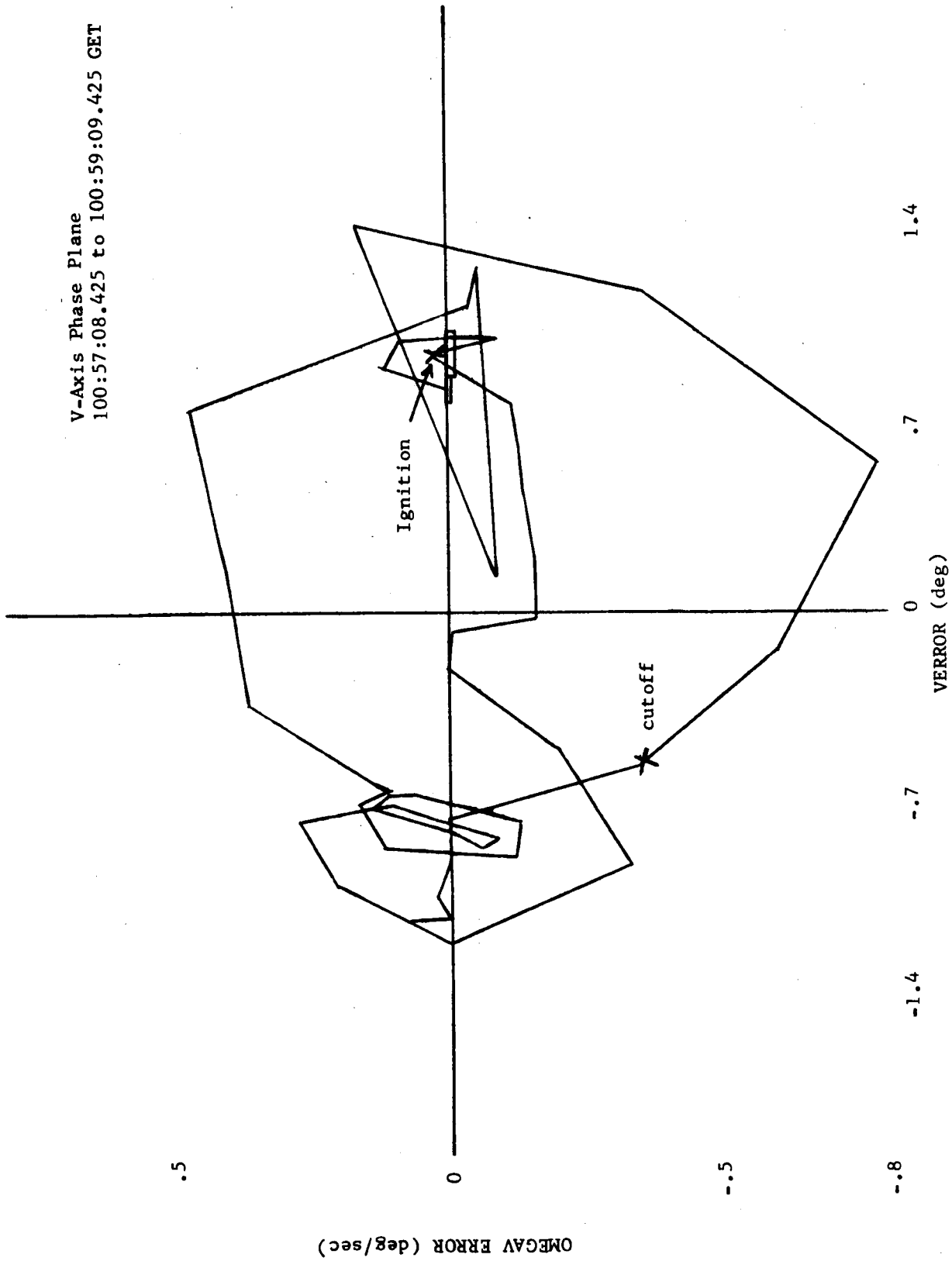

Figure 5-8 DPS PHASING BURN AND ATTITUDE HOLD

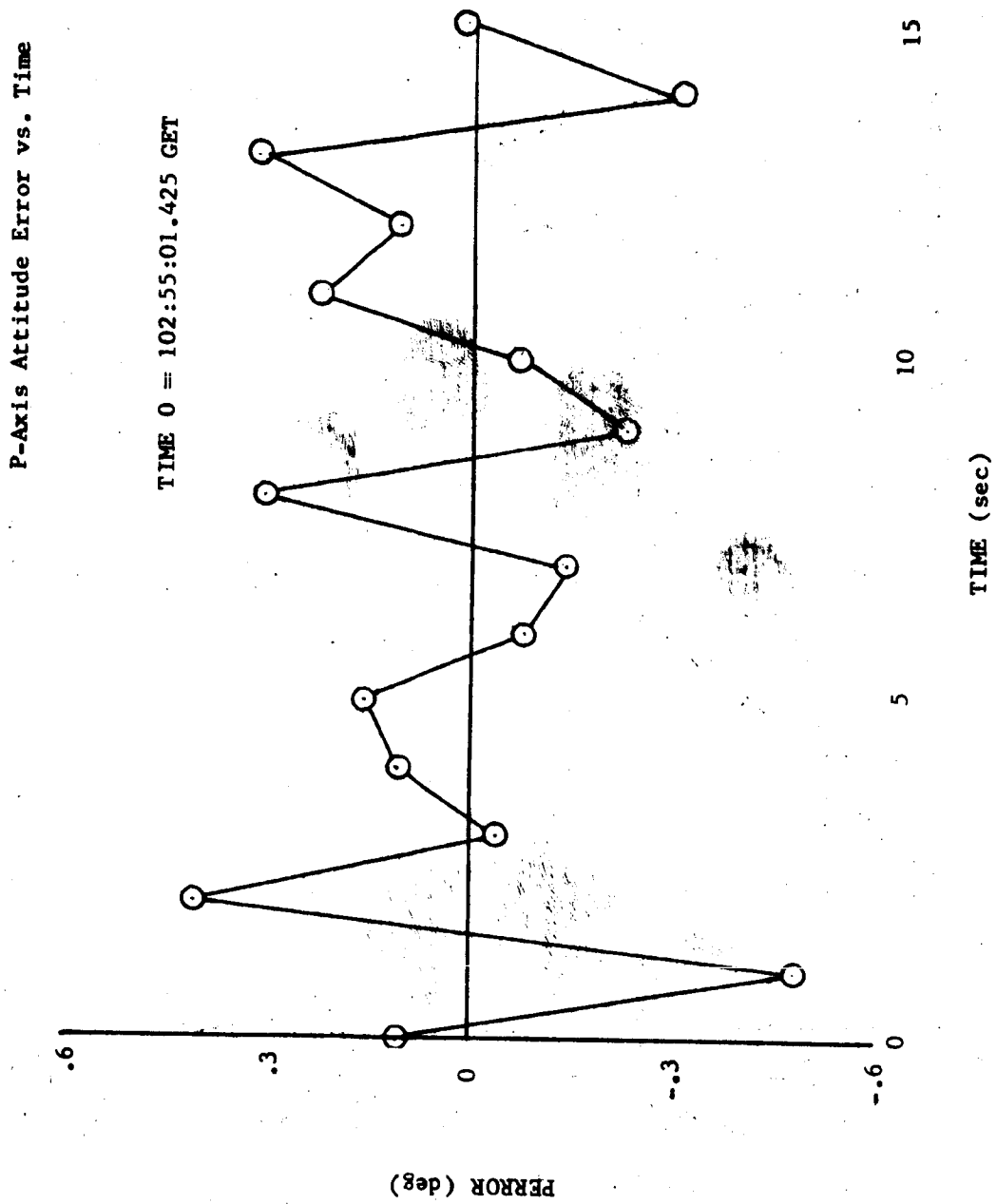

Figure 5-9 APS INSERTION BURN

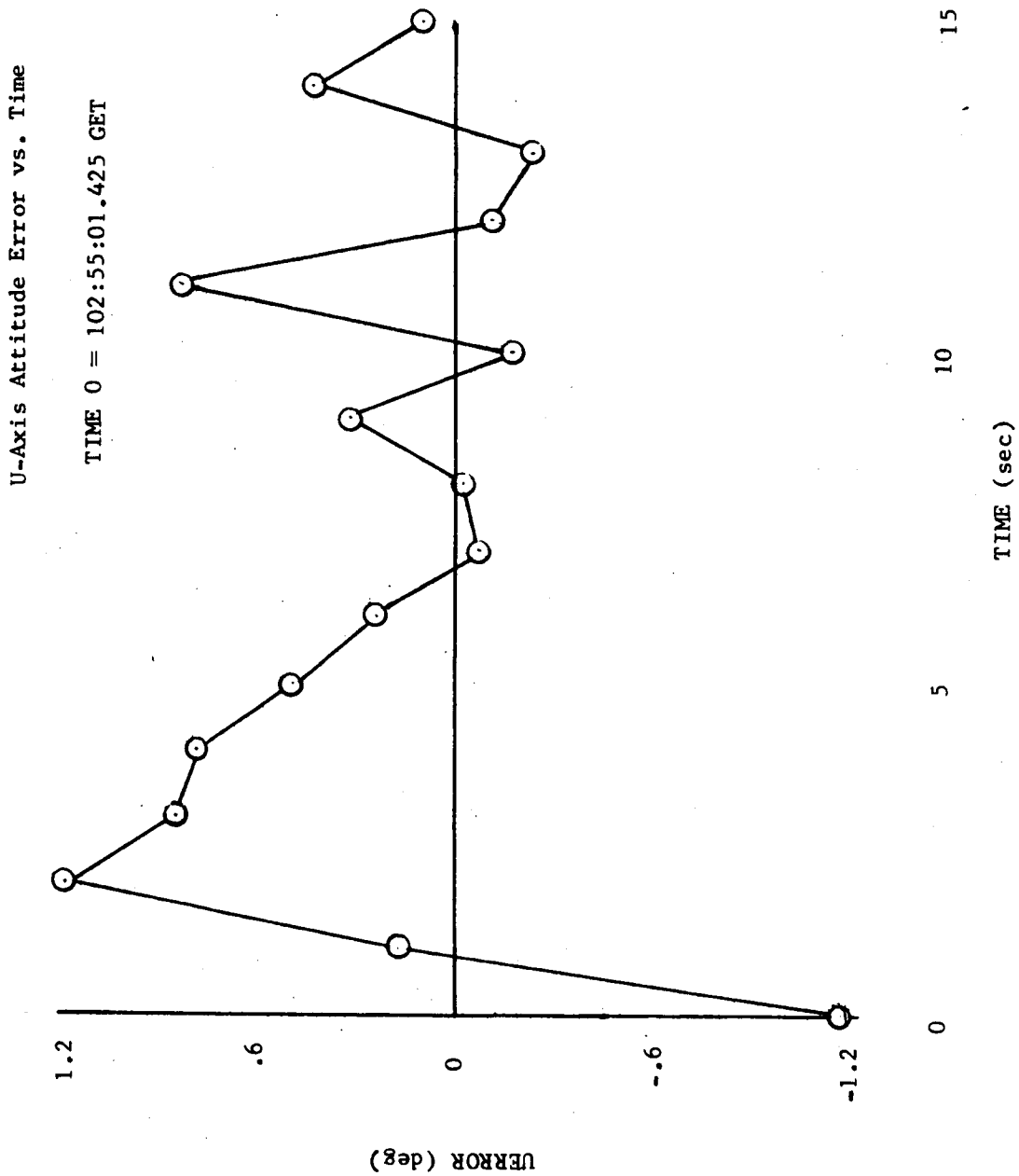

Figure 5-10 APS INSERTION BURN

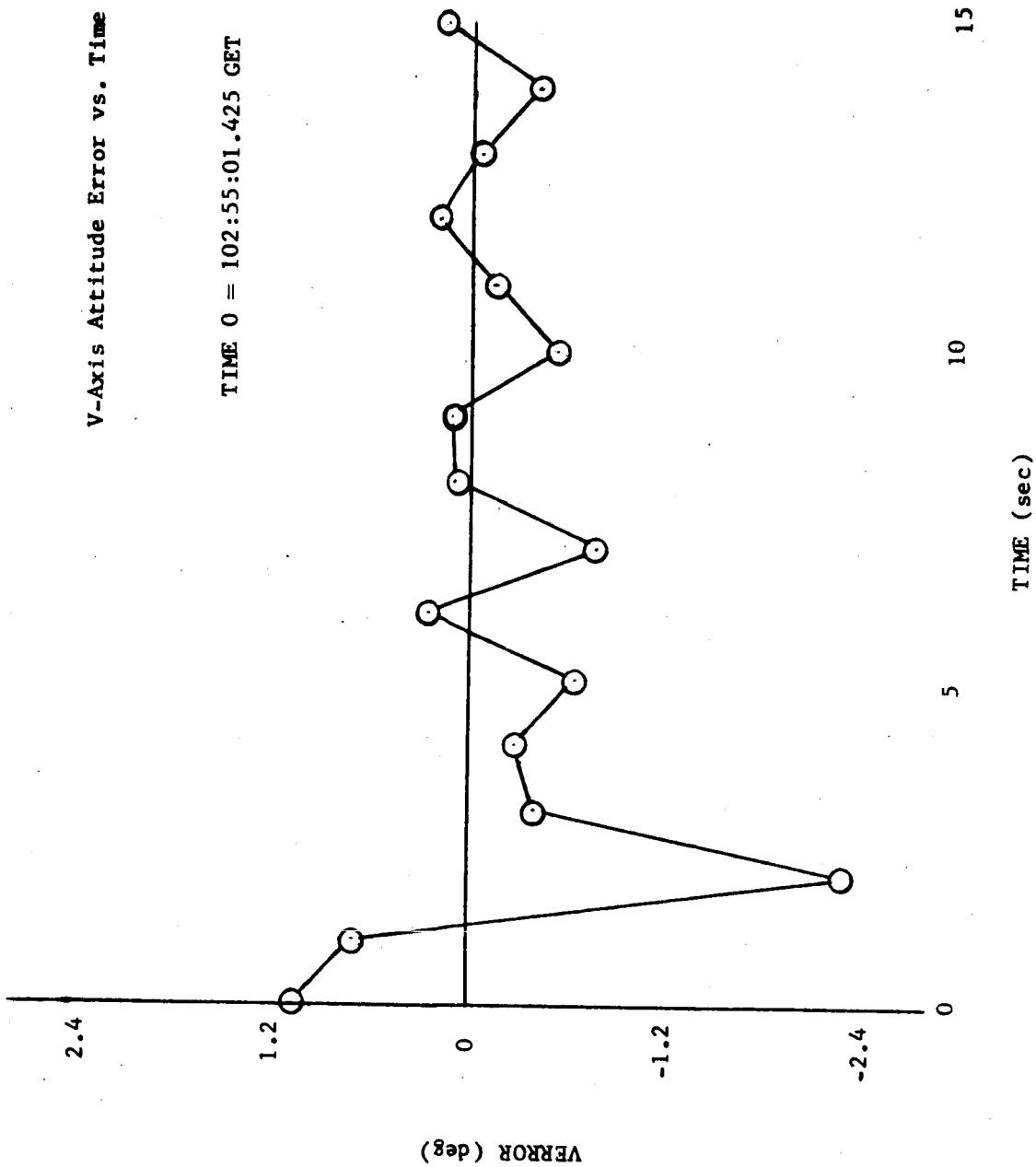

Figure 5-11 APS INSERTION BURN

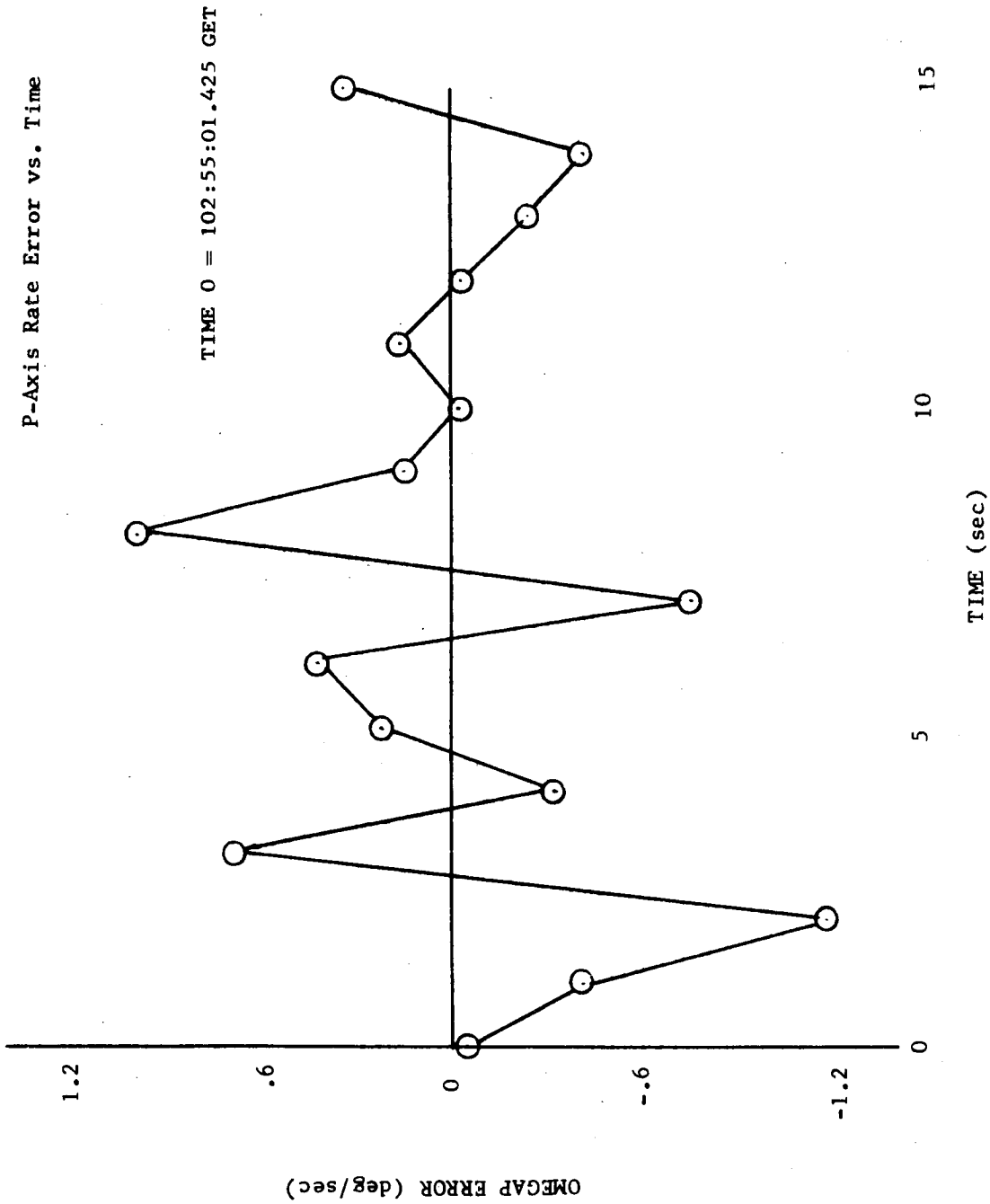

Figure 5-12 APS INSERTION BURN

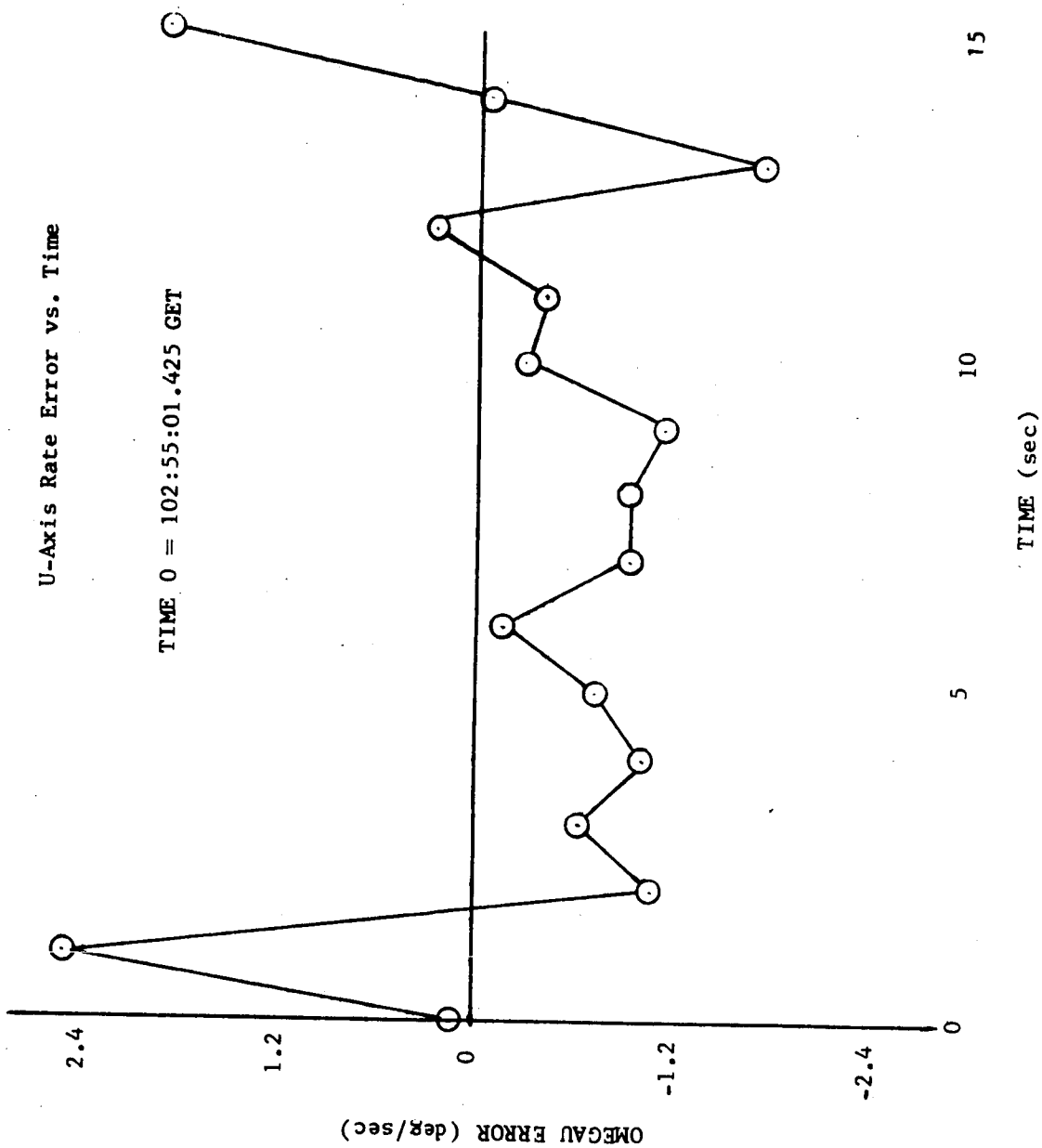

Figure 5-13 APS INSERTION BURN

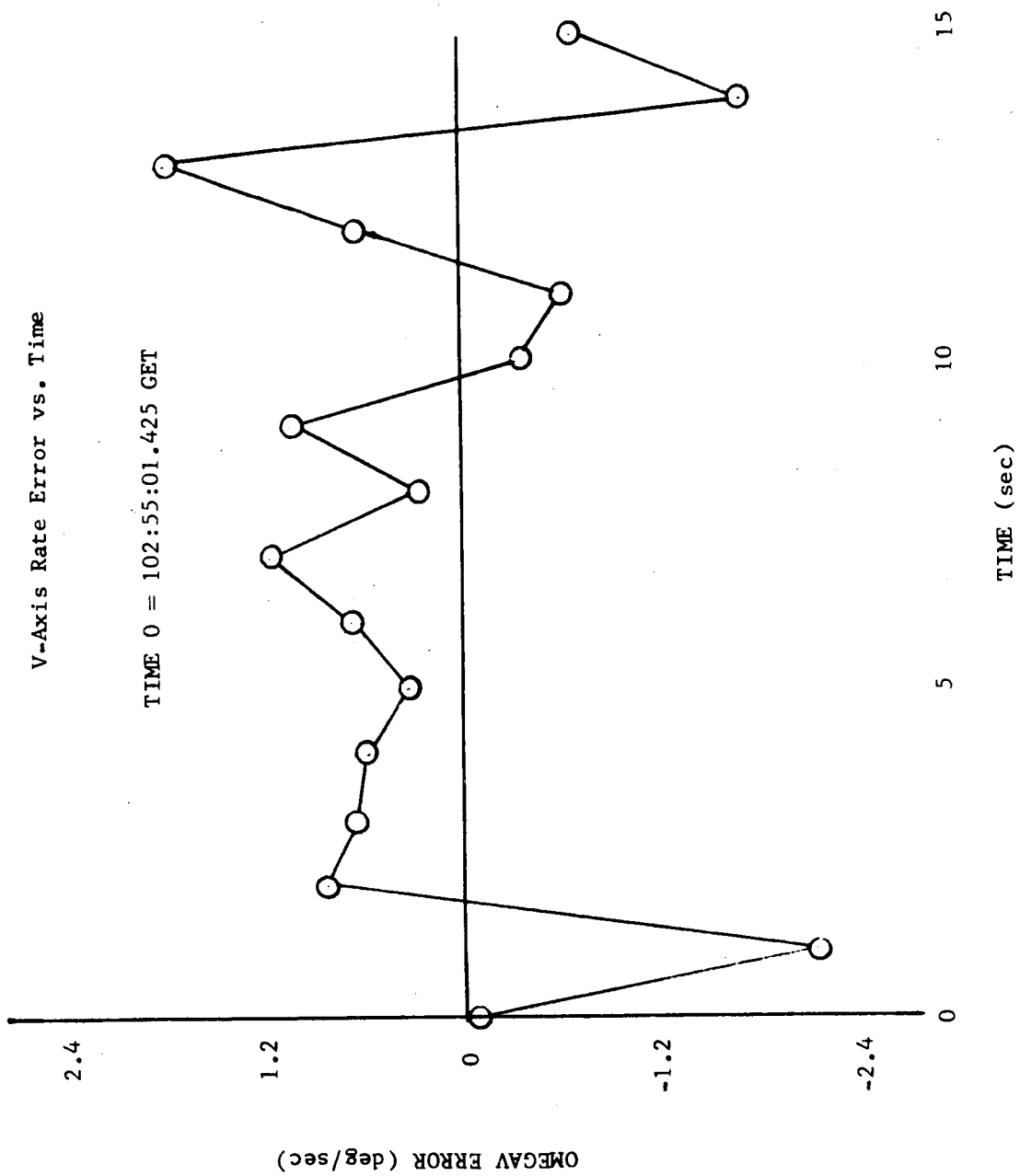

Figure 5-14 APS INSERTION BURN

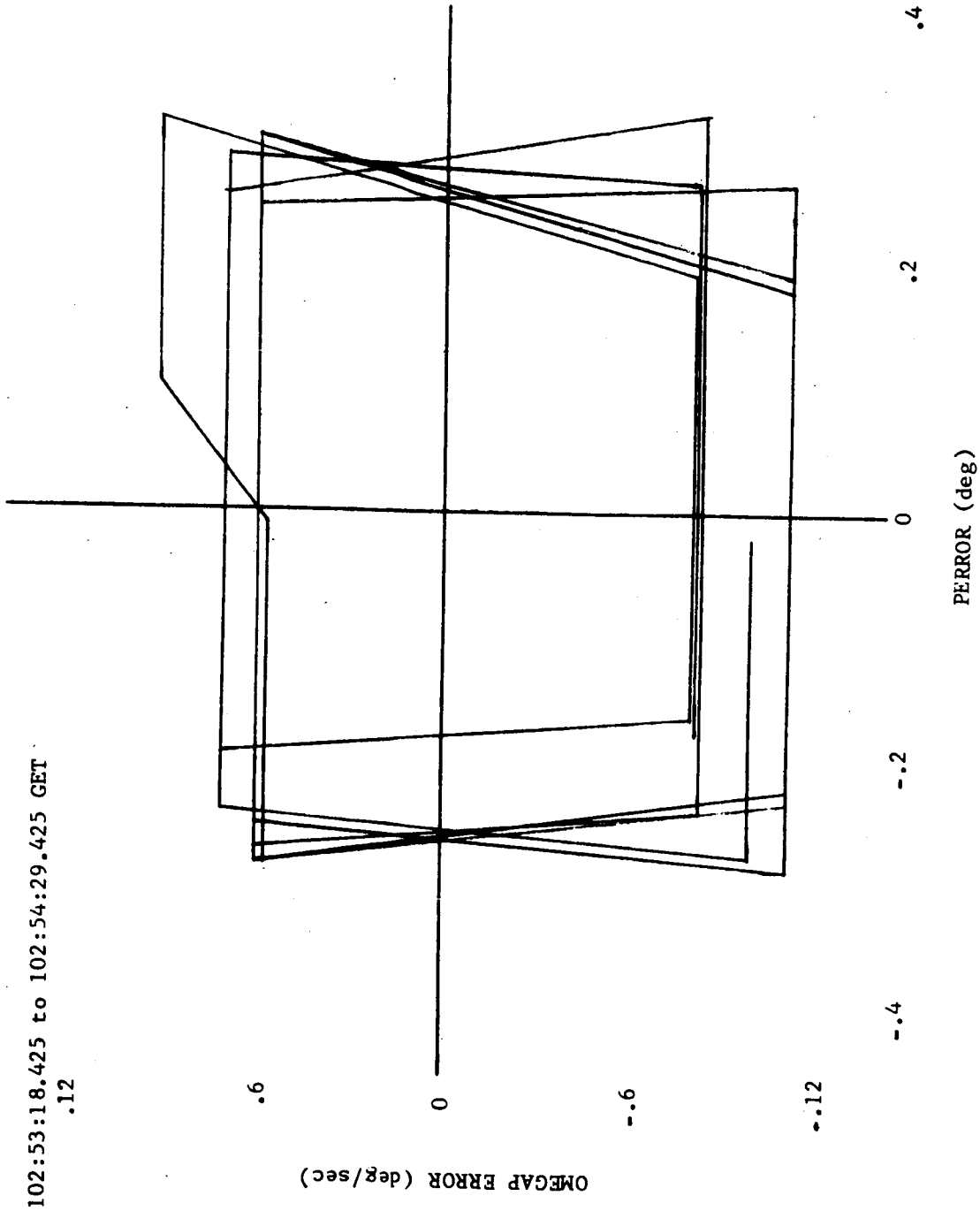

Figure 5-15 P-AXIS PHASE PLANE ATTITUDE HOLD PRIOR TO APS INSERTION BURN

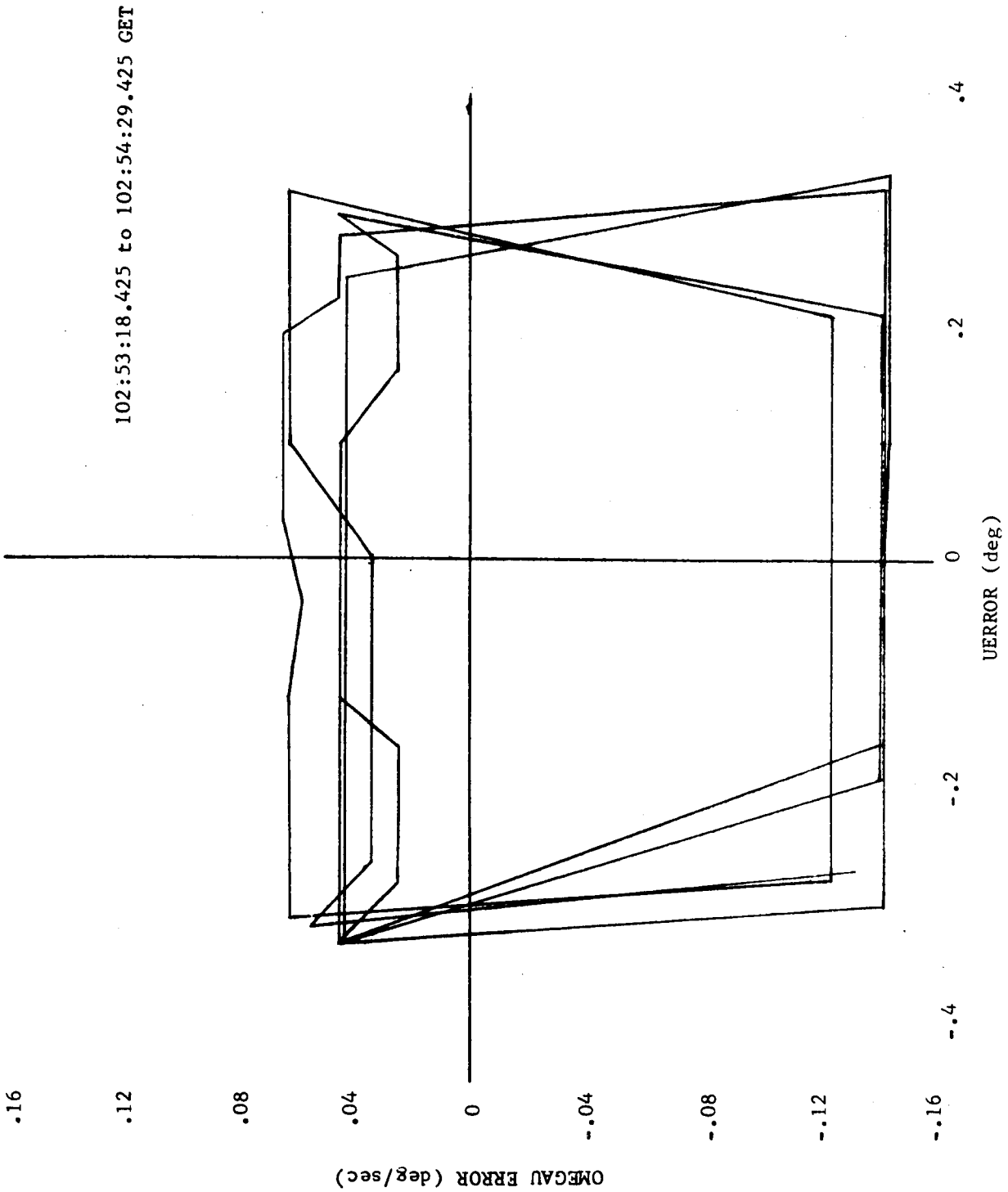

Figure 5-16 U-AXIS PHASE PLANE ATTITUDE HOLD PRIOR TO APS INSERTION BURN

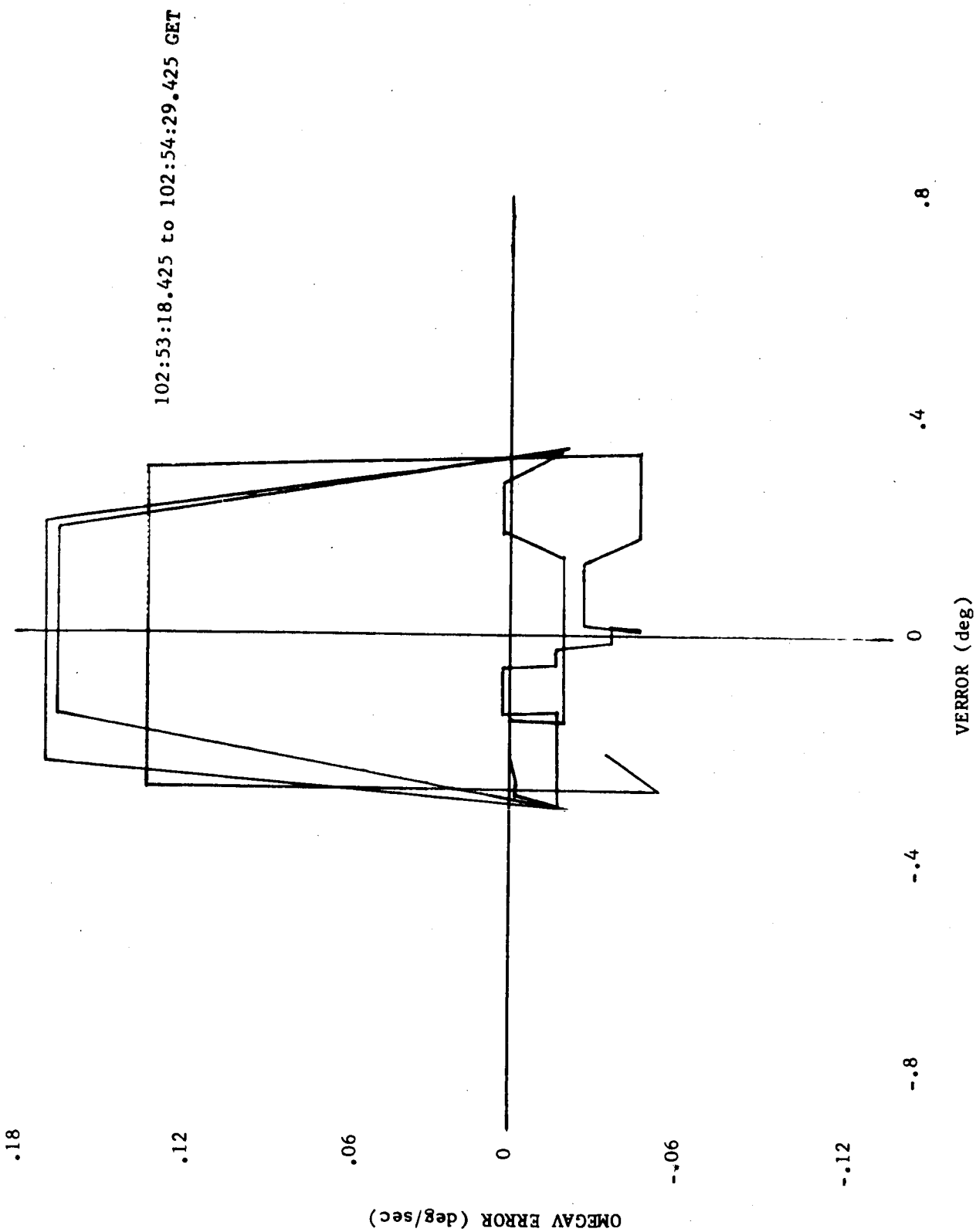

Figure 5-17 V-AXIS PHASE PLANE ATTITUDE HOLD PRIOR TO APS INSERTION BURN

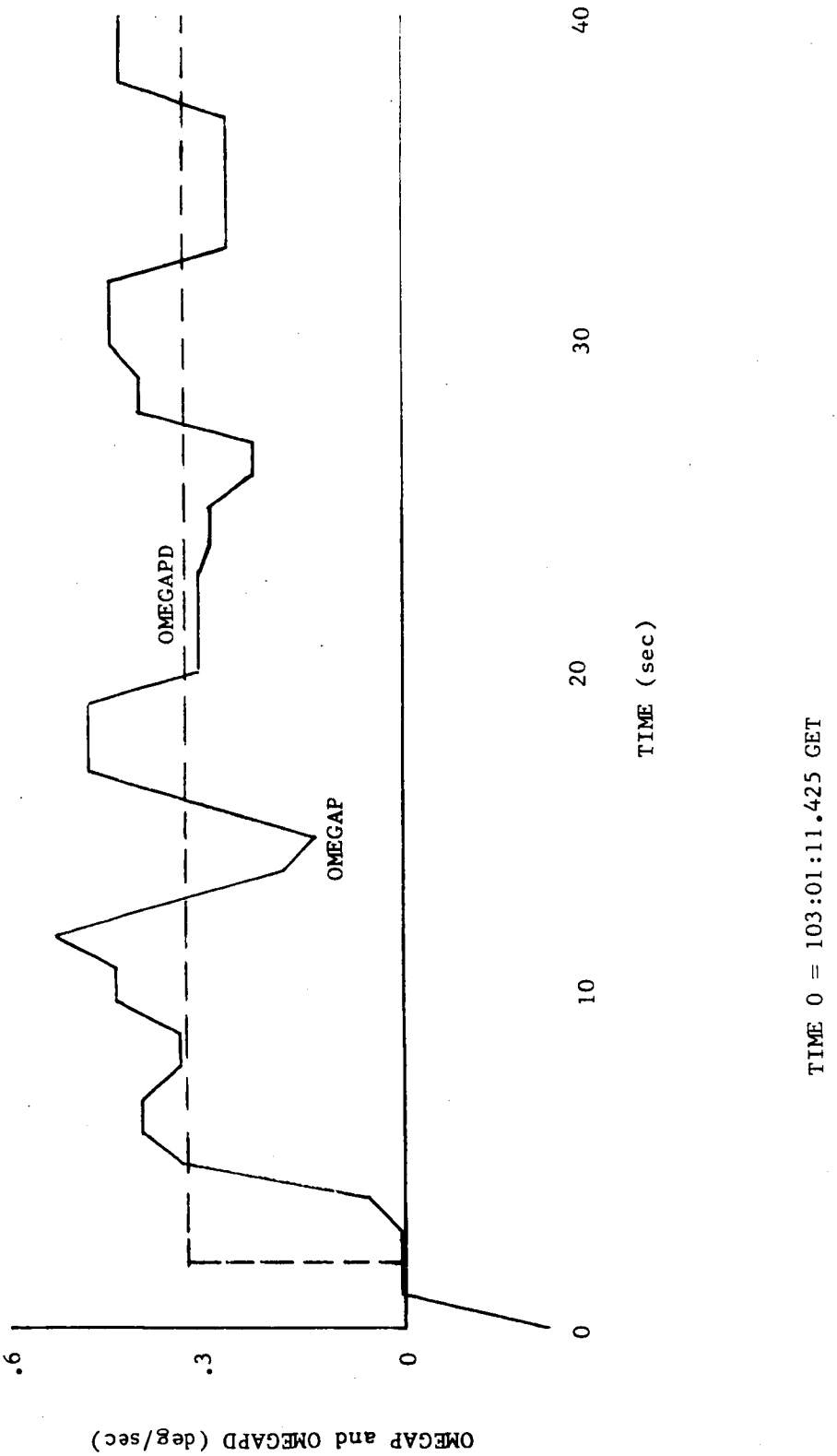

Figure 5-18 AUTOMATIC MANEUVER TO CSI ATTITUDE
DESIRED AND ACTUAL RATES VS TIME P-AXIS

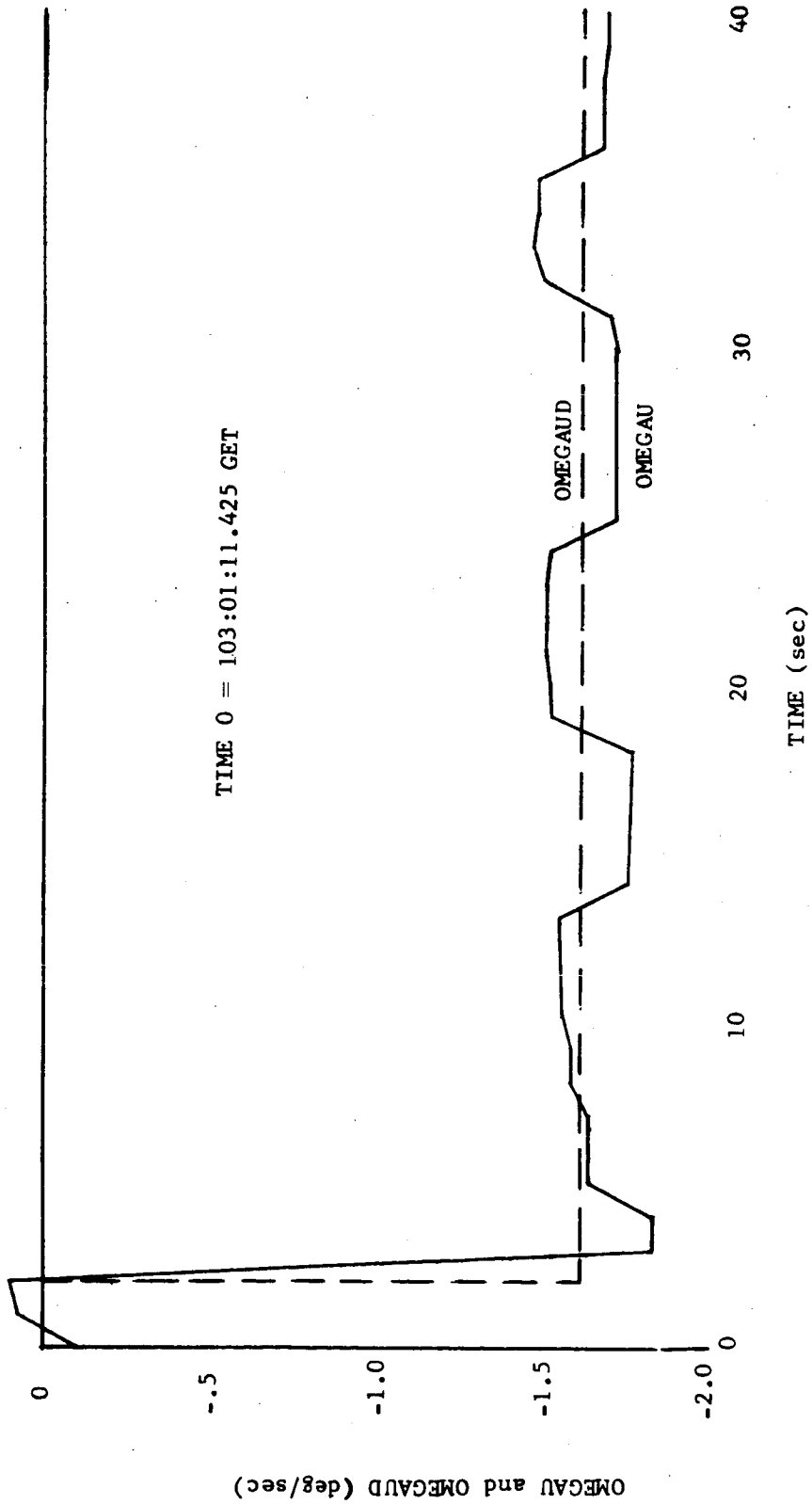

Figure 5-19 AUTOMATIC MANEUVER TO CSI ATTITUDE DESIRED AND ACTUAL RATES VS TIME U-AXIS

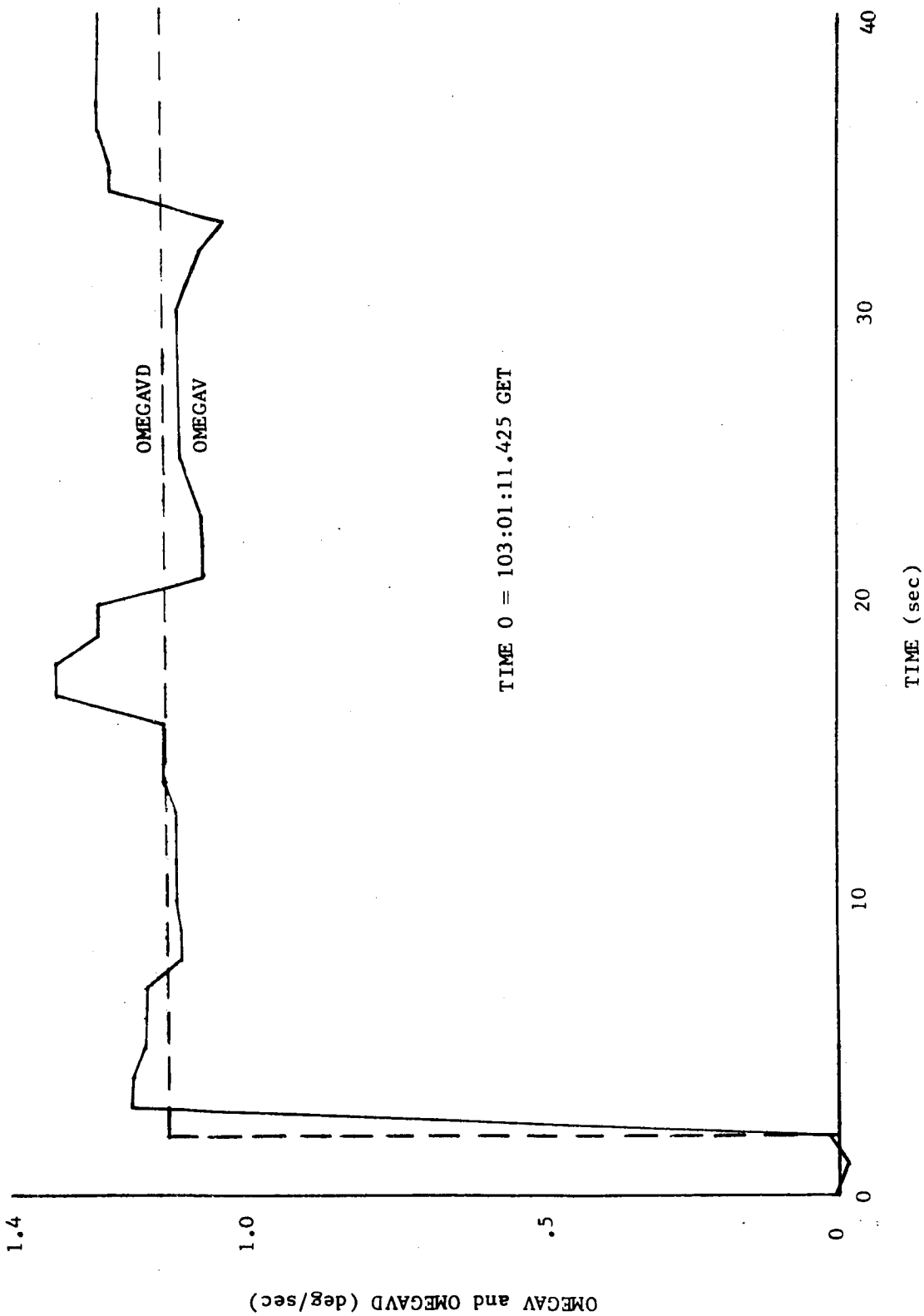

Figure 5-20 AUTOMATIC MANEUVER TO CSI ATTITUDE
DESIRED AND ACTUAL RATES VS TIME V-AXIS

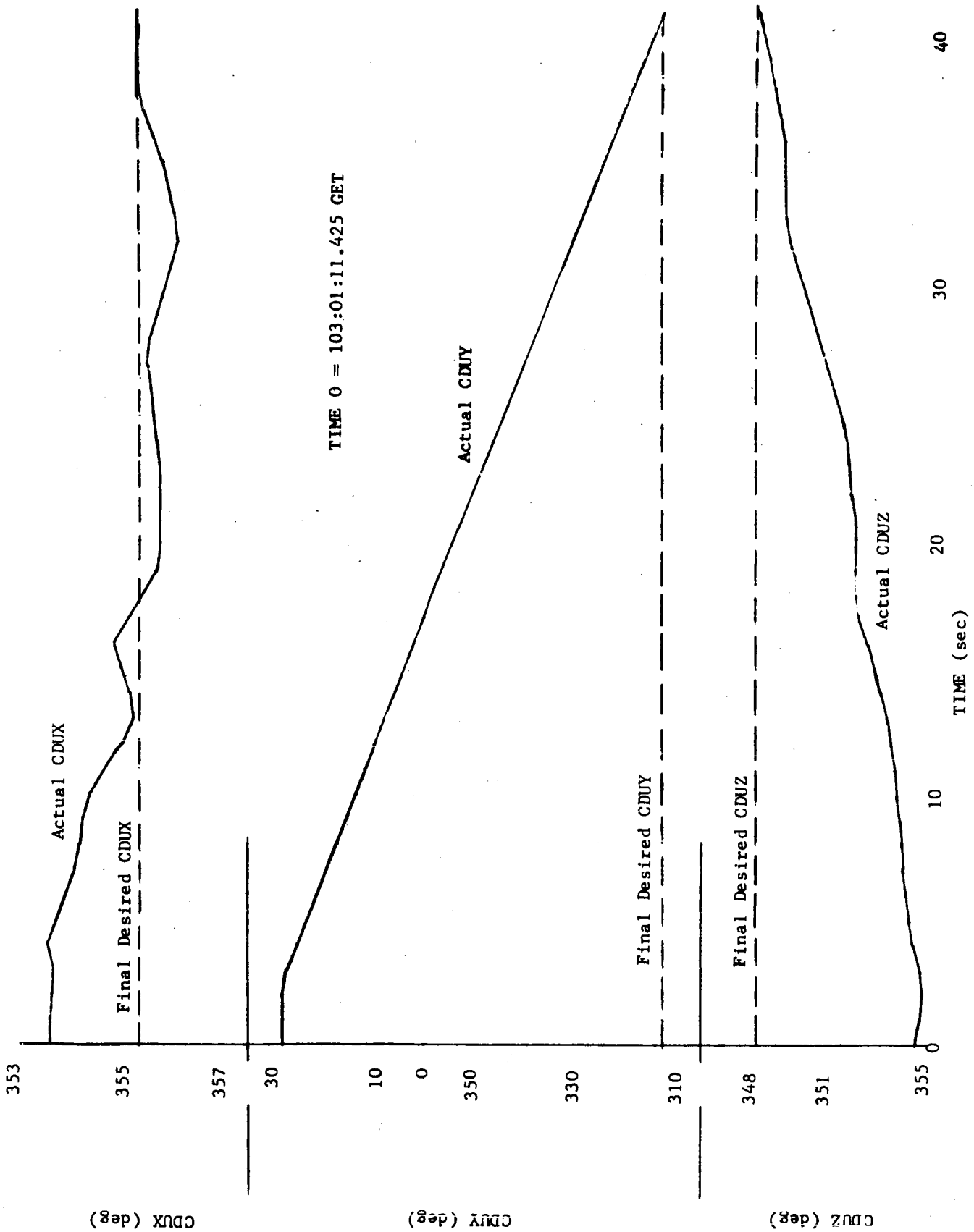

Figure 5-21 AUTOMATIC MANEUVER TO CSI ATTITUDE CDU ANGLES

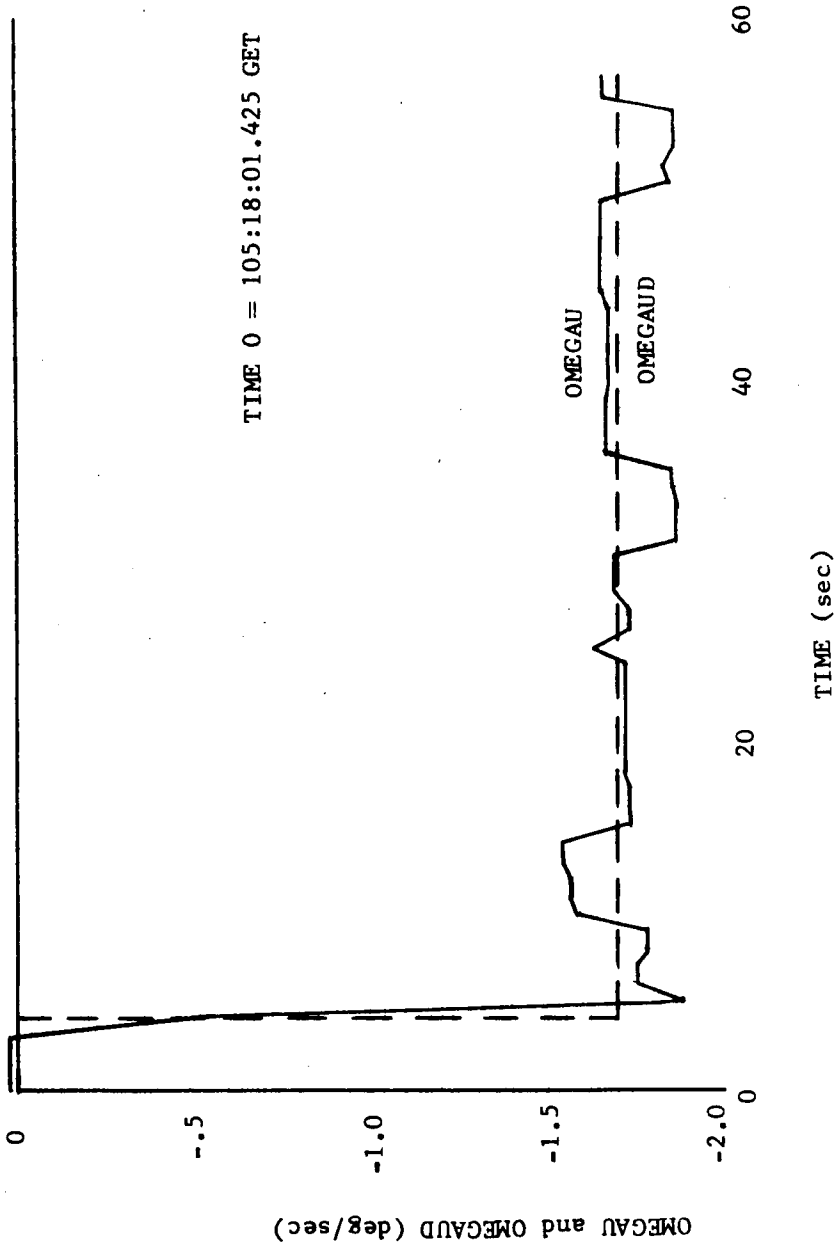

Figure 5-22 AUTOMATIC MANEUVER TO TPI ATTITUDE
DESIRED AND ACTUAL RATES VS TIME U-AXIS

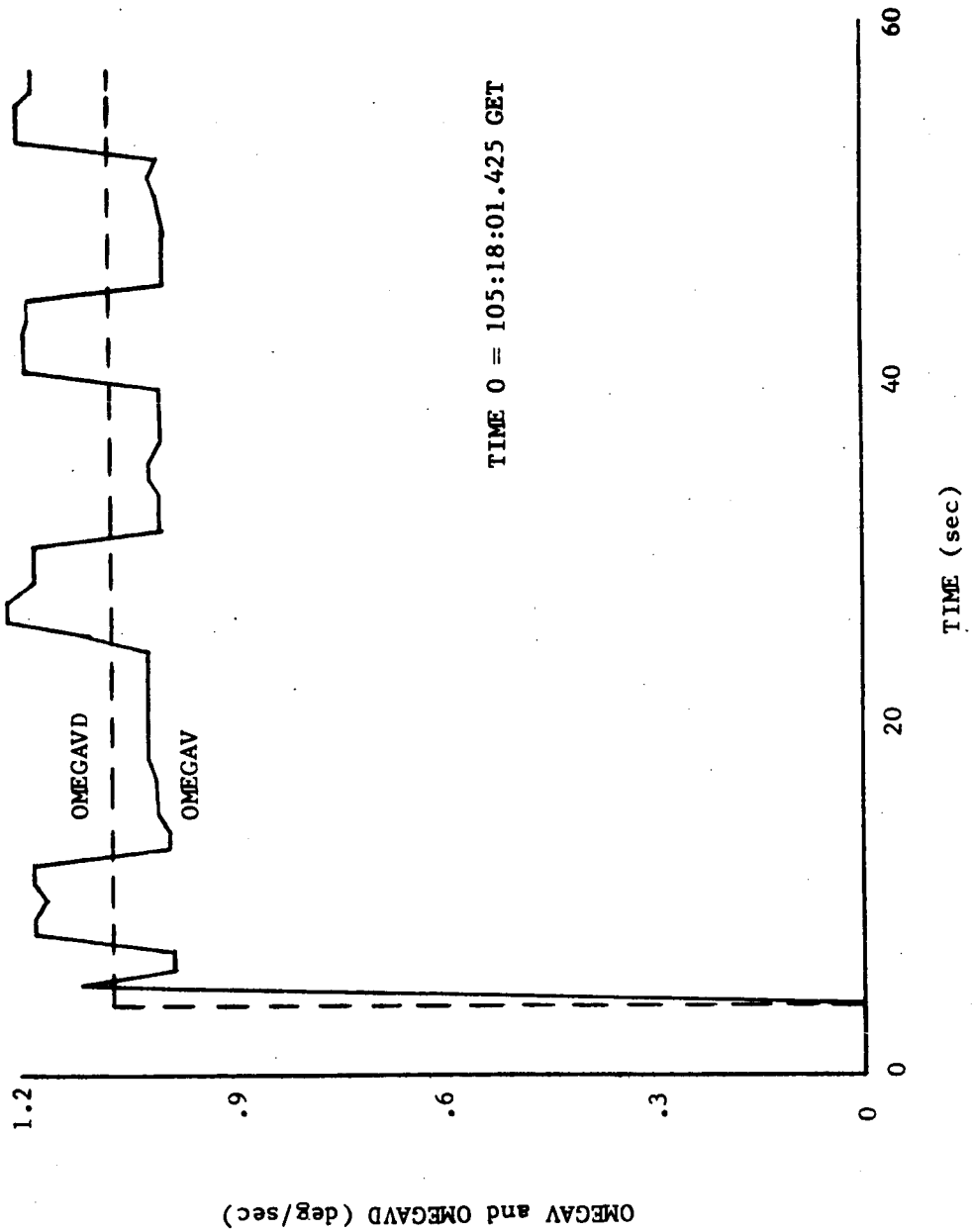

Figure 5-23 AUTOMATIC MANEUVER TO TPI ATTITUDE
DESIRED AND ACTUAL RATES VS TIME V-AXIS

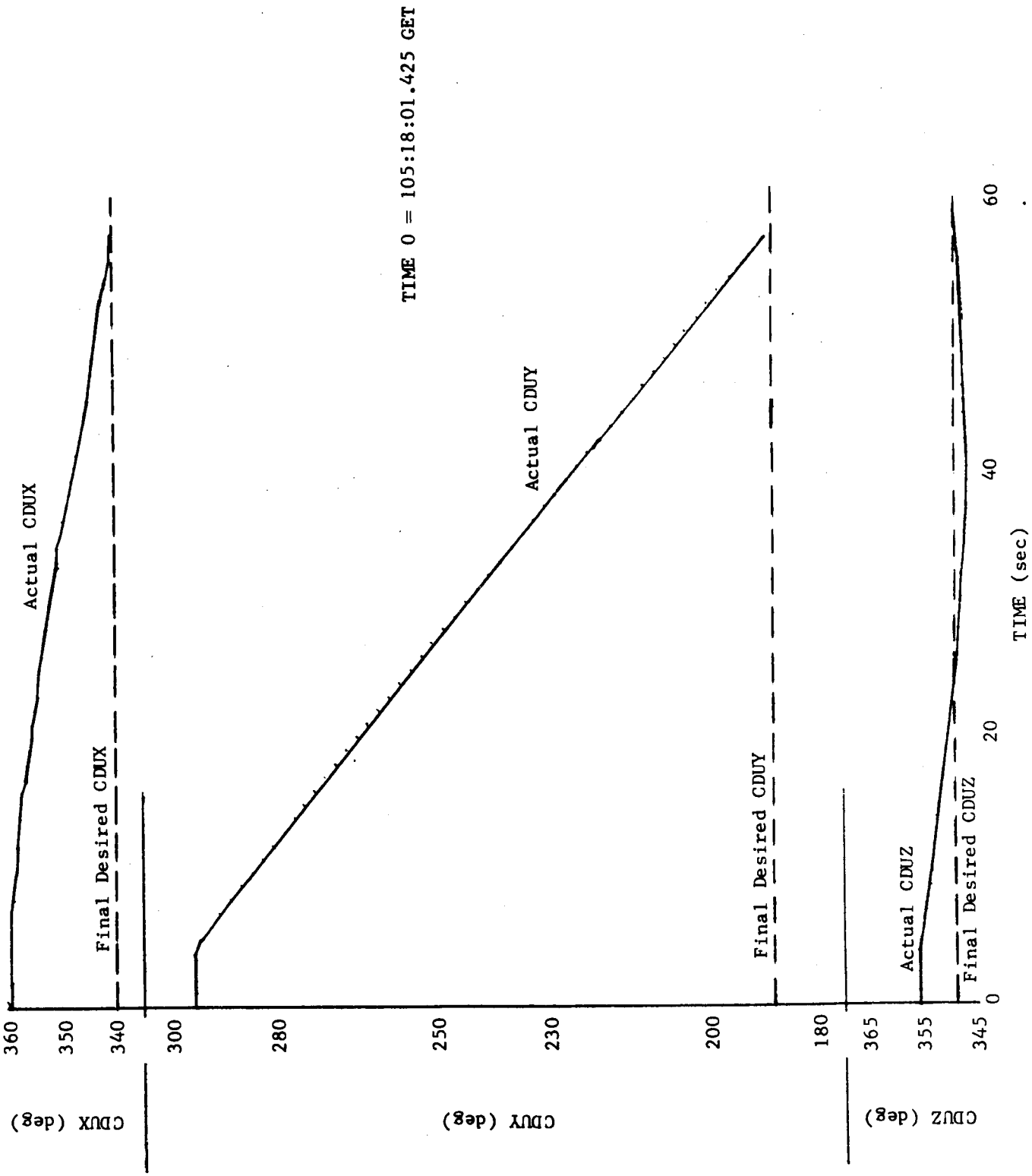

Figure 5-24 AUTOMATIC MANEUVER TO TPI ATTITUDE CDU ANGLES

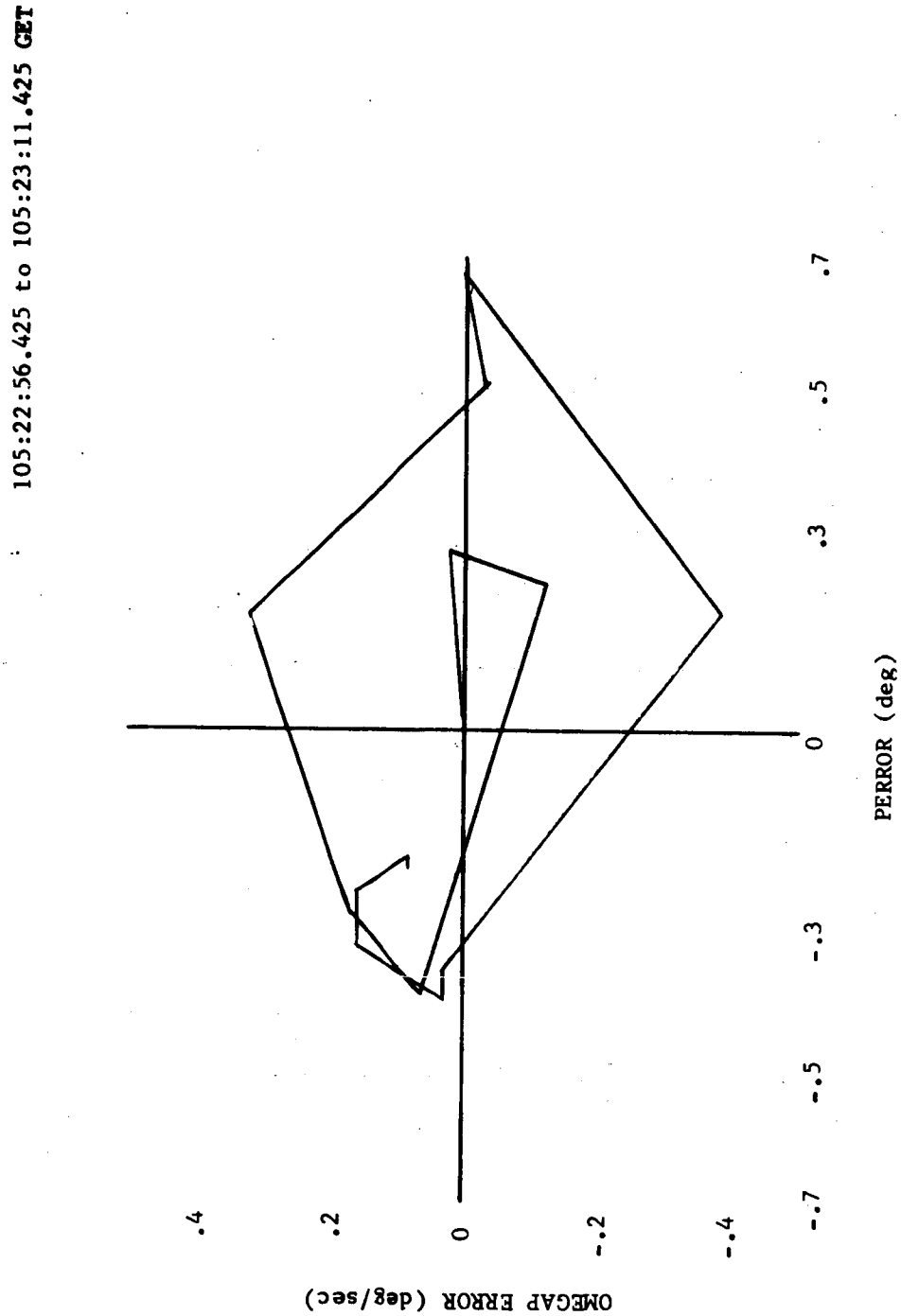

Figure 5-25 TPI BURN P-AXIS PHASE PLANE

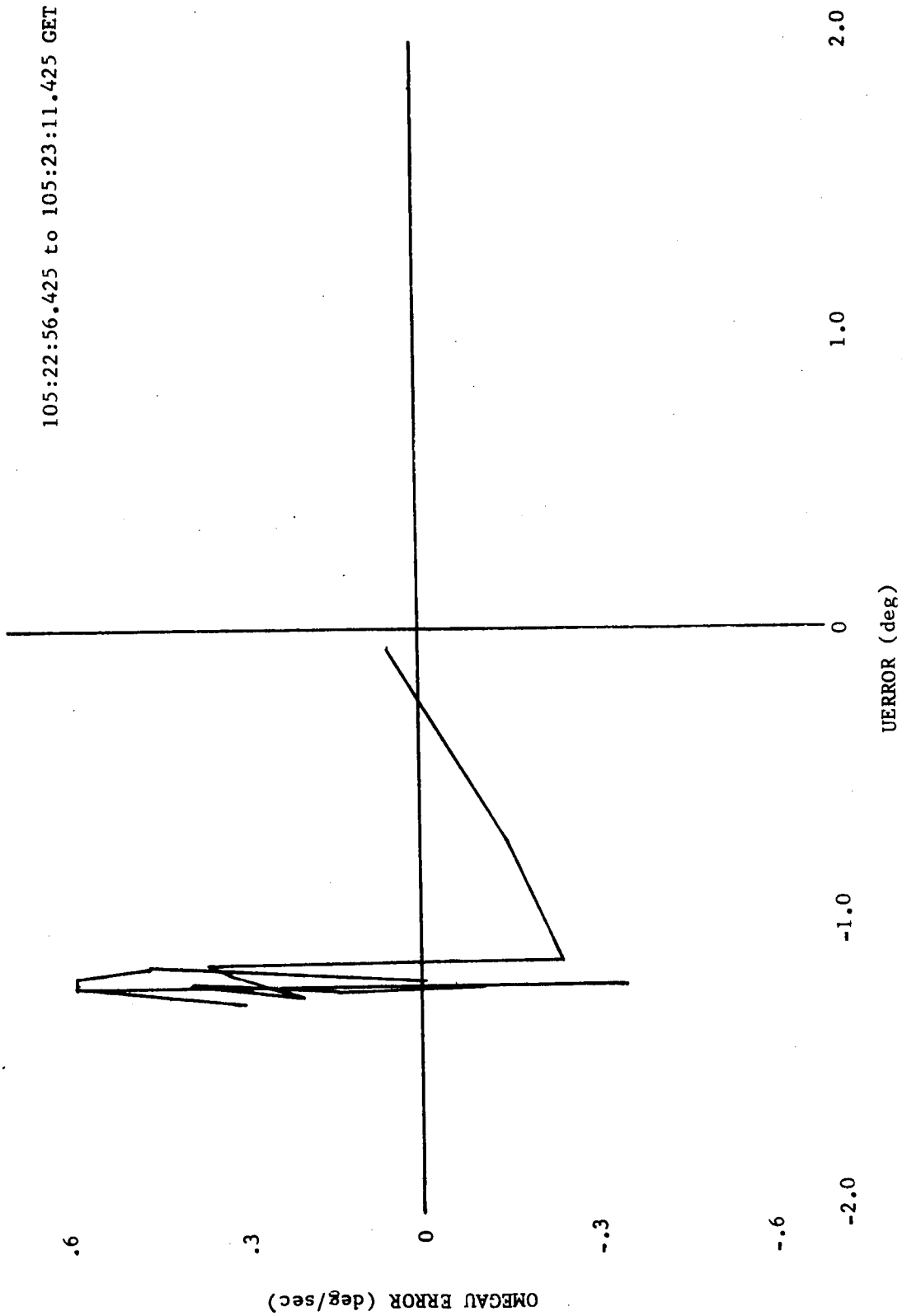

Figure 5-26 TPI BURN U-AXIS PHASE PLANE

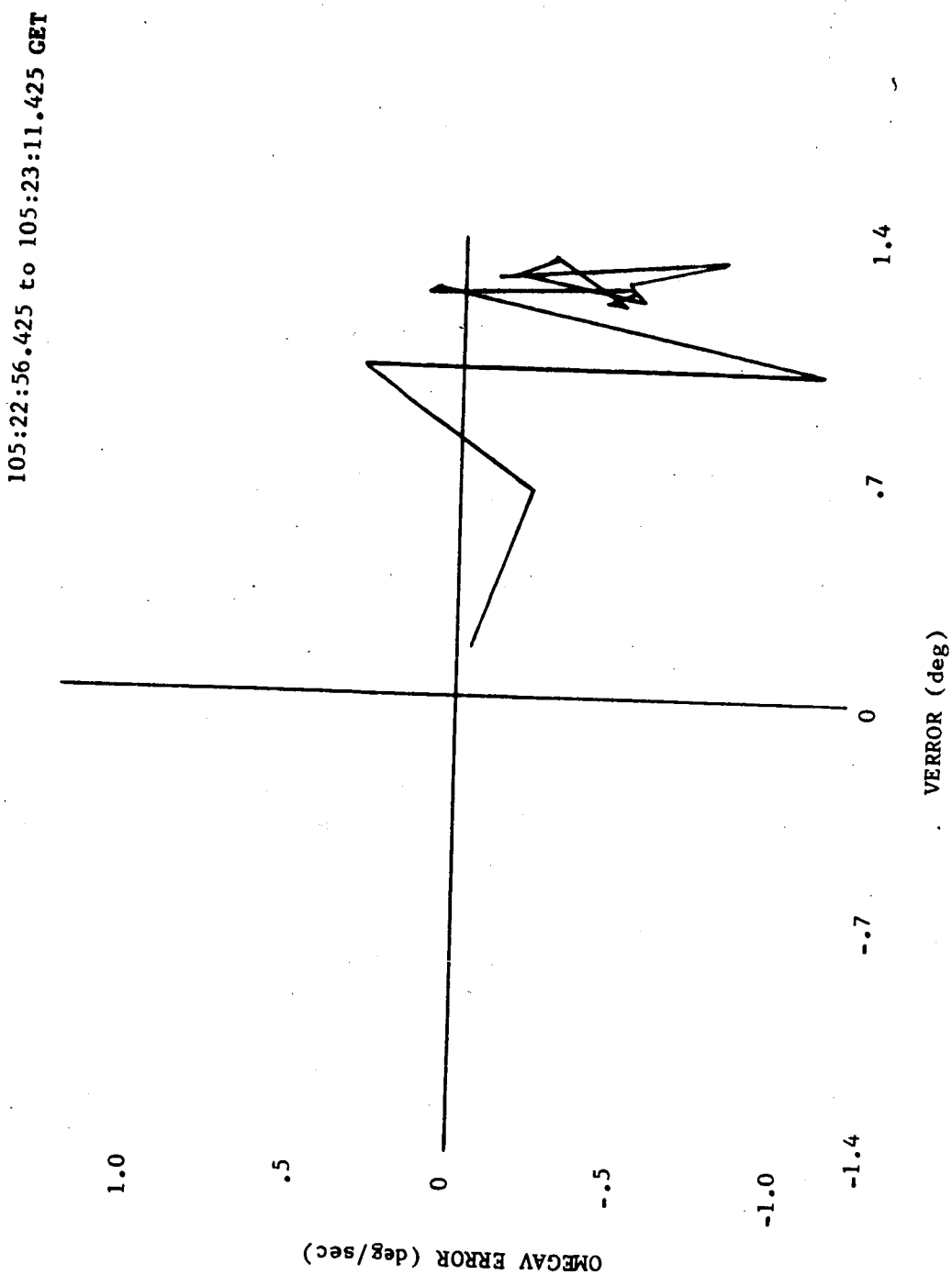

Figure 5-27 TPI BURN V-AXIS PHASE PLANE

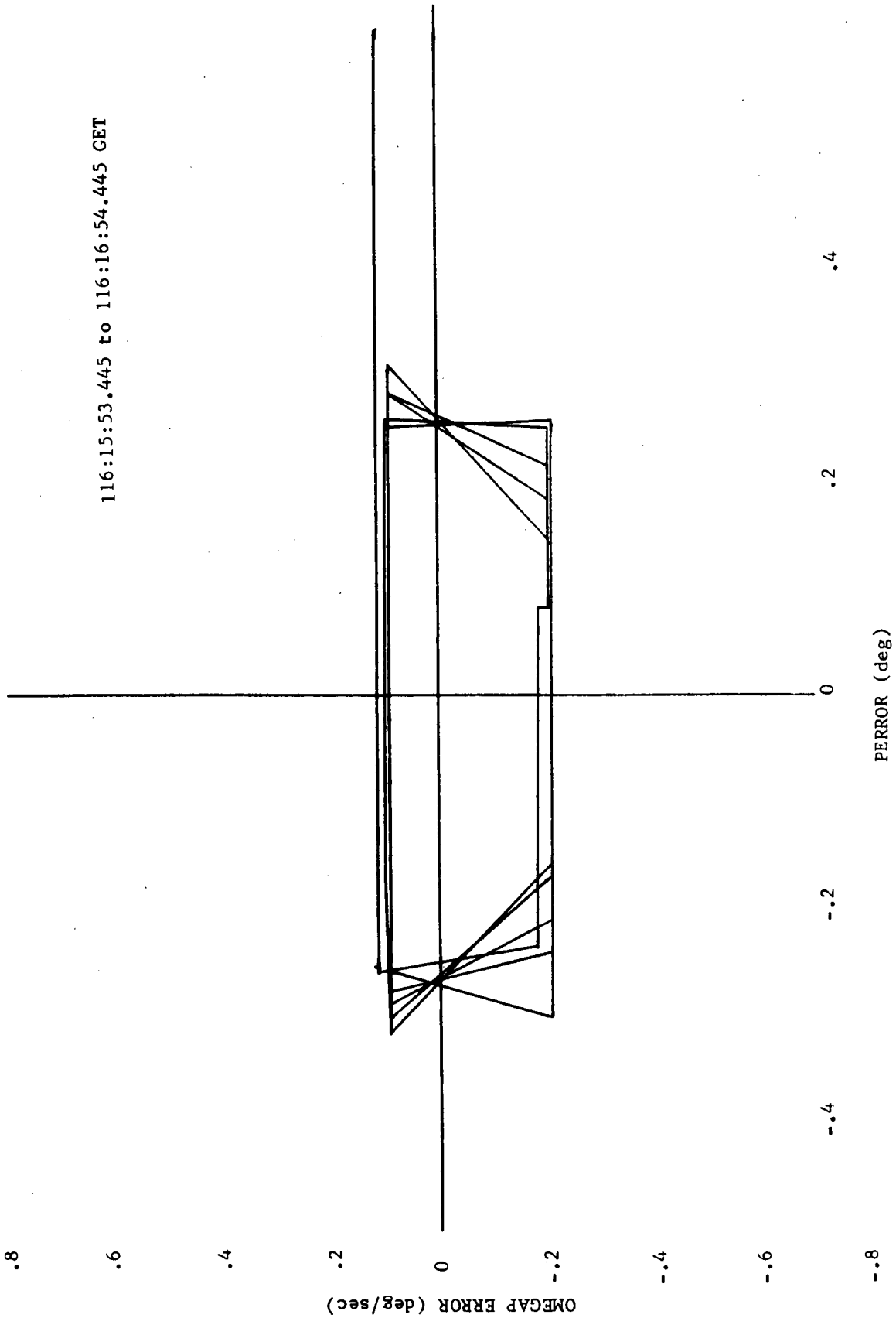

Figure 5-28a ATTITUDE HOLD AFTER APS BURN TO DEPLETION

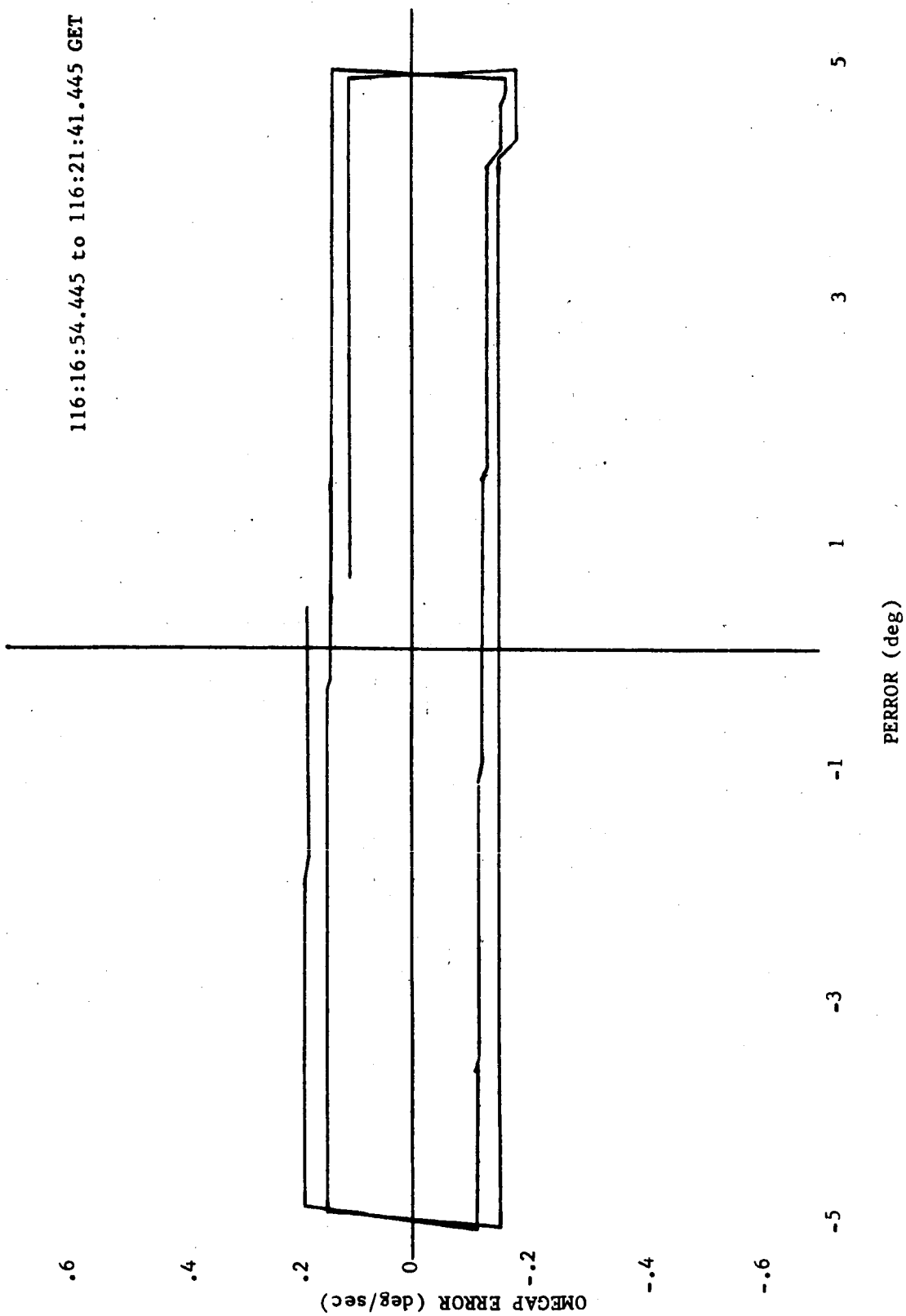

Figure 5-28b ATTITUDE HOLD AFTER APS BURN TO DEPLETION

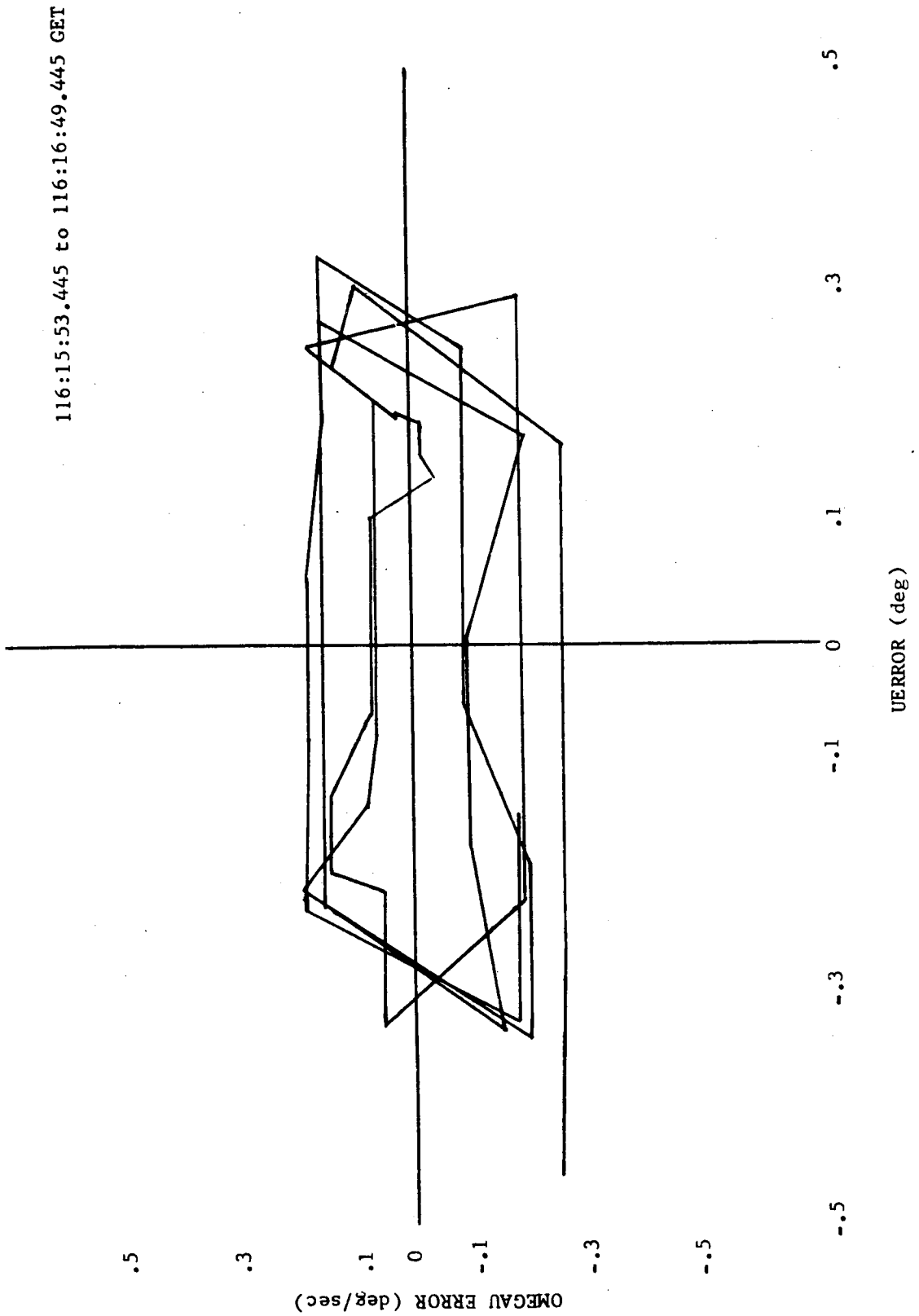

Figure 5-29a ATTITUDE HOLD AFTER APS BURN TO DEPLETION

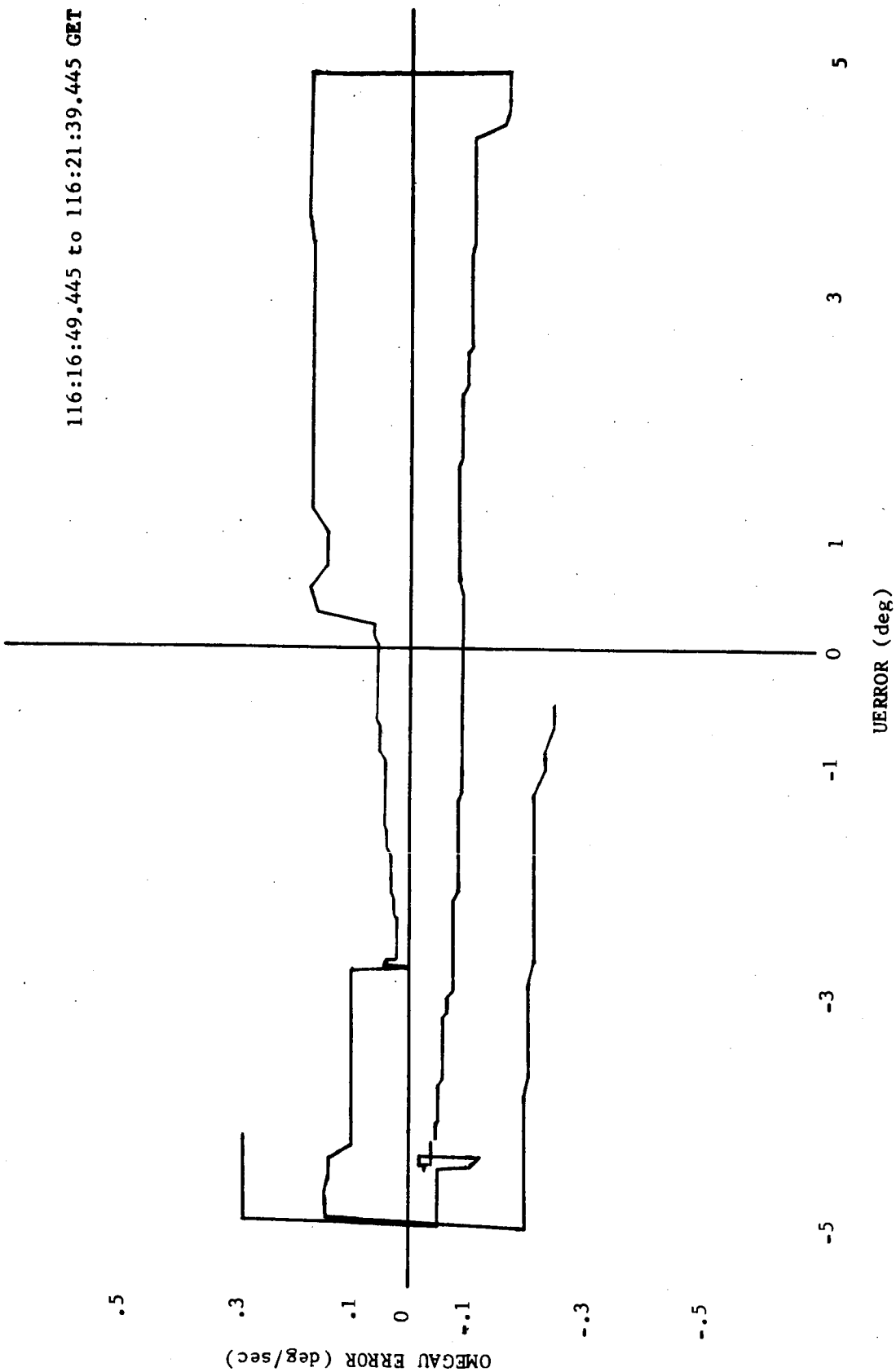

Figure 5-29b ATTITUDE HOLD AFTER APS BURN TO DEPLETION

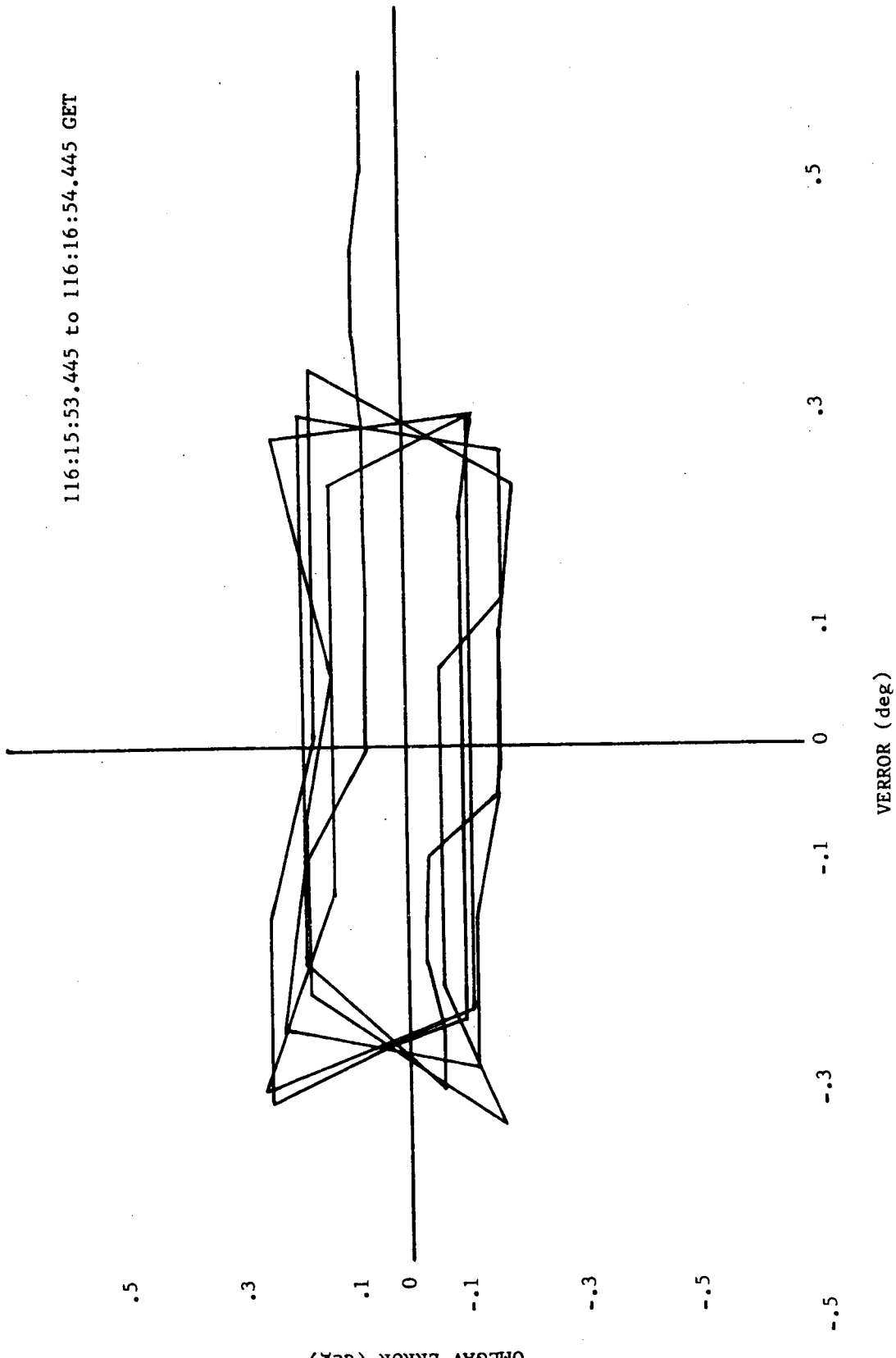

Figure 5-30a ATTITUDE HOLD AFTER APS BURN TO DEPLETION

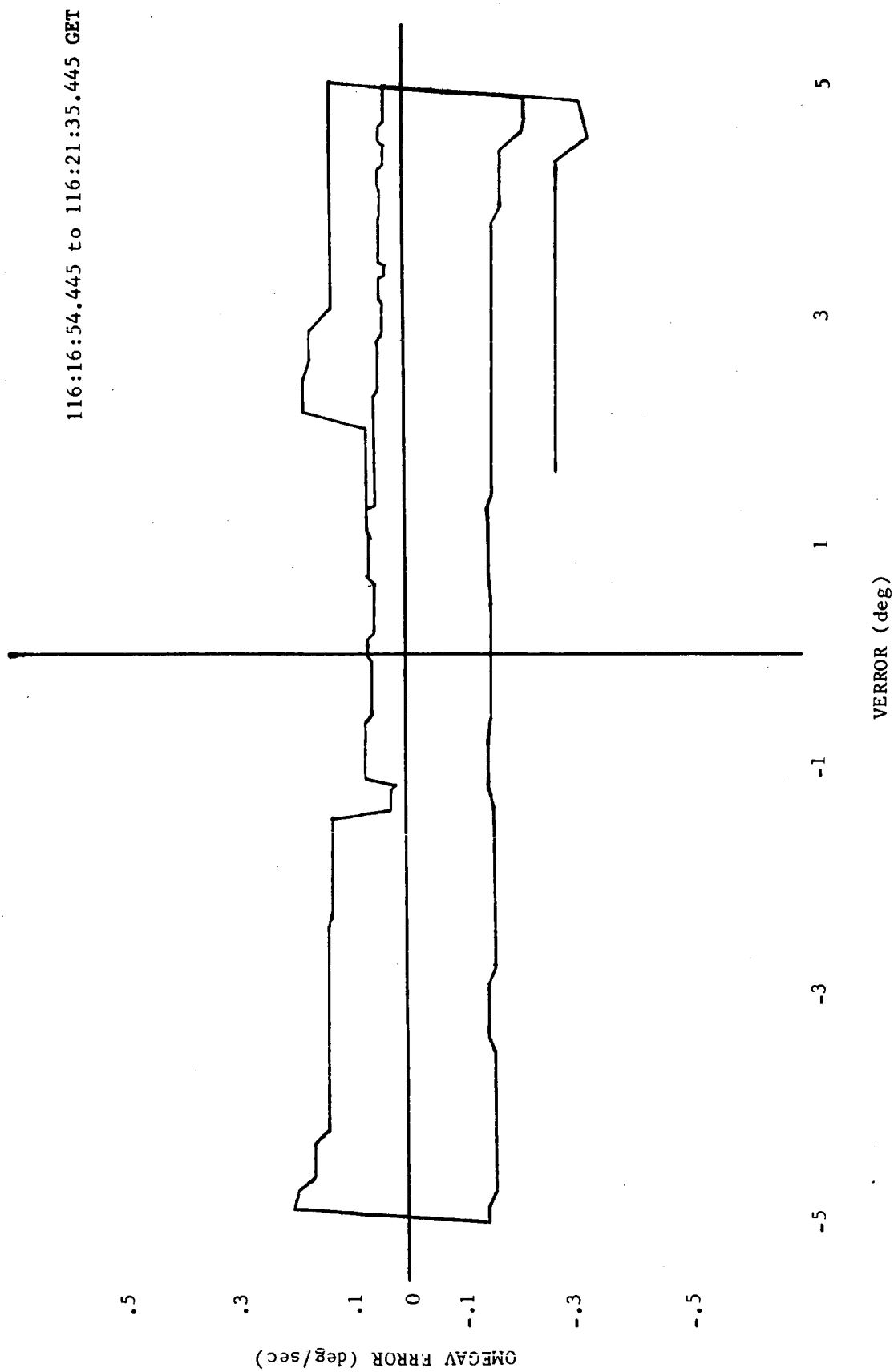

Figure 5-30b ATTITUDE HOLD AFTER APS BURN TO DEPLETION

6.0 AGS ANALYSIS

AGS performance was excellent. Overall AGS performance data are present in the Apollo 10 Mission Report (Reference 1). Apollo 10 AGS accuracy analysis was based primarily on comparisons of the AGS sensed velocity during the APS burn to depletion with PGNCS sensed velocity. Section 6.2 contains the results of an error separation study for that burn.

6.1 OVERALL SYSTEM PERFORMANCE SUMMARY

The AGS provided LM control for the CDH burn and the APS burn to depletion and provided a backup capability during the PGNCS controlled DOI, phasing, insertion and TPI maneuvers.

One AGS inflight calibration was scheduled shortly before undocking but was not performed due to lack of time as the result of a tunnel venting problem which occurred during the preparation for undocking. Accelerometer bias and gyro drift were calculated from the available downlink data and the instrument values were very close to the prelaunch flight load. Therefore, omission of the calibration procedures was of no serious consequence. On a lunar landing mission an inflight calibration should be performed or the mission objectives could be compromised.

In accordance with preflight planning, no AGS radar updates were incorporated during the rendezvous sequence.

During the LM staging operation the LM vehicle experienced high rotational body rates and for the Z body axis, the input rate caused the output of the Z gyro to be saturated for 3 seconds. Subsequent AGS operation was nominal indicating the system was not permanently degraded as a result of the high input rate.

Improved system performance data, formulated after the publication of the Apollo 10 Mission Report, are presented in the following sections.

6.1.1 Velocity-To-Be-Gained Residual Comparisons

The differences between PGNCS and AGS velocity-to-be-gained at the end of LM burns with telemetry coverage are shown in Table 6-1.

The residual Vg comparisons show that the overall AGS performance during the burns was well within the accuracy required for it to have successfully guided the LM through the burns.

The Vg data is also of value in illustrating the behavior of the steering loop during an AGS controlled burn. Figure 6-1 shows the $\overline{V}g$ magnitude for the APS burn to depletion. The smooth approach toward zero indicates that the AGS steering was functioning correctly. The vector never attained zero on this burn since the Vg was set large knowing that propellant depletion would occur before the Vg was reduced to zero.

6.1.2 PGNCS/AGS Alignment Accuracy

The AGS inertial reference was aligned to the PGNCS inertial reference at least ten times during the flight. Differences between the PGNCS gimbal angles and those calculated from the AGS direction cosines for the cases in which telemetry data were available shortly after the alignment are listed in Table 6-2. All differences are within the .067 degree specification.

6.1.3 Environment

During the LM staging operation (initiated at 102:45:16.9 GET) the LM experienced high rotational body rates, apparently the result of misplaced mode control switches. A discussion of the problem and the probable cause is presented in the Apollo 10 Mission Report (Reference 1). As a result of the problem the Z gyro axis input rate exceeded the AGS design limit. The maximum observed body rates based on rate gyro assembly (RGA) data were:

X (Yaw)	=	25 deg/sec
Y (Pitch)	=	17 deg/sec
Z (Roll)	$\cong$	25 deg/sec

A precise yaw and roll rate cannot be established since the instrumentation range was ± 25 deg/sec and the signals were limited during the staging. The AGS sensed body rates derived from changing AGS direction cosines are plotted in Figure 6-2. In the figures, it can be seen that during a period of high angular acceleration the Z body rate suddenly flattened for 3 seconds. During the same 3 second period the Z gyro 20 ms pulse accumulation (sampled each second for telemetry) was 580 counts, which is the maximum possible pulse count over a 20 ms interval. Therefore the gyro was apparently saturated (i.e., the input was greater than 25.347 deg/sec). The X and Y gyros did not indicate saturation. Approximately 3 minutes later the AGS was realigned to the PGNCS inertial reference. Corrections of 0.23, -0.39, and 1.18 deg for X, Y, and Z, respectively, were required to update the AGS to PGNCS.

Subsequent AGS operation was nominal, indicating the system was not permanently degraded as a result of the high rate.

6.2 SENSOR PERFORMANCE

AGS sensor performance was determined from studying several periods of coasting flight and the APS burn to depletion. The coasting flight intervals were used to determine static accelerometer bias and gyro drift. Data taken during the APS burn to depletion were used in estimating misalignments, scale factor errors, dynamic accelerometer bias, and dynamic gyro drift. Two sets of errors were derived, both of which when used to correct the AGS data will result in a fit of AGS sensed velocity to the PGNCS data. Two error sets are presented because accelerometer dynamic bias is inseperable from accelerometer scale factor error and/or misalignment due to the characteristics of the burn analyzed. The methodology used for the powered flight error separation is presented in Appendix A. A compilation of sensor performance during coasting and powered flight is presented in Section 6.2.1 and 6.2.2; comparisons of these results with the AGS error model are presented in Section 6.2.3.

6.2.1 Coasting Flight Analysis

Gyro drift and accelerometer bias data were obtainable from the available telemetry data during the coasting flight.

Gyro drift was determined during three periods of coast. The inflight drifts and time intervals are listed in Table 6-3. Also listed are the final pre-installation calibration (PIC) values (which were the flight compensation values) and the final earth prelaunch calibration (EPC) values. The inflight drifts were obtained by least square fitting the PGNCS/AGS integrated body rate differences. The flight load compensation was removed to obtain total drift. The differences over the last period of free flight listed in Table 6-3 and through the APS burn to depletion (from t_{ags} = 67925 through 68175) are plotted in Figures 6-3, 6-4 and 6-5.

Static accelerometer biases were determined over ten periods of coasting flight; the data are listed in Table 6-4. The numbers were calculated by differencing the sensed velocities accumulated over the measurement period, and dividing by the time intervals. The flight compensation was then removed to obtain total bias.

6.2.2 APS Burn to Depletion Analysis

The APS burn to depletion was used since it was the only LM thrusting maneuver on Apollo 10 which was of sufficient duration and acceleration to permit estimation of other than static sensor errors. The high frequency and amplitude of spacecraft motion (peak-to-peak rates of 10 deg/sec; period of 2-3 sec) during the Apollo 9 mission APS depletion burn (PGNCS controlled) precluded the data's use for sensor error determination. However, because of the tighter deadband for the AGS/CES controlled Apollo 10 burn (0.37 deg pitch and roll, 0.47 deg yaw), the data was suitable for analysis. Peak body rates during the burn were about 0.3 deg/sec (Figures 6-6, 6-7, and 6-8).

Velocity Differences

The X body axis acceleration over the burn is plotted in Figure 6-9. The length of the burn was about 210 seconds; the total body axis ΔV's were 3837 fps in X, -2.4 fps in Y, and 92.2 fps in Z (Figures 6-10,6-11, and 6-12). The uncompensated PGNCS/AGS sensed velocity differences at the end of the burn (Figures 6-19, 6-20, and 6-21) were: $\Delta\dot{X}$ = -0.96 fps; $\Delta\dot{Y}$ = -24.6 fps; $\Delta\dot{Z}$ = 18.1 fps. In comparison the next largest burn, the APS insertion burn, produced a ΔV of about 220 fps and PGNCS/AGS velocity residuals of less than 0.20 fps.

When AGS minus PGNCS differences were first calculated, the 90 hour 0 minute 3 second K factor (constant which when added to AGS clock time yields an equivalent PGNCS clock time) stored in the LGC was used. The differences, particularly along the X (thrust) axis, followed the acceleration profile, indicative of a data timing error. The error in time appeared to be 2.1 seconds. Further investigation revealed that the true K factor was 90 hours 00 minutes 0.87 seconds

rather than the value stored in the LGC. Nominally K would have been an even 90 hours, however, a nominal time synchronization is not always obtainable. RTCC determines the true K factor in near real time and sends an update to the LGC. For this update the value was determined erroneously. The problem was of no consequence to this portion of the mission, since no real time velocity comparisons (PGNCS versus AGS) were required. All velocity comparisons used in this analysis were made using the true K factor to relate PGNCS time to AGS time.

Accelerometer Errors

In Figures 6-13 through 6-15, the PGNCS IMU gimbal angles were used to transform the PGNCS velocities to body coordinates before differencing. Since the gimbal angles are a measure of the orientation of the body axes relative to the PGNCS platform the velocity differences are independent of the AGS attitude reference. Therefore no gyro errors appear in this comparison. The comparison is, however, AGS relative to PGNCS, and thus contains PGNCS accelerometer errors, gimbal angle misalignment and quantization errors as well as the AGS accelerometer errors.

The cause of the +0.25 fps step change in the Z velocity differences (Figure 6-15) at ignition has not been established. It is thought to have occurred in processing the data, and is not considered indicative of hardware error.

The accelerometer errors chiefly responsible for the residuals are dynamic bias, static bias and scale factor error in X, and dynamic bias, static bias and misalignment in Y and Z. Separations of the effects of dynamic bias from scale factor error effects and from accelerometer misalignment effects cannot be accurately made using data from this burn because of insufficient variation in acceleration. Using the Data Comparison program and LM Error Analysis program as discussed in Appendix A, two sets of accelerometer errors sufficient to null the

residuals were determined: static bias plus dynamic bias (Table 6-5) and static bias plus scale factor error in X and misalignment in Y and Z (Table 6-6). No X accelerometer misalignment and no Y or Z accelerometer scale factor errors could be determined since these errors were insensitive during the APS engine burn (majority of thrust was along the X axis). The static bias listed in Table 6-5 and 6-6 is that measured during a period of coasting flight just before the burn (the bias remaining after compensation). The dynamic bias listed was found by subtracting the AGS static bias and PGNCS static bias from the total bias necessary to null the residuals during the burn. This is actually the difference between AGS dynamic bias and PGNCS dynamic bias. The compensated velocity differences appear in Figures 6-16, 6-17 and 6-18.

Attitude Reference Misalignment and Gyro Drift

Figures 6-19, 6-20, and 6-21 are the PGNCS/AGS velocity differences produced after transforming the PGNCS velocities to body coordinates using the AGS direction cosine matrix. These differences are due to the accelerometer errors discussed above plus all gyro errors and initial misalignment of AGS attitude reference relative to PGNCS. The initial misalignment is due to AGS/PGNCS alignment computational errors, PGNCS gimbal angle quantization, and accumulated AGS/PGNCS relative drift since the time of the last alignment.

The values of initial attitude reference misalignment used were found by differencing the PGNCS gimbal angles and the Euler angles calculated from the AGS direction cosine matrix near the beginning of the burn. These values are listed as misalignments about platform axes in Tables 6-5 and 6-6. They account for all but one foot per second or less of the residuals and are primarily due to gyro drifts accumulated over a period of about 1½ hours since an alignment.

The gyro drifts listed were calculated as the slopes of straight lines fit by the method of least squares to the integrated PGNCS/AGS body rate differences during the burn (Figures 6-3, 6-4, and 6-5).

They are listed in Tables 6-5 and 6-6 and include the effects of AGS static and dynamic gyro biases, AGS X-gyro spin axis mass unbalance, and all PGNCS gyro errors.

Having determined the gyro drift and initial attitude reference misalignment and having found the accelerometer errors, the AGS velocity data were corrected for these errors and compared with the PGNCS data. The compensated velocity differences (using AGS direction cosines for the platform to body coordinate transformation) are plotted in Figures 6-22, 6-23 and 6-24. All residuals (except the 0.25 fps processing - caused step change in the Z residuals) were reduced to less than 0.10 fps.

6.2.3 Comparison of Sensor Analysis Results to AGS Error Models

The estimates of the sensor errors that were derived from the inflight data are all within the 3σ ranges expected, based on the AGS capability estimate, and are all within the AGS error budget. The ratio of ASA 016 parameter values to one sigma values from the capability estimate or ASA 016 preflight performance estimate are given in Table 6-7. These data show the AGS performance in terms of expected standard deviation and as a whole show excellent corroboration of the a priori system error modeling. The general conclusion is that ASA 016 performed with high accuracy, well within that required for the mission, and the gyro bias stability was exceptional.

Error Model Comparison

Tables 6-8 and 6-9 present the inflight error estimates from Section 6.2.2 in the form of the error model used in the AGS Capability Estimate (Reference 7).

Two comparison models are listed. The first is an estimate of ASA 016 performance prepared for the FP5 FRR. The second comparison model is the Error Budget from the AGS capability estimate (Reference 7) which

is a breakdown of the specification numbers in the current versions of the AGS Performance and Interface Specification (Reference 8). In addition to the terms listed in Tables 6-8 and 6-9 the Apollo 10 mission yielded data on gyro and accelerometer long term stability and short term repeatability, which are compared with the capability estimates in Tables 6-10 through 6-13.

Accelerometer Bias Repeatability

The standard deviations of accelerometer biases over a 12-hour flight interval were computed from the data in Table 6-4 and are given in Table 6-10. The standard deviations compare well with the Error Budget value for acceleromater bias repeatability, which is 20 μg.

Accelerometer Time Stability

Accelerometer instrument biases were derived from the free flight data by determining the apparent bias from velocity data and adding the flight compensation value. The inflight bias values are differenced from the preflight bias values measured in the laboratory 59 days earlier. The average of these deltas are presented in Table 6-11 along with the capability estimate and error budget from Reference 7. These data indicate good accelerometer bias time stability.

Gyro Bias Repeatability

The gyro inflight bias repeatabilities over a period of 12 hours are presented in Table 6-12 below, along with the capability estimate and error budget values from Reference 7.

These data are well within the Error Budget and capability estimate limits, and indicate excellent short term gyro bias stability for this mission.

Gyro Bias Time Stability

The gyro bias shifts from Earth Prelaunch Gyro Calibration (EPC) to free flight measurements are presented in Table 6-13 along with the capability estimate and error budget from Reference 7. The maximum

observed shift was +0.11 deg/hr., which is well within the capability and error budget limits.

6.2.4 Analysis Accuracy

The estimation of the modeled sensor errors (accelerometer biases, gyro drifts and inertial reference misalignments) is subject to a number of errors. These include errors caused by the following effects.

- o Data readout quantization.
- o PGNCS errors.
- o AEA Computational Errors
- o Sampling and Processing Errors

These are discussed below.

Quantization

On Apollo Flight 10 the AGS sensed body axis accumulated velocities (V_{dx}, V_{dy}, V_{dz}) were quantized at 0.0625 ft/sec. Assuming $\pm$ 0.03125 ft/sec as the limits of a uniform distribution, the 3σ uncertainty in the accelerometer biases calculated from the differences of these velocities is $\pm \frac{.03125\sqrt{6}}{t}$ ft/sec^2, where t is the bias measurement interval. This uncertainty is very small in the measurement of static bias because of the long time periods used. For example, for the bias measured over a 1510 second period just before the APS burn to depletion (Table 6-4), the error is about $\pm$ 1.5 μg. Even for measurements of total dynamic drift during the burn, this error contributes only $\pm$ 11 μg

The velocity quantization also causes uncertainties in determination of accelerometer misalignment and scale factor error. For Y and Z accelerometer misalignment and X accelerometer scale factor, the measurement uncertainties are both approximately $\pm \frac{.03125\sqrt{3}}{\Delta V_x}$, where ΔV_x is the total X velocity change over the burn. For the APS depletion burn, these uncertainties are about 3 $\widehat{\text{sec}}$ in misalignment and 14 ppm in scale factor error.

The PGNCS gimbal angle CDU readouts are quantized at 40 $\widehat{sec}$. These are the source of PGNCS angular measurements and are responsible for 3σ uncertainties of $\pm 20\sqrt{3}$ $\widehat{sec}$ in the estimates of initial misalignment and $\pm 20\sqrt{3/t}$ deg/hr in the estimates of gyro bias, where t is the analysis interval in seconds. For the shortest coasting flight interval used to measure static gyro bias, this uncertainty is $\pm$ .04 deg/hr; for bias measured during the APS burn to depletion, it is $\pm$ 0.16 deg/hr.

PGNCS Errors

All AGS errors derived from the PGNCS/AGS velocity differences are those relative to PGNCS; i.e., they contain both PGNCS and AGS errors. PGNCS gyro drifts as determined inflight were samll enough relative to the AGS drifts that their effects may be neglected. PGNCS accelerometer biases are significant and were measured inflight as -50 μg in X, -160 μg in Y, and 30 μg in Z, (in body coordinates: +47 μg in X, -155 μg in Y, and +50 μg in Z). These biases are accounted for in the analysis.

AEA Computational Error

The AEA computational error in the attitude reference (direction cosine) data due to truncation, roundoff and algorithm errors can be as large as 0.14 deg/hr (Reference 9).

Sampling and Processing Errors

The effects of the low (1 sample per second) telemetry sampling rate and PGNCS to AGS data time interpolation produce errors which are a function of the vehicle oscillatory motion as described in Section 2.4-3 of Reference 9.

The limit cycling experienced in the APS burn to depletion was on the order of 0.2 deg/sec p-p at 0.1 to 0.2 cps and the same estimate of sampling and processing errors is used as for Apollo 9; i.e., 0.2 deg/hr gyro drift uncertainty and 25 μg accelerometer bias uncertainty.

During coasting (free) flight these same error sources contribute approximately 0.10 deg/hr gyro fixed drift uncertainty and $\sqrt{10^2 + \left(\frac{100}{t}\right)^2}$ μg

accelerometer bias uncertainty, where t is the analysis measurement interval in minutes.

Table 6-1 VELOCITY-TO-BE-GAINED RESIDUAL MAGNITUDES

Burn	V_g Magnitude - Fps AGS	PGNCS
Phasing	2.19	1.74
Insertion	1.25	1.17
CDH	0.50	0.54
TPI	2.25	2.26
APS DEPLETION*	762	765

*The targeted value of V_g was larger than could be attained with the fuel onboard.

Table 6-2 PGNCS/AGS ALIGNMENT ACCURACY

Alignment Time	CDU - AEA Angular Difference X (Deg)	Y (Deg)	Z (Deg)
97:29:18	0.006	0.003	-0.002
98:57:58	-0.02	0.03	0.03
100:52:25	0.005	0.001	0.001
102:48:18	-0.007	0.02	0.04
104:36:48	-0.05	-0.02	*
105:09:45	-0.03	-0.04	-0.04

*Data quality is not sufficient to establish an accurate value; however, the difference appears to be less than 0.067 degree.

Table 6-3 GYRO STATIC DRIFT MEASUREMENTS (DEG/HR)

Axis	Final PIC	EPC	INFLIGHT MEASUREMENTS * (With Compensation Removed) (97:06:20→ 97:19:55)	(102:27:35→ 102:44:56)	(108:24:53→ 108:50:01)
X	- 0.11	- 0.28	- 0.17	- 0.12	- 0.20
Y	- 0.41	- 0.61	- 0.65	- 0.58	- 0.61
Z	- 0.44	- 0.62	- 0.64	- 0.60	- 0.69

*All ± 0.17 deg/hr.

Table 6-4 ACCELEROMETER STATIC BIAS MEASUREMENTS

			BIAS (μg)*		
			X	Y	Z
FINAL CALIBRATION			59	- 107	17
FLIGHT LOAD			47	- 119	24
INFLIGHT MEASUREMENTS (WITH FLIGHT LOAD REMOVED)					
From	To	Δt(sec)			
96:58:15	97:08:13	598	- 5	- 106	- 67
98:08:13	98:33:07	1494	+ 4	- 113	- 80
98:51:11	99:00:43	572	- 8	- 119	- 85
100:36:22	100:56:24	1202	- 18	- 119	- 93
101:02:26	101:16:24	838	- 9	- 110	- 96
102:28:04	102:43:52	948	- 19	- 119	- 99
102:47:16	102:54:29	433	- 7	- 101	- 84
104:35:41	104:43:15	454	- 21	- 102	- 78
104:43:57	105:01:23	1046	- 35	- 126	- 95
108:24:53	108:50:01	1508	- 25	- 114	- 84

*Measurement Error = ± 11 μg

Table 6-5 ERROR SET #1 - APS BURN TO DEPLETION

Axis	Accelerometer Static Bias (μg)	Accelerometer Dynamic Bias (μg)	Total Gyro Bias (deg/hr)	Initial Attitude Reference Misalignment (About Platform Axes) (sec)
X	- 72 ± 11	+ 50 ± 29	- 0.22 ± 0.28	- 1400 ± 32
Y	+ 5 ± 11	+ 6 ± 29	- 0.26 ± 0.28	+ 956 ± 32
Z	- 108 ± 11	+ 84 ± 29	- 0.08 ± 0.28	- 130 ± 32

Table 6-6 ERROR SET #2 - APS BURN TO DEPLETION

Axis	Accelerometer Static Bias (μg)	Accelerometer Misalignment ($\widehat{sec}$)	Accelerometer Scale Factor Error (PPM)	Total Gyro Bias (Deg/Hr)	Initial Attitude Reference Misalignment (About Platform Axes) ($\widehat{Sec}$)
X	- 72 ± 11	*	+ 115 ± 44	- 0.22 ± 0.28	- 1400 ± 32
Y	+ 5 ± 11	+ 3 ± 9	*	- 0.25 ± 0.28	+ 956 ± 32
Z	- 108 ± 11	+ 42 ± 9	*	- 0.08 ± 0.28	- 130 ± 32

*Error is not sensitive to burn analyzed.

Table 6-7 PERFORMANCE SUMMARY

	Ratios of Parameter Value to the Expected 1σ Values*		
	X	Y	Z
Accelerometer Bias Repeatability	2.28	1.64	1.96
Accelerometer Bias Time Stability (60 days)	1.18	0.10	1.67
Accelerometer Dynamic Error*	0.99	0.40	0.79
Total Accelerometer Powered Flight Error*	0.41	0.32	0.15
Gyro Bias Repeatability	0.81	0.81	1.04
Gyro Bias Time Stability (20 days)	0.61	0.00	0.11
Gyro Dynamic Error*	0.11	1.23	0.81
Total Gyro Powered Flight Error*	0.63	0.76	0.40

* From the AGS capability estimate or ASA 016 Performance Estimates.

Table 6-8 EQUIVALENT ACCELEROMETER BIAS ERRORS (APS BURN-TO-DEPLETION), μg

		ASA 016 Inflight Estimate	ASA 016 Preflight (4) Performance Estimate		Error Budget from AGS P&I Specification	
			Mean	3σ	Mean	Gaussian 3σ
Accelerometer Bias and Nonlinearity (1)	X	- 72 ± 11		191		479
	Y	+ 5 ± 11		179		479
	Z	-108 ± 11		179		479
X-Scale Factor and Dynamic Errors (2)	X	+ 50 ± 29	9	124	27	159
Y and Z Dynamic Errors, ASA Accelerometer Internal Misalignment and ASA to IMU Mounting Points Misalignment (2)	Y	+ 6 ± 29	+52	346		723
	Z	+ 96 ± 29	- 5	337		723
Total (μg) (3)	X	- 22 ± 27	9	228	27	506
	Y	+ 11 ± 27	+52	390		867
	Z	- 24 ± 27	- 5	382		867

NOTES: (1) Inflight Estimate: Last Free-Flight Data Period

(2) Inflight Estimate: Difference between measured total error and measured fixed bias.

(3) Inflight Estimate: Derived from velocity comparisons.

(4) Data are from Reference 3, except time stability and accelerometer bias from Reference 2 were incorporated to make them compatible with the actual flight conditions without an IFC.

The alignment and scale factor errors in this table appear dissimilar to the capability estimate tables because they have been converted to equivalent bias errors in μg's.

Table 6-9 EQUIVALENT GYRO BIAS ERRORS (APS BURN-TO-DEPLETION), DEG/HR

		ASA 016 Inflight Estimate	ASA 016 Preflight Performance Estimate		Error Budget From P&I Specification
			Mean	3σ	Gaussian 3σ
Gyro Fixed Drift (1)	X	-0.09 ± 0.20	0	0.75	.95
	Y	-0.20 ± 0.20	0	0.75	.94
	Z	-0.25 ± 0.20	0	0.75	.94
X-Gyro Dynamic Drift (2) (4)	X	-0.13 ± 0.34	-0.11	0.37	.77
X-Gyro Spin Axis Mass Unbalance (2)	X		0	0.41	.58
Y and Z Gyro Dynamic Drift (2) (4)	Y	-0.06 ± 0.34	-0.24	0.44	.69
	Z	+0.17 ± 0.34	+0.04	0.48	.90
Total (deg/hr) (3) (5)	X	-0.22 ± 0.29	-0.11	0.93	1.35
	Y	-0.26 ± 0.29	-0.24	0.88	1.16
	Z	-0.08 ± 0.29	+0.04	0.90	1.30

NOTES:

(1) Inflight Estimate: Last Free-Flight Data Period.

(2) Inflight Estimate: Difference between measured total error and measured fixed bias.

(3) Inflight Estimate: Derived from attitude rate comparisons.

(4) The Error Budget values were derived from the oGS Capability Estimate as follows: Multiply $\sqrt{3}$ times uniform error and RSS the result with the Gaussian (3σ) errors.

(5) The Error Budget values are the RSS of the above dynamic errors and 3σ fixed drift.

Table 6-10 STANDARD DEVIATION OF ACCELEROMETER BIASES

B_X^A = 11.4 μg

B_Y^A = 8.2 μg

B_Z^A = 9.8 μg

RMS = 9.9 μg
(Standard Deviation)

Table 6-11 ACCELEROMETER BIAS TIME STABILITY (Averages of 10 Free-Flight Measurements Differenced with PIC Values).

Channel	Δ-Time (days)	Δ-Bias	Ensemble* Capabity Estimate (60 days)	Error* Budget (60 days)
X	59	- 73	185	489
Y	59	- 6	185	489
Z	59	103	185	489

Table 6-12 GYRO BIAS REPEATABILITY

	Standard Deviation of Free Flight Meas.	Capability Estimate (3σ)	Error Budget
X	0.035	0.13	0.10
Y	0.035	0.13	0.10
Z	0.045	0.13	0.10

Table 6-13 GYRO BIAS TIME STABILITY

Axis	Mean of Inflight Meas. -EPC (20 days)	Ensemble Capability (18 days)	Error Budget (18 days)
X	+ 0.11	0.54	0.68
Y	0.00	0.54	0.68
Z	+ 0.02	0.54	0.68

Table 6-14 UNCERTAINTY IN SENSOR PERFORMANCE MEASUREMENTS (3σ)

Period	Accelerometer Bias (μg)	Accelerometer Scale Factor (PPM)	Accelerometer Misalignment (Sec)	Gyro Bias (deg/hr)	Initial Misalignment (sec)
Free Flight	11	----	----	0.17	----
Depletion Burn	27	44	9	0.28	31.5

*Errors computed are based on the time duration of the last free flight interval.

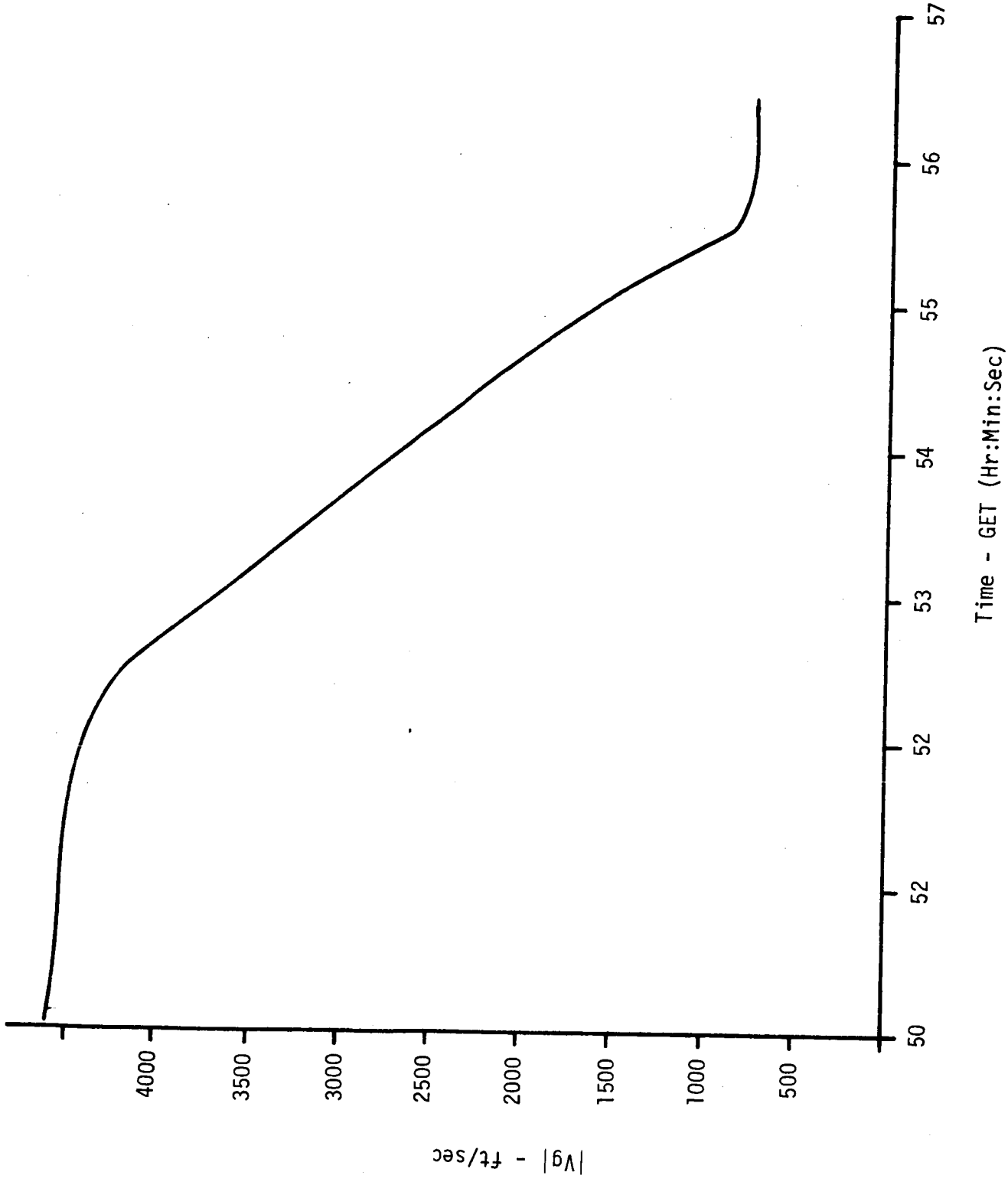

Figure 6-1 AGS VELOCITY-TO-BE-GAINED MAGNITUDE; APS BURN TO DEPLETION

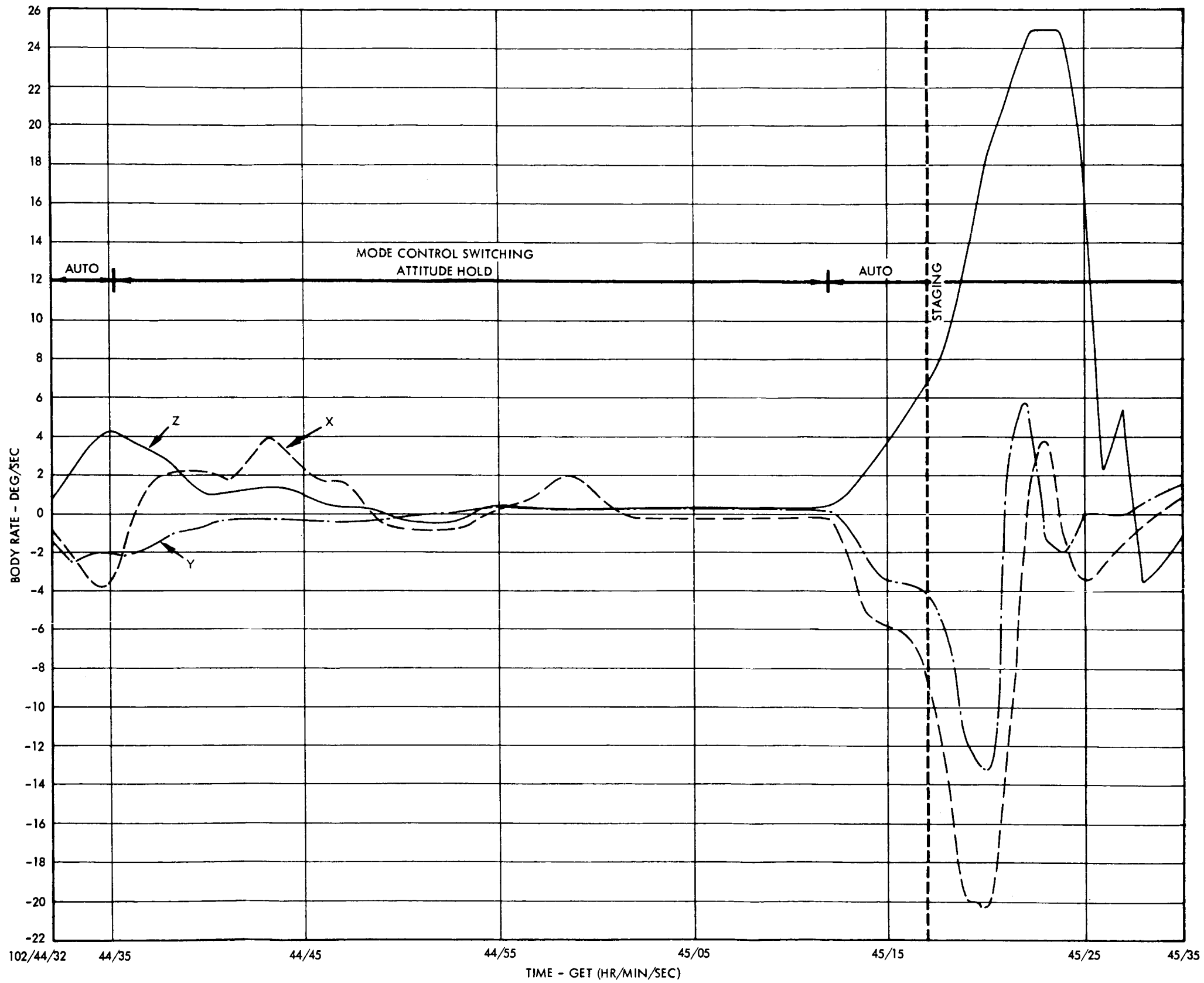

Figure 6-2 BODY RATE DATA DERIVED FROM CHANGING AGS DIRECTION COSINES

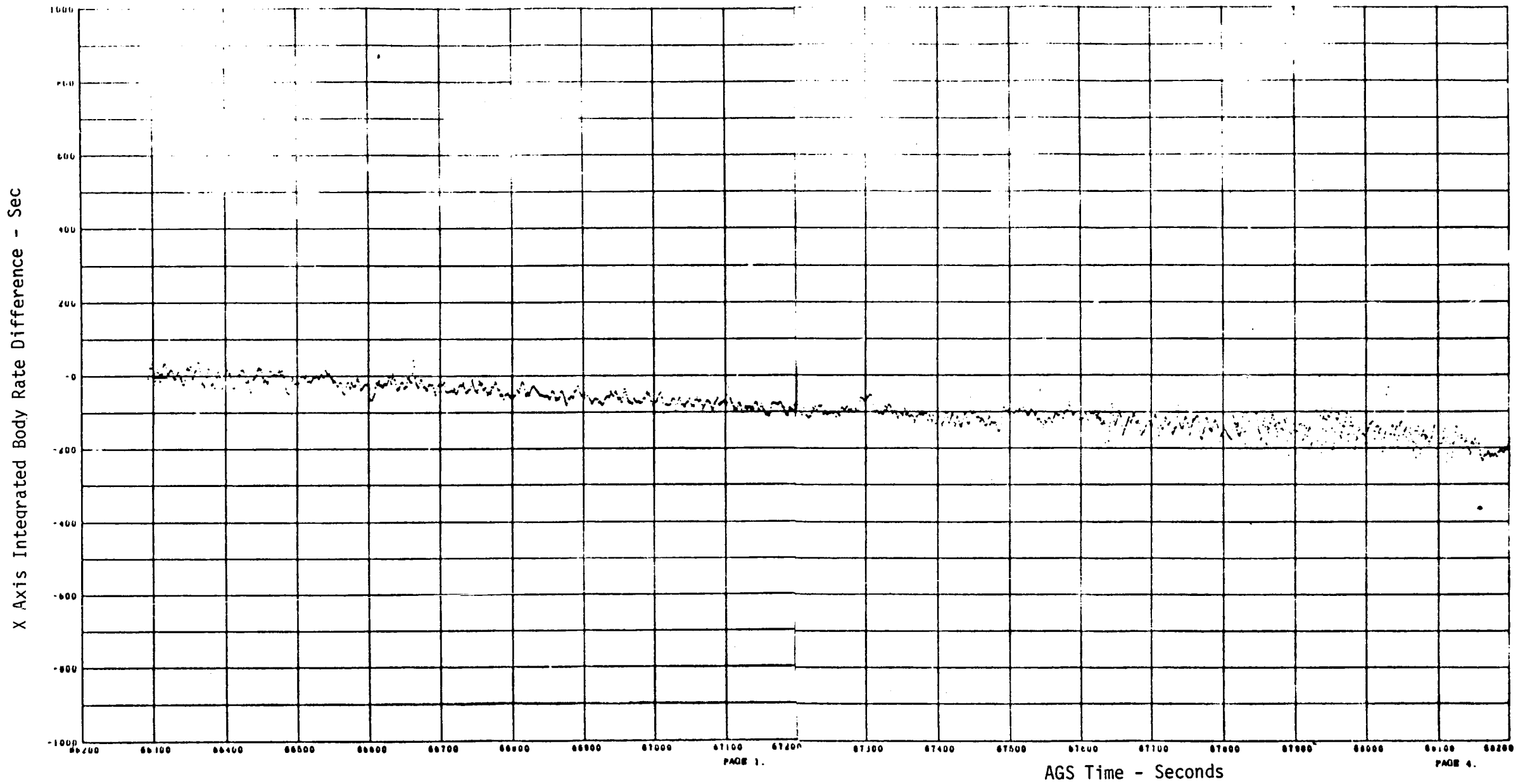

Figure 6-3 AGS/PGNCS X AXIS INTEGRATED BODY RATE DIFFERENCES; COASTING FLIGHT AND APS BURN TO DEPLETION

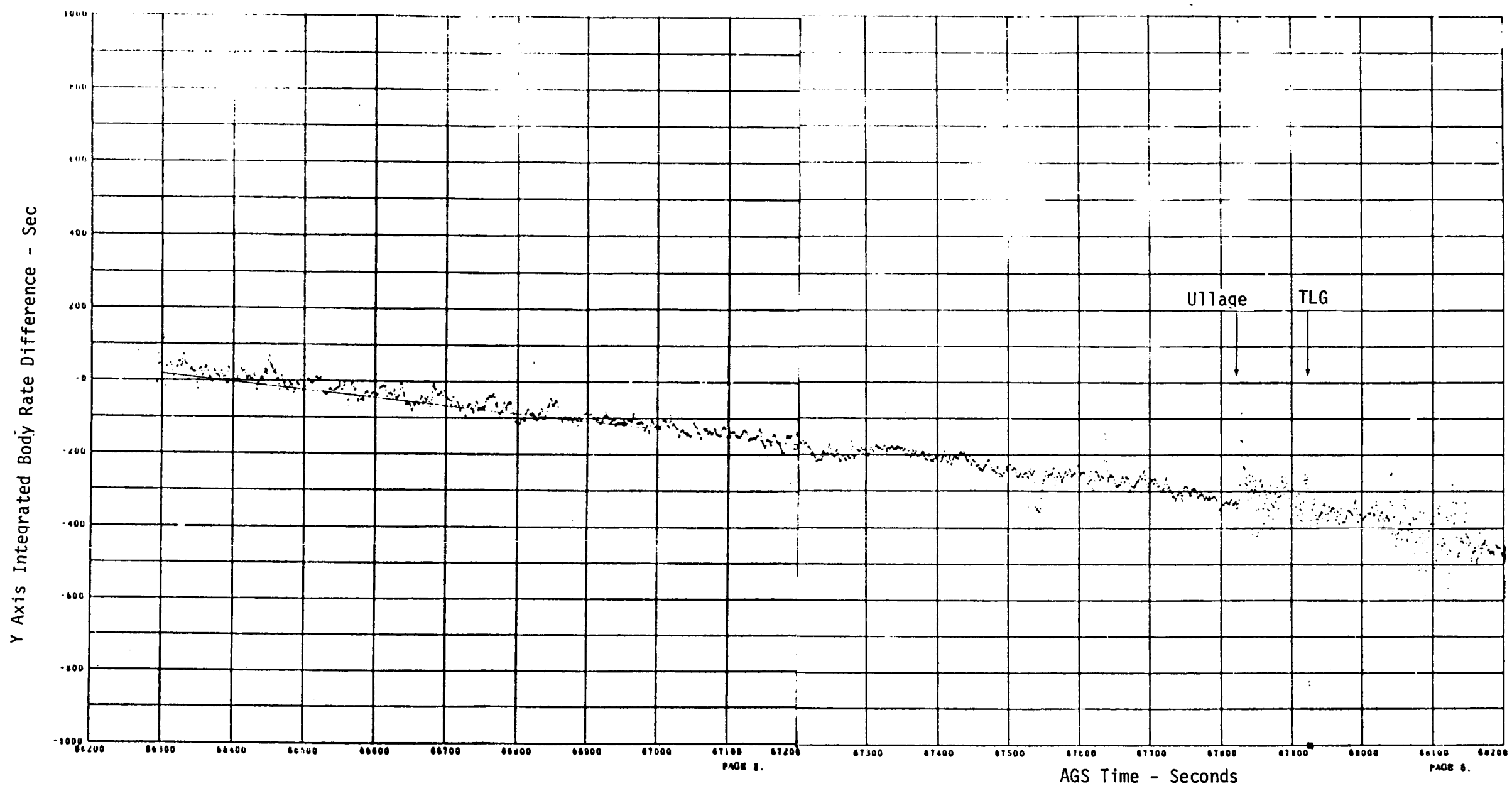

Figure 6-4 AGS/PGNCS Y AXIS INTEGRATED BODY RATE DIFFERENCES; COASTING FLIGHT AND APS BURN TO DEPLETION

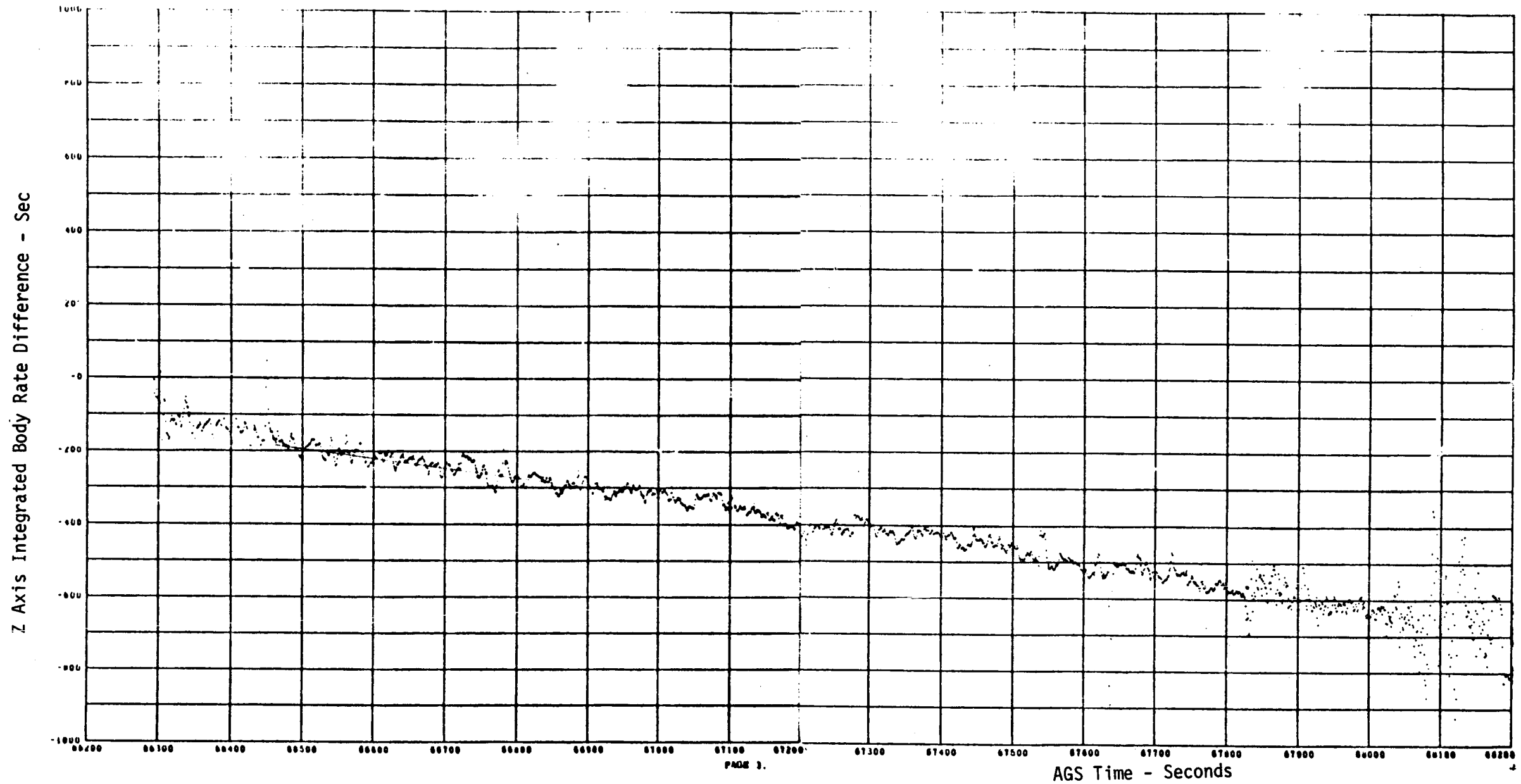

Figure 6-5 AGS/PGNCS Z AXIS INTEGRATED BODY RATE DIFFERENCES; COASTING FLIGHT AND APS BURN TO DEPLETION

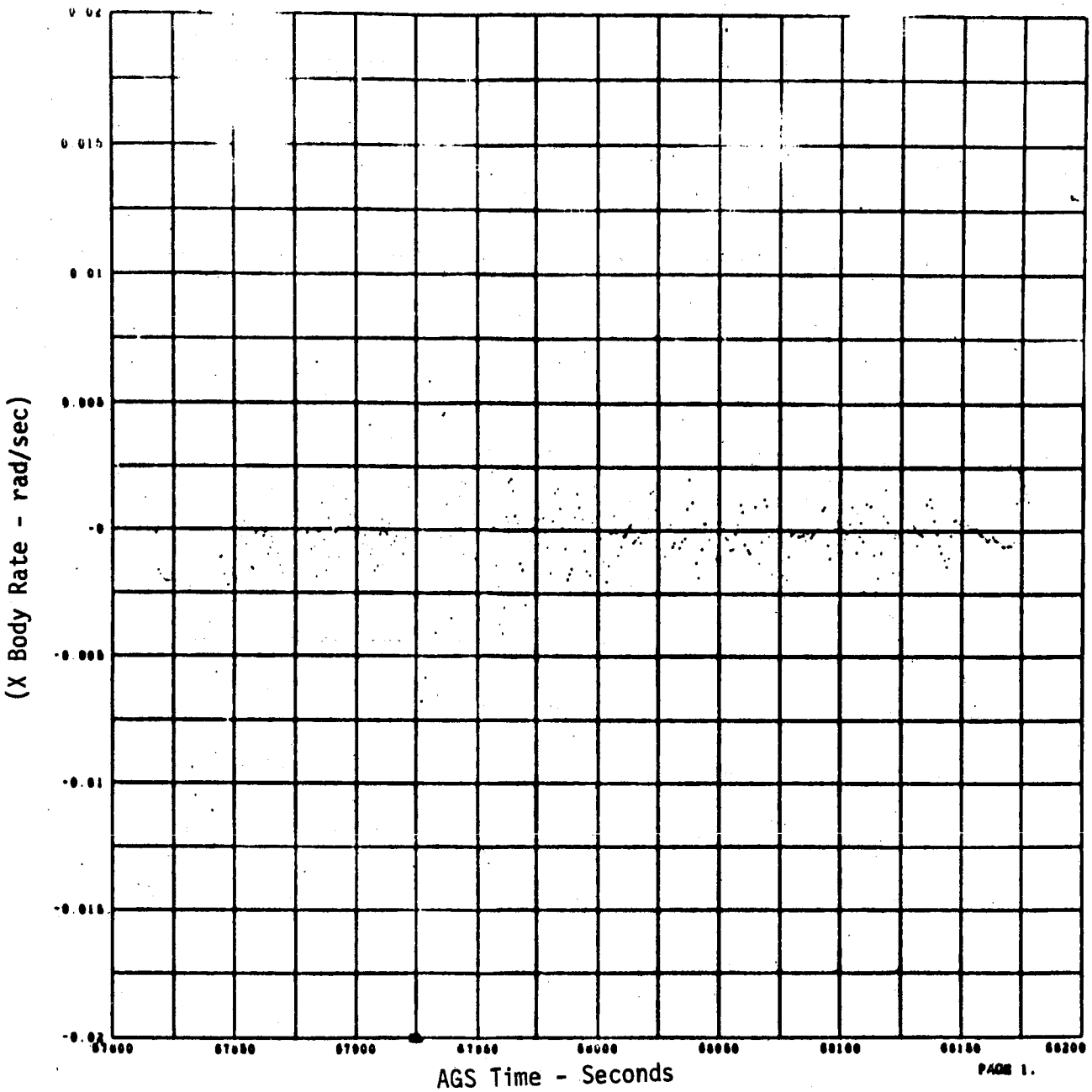

Figure 6-6 X BODY RATE - APS BURN TO DEPLETION

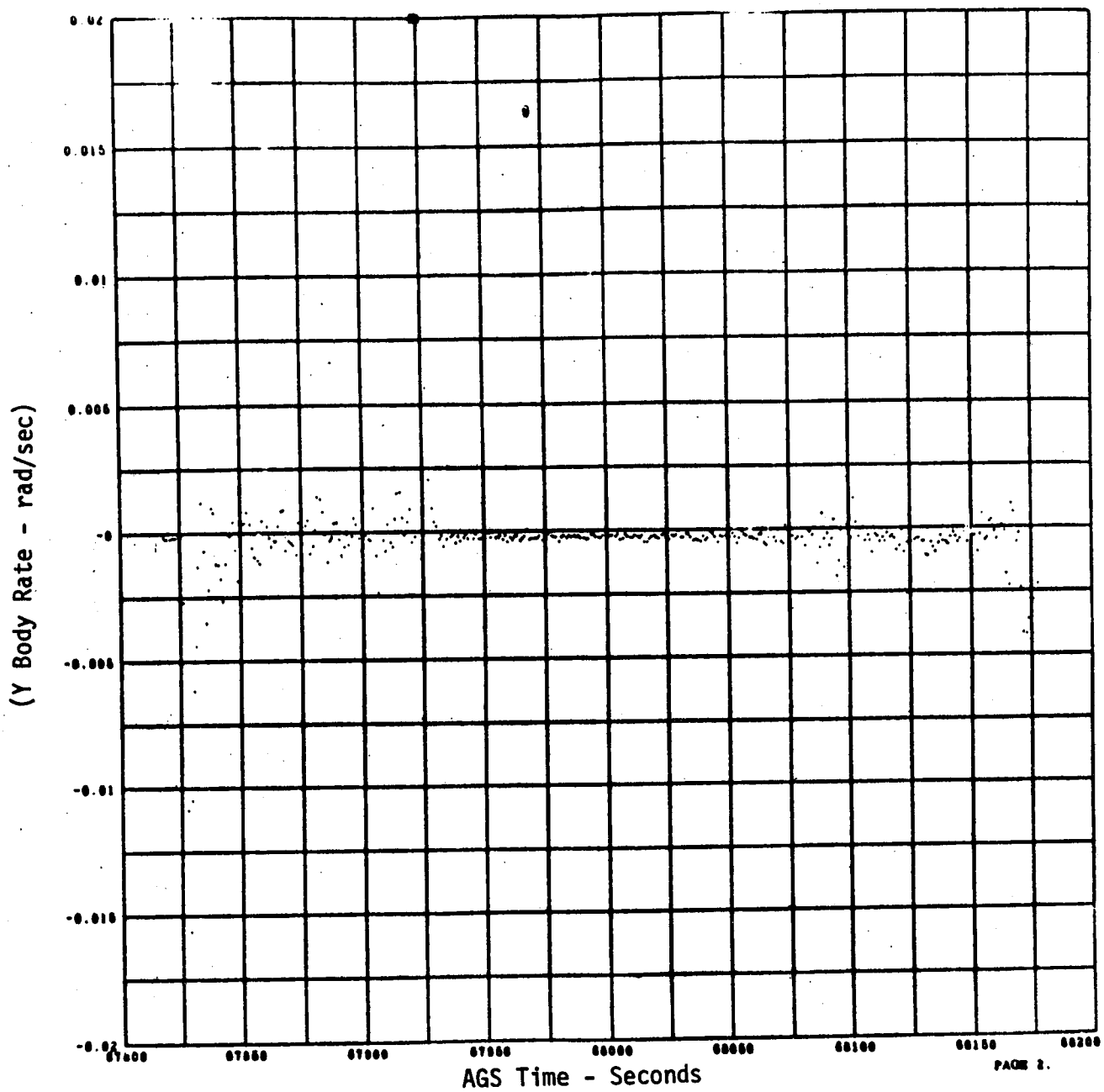

Figure 6-7 Y BODY RATE - APS BURN TO DEPLETION

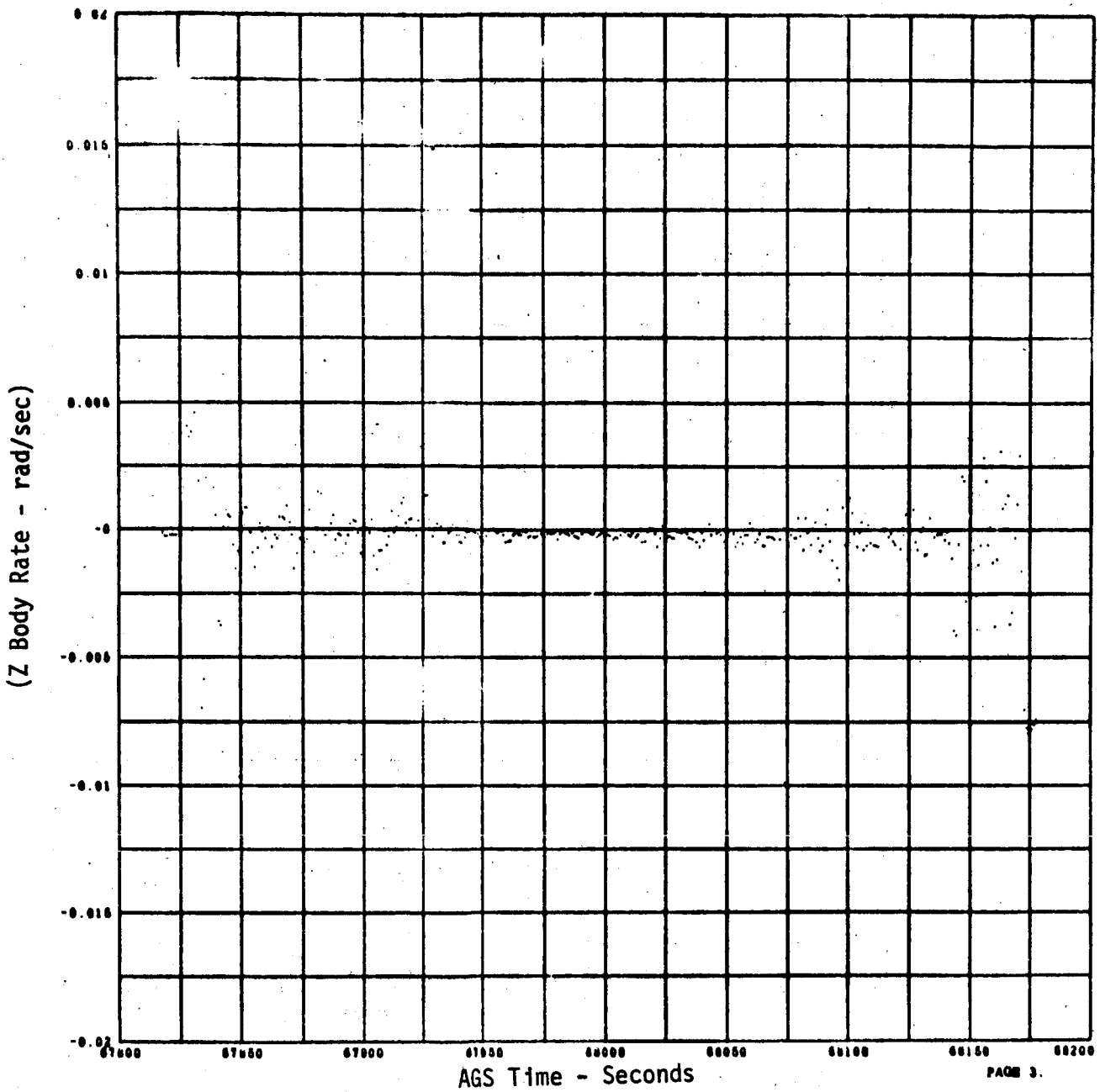

Figure 6-8 Z BODY RATE - APS BURN TO DEPLETION

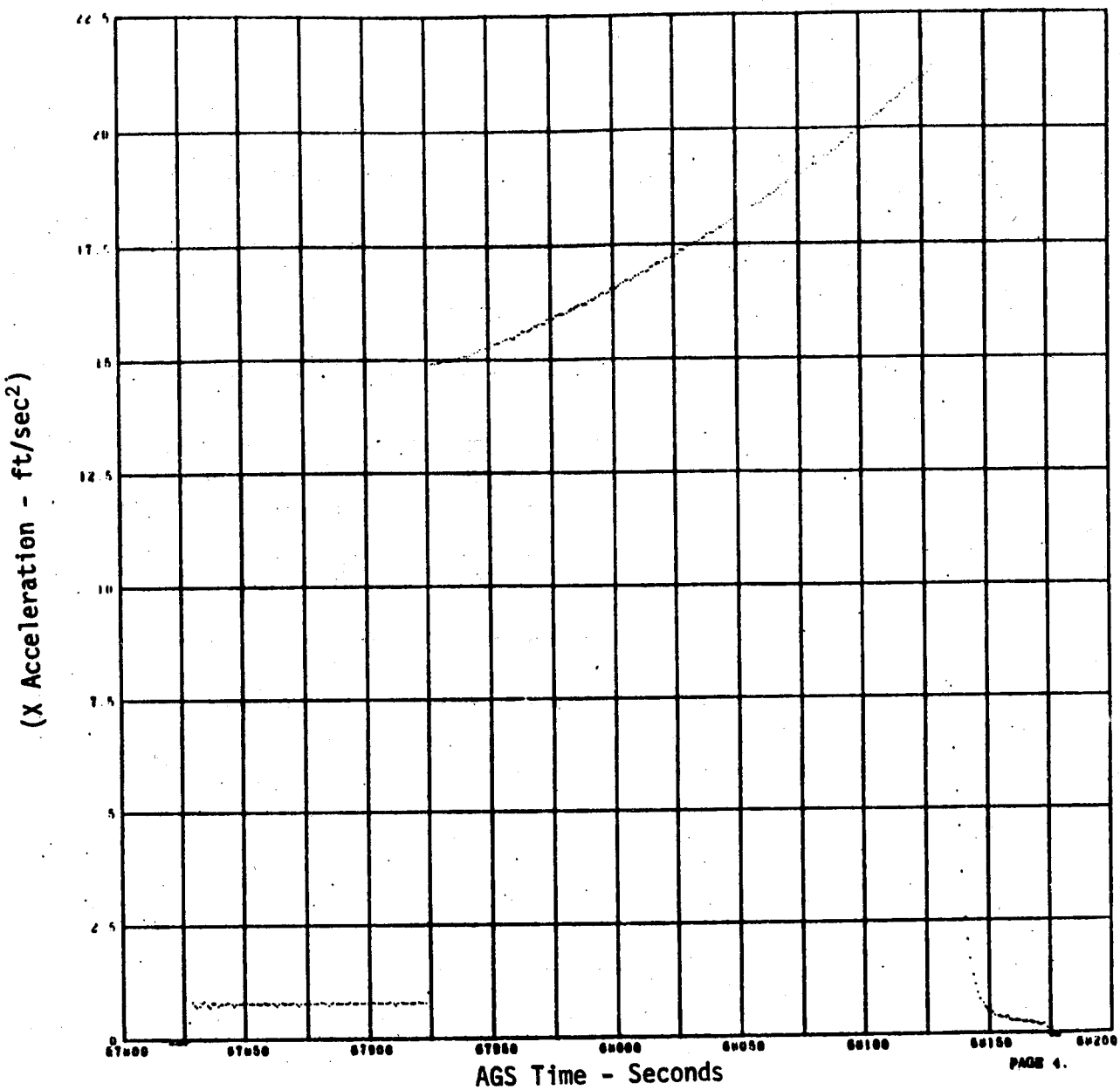

Figure 6-9 X AXIS SENSED ACCELERATION - APS BURN TO DEPLETION

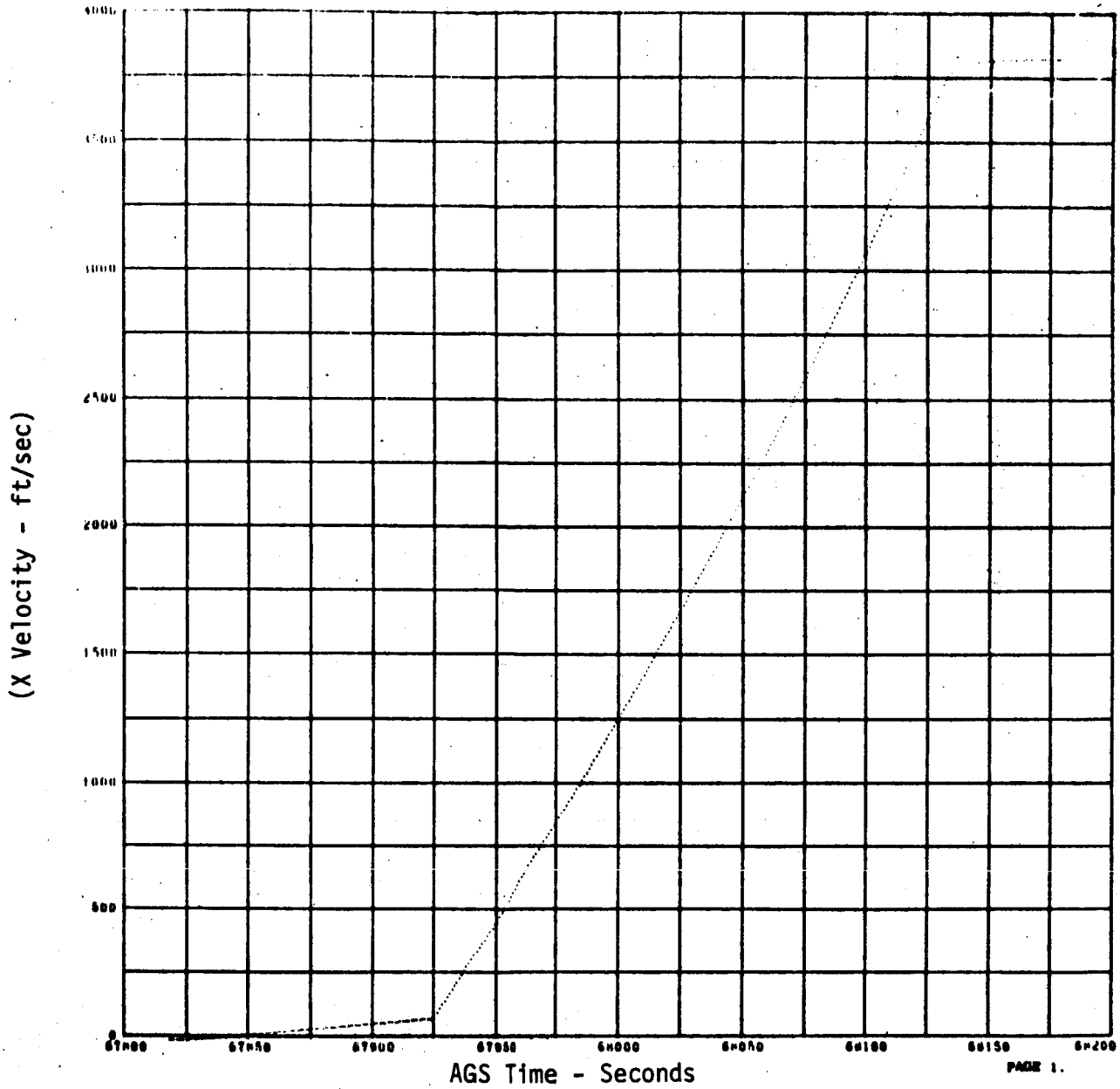

Figure 6-10 X AXIS SENSED VELOCITY - APS BURN TO DEPLETION

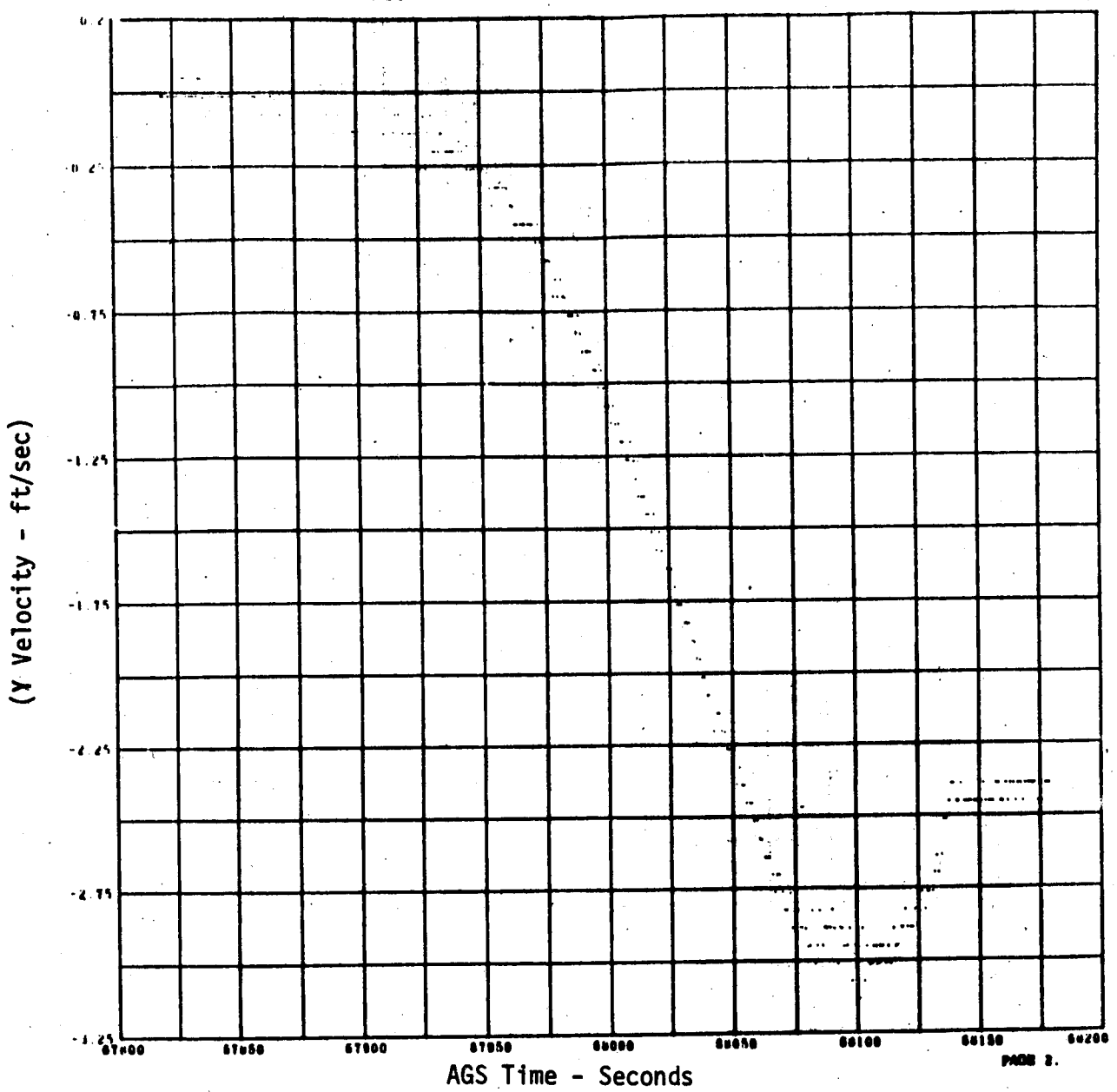

Figure 6-11 Y AXIS SENSED VELOCITY - APS BURN TO DEPLETION

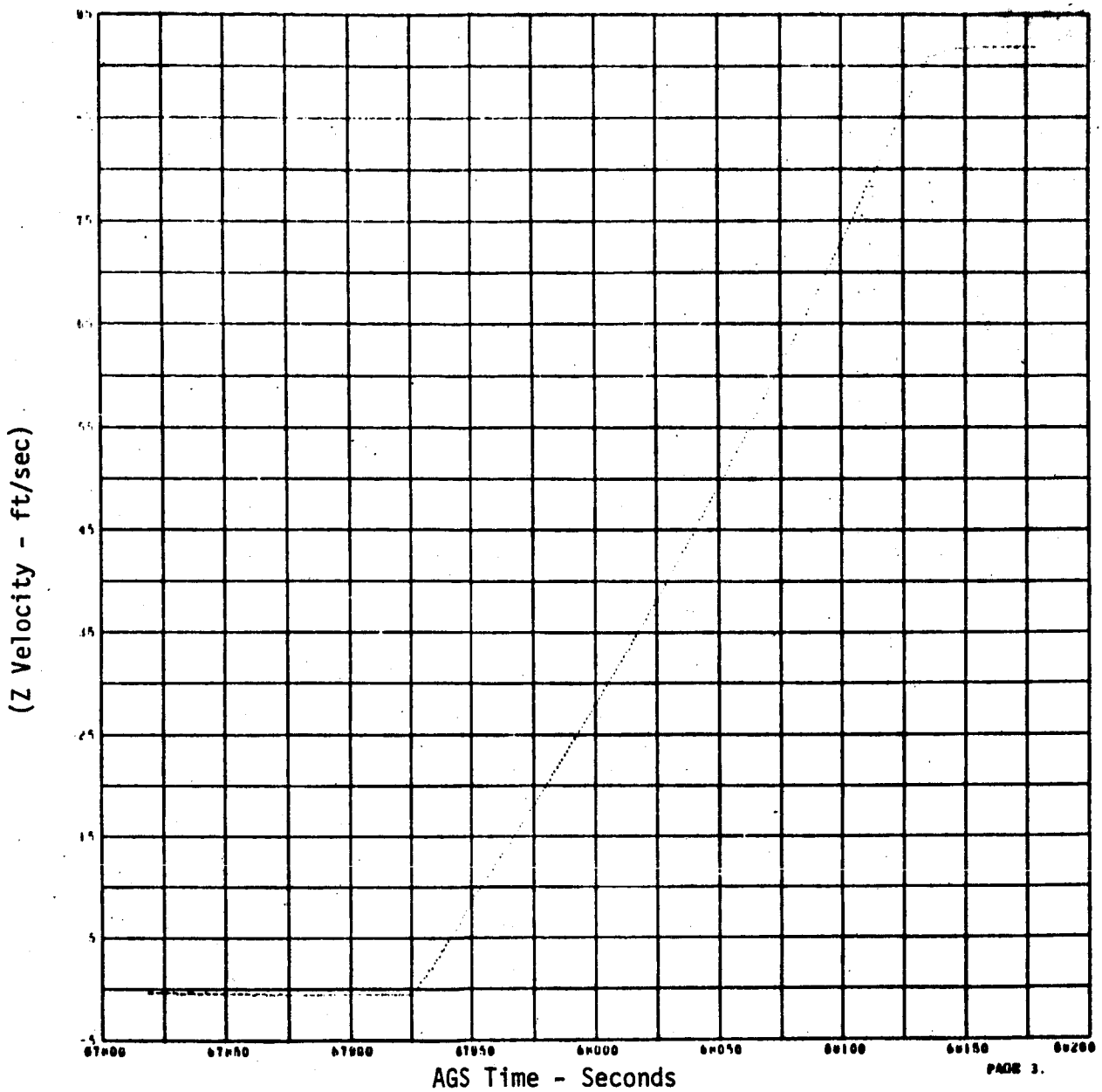

Figure 6-12 Z AXIS SENSED VELOCITY - APS BURN TO DEPLETION

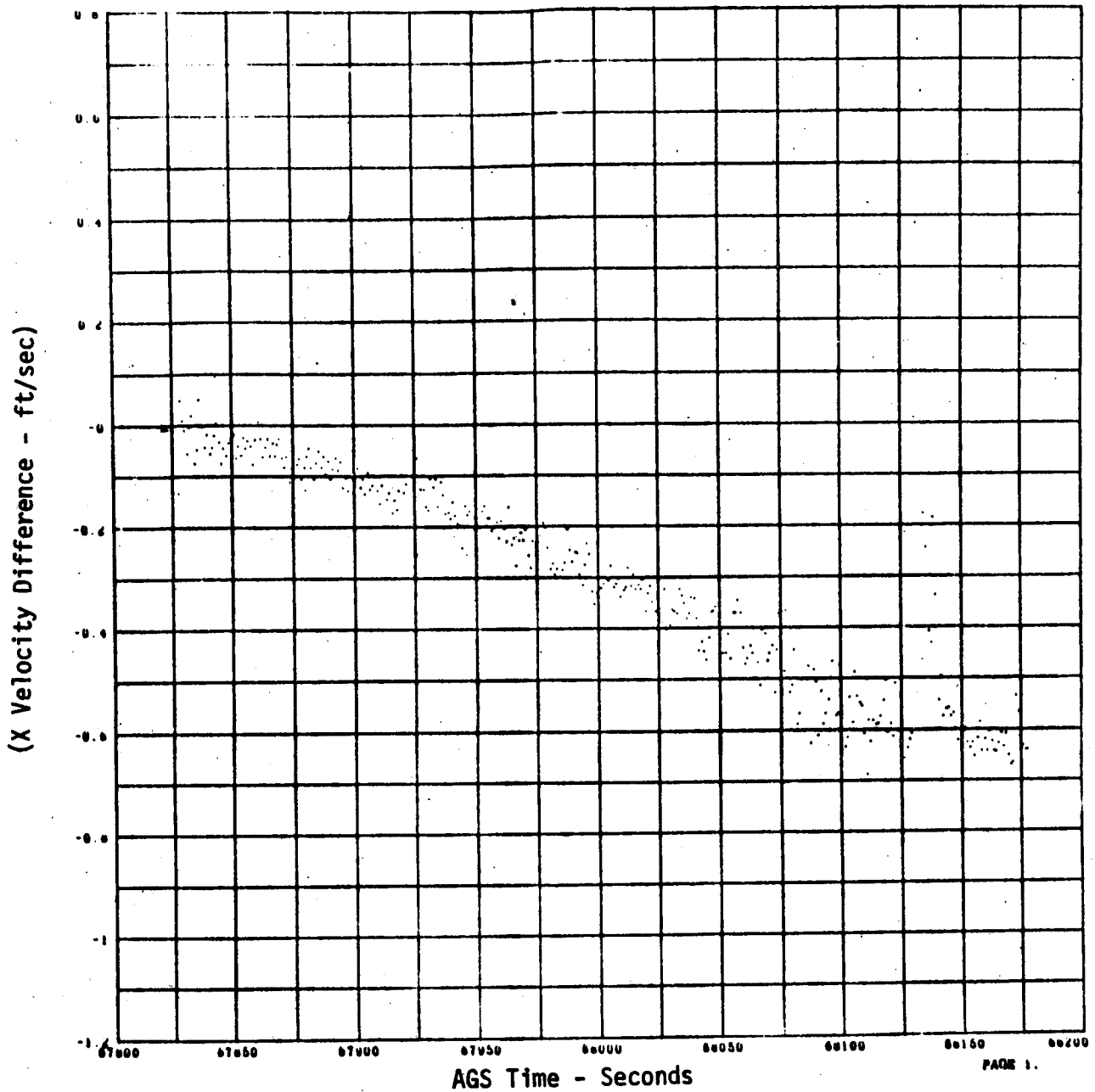

Figure 6-13 UNCOMPENSATED SENSED X-AXIS VELOCITY DIFFERENCE; PGNCS GIMBAL ANGLES USED FOR TRANSFORM - APS BURN TO DEPLETION

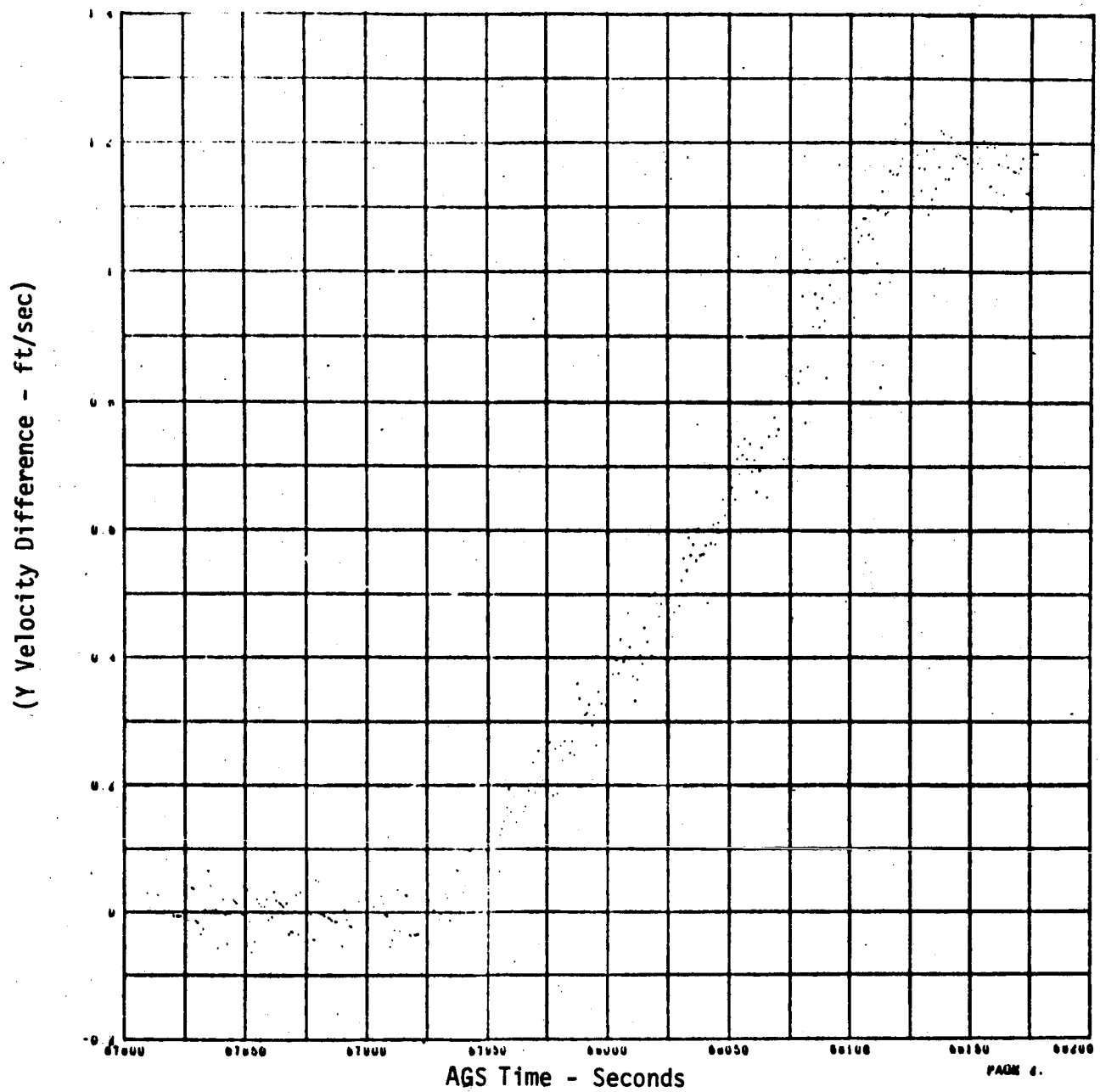

Figure 6-14 UNCOMPENSATED SENSED Y-AXIS VELOCITY DIFFERENCE; PGNCS GIMBAL ANGLES USED FOR TRANSFORM - APS BURN TO DEPLETION

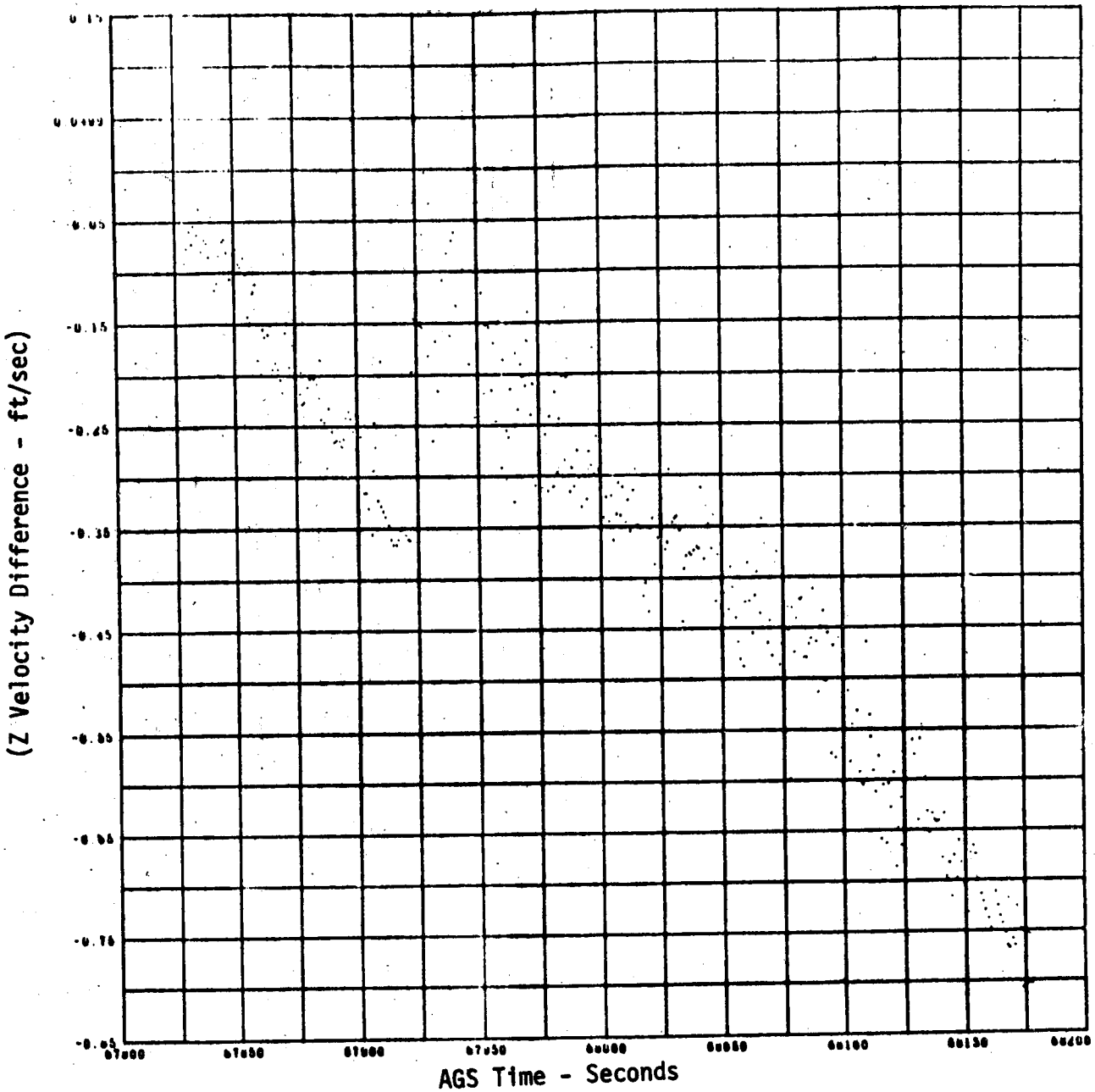

Figure 6-15 UNCOMPENSATED SENSED Z-AXIS VELOCITY DIFFERENCE; PGNCS GIMBAL ANGLES USED FOR TRANSFORM - APS BURN TO DEPLETION

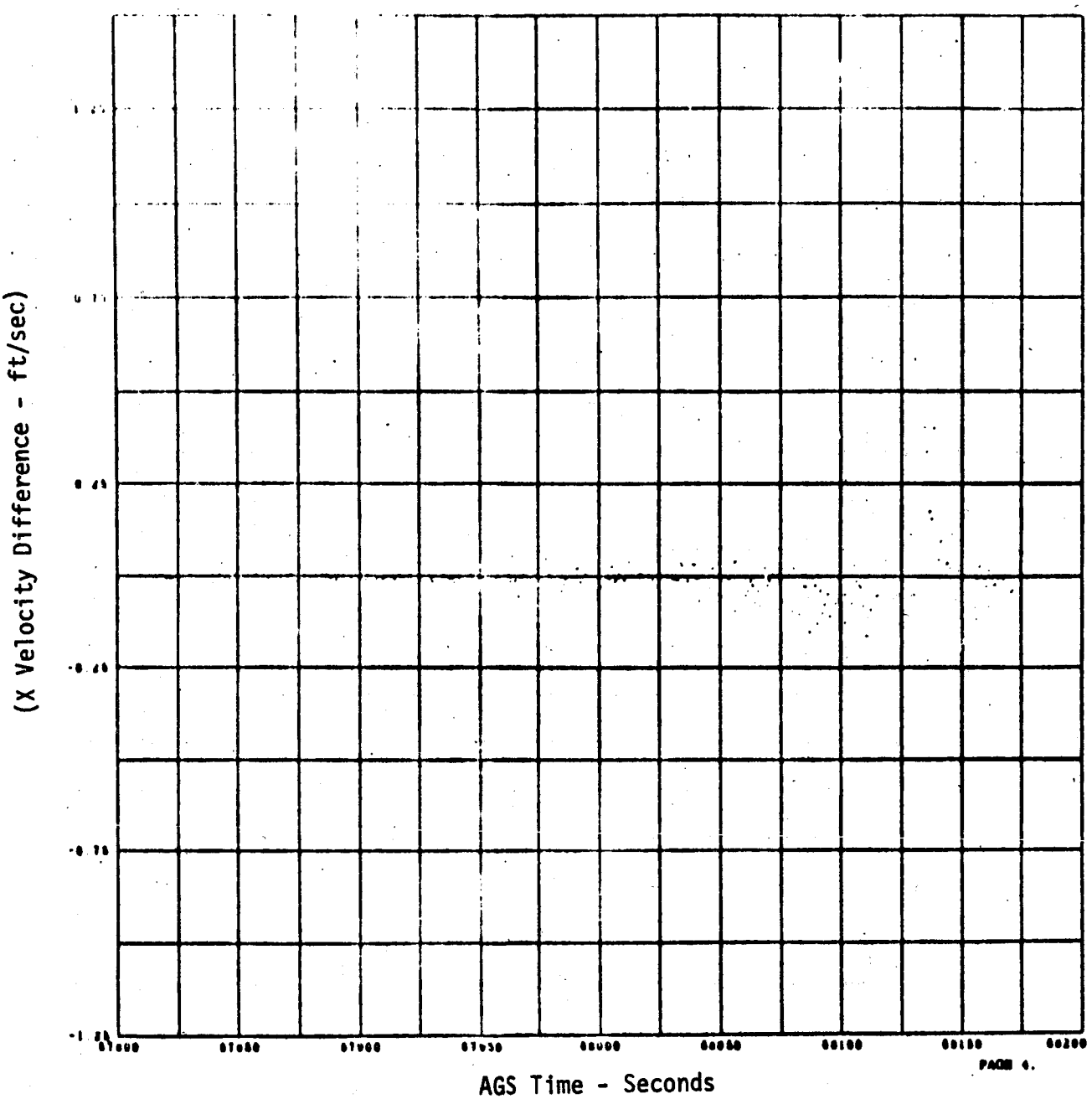

Figure 6-16 COMPENSATED SENSED X-AXIS VELOCITY DIFFERENCE; PGNCS GIMBAL ANGLES USED FOR TRANSFORM - APS BURN TO DEPLETION

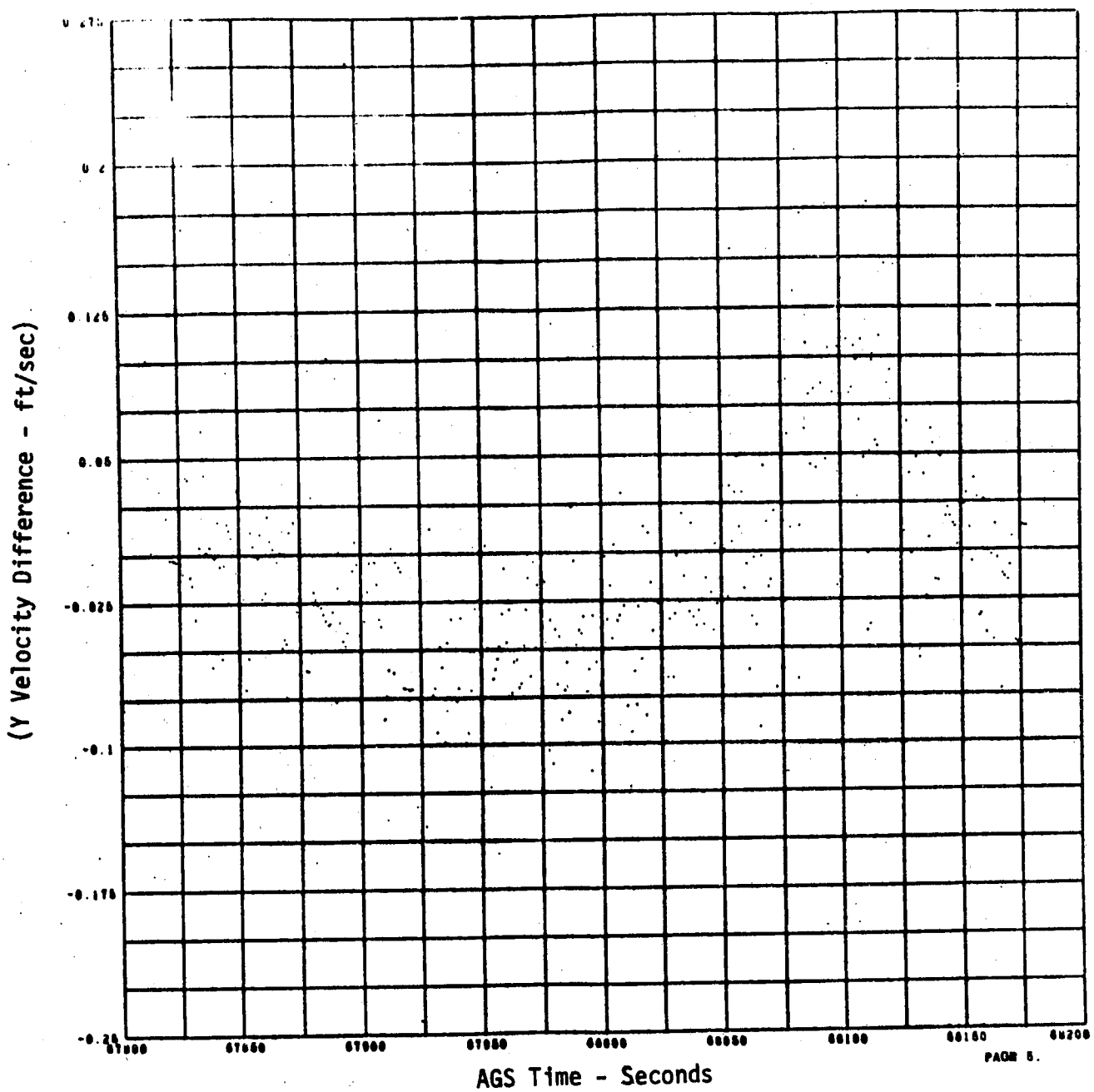

Figure 6-17 COMPENSATED SENSED Y-AXIS VELOCITY DIFFERENCE; PGNCS GIMBAL ANGLES USED FOR TRANSFORM - APS BURN TO DEPLETION

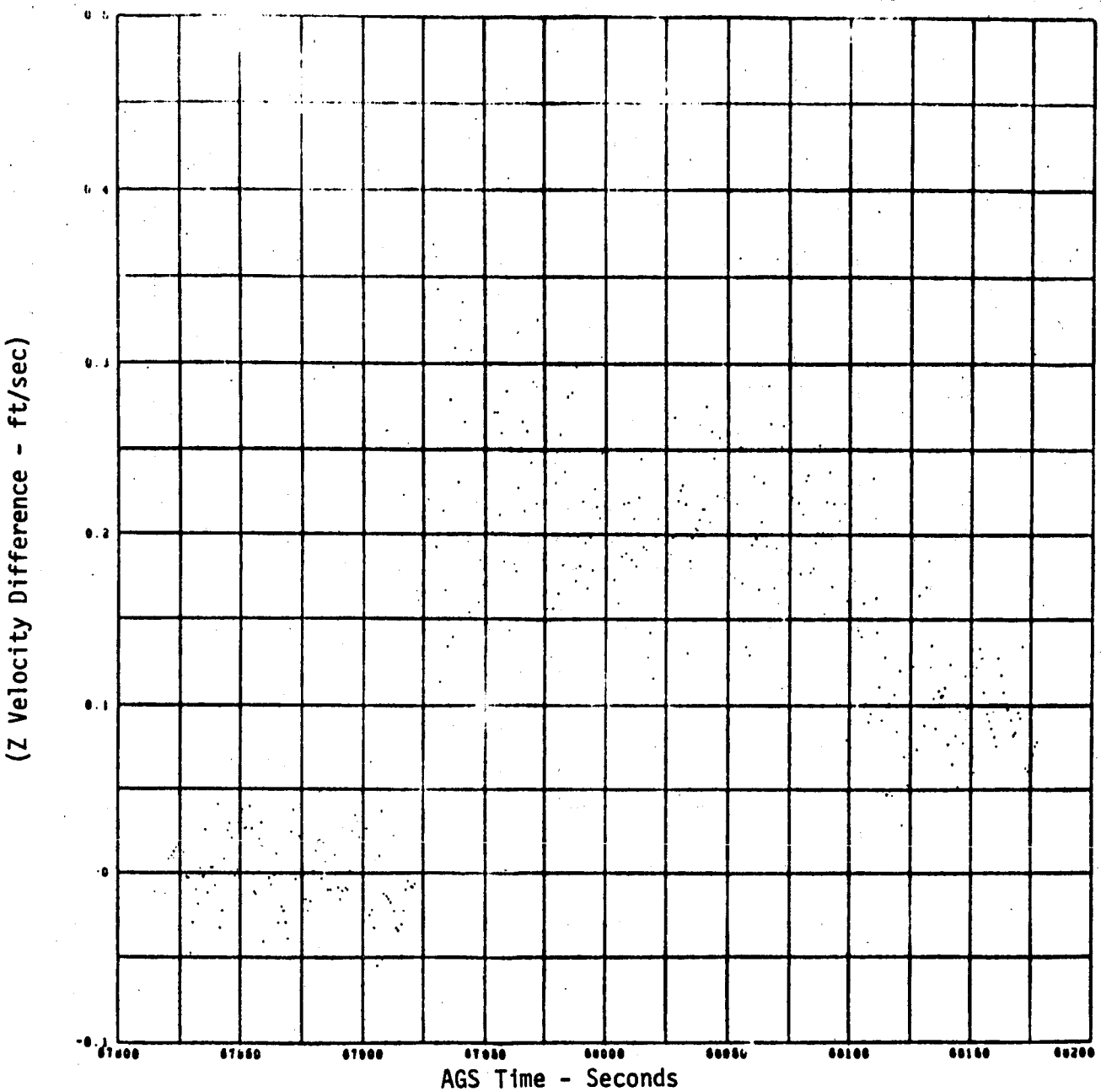

Figure 6-18 COMPENSATED SENSED Z-AXIS VELOCITY DIFFERENCE; PGNCS GIMBAL ANGLES USED FOR TRANSFORM - APS BURN TO DEPLETION

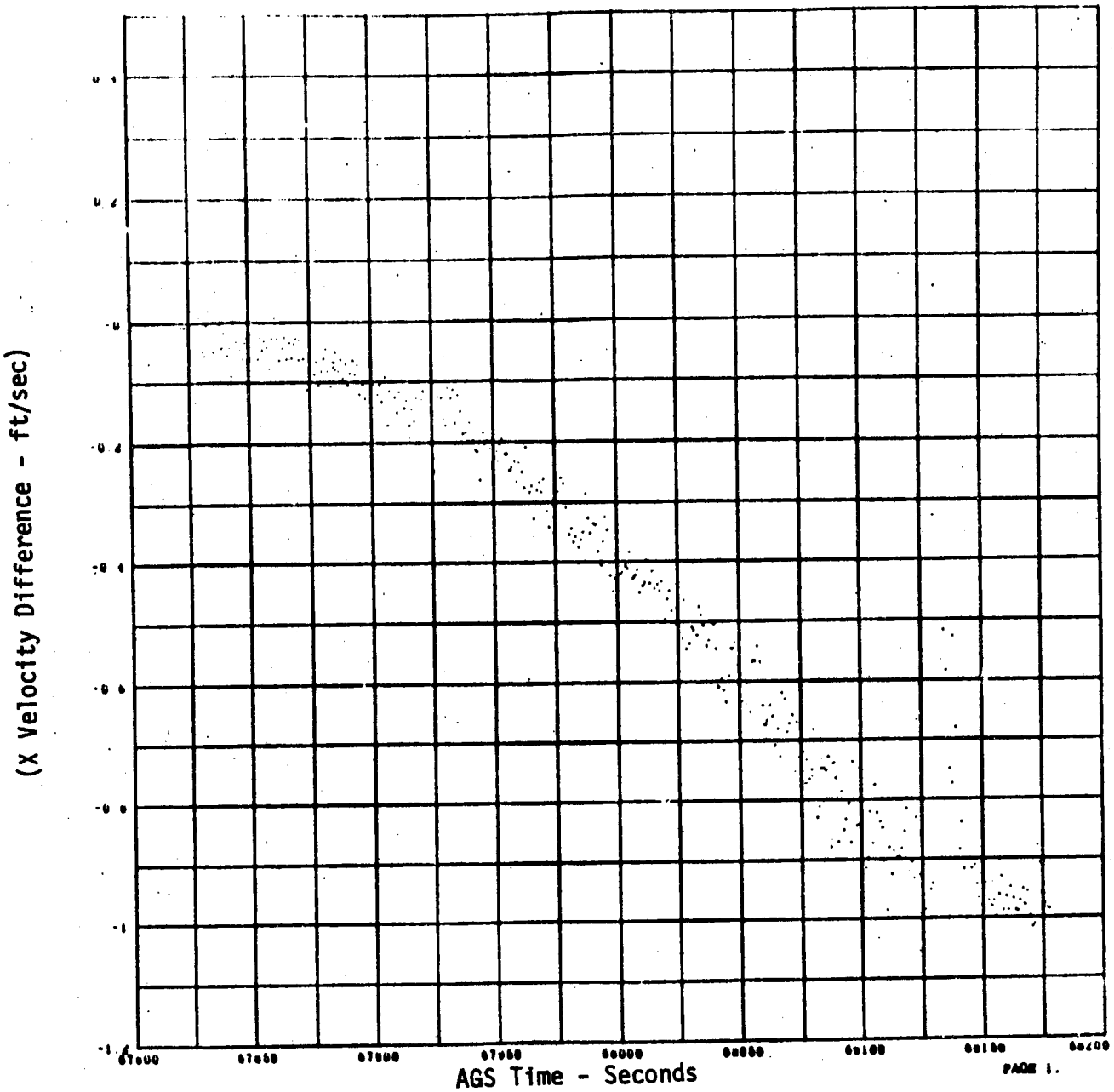

Figure 6-19 UNCOMPENSATED SENSED X-AXIS VELOCITY DIFFERENCE; AGS DIRECTION COSINES USED FOR TRANSFORM - APS BURN TO DEPLETION

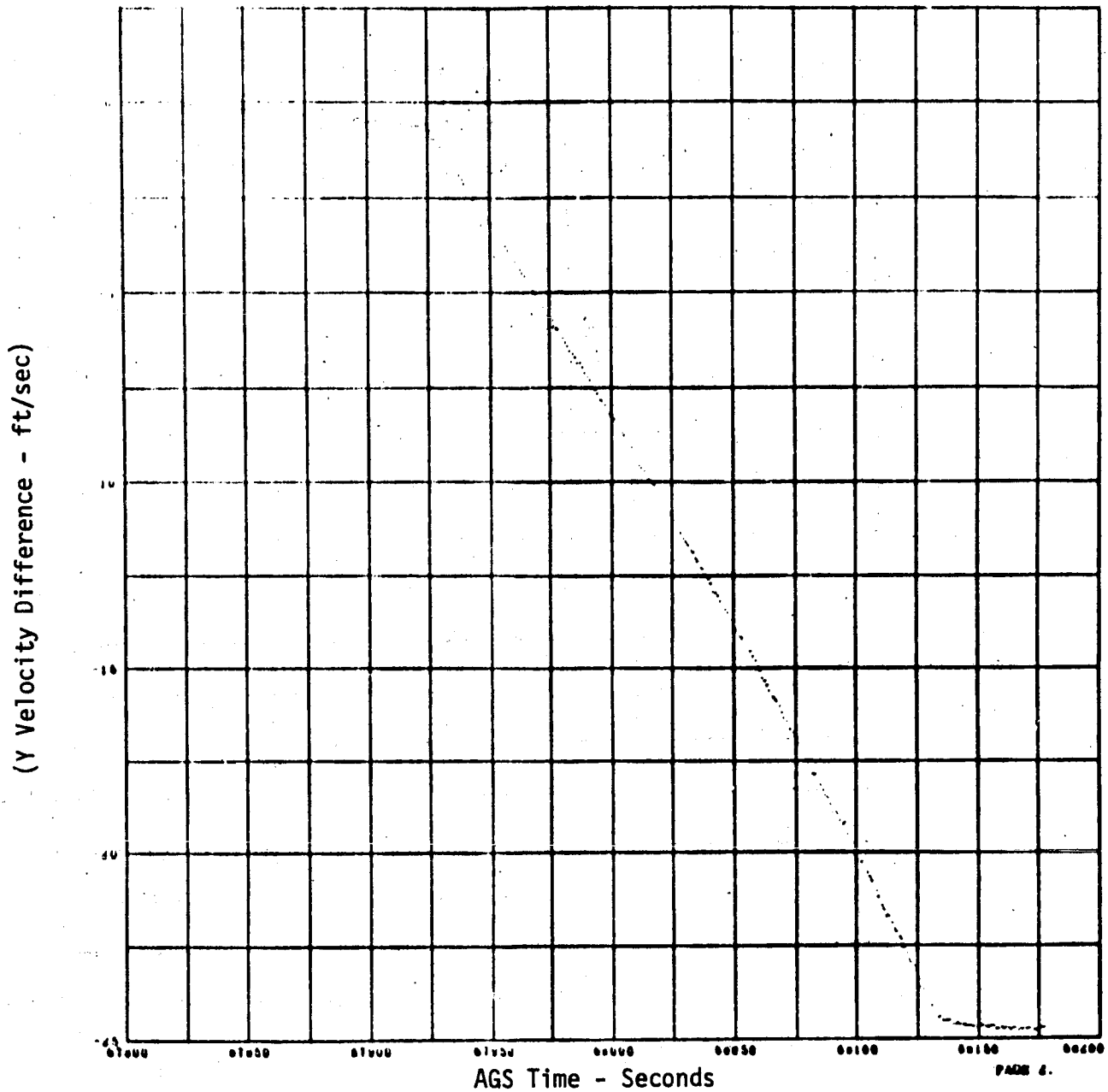

Figure 6-20 UNCOMPENSATED SENSED Y-AXIS VELOCITY DIFFERENCE; AGS DIRECTION COSINES USED FOR TRANSFORM - APS BURN TO DEPLETION

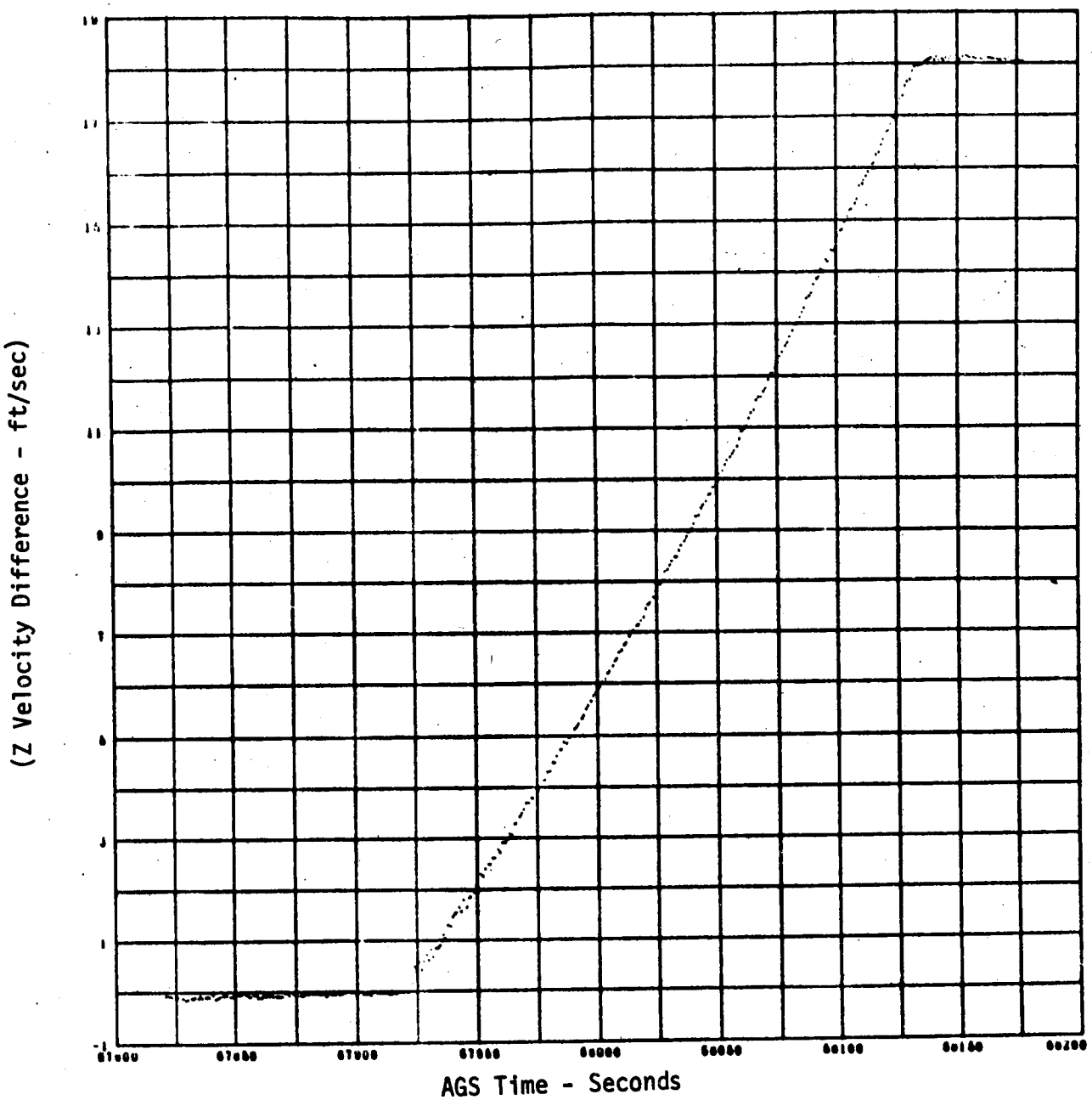

Figure 6-21 - UNCOMPENSATED SENSED Z-AXIS VELOCITY DIFFERENCE; AGS DIRECTION COSINES USED FOR TRANSFORM - APS BURN TO DEPLETION

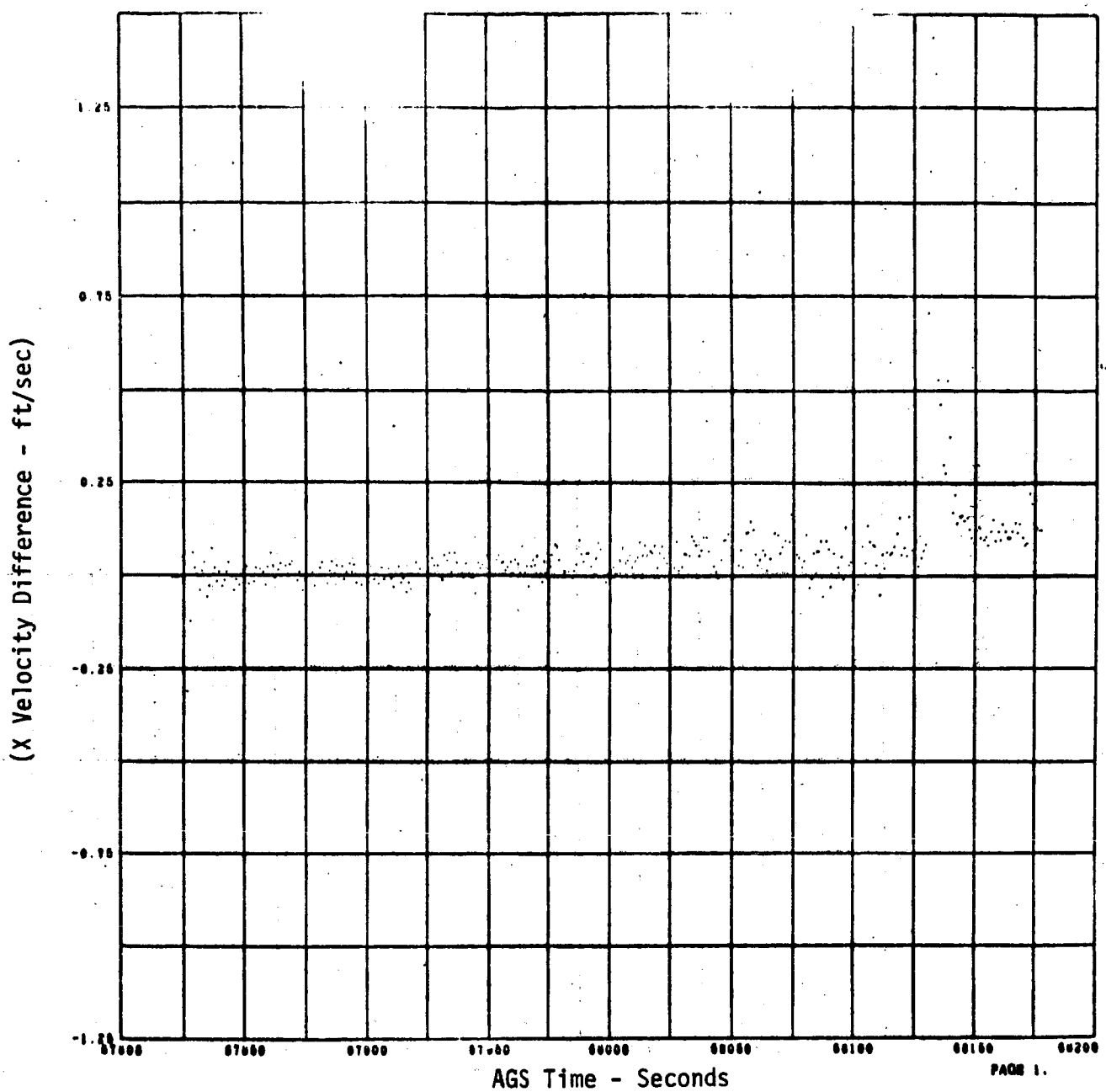

Figure 6-22 COMPENSATED SENSED X-AXIS VELOCITY DIFFERENCE; AGS DIRECTION COSINES USED FOR TRANSFORM - APS BURN TO DEPLETION

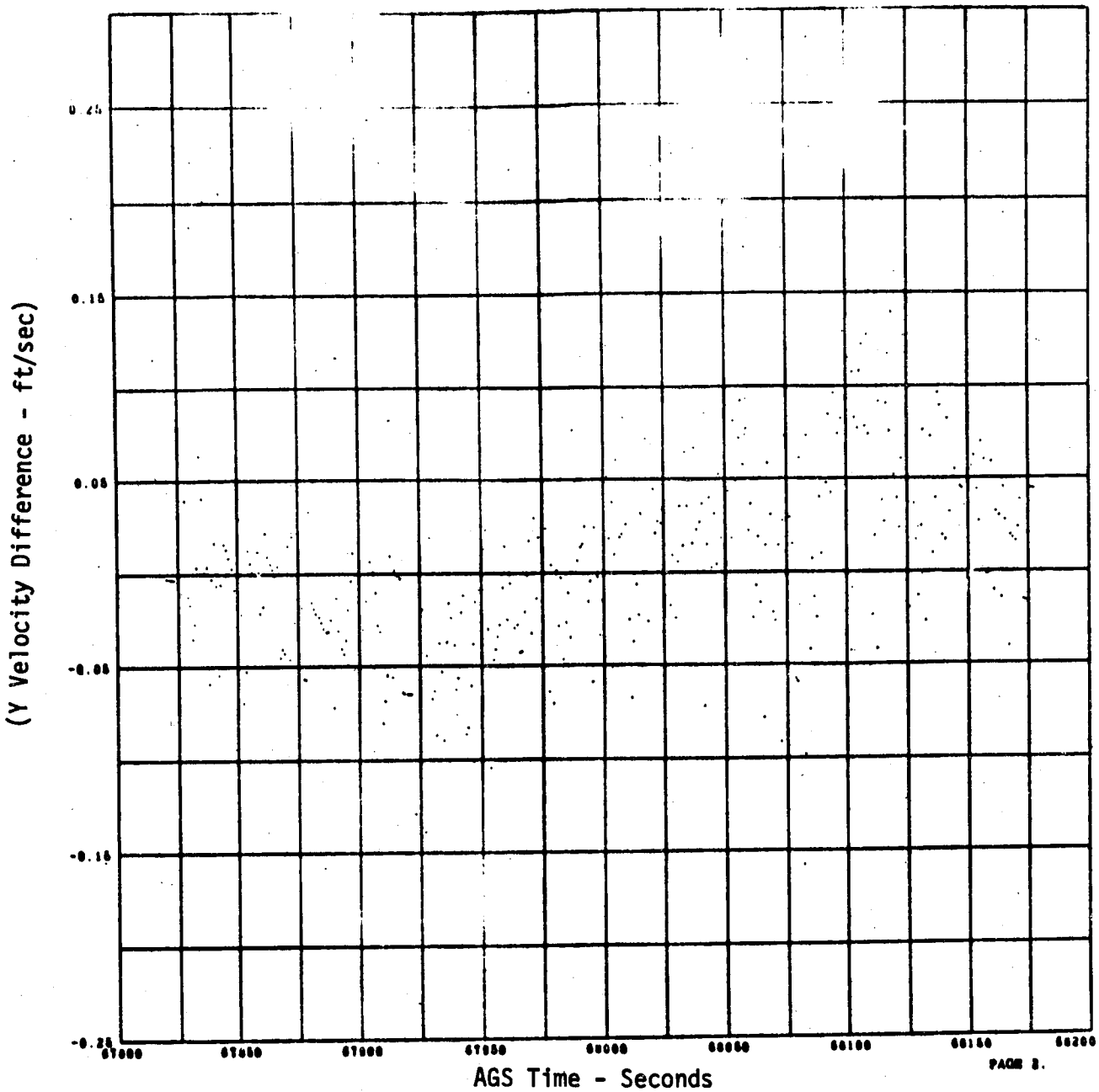

Figure 6-23 COMPENSATED SENSED Y-AXIS VELOCITY DIFFERENCE; AGS DIRECTION COSINES USED FOR TRANSFORM - APS BURN TO DEPLETION

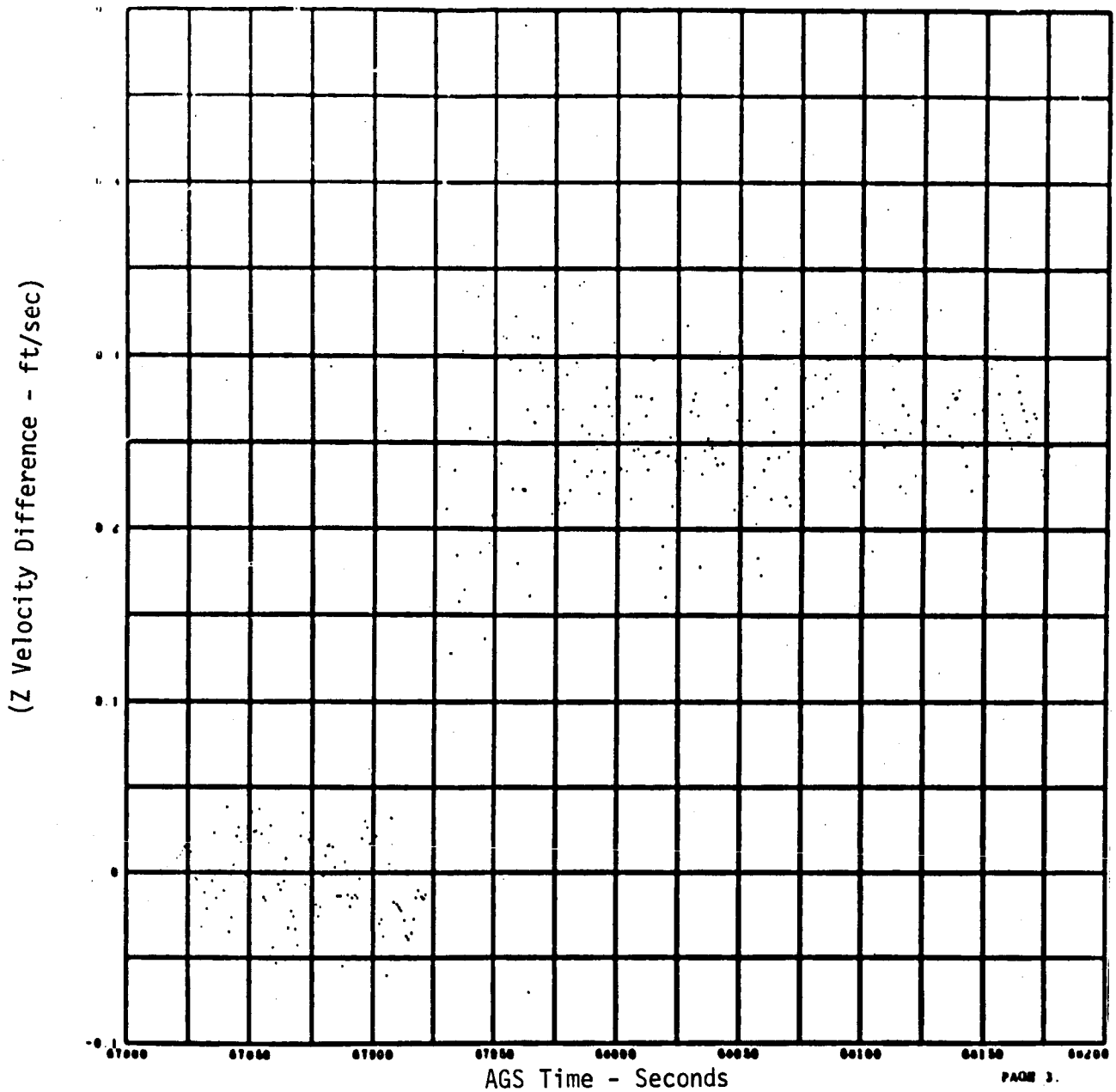

Figure 6-24 COMPENSATED SENSED Z-AXIS VELOCITY DIFFERENCE; AGS DIRECTION COSINES USED FOR TRANSFORM - APS BURN TO DEPLETION

7.0 OPTICS NAVIGATION SIGHTINGS

7.1 STAR-HORIZON SXT SIGHTINGS

The star-horizon navigation data for Apollo 10 consisted of six batches or groups of sightings. The data were processed with the HOPE program. The results are summarized below for trunnion bias, standard deviation and horizon bias by batch number. Each batch consists of sightings taken on three different stars and using both near and far horizon.

Batch	Trunnion Bias (deg)	Sigma (deg)	Horizon Bias (K_m)
1	- .005	.004	33.4
2	- .005	.002	18.7
3	+ .004	.002	21.4
4	- .002	.002	23.6
5	- .003	.004	7.9
6	- .005	.003	14.5

The results for trunnion bias and standard deviation are comparable with previous flights, but the wide variation in horizon bias is peculiar to Apollo 10. An effort was made to ascribe this variation to the latitude of the sub-stellar tangent point and/or the angle between the lines-of-sight and the sun direction. The conclusion is that there is no obvious correlation between the horizon bias variation and either of the above.

TRW program HOPE was used to determine the computed tangent point for each sighting and from this point the latitude was determined. The results indicate that the horizon bias altitude variation is not a simple function of latitude of the point of tangency of the line-of-sight.

The second approach was to calculate the sun line relative to each SXT LOS. Using the downlinked computer words, REFSMMAT, CDU angles and shaft and trunnion angles, the landmark and star lines-of-sight were computed in body coordinates. An ephemeris tape plus computer values for vehicle position were used to compute the sun direction in the same coordinates. The angle between the sun direction and each line-of-sight was then computed. The results are contained in Table 7-1. Batch 3 was not processed because of a tape problem. The individual horizon biases were determined by computing the trunnion bias for each batch of sightings, then using the computed value of trunnion bias to determine the horizon bias for each star within that batch. In every case the horizon bias was determined from three or more measurements.

Based on the two studies above, there is no obvious correlation between the horizon bias variation and latitude of the substellar point or sun direction. No explanation presently exists for the large variations in horizon bias.

A detailed evaluation of Apollo 10 midcourse navigation using star-horizon sightings will be reported separately.

7.2 LANDMARK TRACKING

Landmark tracking data from Apollo 10 were used in an effort to evaluate the optical subsystem accuracy. No conclusions concerning the performance of the optical system were drawn for the following reason:

The trunnion/shaft biases and standard deviations were very large as compared to previous flight results. A direct comparison was made between landmark tracking and star-horizon navigation for trunnion bias and standard deviation, with the former much larger. An attempt was made to isolate an error source which would consistently account for the difference. The error sources considered were landmark location, state vectors (in part and in whole), clock bias (or essentially position along the pre-determined orbit) and initial state vector error. Failure to effectively reduce the residuals lead to the conclusion that some

other unmodeled error source such as observer error was predominant and that any attempt to evaluate the optical subsystem accuracy from the landmark tracking data would be misleading.

A detailed evaluation of Apollo 10 orbital navigation using landmark tracking observations will be reported separately.

Table 7-1 SXT LINES-OF-SIGHT RELATIVE TO SUN LINE

Star*	Line-Of-Sight to Sun Angles LMK LOS	Star LOS	Horizon Bias	Trunnion Bias	Batch Number
02 N(3)	87°	63°	74,000 ft	-.002°	4
02 N(4)	85°	63°	29,000 ft	-.003°	5
02 N(4)	84°	63°	57,000 ft	-.005°	6
27 F(6)	143°	173°	108,000 ft	-.005°	1
31 N(3)	145°	140°	125,000 ft	-.005°	1
31 F(9)	127°	142°	45,000 ft	-.005°	2
30 N(6)	145°	121°	103,000 ft	-.005°	1
36 N(3)	127°	92°	48,000 ft	-.005°	2
36 F(3)	87°	92°	71,000 ft	-.002°	4
36 F(3)	85°	92°	5,000 ft	-.003°	5
36 F(3)	85°	92°	57,000 ft	-.005°	6
37 N(3)	127°	90°	21,000 ft	-.005°	2
37 F(3)	87°	90°	80,000 ft	-.002°	4
37 F(3)	86°	90°	41,000 ft	-.003°	5
37 F)3)	84°	90°	29,000 ft	-.005°	6

* N - Near Horizon
F - Far Horizon
(a)- Number of marks used to determine horizon bias.

8.0 RENDEZVOUS NAVIGATION

8.1 ONBOARD NAVIGATION

Rendezvous navigation performance was satisfactory based on the near nominal rendezvous burn solutions and pilot reports on the minimal amount of corrective thrusting required during the final intercept trajectory. All of the LM executed solutions were solved for by the LGC based solely on rendezvous radar data to correct for any trajectory dispersions as the result of orbit integration and ISS errors. Figure 8-1 presents a comparison of RR range data and and CSM VHF ranging data for intermittent periods between phasing and TPI. The close agreement in these two completely independent measurement systems lends evidence to the validity of both data. Also presented on the same figure is the BET range estimate during the rendezvous period. Figure 8-2 shows the RR range rate data and the BET range rate estimates. Satisfactory incorporation of these data into the respective computers is deduced based on the data presented in Figure 8-3. The relative position and velocity vectors (CSM-LM) were derived based on the current state vectors in the two computers during the rendezvous period. The figure shows that the relative state vectors were being held in close agreement.

8.2 RENDEZVOUS TARGETING

Comparisons of all executed ΔV solutions during the rendezvous with the pre-mission nominal ΔV's are shown in Table 8-1. The total ΔV required to perform the LM maneuvers was within one percent (minus) of the nominal ΔV.

During the rendezvous sequence, various maneuver solutions were available to the LM crew. Table 8-2 presents the available rendezvous targeting solutions. It should be noted that the out-of-plane velocity component ($\dot{Y}$) was calculated during CSI (P32) and CDH (P33), but was not used in the burn targeting. This accounts for the ΔVY component of -5.7 fps at TPI (would nominally be zero).

Table 8-1 RENDEZVOUS TARGETING SUMMARY

Maneuver	V Nominal *(ft/sec)	V Actual (ft/sec)	Solution Executed
CSM Separation	2.5	2.5	RTCC
DOI	71.1	71.3	RTCC
Phasing	195.4	176.9	RTCC
Insertion	207.0	220.9	RTCC
CSI	50.5	45.3	LGC
CDH	3.4	3.0	LGC
TPI	24.6	24.4	LGC
MCC 1	0	1.2	LGC
MCC 2	0	1.8	LGC
Braking	30.0	32.0	
TOTAL	584.5	579.3	

Percent Below Nominal = 0.89

*Apollo 10 Flight Plan, AS-505/CSM-106/LM-4 April 17, 1969

Table 8-2 RENDEZVOUS TARGETING SOLUTIONS

Maneuver \ Source	RTCC		CMC		LGC		AEA		CHARTS	
Separation	ΔVX = 0 ΔVY = 0 ΔVZ = 2.5	RSS 2.5								
DOI	ΔVX = -69.9 ΔVY = 0 ΔVZ = -13.8	71.3								
Phasing	ΔVX = +166.6 ΔVY = 0 ΔVZ = -59.4	RSS 176.9								
Insertion	ΔVX = -183.2 ΔVY = 0 ΔVZ = -123.5	RSS 220.9								
CSI	ΔVX = +45.3 ΔVY = 0 ΔVZ = 0	RSS 45.3	ΔVX = -46.9 ΔVY = 0 ΔVZ = 0	RSS 46.9	ΔVX = +45.3 ΔVY = 0 ΔVZ = 0	RSS 45.3				
CDH			ΔVX = -0.5 ΔVY = 0 ΔVZ = -2.9	RSS 2.9	ΔVX = 0.1 ΔVY = 0 ΔVZ = +3.0	RSS 3.0			ΔVX = 0.2 ΔVY = 0 ΔVZ = +1.2	RSS 1.2
TPI			ΔVX = -21.8 ΔVY = +4.5 ΔVZ = +10.4	RSS 24.6	ΔVX = +21.7 ΔVY = -5.7 ΔVZ = -9.6	RSS 24.4	Components Not Available	RSS 24.3	F25 D4	RSS 25.3
MCC #1			ΔVX = -0.7 ΔVY = -0.2 ΔVZ = -0.6	RSS 0.9	ΔVX = -0.8 ΔVY = -0.4 ΔVZ = +0.8	RSS 1.2			0 0	
MCC #2			ΔVX = +0.8 ΔVY = -1.7 ΔVZ = +3.0	RSS 3.5	ΔVX = +0.8 ΔVY = +1.4 ΔVZ = -0.8	RSS 1.8			0 0	
TPF					32.0					

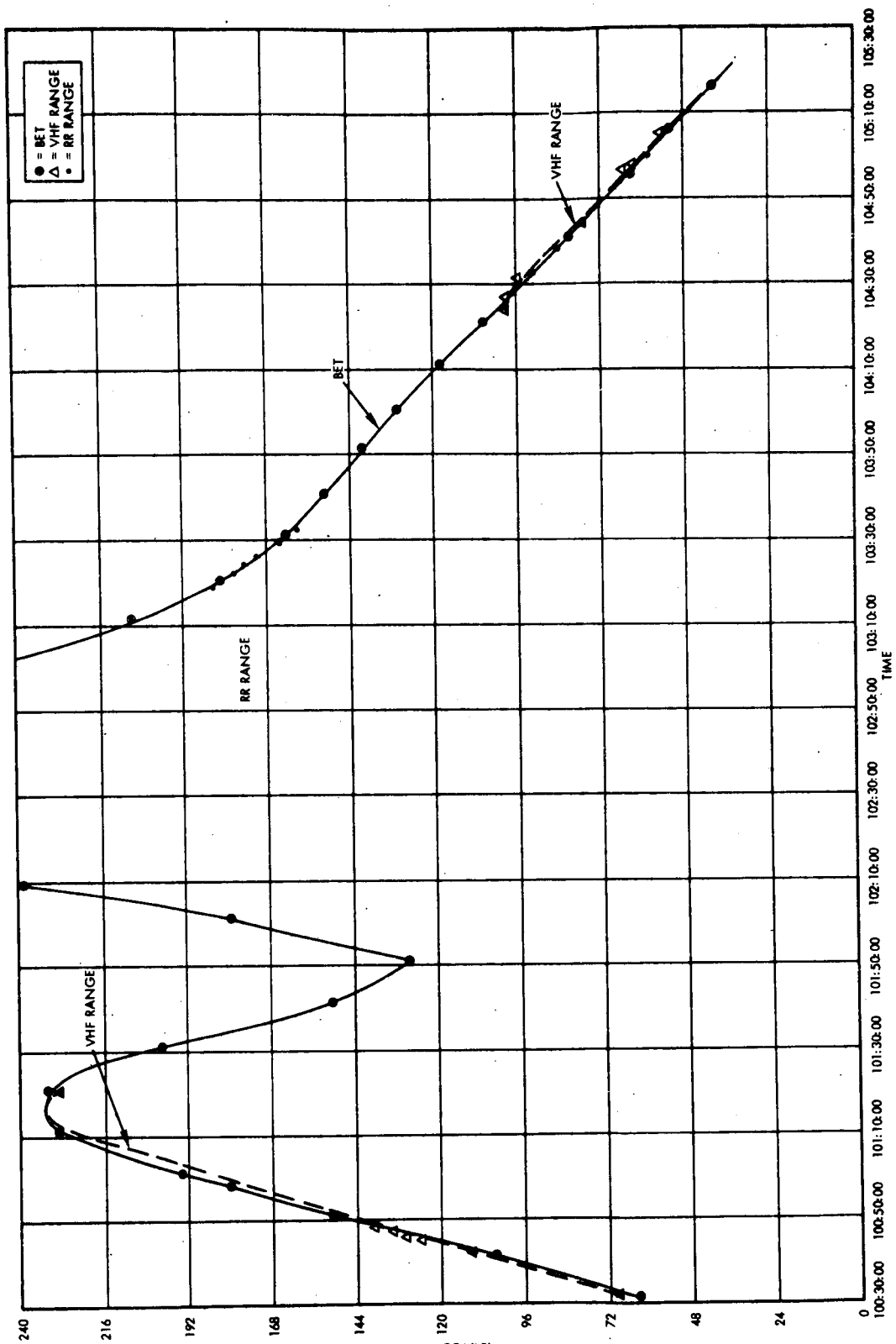

Figure 8-1 COMPARISON OF CSM VHF RANGE & LM RR RANGE WITH BET RANGE

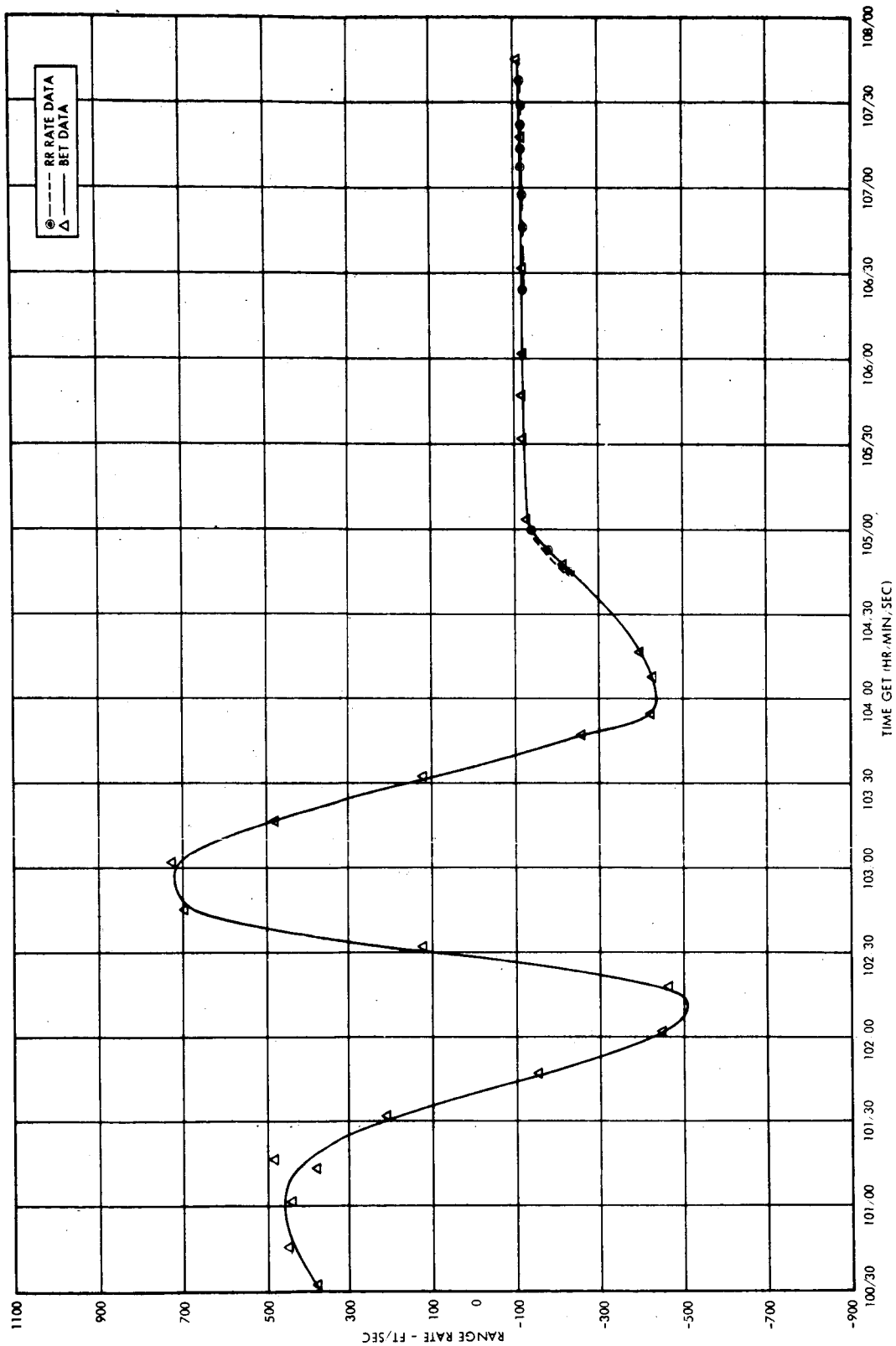

Figure 8-2 COMPARISON OF LM RANGE RATE WITH BET RANGE RATE

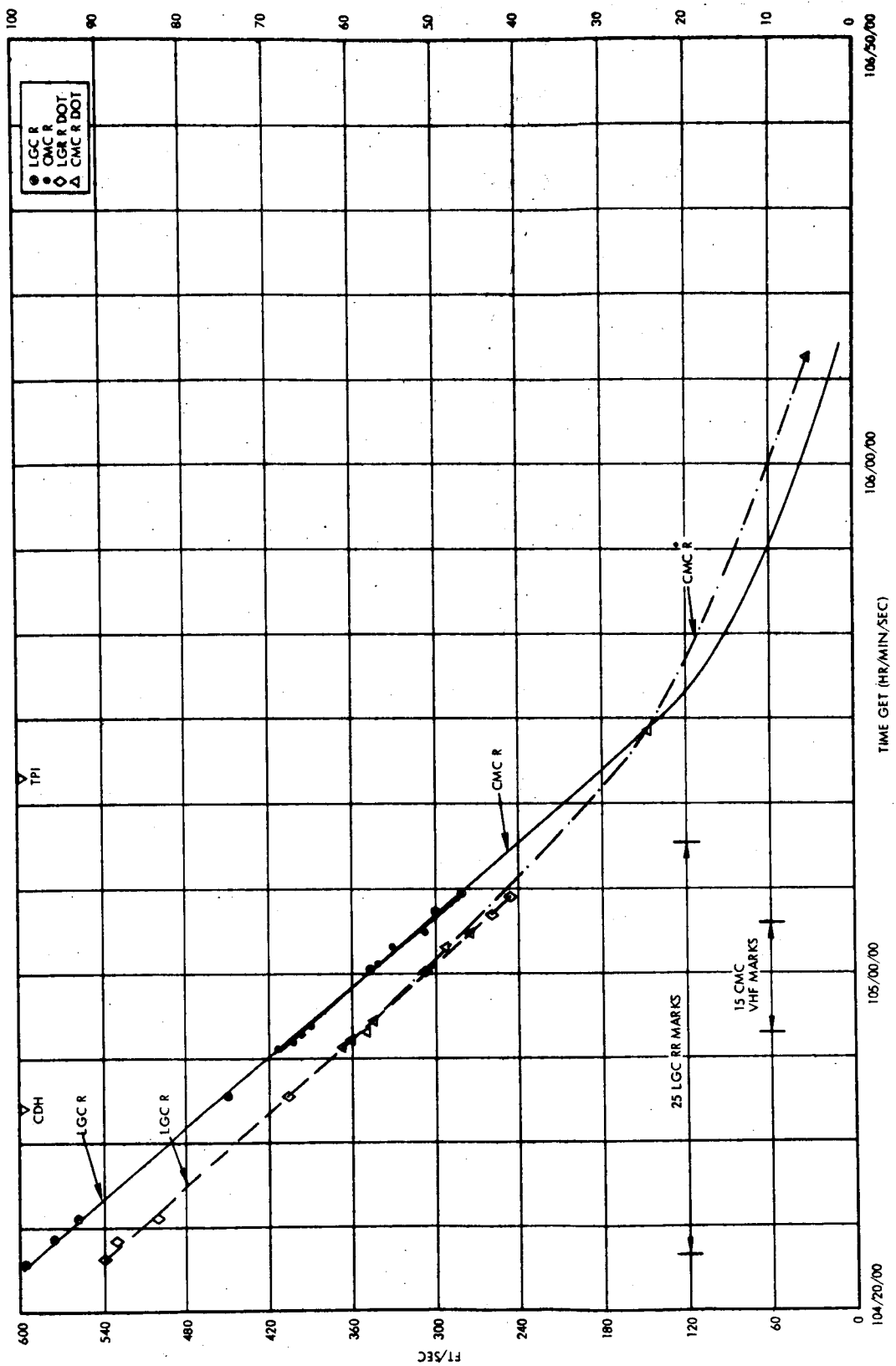

Figure 8-3 COMPARISON OF LGC & CMC RANGE & RANGE RATE DATA DURING RENDEZVOUS

9.0 LANDING RADAR VELOCITY AND ALTITUDE MEASUREMENTS

9.1 RESULTS

Based on data obtained during the first pass through perigee after the DOI burn, the LR was functioning properly and the measured altitude and velocities agreed favorably with BET and guidance trajectory data. Also, terrain features measured by the LR altitude beam agreed with the lunar terrain along the flight path as determined from lunar maps.

The landing radar data was available on the LM downlink from 100:32:22 GET to 100:50:34 GET. During this time, the radar antenna was in position 2. The data from 100:39:03 to 100:50:34 GET was not processed because of the intermittant data.[1] The landing radar measured velocity minus the G&N measured velocity are shown in Figures 9-1 to 9-3. The out-of-plane ΔV indicates a total misalignment of the LR antenna and the stable member of approximately 0.73 degrees. Total misalignments of this magnitude were expected on this mission. Figure 9-4 is a comparison of the computed landing radar altitude and the BET. The divergence is the result of the radar measuring the lunar surface below the mean lunar surface, as the radar gives an indication of the surface features and is not an approximation. Figure 9-5 is a plot of the lunar surface profile from 100:32:24 to 100:39:08 GET and 75.3 to 53.1 deg selenographic longitude.

9.2 DATA PROCESSING

The landing radar hardware for LM-4 was modified so that the individual frequency tracker outputs could be monitored rather than the composite velocity terms Vxa, Vya, and Vza; and the doppler compensation term was removed from the slant range measurement. To obtain the radar antenna velocities and slant range, the following equations were used:

---

[1] Problem was associated with the LM antenna position and ground track during perigee.

$$Vxa' = Vxa - 0.3715Vza \quad (1)$$

$$Vza' = -Vya - 3.7627Vxa \quad (2)$$

$$Vza' = Vza - 0.7153Vya \quad (3)$$

$$Rs' = 7.854Vxa - 2.087Vya + Rs \quad (4)$$

where Vxa, Vya, Vza and Rs are telemetry downlink words. These data and associated time, CDU angles and position components were processed using the TRW landing radar program to obtain the lunar surface profile. The general equations used were:

$$\vec{V}sm = \left[SMNB\right]^T \left[A\right] \vec{V}ant \quad (5)$$

$$Hmeas = Hslant \left[\vec{H} \text{ beam sm}\right] \cdot \text{Unit } \vec{R} \quad (6)$$

$$\vec{H} \text{ beam sm} = \left[SMNB\right]^T \left[A\right] \left[H\right] \text{beam ant} \quad (7)$$

$$H \text{ beam ant} = \begin{bmatrix} -\cos\xi \\ -\sin\xi \end{bmatrix} \quad (8)$$

$$Rm - Rm\,(anwg) - Hmeas = \text{Lunar Surface Above or below Mean Lunar Surface} \quad (9)$$

where:

$\vec{V}sm$	=	Velocity in stable member coordinates
SNMB	=	Stable member to navigation base matrix
A	=	Matrix for radar antenna position 1 or 2
$\vec{V}$ ant	=	Velocity in antenna coordinates
Hmeas	=	Computed altitude
Hslant	=	Rs'
unit $\vec{R}$	=	Position Components
H beam ant	=	Range beam orientation angle
Rm	=	Distance from SC to moon's center
Rm(anwg)	=	Radius of moon (5,702,395 ft).

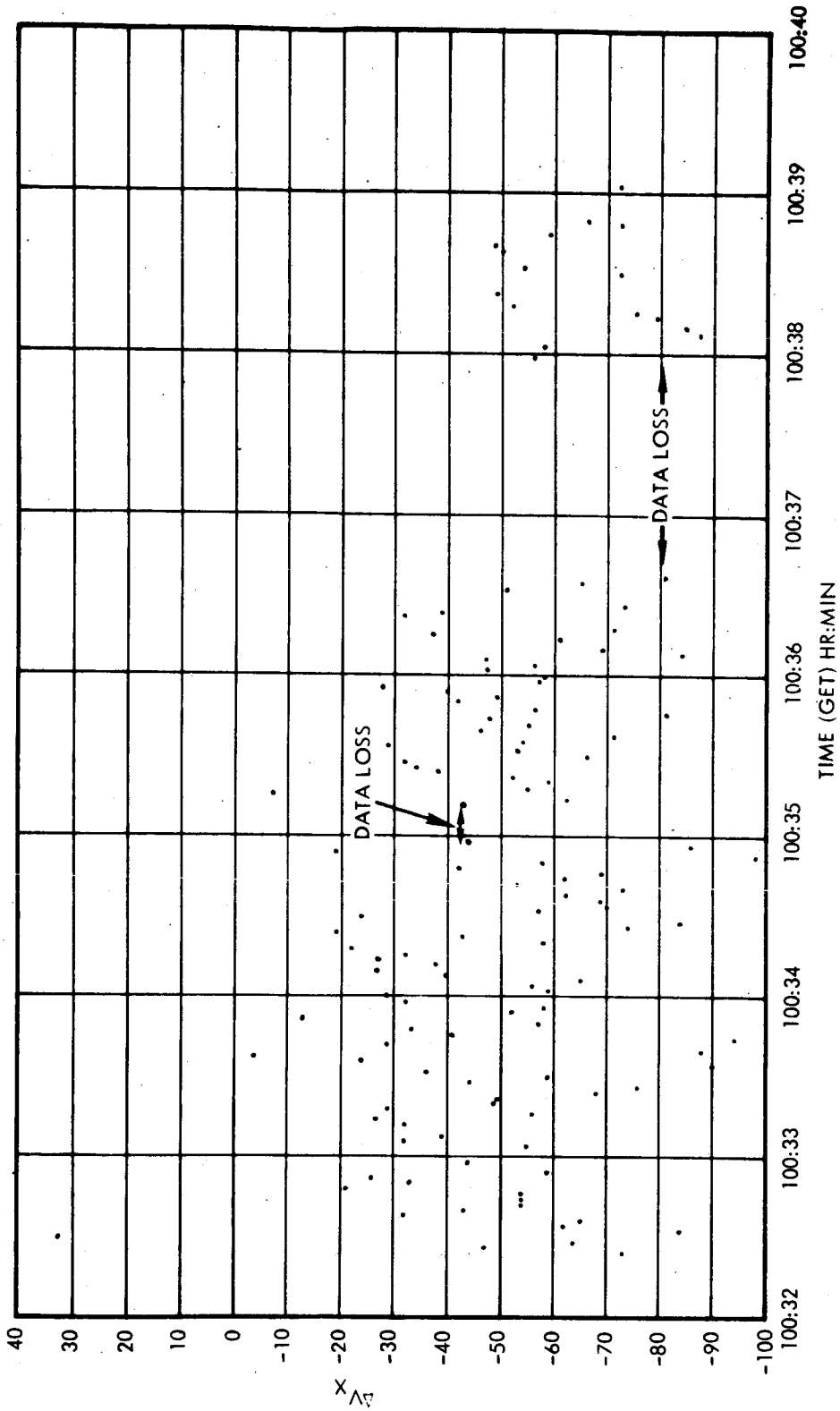

Figure 9-1 LR VELOCITY MINUS G&N VELOCITY (X COMPONENT)

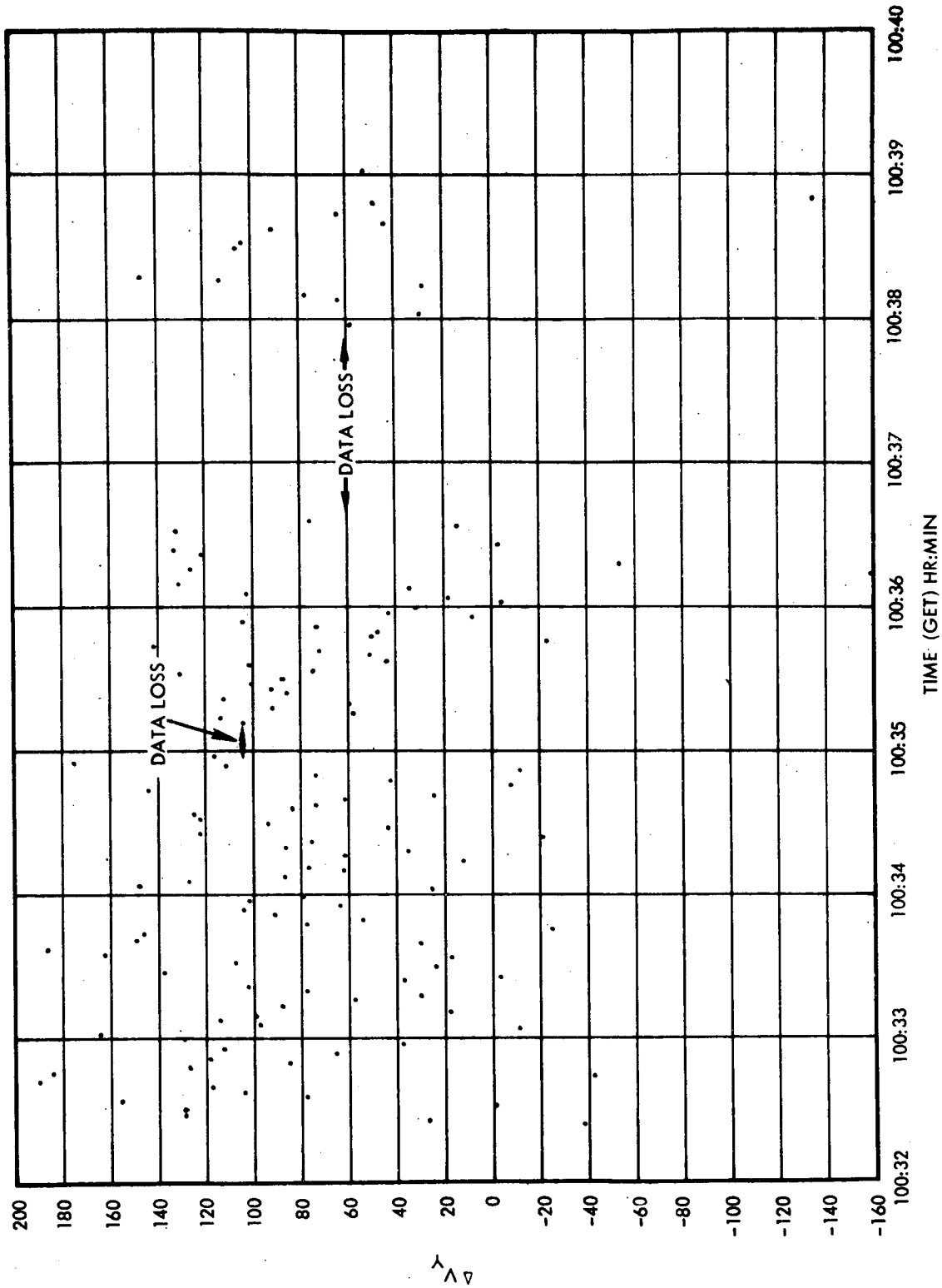

Figure 9-2 LR VELOCITY MINUS G&N VELOCITY (Y COMPONENT)

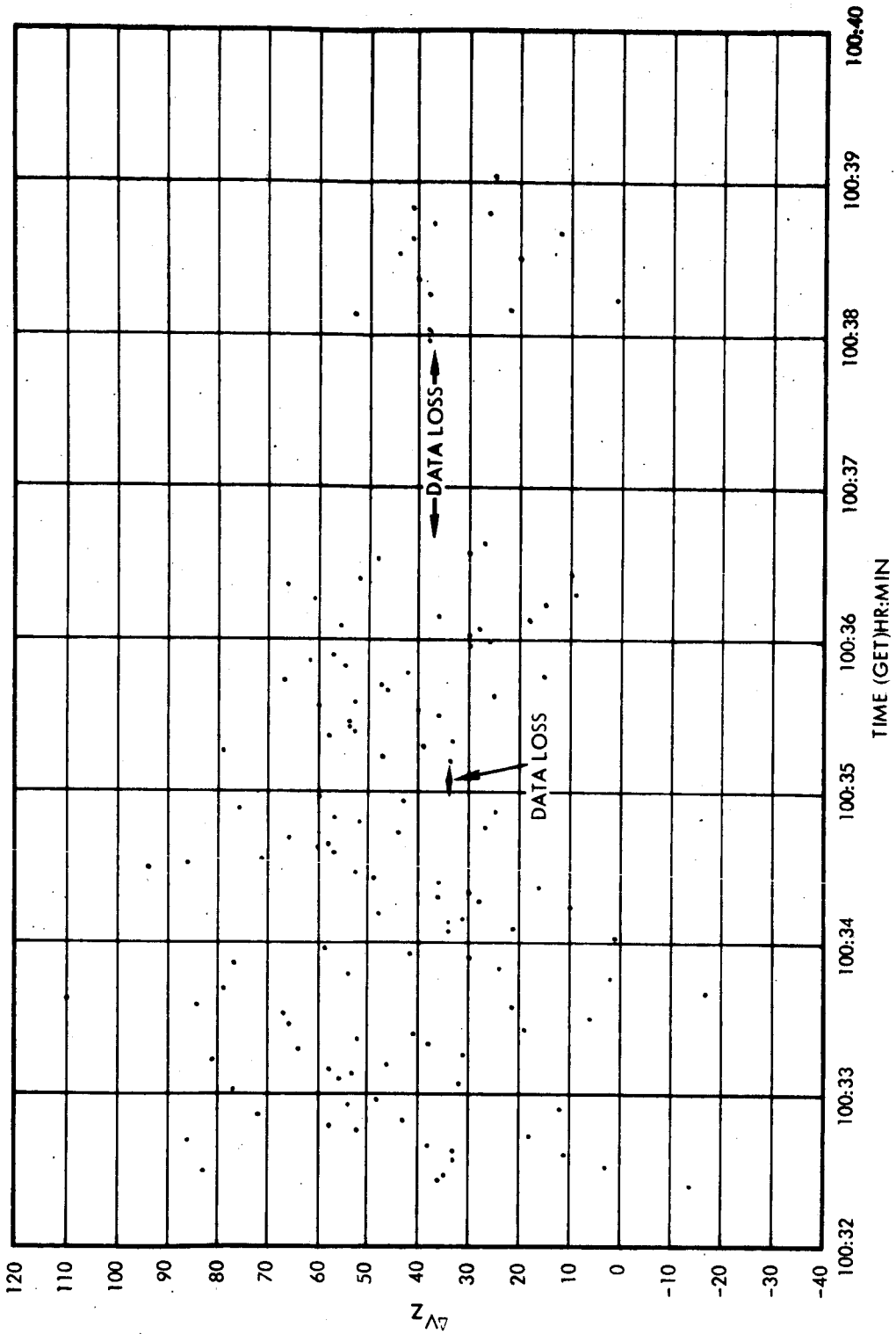

Figure 9-3 LR VELOCITY MINUS G&N VELOCITY (Z COMPONENT)

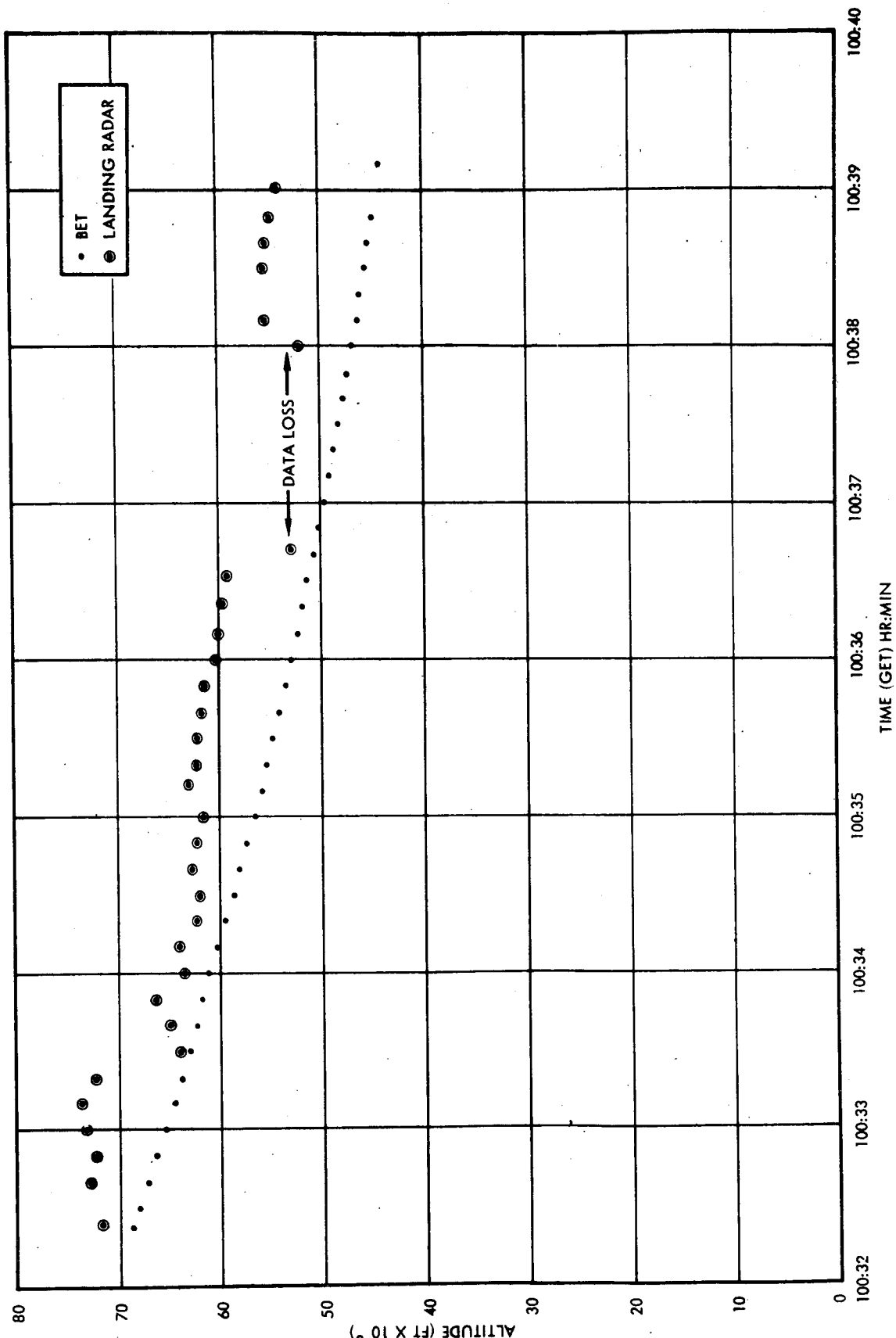

Figure 9-4 COMPARISON OF LR MEASURED ALTITUDE AND BET ALTITUDE

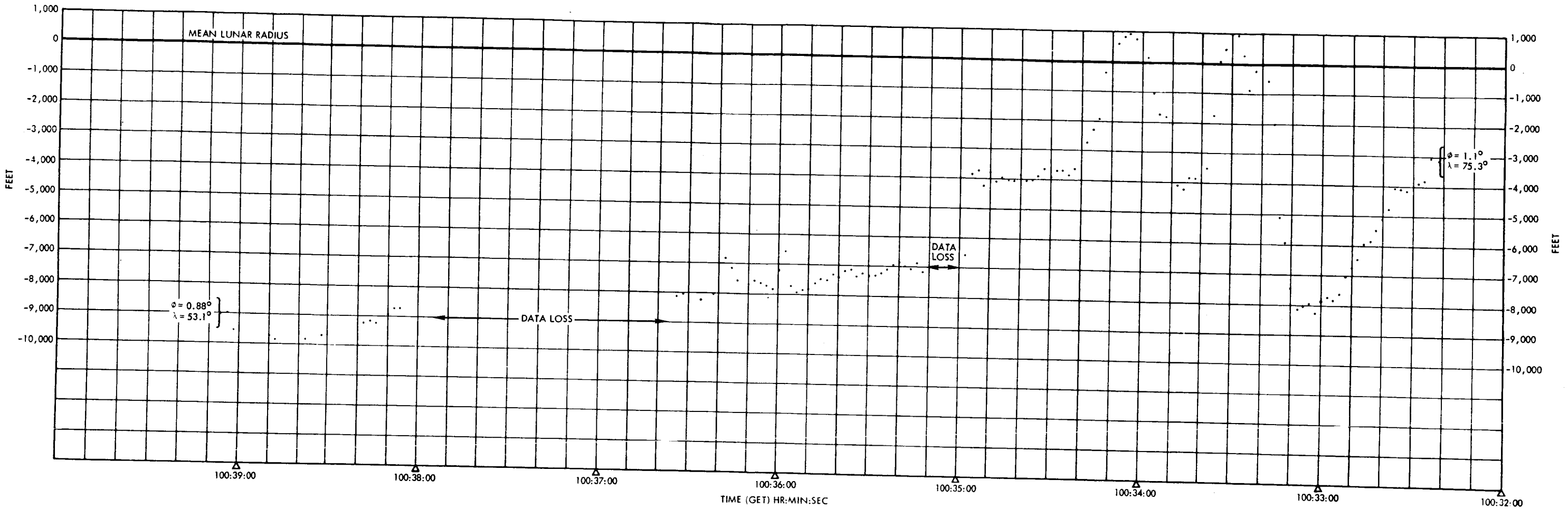

Figure 9-5 LUNAR SURFACE PROFILE MEASURED BY LANDING RADAR

10.0 CES PERFORMANCE

Apollo 10 was the first opportunity to exercise the Control Electronics Section in conjunction with the Abort Guidance System during a simulated lunar ascent. The burn was conducted unmanned after conclusion of the rendezvous period. Data indicates the CES performed nominally.

10.1 APS DEPLETION BURN

A 2-jet ullage burn performed under PGNCS control was initiated between 108:50:27 and 108:50:28 GET. (Time based on TLM sample rate.) The ullage duration was between 93 and 94 seconds. Before astronaut exit from the LM the AGS was setup and targeted such that an "engine on" command was available at the nominal burn time. Between 108:52:04.3 and 108:52:05.3 AGS control was selected by uplink. At 108:52:05.36 (TLM sample rate 5/sec) the AGS started the APS engine. Fuel depletion occurred at 108:56:14.36; yielding a burn duration of 4 minutes 9 seconds.

Items of significant interest appearing in the data that were investigated are discussed below:

1) Jet pulse duty ratio. The APS fixed engine thrust vector is nominally offset from the cg with near full tanks and this offset caused a moment of 717.5 ft-lbs (3500 lbs x .205 ft) at APS ignition. After ignition the thrust offset was balanced by the pulsed firings of jets (balanced couples) 1 and 4 U and 2 and 3 D. The pulse frequency was 9.5 H_z. Referring to Figure 10-1, one may observe that during nominal operation the pulse duty ratio at 9.5 H_z should be 35%. Assuming nominal jet thrust and a total 4-jet moment of 2200 ft-lbs, a 35% duty ratio would compensate for an APS thrust offset of 770 ft-lbs (2200 ft-lbs x .35). (770/ 717.5 - 1) x 100 = 7.31% error. This error is minimal and is considered acceptable.

2) cg travel. As the burn progressed the cg moved towards the thrust vector and was nearly coincident with the thrust vector at cutoff. At cutoff the pulse frequency was approximately 0.5 H_z, the pulse

duty ratio was about 5%, and the on times about 14 milliseconds. Again these figures agree favorably with the nominal design. Motion of the cg was as predicted by the Grumman FCI simulation runs.

10.2 COASTING FLIGHT

Following the APS burn to depletion several tests were performed to obtain data on AGS/CES control modes in coasting flight. Vehicle dynamics were observed with the CES in wide and narrow deadband attitude hold. Satisfactory performance was observed.

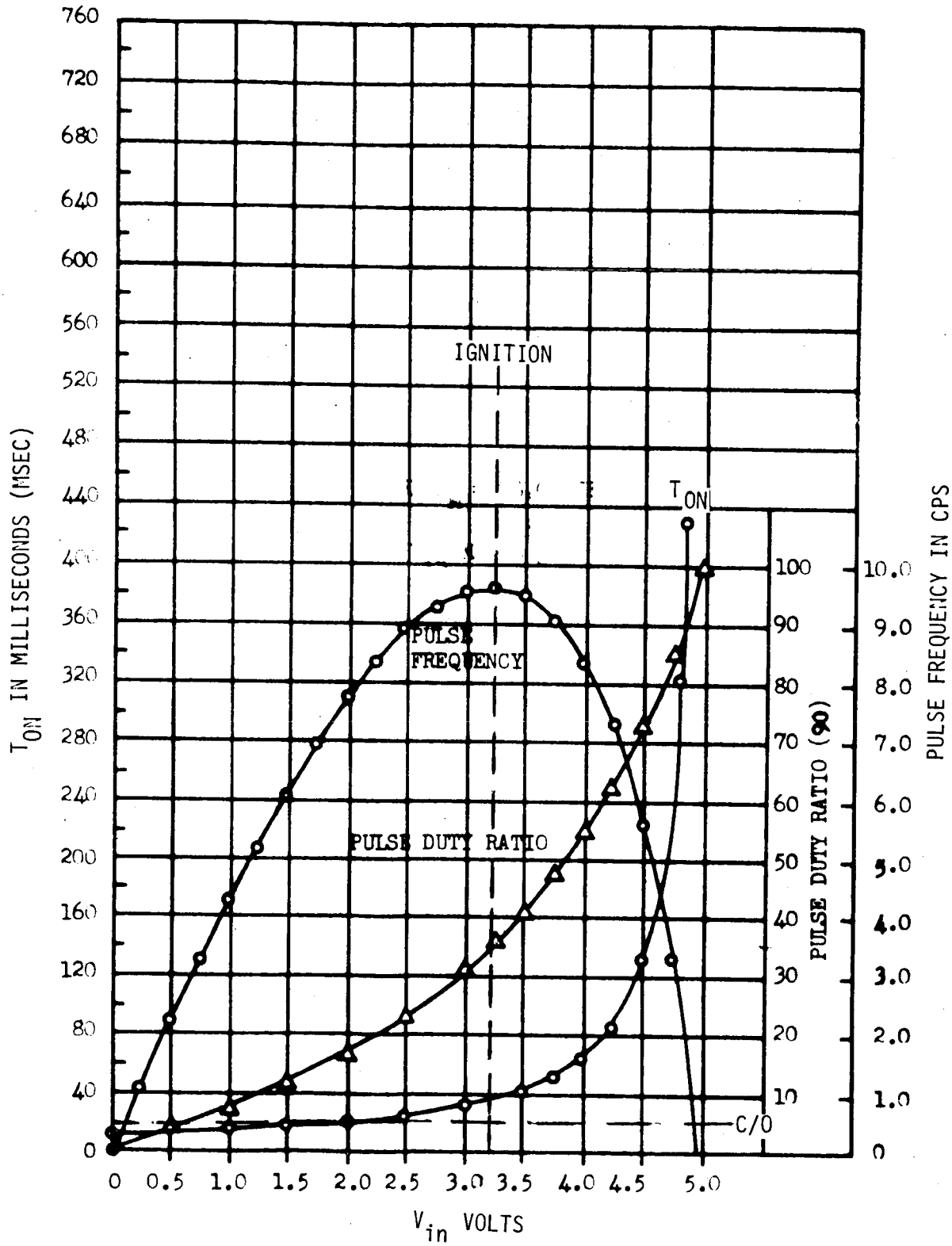

Figure 10-1 PULSE RATIO MODULATOR CHARACTERISTICS

REFERENCES

1. MSC-00126, "Apollo 10 Mission Report," dated August, 1969.

2 TRW Report 11176-H095-RO-00, "Apollo 7 Guidance, Navigation & Control Performance Analysis dated 20 December 1968.

3. TRW Report 05952-H546-RO-00, "Apollo 6 Guidance and Navigation Error Analysis - Final Report," dated 28 June 1968.

4. MIT/IL R-567, "Guidance System Operation Plan, Section 3," dated December, 1968.

5. NAS 9-4810, "LEM G&C Data Book," Revision 1, 1 June 1968, Change A, 1 December 1966, Submittal No. S-39.

6. NASA SNA-8-D-027 (II) Rev. 1, "CSM/LM Spacecraft Operational Data Book, Volume II - LM Data Book, Part I," Revision 1, dated 15 March 1969.

7. TRW Report 0 3358-6134-RO-00, "LM AGS Capability Estimate," dated 30 September 1968.

8. GAEC report LSP-500-1,"Abort Guidance Section Software GFE Performance and Interface Specification," dated August, 1966.

9. TRW Report 03358-6151-RO-00, "LM AGS Postflight Analysis Report (Apollo 9)," dated June, 1969.

APPENDIX A

AGS ANALYSIS METHODS

1.1 DATA SOURCES

There are two possible sources of data for comparison with AGS data; namely,

a) PGNCS acceleration and angle data.

b) Radar tracking data.

The data that has been used to measure AGS performance during the flight is the PGNCS data. The reasons for this are:

a) PGNCS, like AGS, is an inertial measurement unit and thus senses the same quantities, that is, acceleration, or velocity changes, and angular rotations.

b) PGNCS accuracy is high relative to the required AGS performance levels.

c) Radar data does not measure LM attitude.

d) Radar velocity data, while very accurate when appropriately smoothed, does not provide as high a measurement accuracy of velocity transients as PGNCS.

e) Radar data, unlike PGNCS, would have to be corrected to eliminate gravity and geoidal effects.

The PGNCS data that are used in the postflight analysis consist of six quantities: three measured velocities and the three gimbal angles. The velocities each represent the accumulation of inertial velocity during a two second interval along an inertial platform axis. The gimbal, or Euler, angles are a measure of the orientation of the LM body axes relative to the PGNCS platform.

1.2 ANALYSIS PERFORMED

The three basic errors discussed in this report are: accelerometer bias, gyro bias (or drift), and direction cosine misalignment. Accelero-

meter errors are modeled as biases. During non-thrusting intervals this bias quantity does, in fact, represent the accelerometer static bias. During thrusting intervals this error (apparent bias) can be attributed to static bias, dynamic bias, accelerometer scale factor, or accelerometer misalignment. These effects are generally inseparable.

Gyro errors are also modeled as fixed drifts. These apparent fixed drifts include dynamic errors, g sensitive errors, scale factor and misalignment errors. The effects of Y and Z gyro drifts will be observed in the velocity data across a burn as well as in the angular data. X gyro drift is unobservable in the velocity domain because the velocity change during the burn is along the X axis. Direction cosine misalignment is modeled as a constant angular error initialized at the beginning of each burn and includes the initial AGS direction cosine alignment errors and the system drift between the time of alignment and the start of the burn.

1.3 ANALYSIS COMPUTATIONS

Three computer programs are used to process the AGS data. The AGS Edit Program (Figure A-1, Block 1) is used to edit the telemetry data, merge and interpolate PGNCS gimbal angles with AGS data and compute quantities including body thrust acceleration (A_A), direction cosines from the gimbal angles (α_G), body turning rates from both AGS and gimbal angle data (ω_A, ω_G), and the integral of body rate differences $\int(\omega_A, \omega_G)$. This integral indicates the drift of each AGS gyro if no PGNCS drift error is present. Thus, gyro bias is computed from this data. Also, initial misalignment is computed by subtracting CDU angles from equivalent angles computed from the AGS direction cosine matrix at the initial time.

The AGS Error Analysis Program (EAP Figure A-1, Block 3) computes the partial derivatives of thrust velocity and accumulated angular drift with respect to the modeled AGS errors. These partials multiplied by the calculated error coefficients of the modeled AGS errors (Ki) represent the velocity and angular drift errors accounted for by these

modeled errors. Hence, in Block 4 of Figure A-1 the components of gyro bias (K1 $\partial V_A/\partial G_B$), initial misalignment (K2 $\partial V_A/\partial IM$), and accelerometer bias (K3 $\partial V_A/\partial A_B$) are subtracted from the AGS minus PGNCS velocity residuals in order to check how much residual error is unaccounted for by the modeled errors.

The AGS Data Comparison Program computes AGS/PGNCS thrust velocity and angular differences in body coordinates. When PGNCS accelerometer data is transformed through gimbal measured transformation (α_G) no AGS or PGNCS gyro error is involved because the gimbals measure the orientation of the body axes relative to the PGNCS platform independent of any gyro drift. Thus, the velocity residual is only due to accelerometer differences (Block 2). Accelerometer biases are therefore computed from this data. When PGNCS accelerometer data is transformed through AGS direction cosines, AGS to PGNCS misalignment errors are present in the velocity residuals. By removing the calculated gyro drift, initial misalignment and accelerometer errors (Block 4) the velocity residuals should be nulled. Likewise, the angle residuals, $\int(\omega_A - \omega_G)$, are compensated for by the calculated gyro drift and initial misalignment. They too should be nulled. This process should complete the fitting. Recycling through the process can be done if misfit residuals are seen.

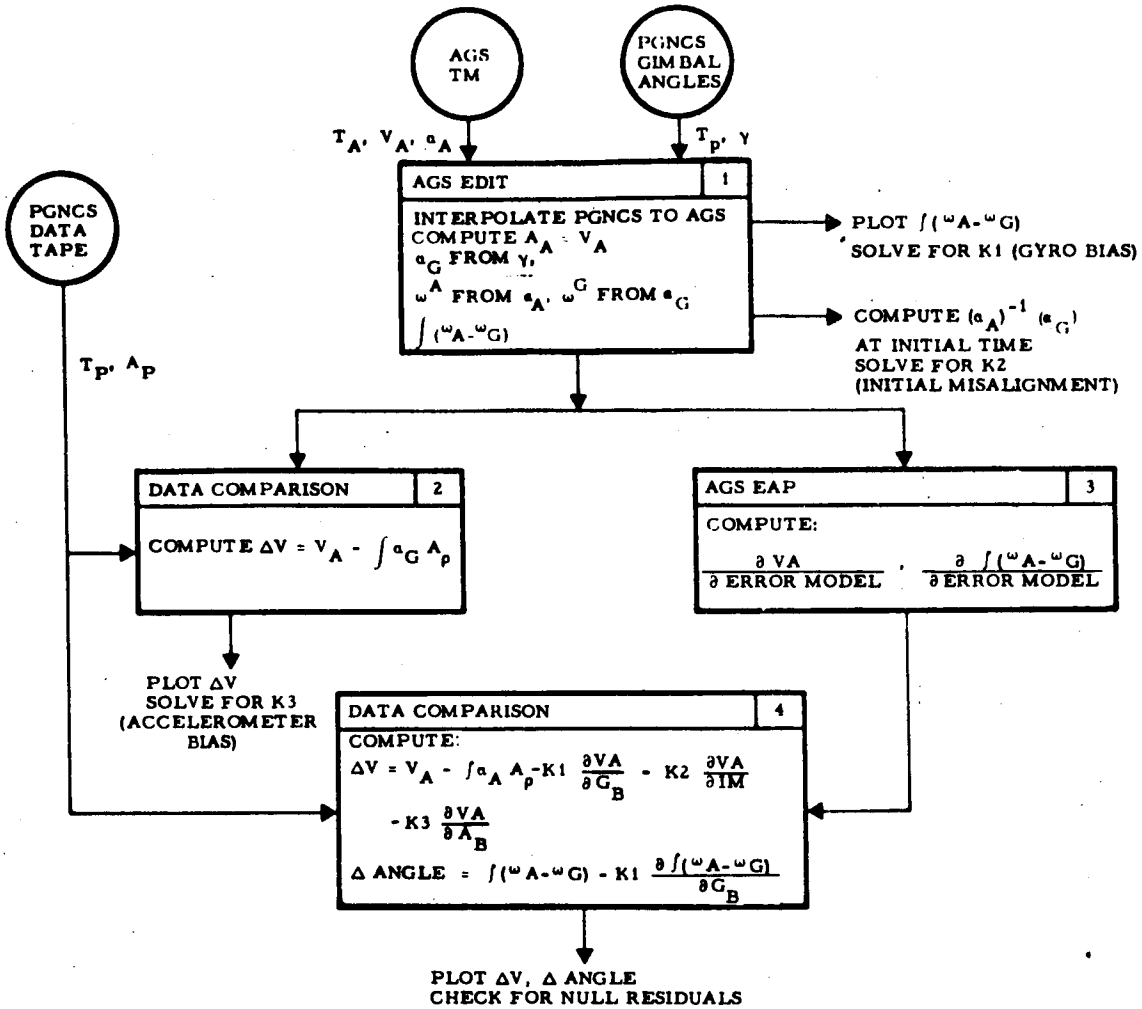

Figure A-1 POSTFLIGHT ANALYSIS BLOCK DIAGRAM

T_A = AGS Time

T_P = PGNCS Time

V_A = AGS Body Thrust Accumulation

α_A = AGS Direction Cosines

γ = Gimbal Angles

A_A = AGS Body Thrust Acceleration

α_G = Direction Cosines from Gimbal Angles

ω_A = Body Rates from AGS

ω_G = Body Rates from Gimbal Angles

$\int(\omega_A - \omega_G)$ = Accumulated AGS Body Angular Difference

K1 = Gyro Bias Coefficients

A_P = PGNCS Platform Thrust Acceleration

$V_A - \int \alpha_G A_P$ = Velocity difference due to accelerometer errors

K3 = Accelerometer Bias Coefficient

$K1 \frac{\partial V_A}{\partial G_B} = K1 \times \frac{\partial V_A}{\partial \text{Gyro Bias}}$ = Velocity Difference due to K1 units of Gyro Bias.

$K3 \frac{\partial V_A}{\partial A_B} = K3 \times \frac{\partial V_A}{\partial \text{Accelerometer Bias}}$ = Velocity difference due to K3 units of Accelerometer Bias

K2 = Direction Cosines Misalignment Coefficient.

$K2 \frac{\partial V_A}{\partial IM} = K2 \times \frac{\partial V_A}{\partial \text{Misalignment}}$ = Velocity Difference Due to Direction Cosine Misalignment.

$V_A - \int \alpha_A A_P - K1 \frac{\partial VA}{\partial G_B} - K2 \frac{\partial VA}{\partial IM} - K3 \frac{\partial VA}{\partial A_B} =$

= Velocity Difference Compensated for all errors.

$K1 \frac{\partial \int(\omega_A - \omega_G)}{\partial G_B}$ = Body Coordinate Angular Differences Due to Gyro Bias

$\int(\omega_A - \omega_G) - K1 \frac{\partial \int(\omega_A - \omega_G)}{\partial G_B}$ = Compensated body Coordinate Angular Difference.

Table A-1 KEY TO ANALYSIS BLOCK DIAGRAM (Figure A-1)

NASA — MSC